Etude de l'effect thermoélectrique magnétique en solidification directionnelle d'alliages Al-Cu.

Jiang Wang

UNIVERSITÉ DE GRENOBLE

THÈSE

Pour obtenir le grade de

DOCTEUR DE L'UNIVERSITÉ DE GRENOBLE

Spécialité : **Matériaux, Mécanique, Génie civil, Electrochimie**

Arrêté ministériel : 7 août 2006

Et de

DOCTEUR DE L'UNIVERSITÉ DE SHANGHAI

Spécialité : **Métallurgie des métaux ferreux**

Présentée par

« Jiang / WANG »

Thèse dirigée par **« Yves/FAUTRELLE » et**
codirigée par **« Zhongming/REN »**

préparée au sein du **Laboratoire SIMAP-EPM**
dans **l'École Doctorale I-MEP2**
et de **Key Laboratoire de la métallurgie avancée**
dans **UNIVERSITÉ DE SHANGHAI**

Etude de l'effet thermoélectrique magnétique en solidification directionnelle d'alliages Al-Cu

Thèse soutenue publiquement le **« 18.10.2013 »**, devant le jury composé de:

M. Alain JARDY
Directeur de Recherche au CNRS – IJL (Président)
M. Claude ESLING
Professeur Université de Metz (Rapporteur)
M. Xiaodong WANG
Professeur Université de l'Académie des sciences de Chine (Rapporteur)
M. Yves FAUTRELLE
Professeur Institut polytechnique de Grenoble (Membre)
M. Zhongming REN
Professeur Université de Shanghai (Membre)

Acknowledgement

Time flies, three years' PhD life flashed by. When I stand at the occasion of graduation, many appreciations beyond words swarm into my heart. However, if it has to be put into words, thousands of words of gratitude can be merged into one sentence --- Thank you all!

I greatly thank my two supervisors, who are Prof. Yves Fautrelle, from Institute National Polytechnique de Grenoble in France, and Prof. Zhongming Ren, from Shanghai University in China, for their continuous supports, helpful guidance and meticulous cares. Without the opportunity they gave me, I cannot spend the last two years of my PhD in SIMaP/EPM laboratory that the global top-ranking one in this field; without their guidance I cannot realize and rectify my faults in time; without their understanding I cannot accomplish my PhD thesis such smoothly. More important, their profound knowledge, humble behavior and kind attitude have been deeply engraved in my heart, and this will guide me in the future.

At the same time, I also want to express my sincere gratitude to Prof. Yunbo Zhong who is my secondary supervisor from Shanghai University in China for his supports; to Dr. Xi Li (Prof. Fautrelle and Ren's previous co-supervised PhD student), my senior fellow apprentice, for his helps when I just arrived at France. On the other aspect, in SIMaP/EPM laboratory, I am indebted to Dr. Yves du Terrail, Dr. Roland Ernst, Dr. Annie Gagnoud and Dr. Olga Budenkova for their helps on the numerical simulations; to Mr. Christian Garnier, Patrick Petitpas and Bon Denis for their helps on the preparation of my experiments; to Mrs. Khadija Rassouli for her helps on my daily documentary works; to Jacqueline Etay for her fruitful discussions.

Gratefully acknowledgment is also given to Prof. Henri Nguyen-Thi, Mr. Georges Salloum Abou Jaoude and Dr. Nathalie Mangelinck-Noel from Aix-Marseille University in France for their helps on the synchrotron X-ray observation experiments; to Prof. Andris Bojarevics, Prof. Leonid Buligins and Dr. Imants Kaldre from University of Latvia in Latvia for their helps on the design of magnet system which used by in-situ observation experiments; to the staffs who work on the BM05 beamline of European Synchrotron Radiation Facility (ESRF, Grenoble, France) for their helps when I performed experiments there. And moreover, many thanks are given to the colleges/friends who have given me many helps without mentioning all their names because I fear of omitting any one of them.

At last but the important as well, I would love to express my best appreciation to my parents and parents in law, although they are in China, their selfless dedications support me walking toward my dream. I would love to say 'thanks' to my wife, Jin Shi, although the

gratitude of mine has been beyond such words. During the past more than ten years, your accompanying, supports, understanding and cares make me pass all the difficulties I met. Without their love, I cannot walk so far and so smoothly.

行愈远，思愈甚；

然，读书尚未万卷，行路不足万里；

故，秉报国为民之心，存上孝高堂之念；

又，卷席上路，以成吾栋梁之才。

Jiang WANG

June 2013 Grenoble

Résumé

Nous étudions l'effet thermo-électrique et les phénomènes qui en résultent, forces et les courants thermoélectriques (TEC) sous l'action d'un champ magnétique externe imposé lors de la solidification d'alliages métalliques. Nous avons utilisé des simulations numériques, des observations directes et des examens de laboratoire. L'interaction entre les courants thermo-électriques et le champ magnétique externe lors de la solidification produit des forces électromagnétiques et donc un écoulement du métal liquide. Le résultat est nommé effet magnétique thermoélectrique (TEME). Les formulations de TEC, les forces et les équations gouvernant les écoulements TEM sont donnés. Afin de mieux prouver l'existence de la TEME, des expériences par méthode d'imagerie à rayons X menées au synchrtron ont été utilisées pour observer in-situ et en temps réel l'action directe des forces et les mouvements TEM pendant la solidification directionnelle des alliages Al-Cu. Nous avons montré la cohérence raisonnable entre les calculs analytiques et des simulations numériques qui ont été exécutes avec les mêmes conditions de traitement. En outre, la capacité des écoulements thermo-électriques à influer sur la microstructure lors de la solidification directionnelle est expérimentalement évaluée dans les autres cas en réalité. La solidification directionnelle d'une seule phase de formation des alliages Al-Cu sous divers champs magnétiques montre que les écoulements TEM sont capables de modifier la forme de l'interface liquide-solide conduisant à des morphologies différentes. L'effet le plus intense se produit dans différents champs magnétiques pour différentes morphologies, en effet, le champ magnétique élevé est nécessaire pour la morphologie à une plus petite longueur typique. Ceci est en accord avec le comportement des vitesses de TEM qui varient avec les champs magnétiques imposés ainsi que les différentes échelles de longueur typique. Cette variation est confirmée par des simulations numériques 3D. Nous montrons que les dendrites primaires et à l'avant de la phase eutectique, peuvent être modifiés par les mouvements TEM et les forces de TEM dans le solide pour améliorer la croissance de la phase de Al_2Cu facettes primaire pendant la solidification des Al-40wt%Cu hypereutectiques. Le mécanisme de renforcement de la croissance de la phase facettes Al_2Cu est confirmé par à électronique observation au microscope transmission, et la raison de la formation de la structure de croissance de couple de Al-26wt% Cu alliages est vérifiée par le test de l'analyse thermique différentielle. Ainsi, nous pouvons affirmer que le champ magnétique élevé facilite la formation de la structure de la croissance de couple pour hypoeutectiques alliages Al-Cu, et favorise la croissance de la phase Al2Cu primaire pour hypereutectiques Al-Cu alliages.

Mots clés:

- ✓ Courants thermoélectriques (TEC)
- ✓ Effet magnétique thermoélectrique (TEME)
- ✓ Forces magnétiques thermoélectriques (TEM forces)
- ✓ Ecoulements magnétiques thermoélectriques (TEM flows)
- ✓ Imagerie par rayons X synchrotron
- ✓ Solidification directionnelle
- ✓ Simulation numérique
- ✓ Champ magnétique
- ✓ Alliage Al-Cu

Abstract

We have investigated the thermoelectric magnetic (TEM) forces and flows resulting from the interaction between the internal thermoelectric currents (TEC) and the imposed external magnetic field during solidification. Numerical simulations, direct observations and experimental examinations were taken. As the natural phenomenon, TEC was discovered almost 200 years ago, therefore, our introduction begins from then on. It is shown that the interaction between TEC and magnetic field during solidification was aware in the context of a rising field named Electromagnetic Processing of Materials. After that, it is discussed how the TEC appear and the TEM effect (TEME, referring to both TEM forces and flows) behaves at the liquid-solid interface in directional solidification under external magnetic field. Meanwhile, formulations of TEC, TEM forces and flows are given, and numerical simulations of TEME are performed to visually display the TEM forces and flows. In order to further prove the existence of TEME, in-situ synchrotron X-ray imaging method was used to observe the direct resultant of TEM forces and flows during directionally solidifying the Al-Cu alloys. The observations show reasonable consistency with the analytical calculations and numerical simulations performed with the same process conditions. Except confirmation the existence of TEME, its abilities to affect the microstructure during directional solidification are experimentally investigated with the bigger samples. The single phase forming Al-Cu alloys are directionally solidified under various magnetic fields, which shows that TEM flows are capable to modify the shape of liquid-solid interface, and the most intensive affect occurs under different magnetic fields for different interface morphologies. Indeed, the smaller the typical length of the morphology is the higher the magnetic field is needed. This is confirmed by 3D numerical simulations and agrees with the estimating regulation of the velocity of TEM flows changing with magnetic fields for different typical length scales. Directional solidification of multiphase forming Al-Cu alloys under various magnetic fields shows that the mushy zone length (distance between the front of primary dendrites and eutectic phases) varies with the magnetic fields, which can be attributed to the redistribution of rejected solutes by TEM flows. In addition, apparent enhanced growth of the primary faceted Al_2Cu phase is found when Al-40wt%Cu alloys are solidified under sufficient high magnetic fields, which should be ascribed to the TEM forces acting on the solid because stresses are able to lead the formation of defects and thus benefit to the growth of faceted phase. This is confirmed by comparison of the dislocations in samples solidified without and with a 10T magnetic field via transmission electron microscopy observation. In another aspect, an almost

entire couple growth structure is achieved when Al-26wt%Cu alloys are directionally solidified under a 4T magnetic field. This can be explained by the effect of high magnetic field on changing the nucleation temperature and growth velocity of primary α-Al and eutectic phases respectively. Moreover, the differential thermal analysis test on the nucleation temperature of each phase verified this explanation. Therefore, we conclude that high magnetic field facilitates the formation of couple growth structure for hypoeutectic Al-Cu alloys, reversely, enhances the growth of primary phase for hypereutectic Al-Cu alloys.

Keywords:

- ✓ Thermoelectric currents (TEC)
- ✓ Thermoelectric magnetic effect (TEME)
- ✓ Thermoelectric magnetic forces (TEM forces)
- ✓ Thermoelectric magnetic flows (TEM flows)
- ✓ Synchrotron X-ray imaging
- ✓ Directional solidification
- ✓ Numerical simulation
- ✓ Magnetic field
- ✓ Al-Cu alloy

Résumé étendu

L’effet thermoélectrique magnétique (TEM) résulte de l'interaction entre le courant thermoélectrique interne (TEC) et le champ magnétique externe, ce qui entraîne l’apparition de forces électromagnétiques dites de TEM. De nombreuses indications expérimentales fragmentaires mentionnant l'existence de ces deux phénomènes ont été signalées dans la littérature lorsqu’un champ magnétique continu était appliqué lors de la solidification. Cependant, il manque des observations ainsi que des études systématiques. Par conséquent, il était nécessaire de découvrir de manière plus détaillée l'effet TEM dans le processus de solidification directionnelle sous l’influence d’un champ magnétique externe. Ce travail constitue une suite du travail de thèse de X. Li [1]. La présente thèse décrit l'effet TEM et donne un état de la littérature dans le chapitre 1. Une illustration numérique dans le chapitre 2 permet de montrer l’action des forces TEM dans une configuration proche de celle que l’on trouve en solidification. Les observations in situ par imagerie par rayons X synchrotron, détaillées dans le chapitre 3 ont donné la preuve de l’existence de ces phénomènes. L’'influence de l'effet TEM dans le processus de solidification directionnelle d’alliages Al-Cu à la fois monophasés et multiphasés dans un champ magnétique externe est analysée respectivement dans les chapitres 4 et 5. Enfin les conclusions générales obtenues et les perspectives sont données dans le chapitre 6.

Chapitre 1

Les écoulements magnétohydrodynamiques thermoélectriques (le même phénomène que nous avons appelé TEM) peuvent exister et affecter les procédés métallurgiques. Cela a été mis en avant en premier lieu par A. Shercliff, dans son article publié en 1979. Cependant, parce que ses principales attentions se sont concentrées sur les écoulements TEM dans les réacteurs nucléaires, la tentative d'analyse de ce phénomène en relation avec la métallurgie a d'abord été faite par certains anciens scientifiques de l'Union soviétique en application au procédés de croissance des cristaux [2-4], puis par d'autres lors de la solidification de alliages métalliques [5-7].

En 1981, Michelson et Karklin ont proposé un mécanisme selon lequel les courants générés par la force électromotrice thermique dans le corps de cristallisation pourraient affecter la croissance des cristaux si un champ magnétique était présent [2], Ils ont confirmé l'existence de TEC via la détection de l'évolution des champs magnétiques comme le montre la figure 1(a). Quelques années plus tard, une preuve explicite des écoulements TEM qui

influent sur la croissance de monocristaux a été donnée par Gorbunov en 1987 [3]. En effet, il a visualisé les écoulements TEM de In-Ga-Sn produits par un gradient de température imposé et un champ magnétique statique à la verticale de la surface de fondus. La Figure 1(b) montre la mesure de la vitesse de rotation de la surface du bain. On peut constater que la vitesse des écoulements atteint un maximum lorsque le champ magnétique est d'environ 0,1 T et diminue avec l'augmentation continue du champ magnétique. Le changement même de tendance a été confirmé par Kaddeche et al. [5] sept ans plus tard. En outre, Gorbunov a inversé la direction du champ magnétique, et la direction de la rotation de la surface a été inversée en même temps, ce qui pourrait démontrer que ces écoulements doivent être reliés au champ magnétique imposé. Après cela, Gorbunov et Lyumkis ont utilisé ce phénomène pour expliquer la forte déformation de la forme des cristaux produite lors du tirage de monocristal InSb qui croissent sous un champ magnétique. D'ailleurs, ils attribuent les stries périodiques de silicium dopé croissant dans un champ magnétique vertical à l'apparition d'écoulements TEM [4].

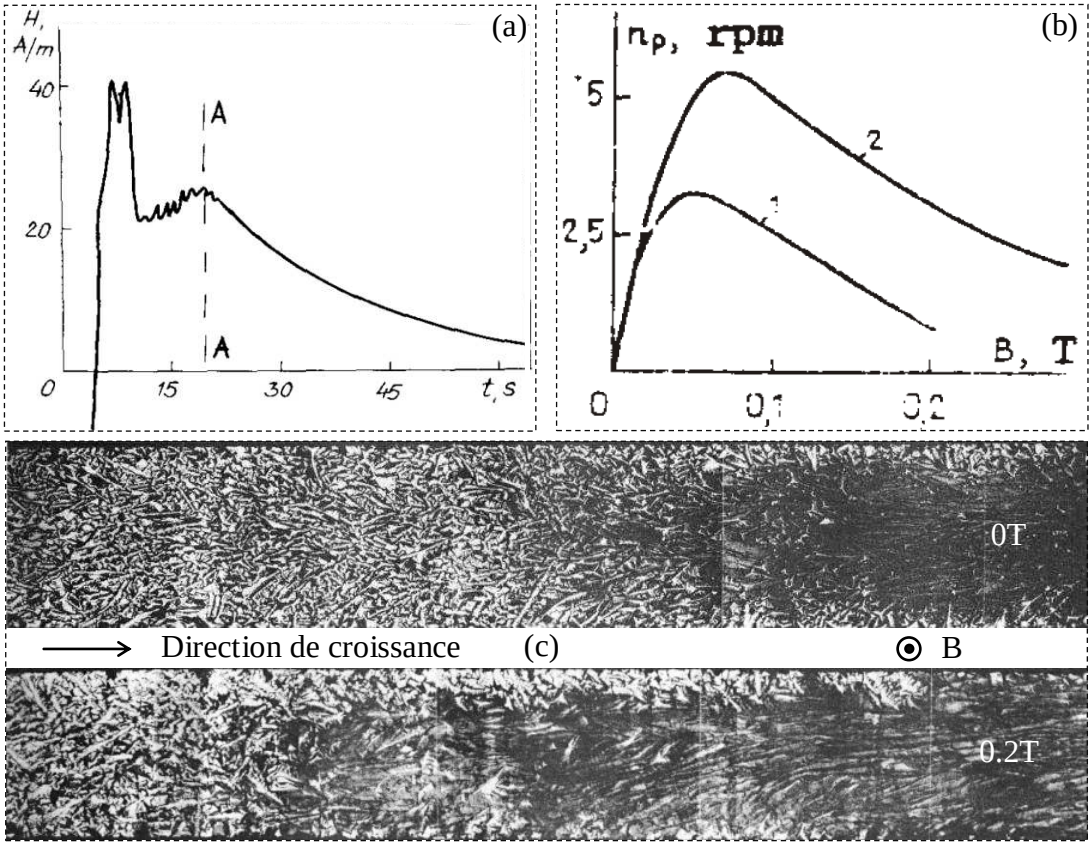

Figure 1 (a) variation temporelle de l'intensité du champ magnétique (H) à proximité d'un échantillon de cadmium solidifié, AA correspond au moment où le spécimen a été solidifié; (b) vitesse de rotation du liquide In-Ga-Sn: 1 et In-Sb: 2 en termes de densités de flux imposé de champ magnétique, (c) Bi-40at% alliages de Sn solidifiés, sans et avec un champ magnétique transversal.

L'exploration des écoulements TEM pendant la solidification des alliages métalliques a été mise en évidence en 1991. Alboussière, Moreau et Camel ont proposé que des

écoulements en régime dendritique peuvent exister pour améliorer le mélange des solutés, et ces écoulements pouvaient être produits par l'interaction entre les courants TEC et le champ magnétique imposé [8]. Afin de vérifier l'existence d'écoulement TEM dans le processus de solidification quand un champ magnétique externe est présent, ils ont réalisé une solidification directionnelle de Bi-Sn et des alliages Pb-Sn avec et sans champ magnétique. Il a été constaté que, pour l'alliage Bi-Sn, le transport solutal sous champ magnétique est plus élevé que celui obtenu sans champ magnétique, comme indiqué à la figure 1 (c), alors que pour Pb-Sn allié, aucun effet apparent n'a été détecté quand il y avait un champ magnétique externe. En outre, parce que le pouvoir thermoélectrique absolu du Pb-Sn est négligeable (ATP, 0.1μV / K) à comparer à Bi-Sn (70μV / K), ces résultats leur ont permis de faire valoir que les écoulements de TEM existaient [9]. Afin d'obtenir une meilleure compréhension, Moreau et al. ont construit un modèle numérique pour estimer la vitesse des écoulements TEM interdendritiques en 1994 [10], D'un autre côté, ils ont analysé les effets Seebeck et Peltier en l'absence de champ magnétique externe et ont constaté que ces deux effets ont déstabilisé l'interface liquide-solide. Cinq ans après, Lehmann et Moreau fournissent un autre modèle pour simuler les écoulements TEM dans la zone pâteuse, et affirment que l'écoulement TEM modifie la convection interdendritique [11, 12].

Parallèlement, les analyses de l'influence des écoulements TEM sur la croissance des cristaux ont été développées. Cröll et al. ont trouvé un nouveau type de stries de dopants prononcées et très différentes de celles provoquées par la convection naturelle ou thermocapillaire lors de l'élaboration de silicium par la méthode de la zone flottante sous un champ magnétique axial [13]. Ils ont pensé que les écoulements TEM pouvaient expliquer ces nouvelles stries. Khine et Walker ont étudié théoriquement les écoulements TEM lors de la croissance Bridgman de semi-conducteurs sous un champ magnétique intense axial et ont constaté que le changement de tendance de l'amplitude des écoulements TEM avec le champ magnétique imposé se comporte de la même manière que celle soulignée par Gorbunov [14]. En outre, ils ont estimé les amplitudes des composantes azimutales des écoulements TEM et ont trouvé qu'elles pouvaient atteindre plusieurs micromètres par seconde, ce qui pouvait générer des stries de rotation en phase de croissance des cristaux. Yesilyurt et al. ont simulé numériquement l'effet des écoulements TEM sur la croissance Bridgman de Ge1-xSix [15] et ont constaté que la convection méridienne avait modifié la composition et la forme d'interface de croissance. Après cela, ils ont prédit les écoulements TEM avec gravité variable [16] en optimisant leur modèle numérique. Les dernières recherches sur l'influence des écoulements TEM pendant la croissance cristalline ont été réalisées par Dold, Szofran, et Benz [17], qui

ont donné expérimentalement la preuve qu'il y avait une vitesse maximum de convection TEM alors que le champ magnétique imposé n'avait cessé d'augmenter.

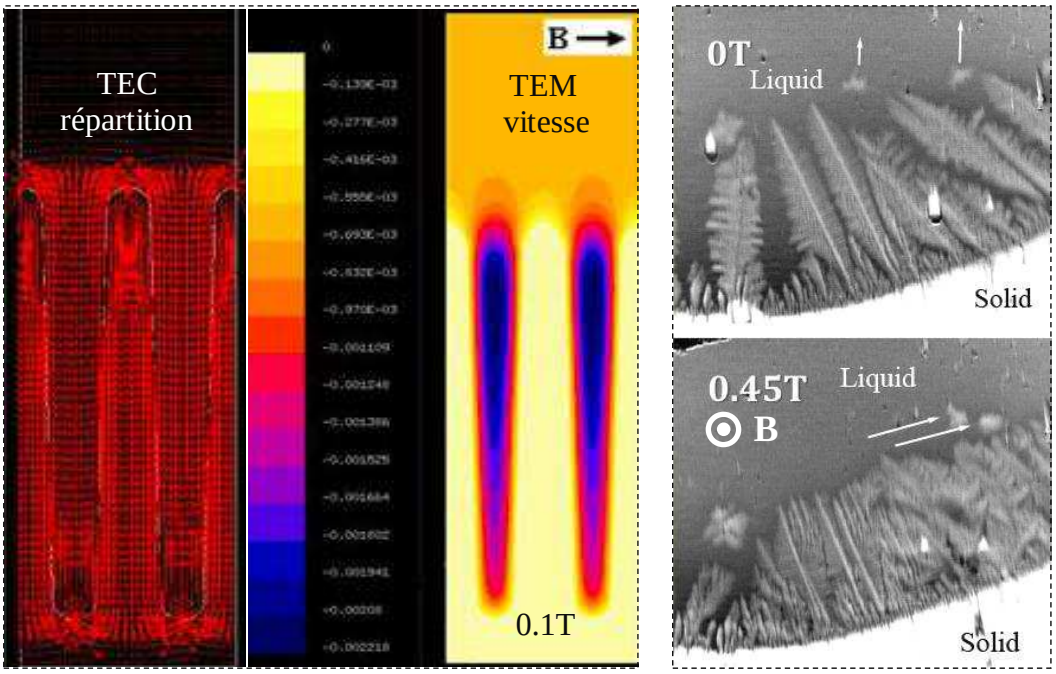

(a) (b)

Figure 2 (a) Calcul des courants électriques TE, quand on impose un champ magnétique transversal; (b) observation in situ d'écoulement TEM généré par un champ magnétique de 0.45T appliqué transversalement, par imagerie par rayons X synchrotron.

En 2002 et 2006, des recherches sur les effets des écoulements TEM pendant la solidification d'alliages métalliques ont été publiées par des chercheurs de l'Université Technique de Liaoning. Ils ont étudié l'influence des écoulements TEM sur la microstructure des Al-Cu et des alliages Al-Si et ont constaté que lorsque la solidification a lieu en présence d'un écoulement TEM de champ magnétique externe ce dernier est capable fait de modifier les structures des matériaux[18, 19]. Dans le cadre d'une coopération franco-chinoise entre les laboratoires SIMAP/EPM et l'Université de Shanghai des recherches ont été entreprises sur ce sujet et se poursuivent jusqu'à présent, animées par le professeur Yves Fautrelle et le professeur Zhongming Ren. En 2007, leur premier doctorant en co-tutelle, Xi Li, a commencé à étudier expérimentalement les écoulements TEM et ses influences sur la solidification en présence d'un champ magnétique externe. Il a constaté que les effets du champ magnétique varie avec différentes morphologies lors de la solidification directionnelle. En effet, plus la longueur du champ magnétique est petite, plus intense doit être le champ magnétique pour produire des écoulements TEM. En outre, il a constaté que les écoulements TEM turbulents peuvent se produire lorsque la solidification directionnelle a eu lieu sous un champ magnétique transversal des écoulements TEM peuvent apparaître [20-21]. En 2009, Cramer, Zhang, et Gerbeth ont publié leurs travaux numériques et expérimentaux sur les écoulements

TEM en étudiant ces écoulements dans une boîte carrée avec un gradient de température imposé et un champ magnétique. Ils ont constaté que les écoulements TEM étaient vigoureux et pouvaient brasser le liquide pendant les procédés métallurgiques [22]. Afin d'étendre les études précédentes, en 2011, Li et Gagnoud ont effectué les simulations d'écoulements TEM sous l'action d'un champ magnétique transversal faible [23] comme le montre la figure 2 (a), en accord raisonnableavec les résultats expérimentaux. Durant cette période, un autre travail remarquable a été réalisé par le professeur Yasuda du Japon [24-25]. en observant pour la première fois, in situ, les écoulements TEM pendant la solidification directionnelle d'alliages métalliques par imagerie par rayons X synchrotron comme dans la figure 2 (b). Avec l'augmentation du nombre de recherches sur les flux de TEM, ses influences dans des systèmes de plus en plus, on a remarqué et étudié. Jusqu'à présent, l'existence de flux de TEM avait été validé dans les superalliages DZ417 par Ren et.al [26], dans hypereutectique alliage Al-Al_2Cu par Shen et.al [27].

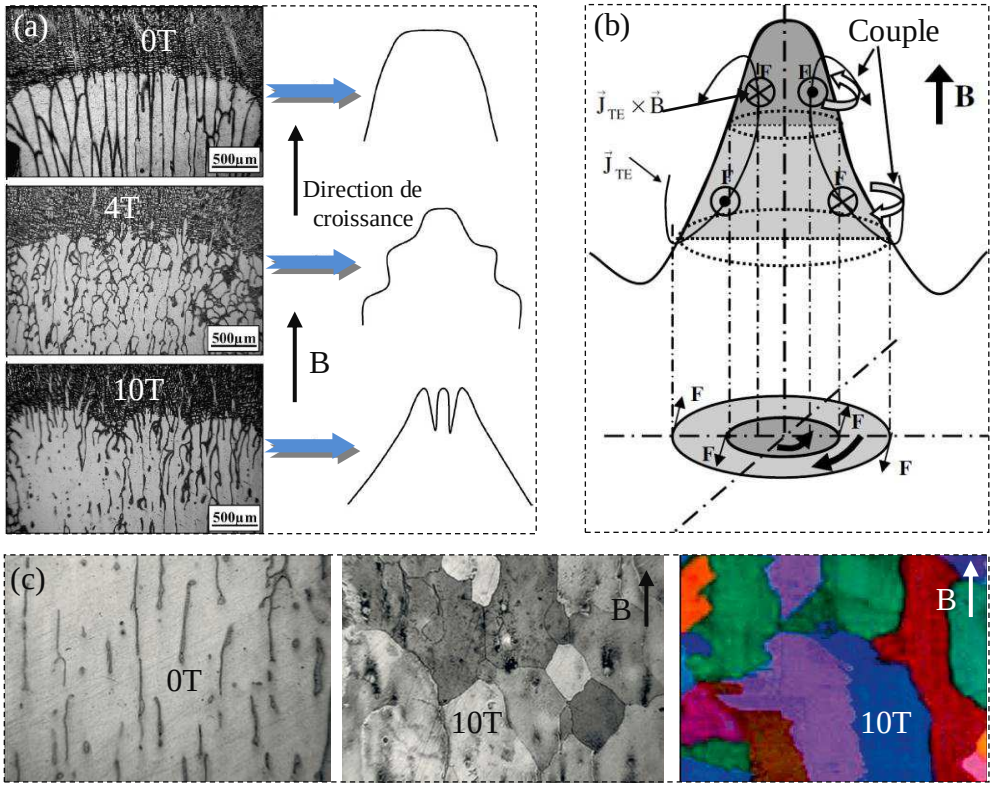

Figure 3 (a) exemple de branchement de la cellule d'Al-0.85wt% Cu solidifié à 5 μm/ s sous différentes intensités de flux de champ magnétique; (b) Illustration du couple provoqué par les forces de TEM de directions opposées au sommet et au fond d'une cellule ou dendrites, (c) et la carte Microstructure EBSD d'Al-4.5wt% Cu alliage solidifié à 5 μm / s avec et sans champ magnétique de 10T.

Il est bien connu que les écoulements TEM sont engendrés par la force de Lorentz induite par l'interaction entre le courant TEC et le champ magnétique imposé. Ces forces, appelées forces TEM, s'appliquent aussi sur le solide [28]. Cependant, les effets des forces TEM sur un solide ont été presque ignorés au tout début de leur découverte car ils étaient difficiles à

détecter. Les écoulements TEM peuvent être intensifs sous champs magnétiques modérés ou faibles [29]. En outre et jusqu'à récemment, la technologies sur les champs magnétiques élevés n'a pas permis le développement des recherches sur les forces TEM sur le solide en phase de solidification [30]. Grâce au développement rapide des matériaux supraconducteurs, on peut aujourd'hui utiliser des champs magnétiques intenses pour la solidification en laboratoire ou pour la métallurgie industrielle [31]. Sous des champs magnétiques élevés, les forces TEM peuvent être très grandes, et compte tenu de l' intérêt croissant pour la solidification sous des champs magnétiques élevés [32], il est intéressant de découvrir comment les forces TEM peuvent influencer un solide. En effet, quelques tentatives pionnières ont déjà été faites.

L'effet des forces TEM sur un solide a été explicitement souligné par Li, Fautrelle, et Ren en 2007 [33]. En analysant les écoulements TEM ils ont constaté que les cellules ont été brisées et l'interface liquide-solide est devenu inégale sous un champ magnétique supérieur. Les écoulements TEM devraient être amortis en raison du champ magnétique élevé. Mais la rupture des cellules et de l'interface peut être causée par les forces TEM dans le solide. En ce qui concerne la rupture des cellules ou dendrites [34], ils ont étudié l'évolution morphologique des cellules et des dendrites lors de la solidification directionnelle dans un champ magnétique élevé. Ils ont mis en évidence que les cellules et les dendrites sont tordues et déviées par rapport à la direction de solidification. Pour des taux de croissance plus faibles, nous avons observé une augmentation de la ramification des troncs primaires ainsi qu'un fractionnement de la pointe des cellules comme le montre la figure 3 (a). Par ailleurs, en 2009 [35], en combinant avec les simulations numériques effectuées par Gagnoud et al. nous avons pu confirmer l'existence d'un couple sur la cellule ou sur les dendrites (figure 3 (b)) et souligner que ce couple peut déclencher la colonne de transitions équiaxes (CET) en cours de solidification directionnelle. Afin de prouver que la CET pouvait être déclenchée par les forces TEM, Li et al. ont réalisé une solidification directionnelle de divers alliages, tels que Al-Cu, Pb-Sn, superalliages, Zn-Cu, Al-Si et Al-Ni avec et sans champ magnétique élevé [36-38], comme le montre la figure 3 (c). L'analyse par diffraction d'électrons rétrodiffusés (EBSD) a confirmé la présence de CET avec les alliages appropriés et sous un champ magnétique suffisamment élevé. En ce qui concerne l'interface inégale [39-41], avec l'aide de Yudong Zhang et Claude Esling, Li et.al ont examiné le plan de désorientation locale des échantillons et ont constaté que l'inadéquation de cristal de l'échantillon solidifié sous champ magnétique 10T était plus sévère que celle sans champ magnétique. Ceci démontre l'existence de forces TEM. Pendant ce temps, considérant l'ensemble des résultats expérimentaux relatifs au changement de forme de l'interface et au fractionnement de l'interface plane, ils ont fait

valoir que les forces TEM sur un solide peuvent provoquer l'instabilité de l'interface lors de la solidification [42]. En effet, les contraintes à l'état solide peuvent changer le potentiel chimique et la tension de surface solide, et cela influence étroitement la stabilité de l'interface liquide-solide [43].

En étudiant en 1979 les écoulements de refroidissement métalliques dans un système de réacteur nucléaire, le professeur Shercliff a mis en évjdence l'existence d 'écoulements TEM pendant le processus métallurgique. L'effet TEM en cause ici, devrait toutefois être classé dans une nouvelle branche des procédés électromagnétiques des matériaux (EPM), en particulier dans le domaine de la solidification sous champ magnétique statique externe. Notons que ce sont les professeurs Youdelis et Dorward qui, en étudiant dans les années 60, l'influence du champ magnétique sur la solidification directionnelle d'alliages Al-Cu, ont donné les premières indications sur l 'existence d'écoulements TEM dans le processus de solidification [45].

Chapitre 2

Il est nécessaire à présent d'introduire l'effet thermoélectrique (TE) si nous voulons clarifier l'effet TEM dans la solidification. L'effet TE est un terme générique utilisé pour décrire les phénomènes de conversion directe des différences de température en tension électrique et vice-versa. Ceci englobe trois effets distincts : les effets Seebeck, Peltier et Thomson [46]. L'effet Seebeck a d'abord été découvert parmi les phénomènes thermoélectriques par un physicien allemand, Thomas Seebeck , en 1821 [47]. Il a constaté qu'un circuit constitué de deux métaux différents avec des jonctions à différentes températures pouvait dévier un aimant d'une boussole et a nommé ce phénomène : «effet magnéto-thermique». Un physicien danois Hans Christian Orsted a reconsidéré la découverte de Seebeck et a constaté qu'une force électromotrice apparaît dans deux matériaux différents. L'effet magnéto-thermique est devenu effet de thermoélectricité, puis effet Seebeck. L'effet Peltier a été découvert par un physicien français, Jean Charles Athanase Peltier, treize ans après la découverte de Seebeck. Il décrit un processus inverse de l'effet Seebeck : un courant électrique passant à travers les jonctions de deux métaux différents produirait du chauffage ou du refroidissement [48]. En 1838, Lenz a mis en évidence les relations entre le chauffage ou le refroidissement et la direction des courants [49]. Parce que la chaleur absorbée ou créée au niveau des jonctions est proportionnelle au courant électrique, un coefficient de proportionnalité appelé coefficient Peltier a été défini pour lier la chaleur et le courant [50]. En 1854 un physicien mathématicien britannique William Thomson (plus tard Lord Kelvin) a tenté d'établir une relation déterminant le coefficient Seebeck-Peltier à l'aide de la

thermodynamique [51]. L'effet Thomson révèle que la chaleur peut être absorbée ou produite lorsque le courant circule dans un milieu unique avec gradient thermique et le coefficient Thomson relie la chaleur aux deux courants électriques et au gradient thermique.

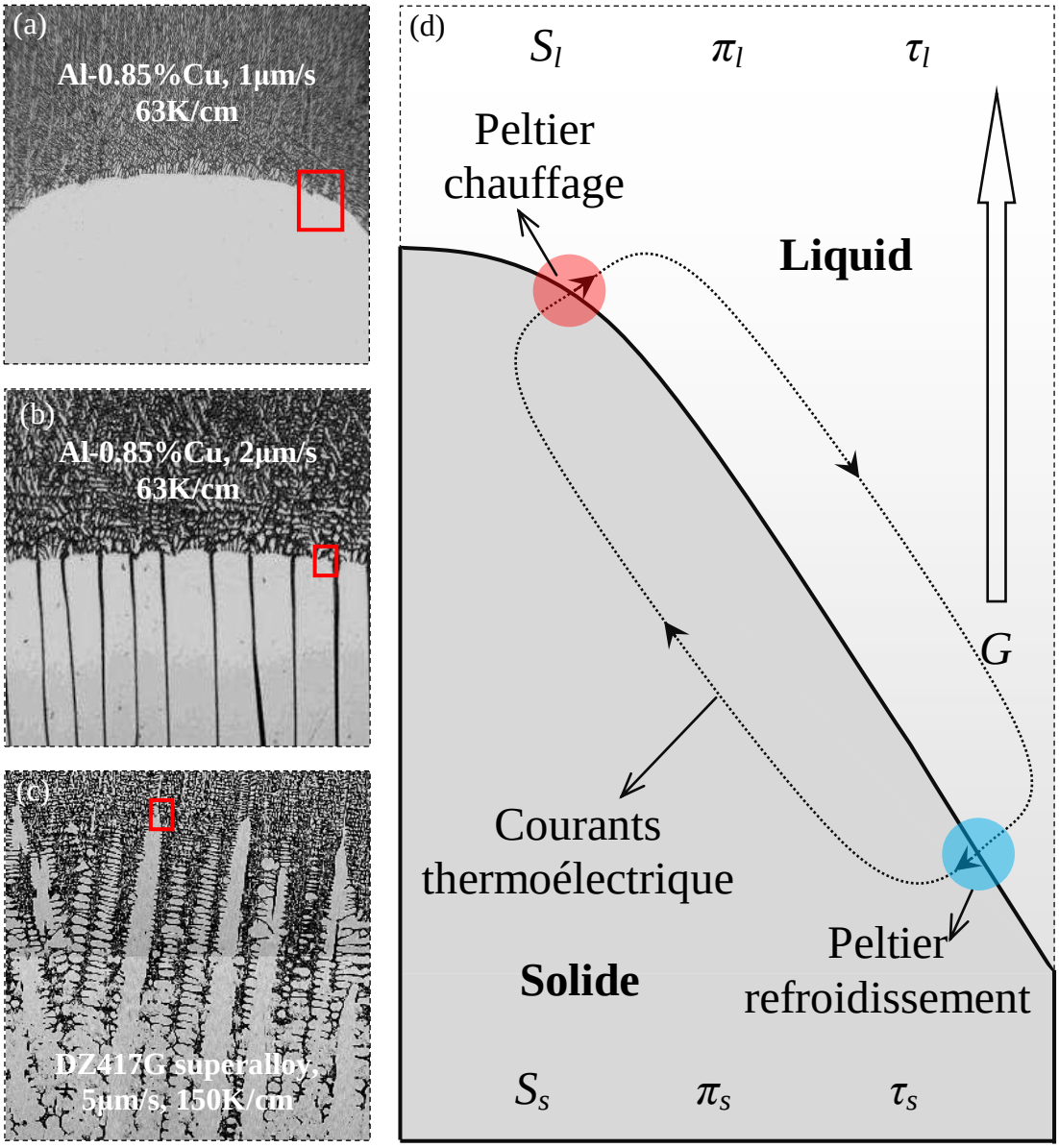

Figure 4 (a) interface plane; (b) interface cellulaire; (c) interface dendritique; (d) Illustration de l'effet TE se produisant au cours de la solidification directionnelle près de l'interface liquide-solide, G est le gradient thermique. S, π et τ représentent les coefficients Seebeck, Peltier et Thomson, respectivement, et les indices L, et S représentent les liquide et solide respectivement.

En introduisant l'effet TE, on peut constater que l'apparition de l'effet Seebeck ou thermoélectrique courants (TEC) doit être le principe des deux autres effets. Les conditions nécessaires pour avoir un effet TEC sont deux conducteurs différents connectés et une différence de température existant entre leurs jonctions. Il se trouve que l'interface liquide-solide dans le processus de solidification directionnelle répond à ces demandes. En règle générale, liquides et solides d'alliages ont des propriétés ATP et physiques telles que la conductivité thermique et électrique.Par conséquent le liquide et le solide au cours du

processus de solidification peuvent être considérés comme deux conducteurs différents et sont reliés les uns aux autres à l'interface. Lorsque l'interface liquide-solide n'est pas parfaitement plane, ce qui est le cas le plus courant, la composante du gradient thermique le long de l'interface existe. Un tel gradient est un facteur important pour l'apparition de courants TE dans le processus de solidification dirigée. En fait, comme le montre la figure 4 (a) à (c) l'effet TE peut avoir lieu dans ces trois morphologies de base plus communément aux interfaces liquide-solide. Considérons un élément de chaque type d'interface (par exemple un côté d'une interface plane de révolution, d'un côté de la pointe de cellules ou dendrites) et encerclé par les rectangles rouges dans la figure 4 (a) à (c), on peut constater que la géométrie comme dessinée dans la figure 4 (d) peut raisonnablement représenter ces trois morphologies typiques. En présence d'un gradient ascendant thermique on observe une différence de température entre le haut et le bas de l'interface. Les solides et les liquides ont des propriétés physiques d'ATP différentes. Le courant TE indiqué par le cercle en pointillés sur la figure 4 (d) est conforme à l'effet Seebeck. A la jonction entre le solide et le liquide, le chauffage ou le refroidissement Peltier peut apparaître comme indiqué par les taches rouges et bleues sur la Figure 4 (d). Pendant ce temps, le TEC dans chacun des milieux solide et liquide provoque l'effet Thomson. Dans les cas étudiés, l'effet Peltier et Thomson est négligeable.

Dans ces phénomènes, une fois imposé un champ magnétique externe, l'effet TEM apparaît. Quand les courants électriques et les lignes de champ magnétique ne sont pas parallèles les forces de Lorentz ou de Laplace apparaissent. Ces forces sont la source fondamentale de l'effet TEM. Par ailleurs, afin d'expliquer intuitivement l'effet TEM dans le processus de solidification directionnelle sous l'effet du champ magnétique axial et transversal, nous avons représenté graphiquement les cas à la fois en 2 dimensions et en 3 dimensions comme le montre la figure 5.

Pour tenir compte quantitativement de l'effet TEC basé sur un mécanisme de potentiel thermoélectrique résultant des différentes réponses des porteurs de charge de matériaux à différentes températures, la loi Ohm doit être modifiée comme suit :

$$\vec{j} = \sigma(\vec{E} + \vec{u} \times \vec{B} - S\vec{\nabla}T) \qquad (1)$$

dans lequel $\vec{u} \times \vec{B}$ est la force électromotrice provoquée par milieu conducteur se déplaçant dans un champ magnétique, σ est la conductivité électrique, $\vec{E}$ désigne le champ électrique, $\vec{u}$ est la vitesse de déplacement du milieu dans un champ magnétique $\vec{B}$, $\vec{\nabla}T$ représente le gradient de température, et *S* est l'ATP. De plus, les courants doivent satisfaire à l'équation de continuité : $\vec{\nabla}.\vec{j} = 0$. L'effet TEC dans la situation illustrée à la figure 5 a été simulé avec le logiciel COMSOL Multiphysics (version 4.2.0.228), qui utilise une méthode d'éléments finis

pour la discrétisation spatiale et pour la résolution de systèmes d'équations dérivées partielle [52]. La figure 6 montre une simulation de l'effet TEC généré par des gradients thermiques constants respectivement de 3000K/m et -3000K/m.

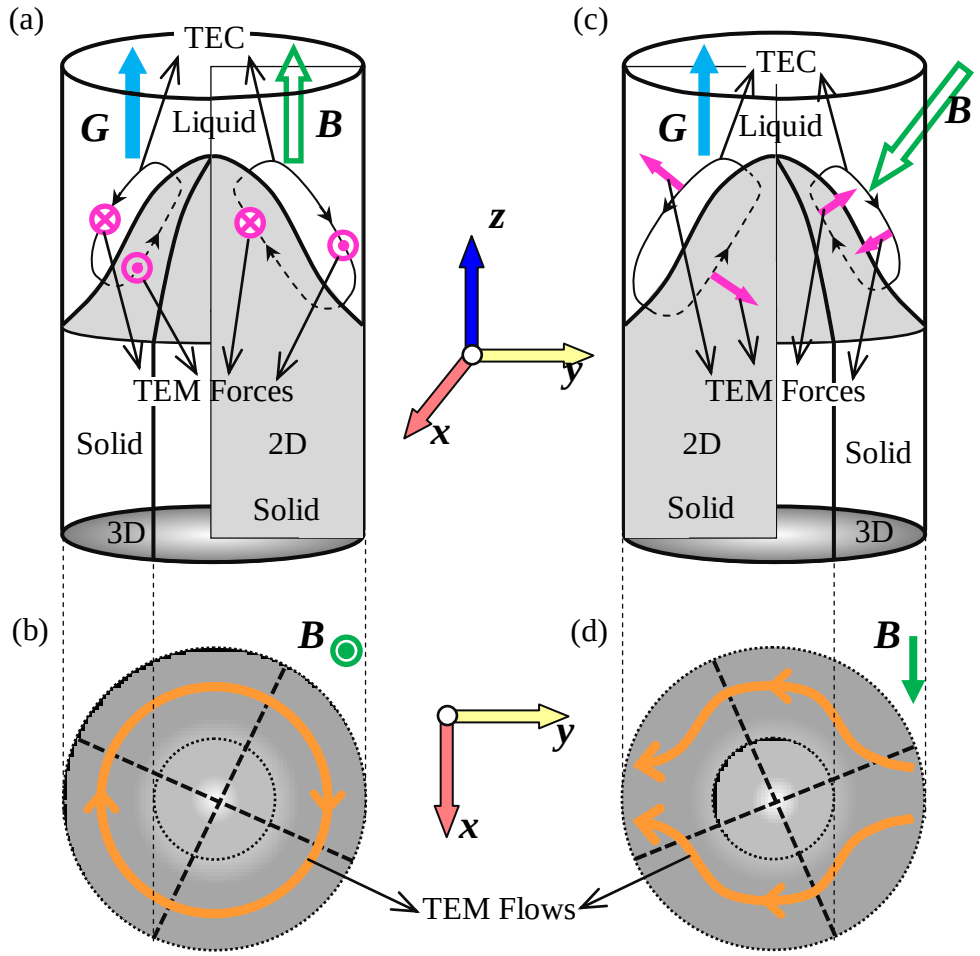

Figure 5 Illustration de l'effet de TEM lors du processus de solidification dirigée à l'interface liquide-solide. (a) 2D et 3D illustration graphique des forces TEM et leur orientation sous champ magnétique axial vers le haut; (b) Vue de dessus des écoulements TEM dans le plan *x-y* générés par les forces TEM à l'état liquide; (c) illustration graphique 3D et 2D des forces TEM et de leur direction dans un champ magnétique transversal; (d) vue de dessus des écoulements de TEM dans le plan *x-y* entraînés par les forces TEM dans le liquide.

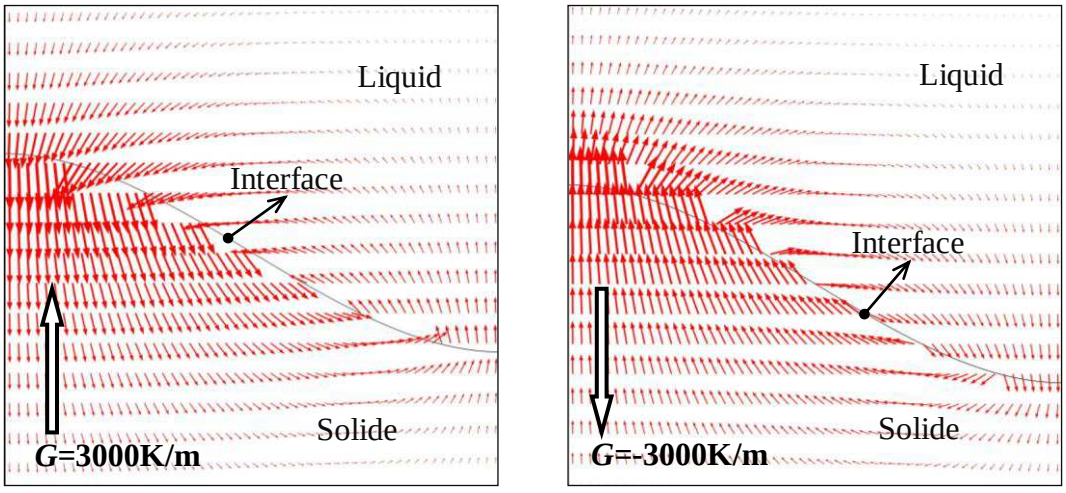

Figure 6 TEC densités de courants électriques générés par les gradients thermiques

Tableau 1 Propriétés physiques de l'alliage d'aluminium utilisés

Symbol	Unit	Solid	Liquid
S	V/K	-1.5×10^{-6}	-2.25×10^{-6}
σ	$(\Omega\cdot m)^{-1}$	7.9×10^{7}	4.0×10^{6}
μ	Pa·s	2.0×10^{6}	2.9×10^{-3}
κ	W/mK	150	95
C	J/KgK	0.9×10^{3}	1.08×10^{3}
ρ	Kg/m^3	2.7×10^{3}	2.4×10^{3}

L'interaction entre les courants électriques et le champ magnétique externe produit dans une force de Lorentz calculée comme suit :

$$\vec{F} = \vec{j} \times \vec{B} \tag{2}$$

Si l'on néglige le champ électrique initiale, les forces TEM solides et liquides peuvent être simplement exprimées comme suit :

$$\vec{F_s} = -\sigma_s S_s \vec{\nabla} T \times \vec{B} \tag{3}$$

$$\vec{F_l} = -\sigma_l S_l \vec{\nabla} T \times \vec{B} \tag{4}$$

D'autre part, les écoulements générés par les forces TEM dans le liquide peut être décrit par l'équation de Navier-Stokes (N-S)

$$\frac{\partial(\rho\vec{u})}{\partial t} + \rho(\vec{u}\bullet\vec{\nabla})\vec{u} = -\vec{\nabla}p + \rho\vec{g} + \mu\nabla^2\vec{u} + \vec{j}\times\vec{B} \tag{5}$$

Puisque le métal liquide est un fluide incompressible, la conservation de la masse doit être la suivante :

$$\vec{\nabla}\bullet\vec{u} = 0 \tag{6}$$

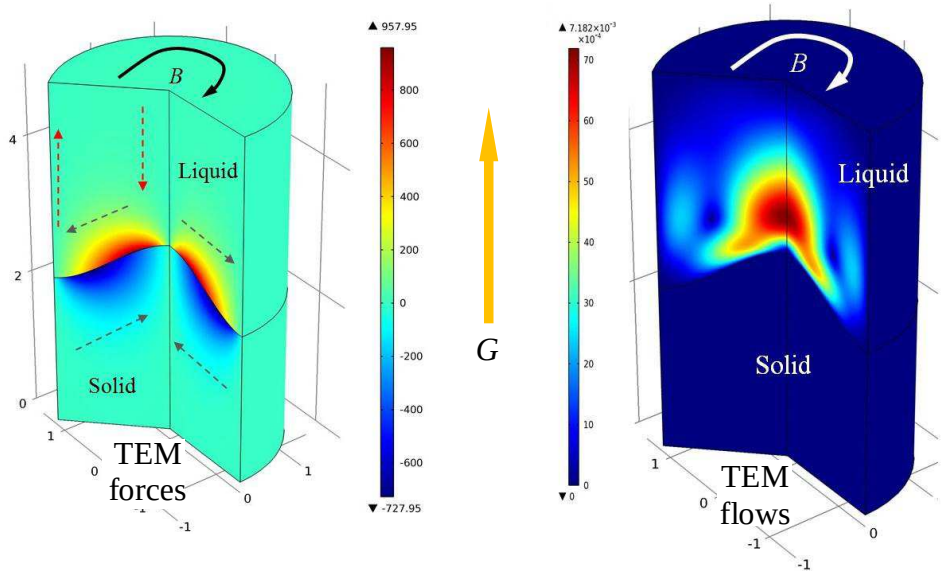

Figure 7 Forces TEM et simulation des écoulements générés par un gradient thermique constant de 6000K / m et un champ magnétique annulaire 0.08T.

Nous avons utilisé les équations et les paramètres du tableau 1. Les forces et les écoulements TEM ont été simulés avec un module 2D axisymétrique. La figure 7 montre les forces TEM simulées et les écoulements causés par un gradient thermique de 6000K / m et un champ magnétique annulaire 0.08T. Ce genre de champ magnétique n'affecte pas l'effet TEM en solidification directionnelle même s'il ne peut pas être atteint dans la réalité. L'augmentation des intensités de champ magnétique imposé conduisent à une augmentation des vitesses d'écoulements TEM. Il a été constaté que les écoulements TEM parviennent à une vitesse maximale lorsque le champ magnétique atteint une valeur critique, puis ils ralentissent lorsqu'on augmente encore le champ magnétique. Ceci concorde avec les résultats examinés précédemment.

Chapitre 3

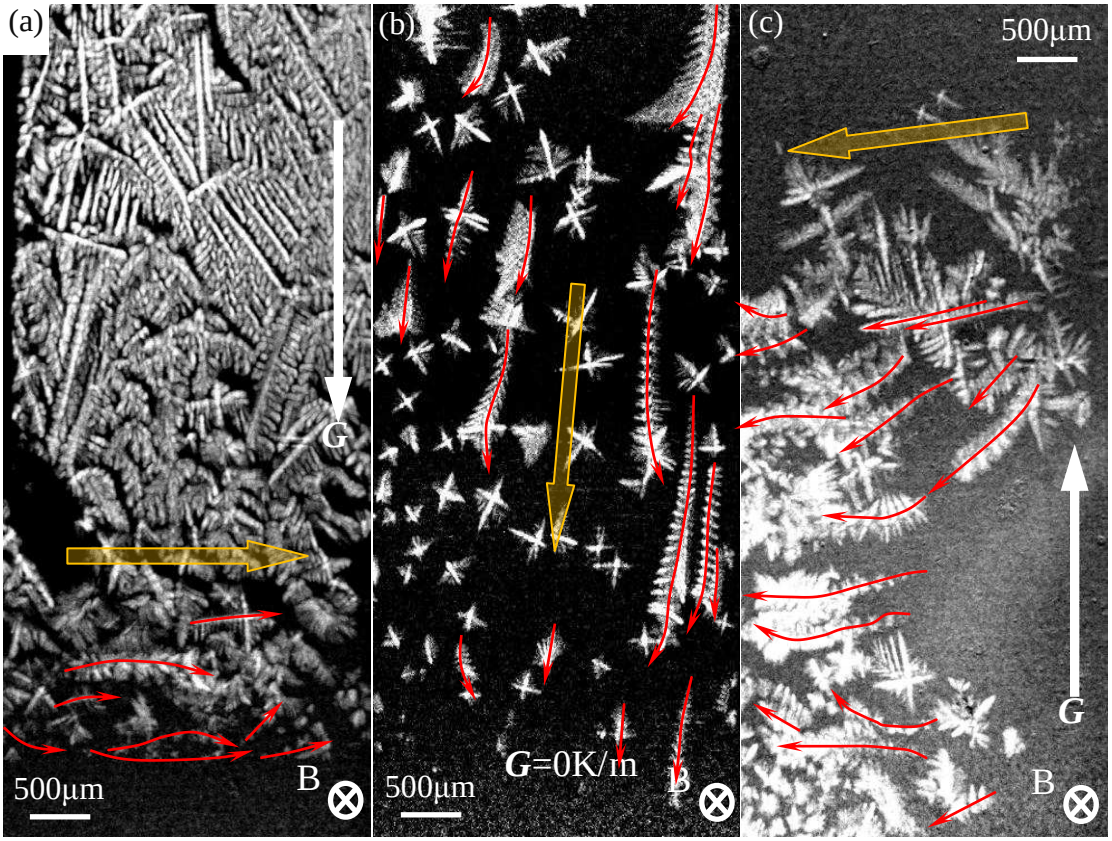

Figure 8 Photographies réalisées à plusieurs instants successifs montrant le mouvement des cristaux pendant la solidification directionnelle des Al-10%wt.Cu avec différentes intensités de gradients thermiques. (a) G =-2000K / m; (b) G = 0K / m; (c) G = 2000K / m. (B =-0.08T; les taux de refroidissement sont 2K/min)

Bien que de nombreuses indications montrent que l'effet TEM peut exister lors de la solidification directionnelle dans un champ magnétique externe, une preuve plus directe est toujours souhaitable, comme de voir directement son influence pendant le processus de solidification. Grâce à la découverte du faisceau de rayonnement de synchronie et au développement des techniques d'imagerie par rayons X, il devient possible d'observer in-situ

et en temps réel la solidification des alliages métalliques opaques [53-55]. Cependant, un autre obstacle apparaît, à savoir que les deux forces à l'état solide et à l'état fondu et les écoulements sont difficiles à détecter directement ou à observer. Alors que, un compromis a été donné que l'effet TEM pourrait être pensé pour être observée directement et a prouvé aussi longtemps que la résultante directe des forces et des flux TEM peut être in-situ vu. En conséquence, les forces de TEM solide sont révélés par le mouvement de cristaux qui ont été détecté seulement lorsque le champ magnétique était présent. En outre, les écoulements TEM sont démontrés par le changement de forme de l'interface liquide-solide qui ne peut s'expliquer que lorsque l'on suppose que le transport des solutés est réalisé par des écoulements TEM.

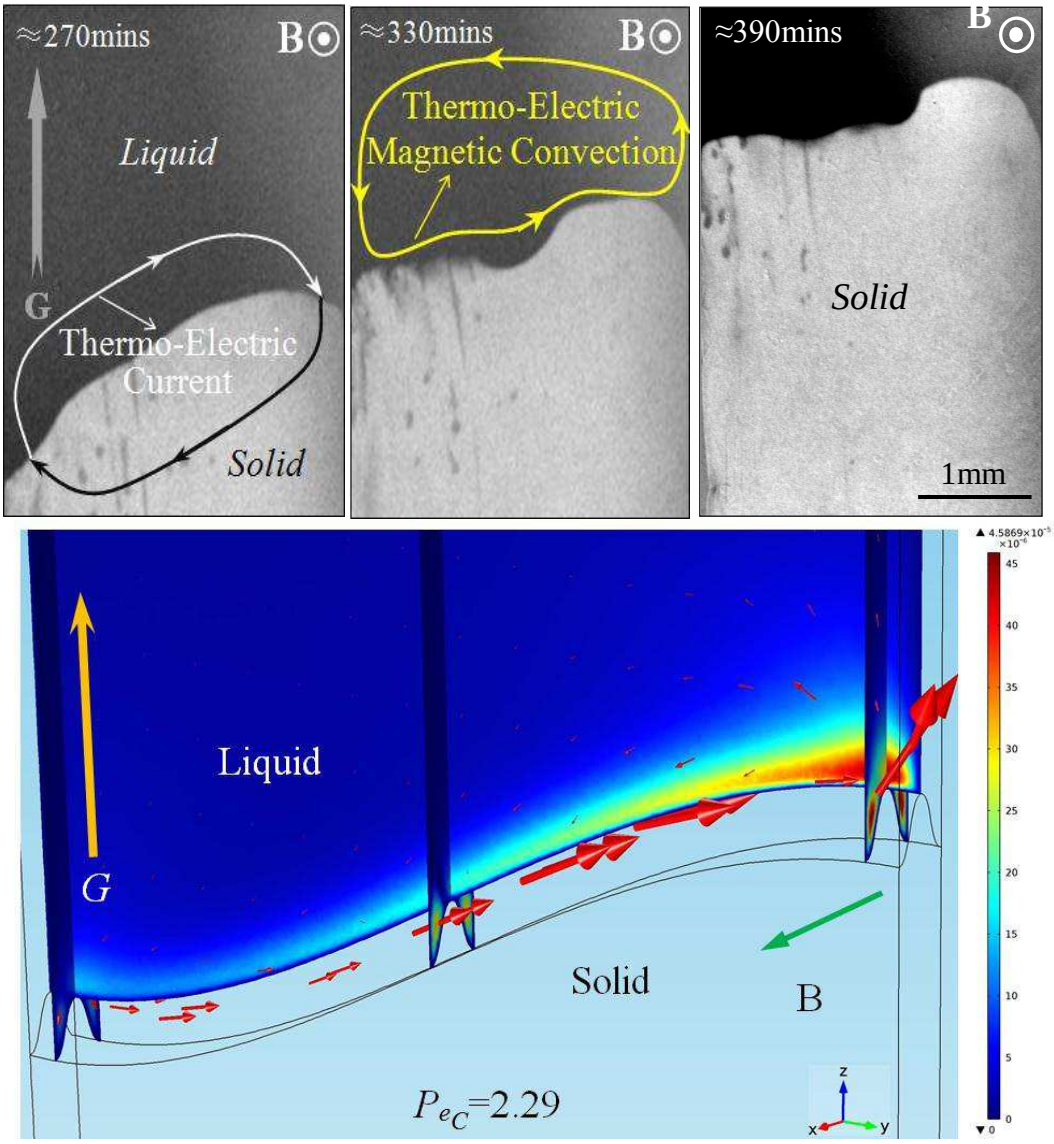

Figure 9 Trois images successives capturées pendant la solidification directionnelle d'un Al-4%wt.Cu avec un gradient thermique de 3500K/m et sous un champ magnétique transversal 0.08T, et écoulements TEM simulés avec la géométrie et les mêmes paramètres. (Taux de refroidissement : 0.1K/min)

Pour révéler les mouvements des cristaux, plusieurs images prises pendant la solidification sont superposées en une seule image. En effet, ces images représentent les mêmes cristaux mais à des positions différentes, l'image de projection unique permet de voir le déplacement des cristaux. La figure 8 montre les images de projection obtenues à partir des images prises lors de la solidification directionnelle des Al-10% en poids des alliages Cu avec différents gradients thermiques de direction. Comme indiqué par les flèches jaunes et rouges, la direction de déplacement des cristaux est inversée lorsque le gradient thermique est appliqué dans la direction opposée, et les cristaux coulent verticalement sans gradient thermique. Ceci suggère que le déplacement de ces cristaux est directement lié au gradient thermique lorsque le champ magnétique externe est présent et stable. Après avoir analysé ces situations, nous nous trouvons face à deux possibilités : la première est que les pressions engendrées par les forces TEM circulent autour des cristaux et la seconde est que les forces TEM agissent sur les cristaux. Si l'on considère les cristaux comme une sphère solide, le fluide s'écoule autour de cette sphère par l'effet TEM. La vitesse engendrée par les forces TEM a été calculée analytiquement, et le détail de ces calculs sont décrits dans le chapitre 3. Ils montrent que les pressions causées par les écoulements TEM devraient être nulles, et que les vitesses de calcul des mouvements engendrés par l'effet TEM étaient comparables à ceux mesurés par l'observation in-situ. Cela peut démontrer que le mouvement des cristaux pendant la solidification directionnelle Al-10% en poids des alliages Cu sous un champ magnétique transversal 0.08T est entraîné par les forces TEM qui agissent sur eux. En d'autres termes, on peut dire que le mouvement des cristaux est directement causé par les forces TEM sur un solide, et nous pouvons donc affirmer que les forces TEM sur un solide sont directement observées et avérées. D'autre part, on a pu observer in-situ et en temps réel le changement de forme de l'interface liquide-solide comme le montre la figure 9. Comme le soluté Cu rejeté est plus lourd que la matrice liquide environnante, si l'interface est déjà inclinée, ce soluté a tendance à s'enfoncer dans la partie concave de l'interface, qui s'enrichit et l'interface devient de plus en plus inclinée. Cela a été prouvé par Bogno et al. [56] quand ils ont étudié l'évolution de l'interface plane pendant la solidification directionnelle des Al-4wt%Cu. Par conséquent, à partir d'une l'interface initialement plate, il y a suffisamment d'écoulements dans la direction de l'enfoncement pour transférer le soluté les plus lourd à partir de la partie concave vers la partie convexe de l'interface. On peut voir sur la figure 9. Nous avons gardé les paramètres de condition utilisés par Bogno et.al , et nous imposons un champ magnétique transversal 0.08T. Alors l'interface initialement inclinée devient progressivement plate comme dans le processus de solidification directionnelle. Cela suggère que les écoulements suffisamment intenses et sont apparus et que le soluté Cu a été rejetés de la partie concave

vers la partie convexe. Bien qu'il semble que l'écoulement TEM puisse se produire dans un tel cas, il est nécessaire de vérifier si oui ou non les écoulements TEM peuvent correspondre à ceux permettant à une interface initialement inclinée de devenir presque plane. Des simulations 3D des écoulements TEM ont été effectués dans les mêmes conditions que celles des expériences in-situ .et avec la même la forme d'interface obtenus par les expériences in situ ont été effectuées. La figure 10 montre les écoulements TEM simulés, et il peut être observé que TEM coule dans ce cas de la partie concave de l'interface vers la partie convexe, contrairement à la direction d'amortissement des solutés lourds. En outre, le calcul du nombre de Peclet chimique a montré que les écoulements TEM de grande amplitude étaient capables de transporter des solutés Cu rejetés. Par conséquent, on peut certainement affirmer que dans ce cas, le changement de forme de l'interface liquide-solide est directement issu des écoulements de grande amplitude TEM, et qu'ayant pu observer directement les écoulements TEM, ceux-ci sont avérés.

Chapitre 4

Bien que l'effet TEM ait été prouvé par l'observation directe, la taille des échantillons utilisés par des expériences in situ, par exemple épaisseur 200 um, ne sont pas communs pour les lingots de métal. Par conséquent, il est intéressant de vérifier l'effet TEM dans des situations plus réalistes. Les échantillons d'alliages Al-Cu d'un millimètre de taille dans les trois dimensions ont été solidifiés de façon directionnelle sous différentes intensités d'écoulements magnétiques transversaux. Par ailleurs, afin de concevoir des expériences plus précises, les écoulements TEM ont été évalués analytiquement au préalable.

La vitesse de ces écoulements peut être obtenue simplement par l'équilibre entre les forces TEM et les forces de viscosité ou d'inertie. Les valeurs du nombre de Reynolds peut permettre de choisir l'équilibre pertinent en fonction du champ magnétique imposé et de la longueur typique de la morphologie concernée. D'autre part, en vertu du principe de la magnétohydrodynamique (MHD), un métal liquide circulant dans un champ magnétique pourrait induire des courants électriques qui peuvent engendrer des forces de Lorentz s'opposant à l'écoulement. Ainsi, des forces de freinage des écoulements TEM ont été produites et rivalisent avec les forces TEM . Les écoulements TEM accélèrent au maximum sous l'intensité du champ magnétique, puis ralentissent à mesure que le champ magnétique imposé croît, parce que les forces de freinage sont proportionnelles à B^2, tandis que les forces de TEM sont proportionnelles à B. Comme le montre la figure 10, les vitesses des écoulements TEM sous champ magnétique différent ont été évaluées pour trois longueurs typiques, et les détails de ce calcul peuvent être trouvés dans le chapitre 4.1 de cette thèse. En

outre, la courbe des écoulements réalistes TEM avec des champs magnétiques variables est indiquée par la ligne en pointillés jaune dans la figure 10 (c). car l'estimation de la vitesse pour la première phase d'accélération n'a pas pris les forces de freinage en considération.

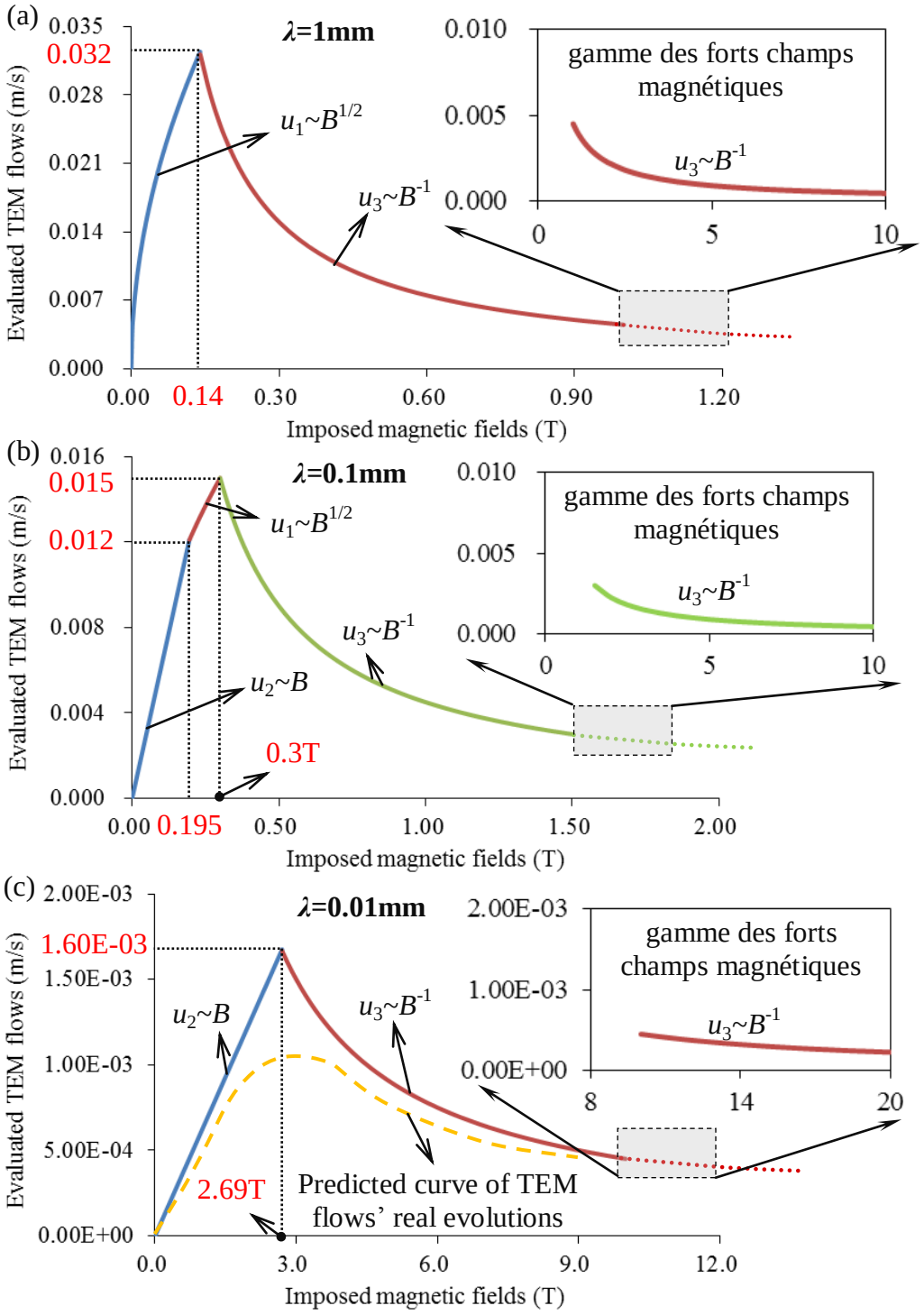

Figure 10 Courbes d'évaluation des écoulements TEM en fonction des champs magnétiques imposés pour différentes échelles typiques: (a) λ = 1mm; (b) λ = 0,1mm (c) λ = 0,01mm.

Les morphologies de solidification faisant apparaître différentes échelles de longueur, les évaluations présentées dans la figure 10 peuvent être considérées comme un outil de prévision des écoulements TEM dans divers processus de solidification de la morphologie. En

conséquence, nous pouvons connaître quelle fourchette de champ magnétique doit être choisie pour réaliser les écoulements TEM les plus intenses par rapport à différentes morphologie. Par exemple, les champs magnétiques de 0 à 0,3 T ont été imposés lorsque les conditions de solidification ont imposées pour réaliser la croissance d'interface plane, car la longueur typique d'une telle morphologie a été prise égale à 1mm.

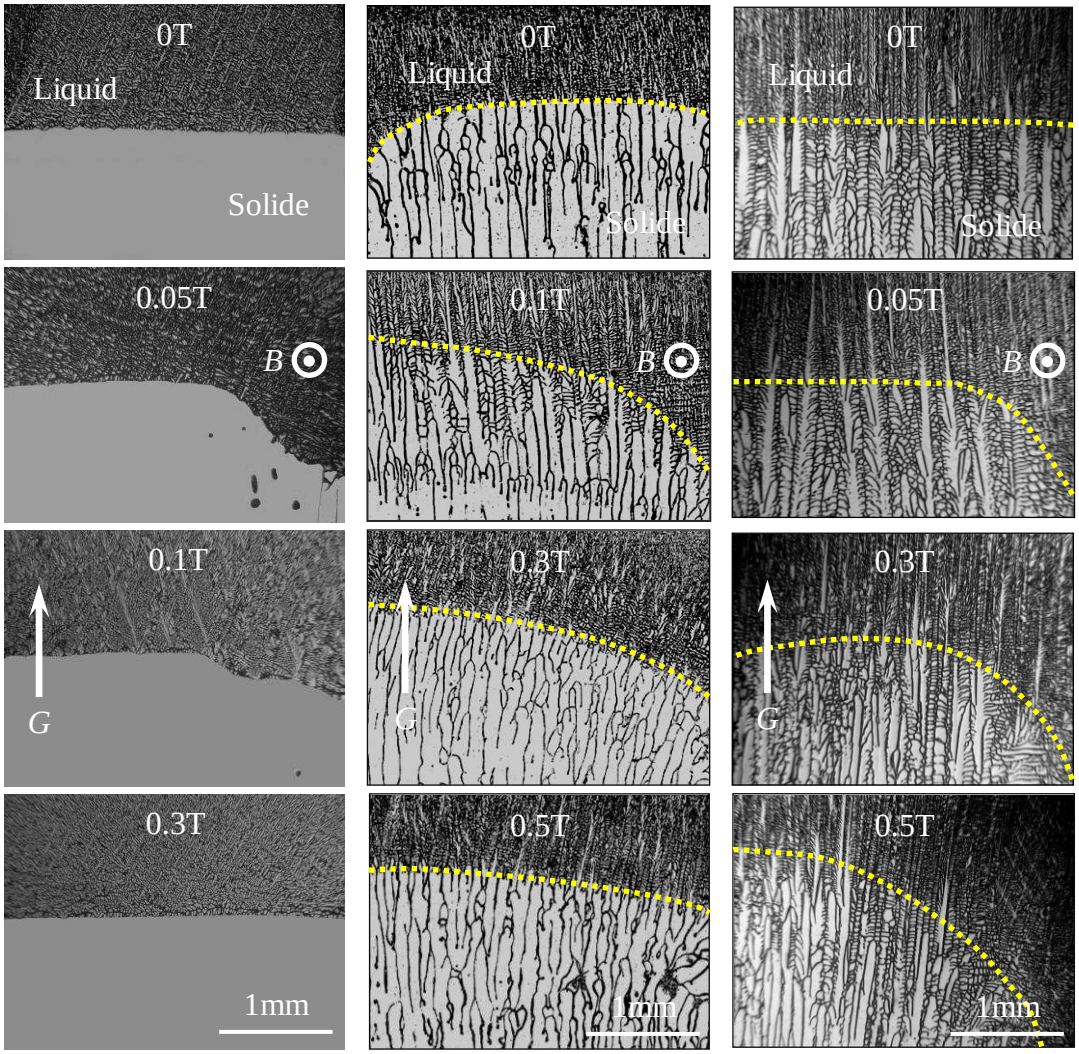

(a) (b) (c)

Figure 11 Coupe longitudinale (parallèle à la direction de croissance et perpendiculaire au champ magnétique) de la structure de l'interface liquide-solide des alliages Al-Cu obtenu sous diverses intensités de TMF solidifiée (G=6000K/m) et après trempe: (a) cas de l'interface plane, Al-0,85wt%Cu, *R*=0.6μm/s, (b) interface cellulaire, Al-0.85wt%Cu, *R*=5μm/s; (c) interface dendritique, Al-Cu2,5wt%Cu, *R*=50μm/s.

La figure 11 montre l'interface liquide-solide avec des alliages Al-Cu obtenue sous différentes intensités de champ magnétique. Il peut être observé que quelle que soit la morphologie, la forme de l'interface change lorsqu'on impose un champ magnétique transversal. En effet, les interfaces sont alors toutes inclinées. Cette forme d'inclinaison de l'interface doit être attribuée aux écoulements TEM car les simulations numériques 3D ont montré que les écoulements TEM dans ces cas étaient des écoulements unidirectionnels qui

transféraient les solutés rejetés d'un côté vers l'autre du lingot. Les solutés enrichis dégénèrent progressivement l'interface au cours du processus de solidification directionnelle, ce qui pourrait causer l'inclinaison de l'interface. Nous pouvons constater que l'inclinaison de l'interface plane réalisée dans un champ magnétique de 0,05 T et avec des interfaces cellulaires et dendritiques survient à moins de 0,1 et 0,5 T respectivement. L'écart entre la valeur exacte de l'intensité de l'écoulement et celle du champ magnétique critique pour la vitesse maximale de l'écoulement TEM est du aux imprécisions intrinsèques à l'évaluation. Le véritable gradient thermique dans un liquide et solide doit être différent de celui initialement appliqué.

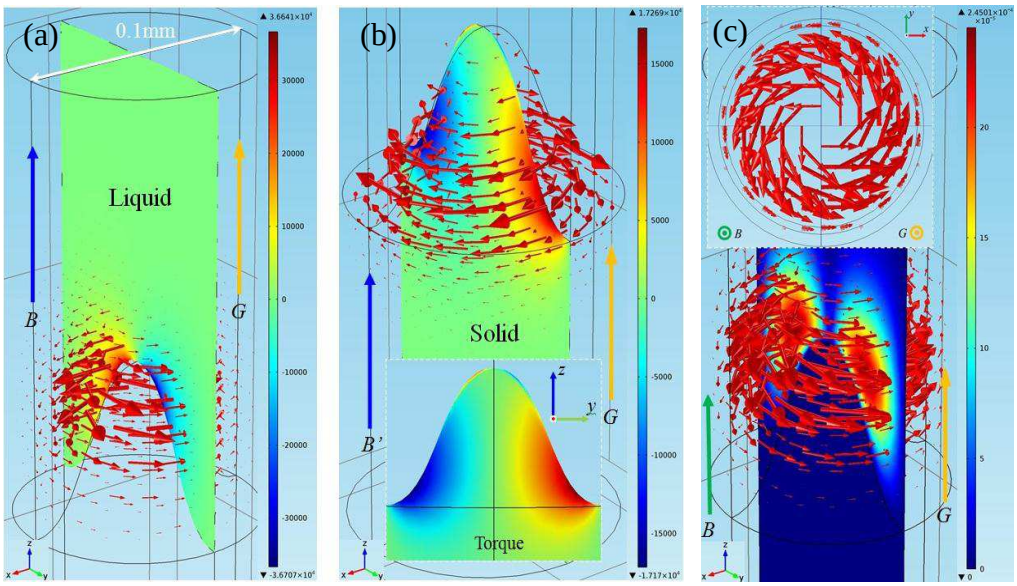

Figure 12 Calculs numériques des forces TEM et des écoulements générés par l'application d'un gradient thermique de 6000K / m et d'un champ magnétique axial de 0,1 T: (a) les forces TEM dans le liquide (B) des forces TEM dans le solide; (c) distribution des écoulements TEM.

Si l'on excepte l'effet TEM quand la solidification directionnelle se déroule dans un champ magnétique transversal, la situation sous un champ magnétique axial a été étudiée par des simulations numériques 3D. Ces simulations ont été utilisées dans les mêmes conditions de solidification et avec une forme d'interface correspondante. La figure 12 montre les forces TEM simulées et les écoulements générés par le gradient thermique de 6000K/m et un champ magnétique axial de 0,1 T. On peut observer que les forces TEM dans le liquide forment un tourbillon qui tourne dans le sens des aiguilles d'une montre autour de l'interface liquide-solide, et que leur plus grande amplitude se situe au sommet et à proximité de l'interface. Par conséquent, ce modèle de forces a entraîné un tourbillon TEM qui tourne autour de l'interface tel qu'il apparaît dans la figure 12 (c). Généralement, on ne pense pas que ce type d'écoulement soit en mesure de redistribuer des solutés. Toutefois, si nous prenons la différence de densité entre les solutés enrichis au fond et les différences initiales, les

turbulences peuvent redistribuer les solutés rejetés conformément à leur effet centrifuge. Ceci devrait modifier la structure au cours de la solidification directionnelle. En plus des écoulements TEM, comme le montre la figure 12 (b), l'existence de forces TEM sur un solide ont également été confirmées par des simulations numériques. Celles-ci ont révélé que deux couples opposés formés respectivement sur le haut et le bas de l'interface sous l'AMF ont tendance à tourner dans le sens des aiguilles d'une montre en haut et dans le sens contraire en bas. Horaire. Enfin, nous avons vérifié comment les vitesses des écoulements TEM variaient avec les champs magnétiques et avons constaté que les évaluations, les expériences et les simulations indiquaient toutes une évolution en constante croissance des écoulements TEM avec le champ magnétique.

Chapitre 5

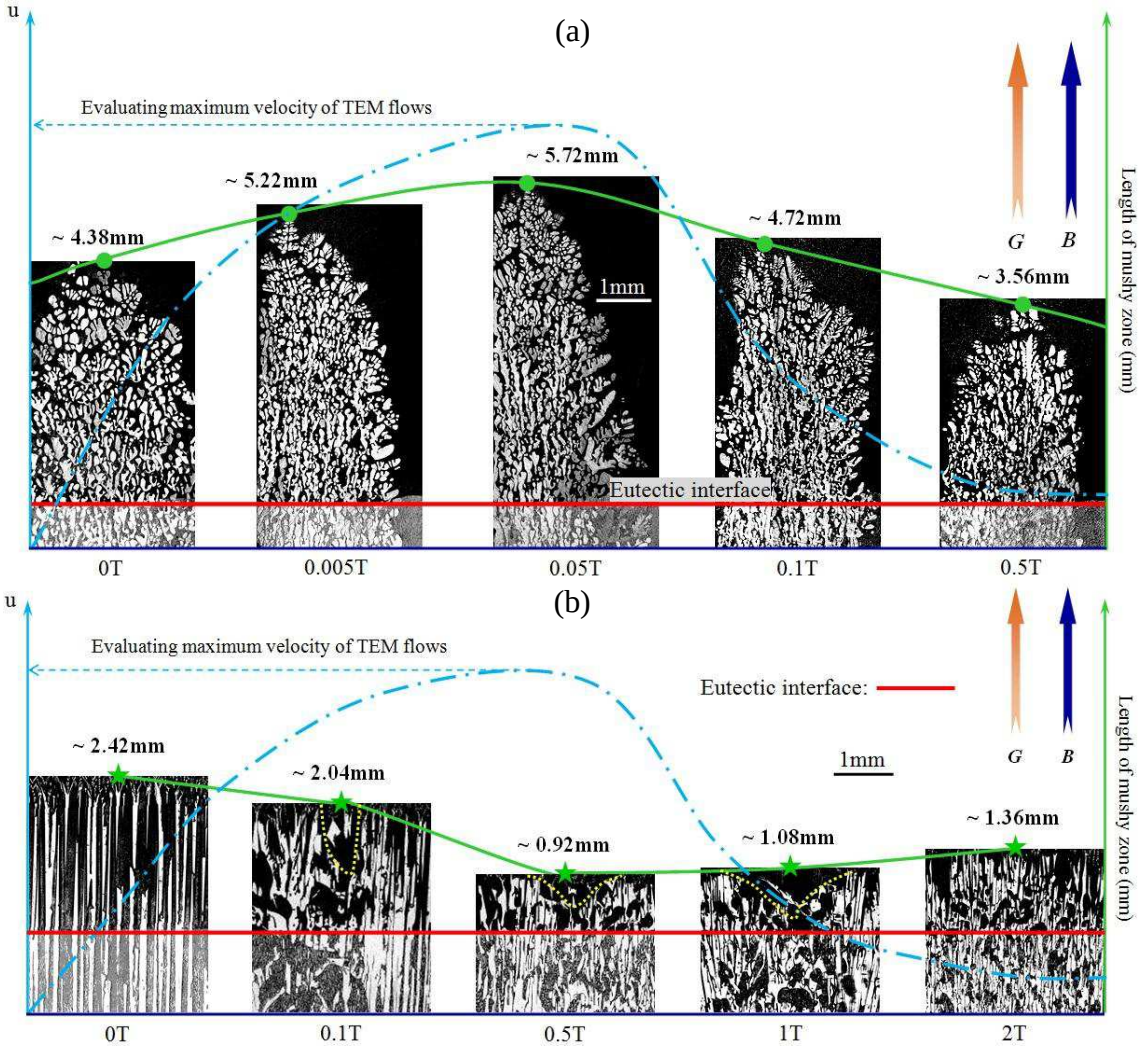

Figure 13 Coupes longitudinales (parallèle à la fois la croissance et la direction du champ magnétique) montrant la structure de l'interface réalisées avec Al-26wt%Cu (a) et Al-40wt%Cu ; (b) alliages solidifiés sous des intensités différentes de champ magnétique. La ligne rouge marque les interfaces eutectiques et les points verts les interfaces dendritiques, le pointillé bleu illustre comment les vitesses d'écoulement TEM varient en fonction de l'AMF. Les longueurs mesurées en zone pâteuse sont donnés dans la partie supérieure de chaque figure. (R=2μm/s, G=6200K/m).

Afin d'étudier l'influence du champ magnétique externe sur la solidification directionnelle d'alliages hors eutectiques, et afin d'examiner l'effet TEM pendant le processus de formation de la structure multi-phase, nous avons étudié la solidification directionnelle d'un alliage hypo-eutectique Al-26wt%Cu et hyper-eutectique 40wt%Cu sous différentes intensités de champ magnétique statique axial. Il a été constaté que, dans le cas sans champ magnétique, la structure dendritique-plus-eutectique typique a été atteint pour les deux alliages hypo- et hyper-eutectiques avec gradient thermique appliqué de 6200K/m et une vitesse de tirage de 2μm/s. De plus, la dendrite primaire de Al-26wt%Cu est la phase α-Al, et celle de Al-Cu40wt%Cu est la phase Al_2Cu comme le montre la figure 13. Par l'mposition d'un champ magnétique axial statique (AMF), la longueur de la zone pâteuse et la distance entre la pointe de la dendrites primaires et le front eutectique a été modifiée. En effet, comme indiqué dans la figure 13, la longueur de la zone pâteuse de Al-26wt%Cu d'abord augmente, puis diminue de manière continue lorsqu'on augmente le champ magnétique appliqué. Inversement, la zone pâteuse de Al-40wt%Cu d'abord courte, s'allonge en augmentant le champ magnétique à partir d'une intensité critique. On pense qu'un tourbillon TEM circulant autour des dendrites primaires peut se produire et rendre cette longueur de zone pâteuse variable. Le contenu des solutés au fond de la zone pâteuse pourrait être affecté par ces écoulements et devrait être en mesure de faire varier la longueur de la zone pâteuse pendant solidification directionnelle. Toutefois, avant de détailler la façon dont les écoulements TEM modifie la longueur de la zone pâteuse, ces cas ont été vérifiés par des simulations avec les mêmes conditions que celles utilisées et la géométrie similaire à celle obtenue dans les expériences.

La Figure 14 (a) et (b) montre les distributions simulées des courants TE dans les deux cas pour lesquels les cellules/dendrites sont des phases Al_2Cu et α-Al respectivement. Il peut être constaté que le courant TE peut apparaître dans ces deux cas et former des circuits autour du tronc principal de dendrites. En outre, la figure 14 (c) et (d) illustrent schématiquement comment les forces et les écoulements TEM pourraient se comporter après application d'un champ magnétique statique axial. On peut observer qu'un écoulement vortex similaire à celui découvert par des simulations numériques dans le chapitre 4 sont produites par des forces TEM à l'état liquide et l'écoulement est dans le sens antihoraire autour des dendrites. Comme le soluté Cu lourd est rejeté lors de la solidification directionnelle les hypoeutectiques Al-26wt%Cu, l'effet centrifuge des écoulements TEM peuvent éloigner le soluté Cu loin des dendrites comme indiqué par les pointillés jaunes dans la figure 14 (c). Cet effet dilue la teneur en Cu au fond dans la zone pâteuse et donc accroit sa longueur. Avec les mêmes écoulements, si le soluté rejeté est plus léger, l'effet centrifuge rassemblera le soluté dans

l'avant de la dendrite, en particulier, au centre de l'écoulement. Dans le cas de la solidification directionnelle de Al-40wt%Cu, l'écoulement vortex TEM rassemble les éléments de soluté les plus légers et enrichit localement la matrice d'aluminium. Cela fait fondre l'avant des dendrites Al_2Cu comme illustré par la figure 14 (d), court-circuitant ainsi la zone pâteuse. Dans un autre aspect, la dégénérescence des dendrites Al_2Cu au centre de l'échantillon, comme indiqué dans la figure 13 (b) confirme en outre l'argument selon lequel un écoulement vortex TEM regroupe les plus légers solutés au centre de l'échantillon. Lorsque l'AMF est supérieur à l'intensité critique, la vitesse maximale de l'écoulement TEM ralentit, et donc la longueur de la zone pâteuse a tendance à revenir à l'état sans champ magnétique.

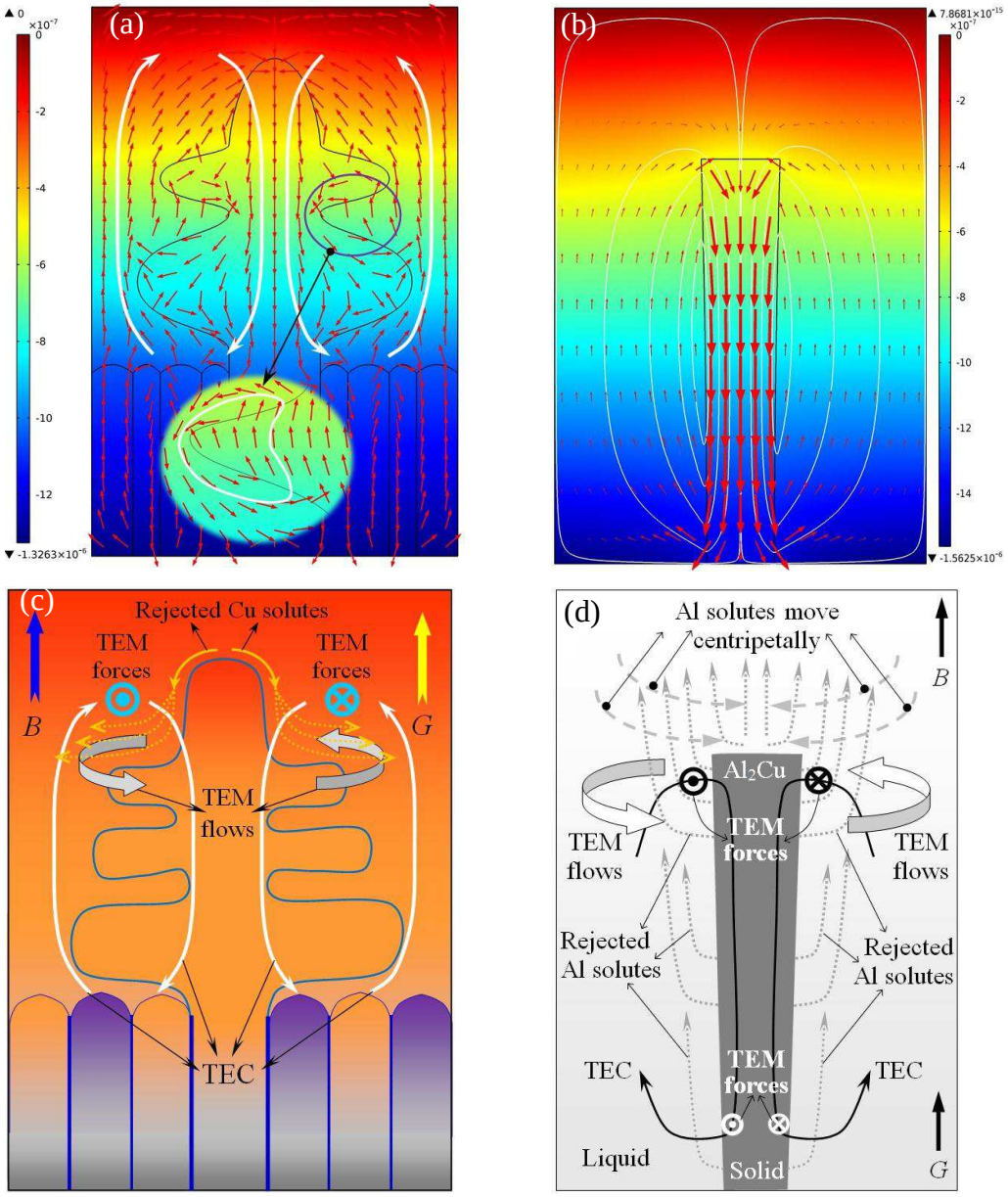

Figure 14 Simulation numérique des courants TE dans les cas de solidification directionnelle d'alliages Al-26wt%Cu (a) et Al-40wt%Cu (b). Illustration qualitative de la façon dont les forces et les écoulements TEM apparaissent sous un champ magnétique axial. (c) se rapporte à (a) tandis que (d) se rapporte à (b).

Comme le montre la figure 15, zone pâteuse plus courte que celle obtenue sans champ magnétique a été observée lors de solidification directionnelle d'un Al-26wt% Cu sous AMF supérieur à 1T, et presque toute la structure de la croissance couplée est apparu quand AMF était égal à 4T. Nous pensons que cela peut être attribué à l'effet du champ magnétique élevé sur les phases '(α-Al et phases eutectiques), par exemple la température de nucléation et la vitesse de croissance. En effet, selon l'analyse thermique différentielle (DTA) testée sur la solidification d'alliages hypoeutectiques Al-Cu sous champ magnétique élevé, il a été constaté que les mécanismes supposés ci-dessus ont eu lieu dans ce cas. Les détails de la DTA peuvent être trouvés dans le chapitre 5 de cette thèse. Ainsi, nous pouvons conclure que le champ magnétique élevé est bénéfique pour la formation de la structure de la croissance au cours de la solidification directionnelle couplée hypoeutectiques les alliages Al-Cu.

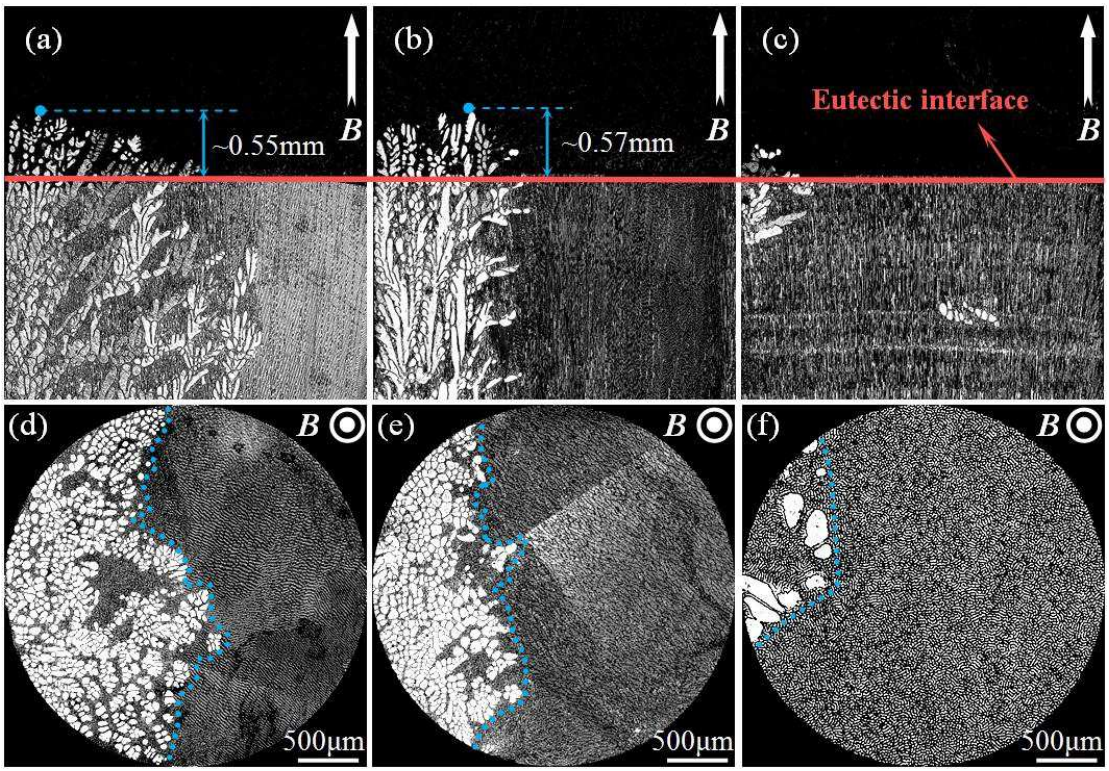

Figure 15 Coupe longitudinale (perpendiculaire à la fois à la direction de croissance et le champ magnétique) montrant la structure trempée de l'interface d'un Al-26wt%Cu obtenus sous différentes intensités de champ magnétique et leur structure correspondante dans une coupe transversale (parallèle à la fois à la direction de croissance et le champ magnétique): (a) et (d), 1T, (b) et (e) 2T, (c) et (f) 4T. (R=2um/s G=6200K/m)

Par ailleurs, pour un alliage Al-40wt%Cu solidifié sous champ magnétique élevé, l'amélioration de la croissance des facettes phases Al_2Cu primaires a été observée. Afin de permettre de définir quantitativement l'amplitude de l'effet de l'amélioration de la croissance du champ magnétique élevé, les fractions de la région de la phase Al_2Cu primaire obtenue sous différentes intensités de l'AMF ont été mesurées. Le résultat est montré dans la figure 16. Celle-ci montre que l'amélioration de la croissance est devenu évident lorsque l'AMF est

supérieur à 1T. Or il a été prouvé et largement accepté que les contraintes dans les cristaux lors de leur croissance sont capables de déclencher la formation et la propagation de défauts. Ces défauts sont bénéfiques en ce qui concerne la croissance des cristaux à facettes. On peut donc conclure que la croissance accrue de la phase Al_2Cu peut être attribué aux forces TEM agissant sur les cristaux lors de la solidification directionnelle d'Al-40wt%Cu sous un champ magnétique élevé. Par conséquent, nous sommes capables d'obtenir une autre conclusion selon laquelle le champ magnétique élevé freine mais ne favorise la formation de la structure de la croissance associée aux alliages hyper-eutectiques Al-Cu.

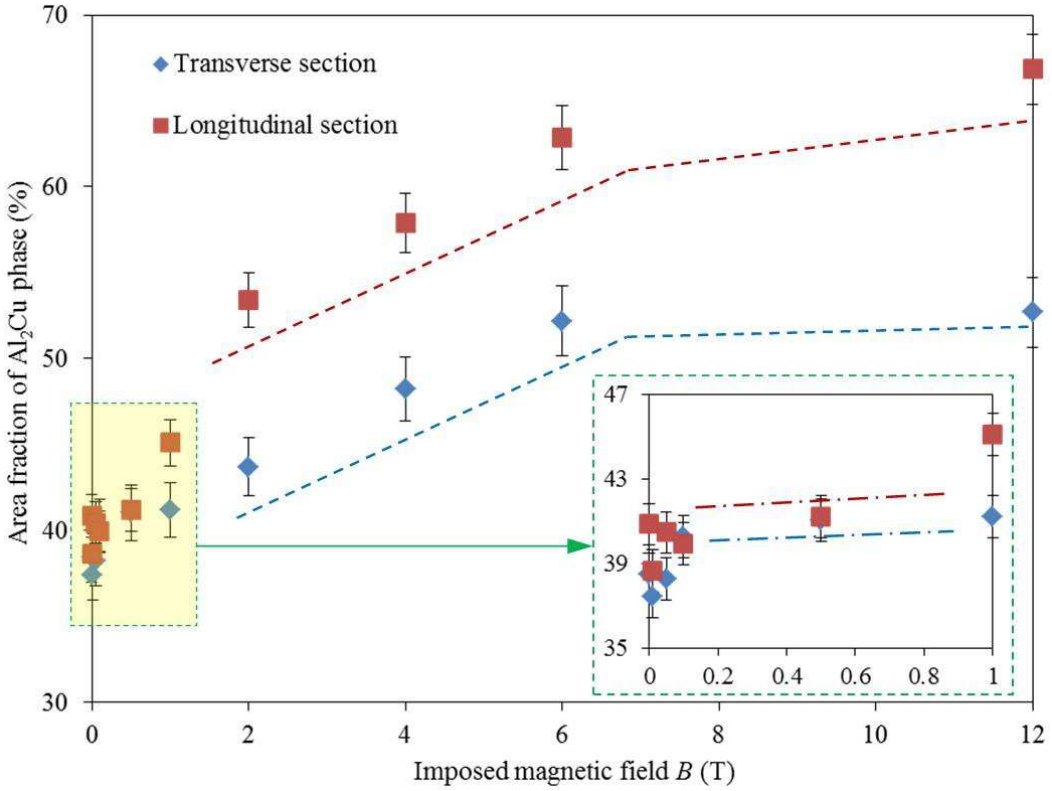

Figure 16 Courbes de fractions de surface mesurées des phases Al_2Cu primaires de structures entièrement solidifiés tracées en fonction de l'intensité du champ magnétique imposée, et vue agrandie des données marquées par la boîte jaune.

Chapitre 6

En conclusions générales de cette thèse, nous avons montré que l'effet thermo-électrique existait dans les métaux liquides en cours de solidification et pouvait produire de nombreux effets sur le solide formé, grâce :

- à des expériences de solidification sur lingot et analyses post-mortem des structures
- à des expériences de solidification avec observation in situ par imagerie X.

Cela ouvre de nouvelles perspectives concernant le contrôle et la maîtrise de la solidification d'alliages en fonderie.

Content

Chapter 1: Introduction

1.1 Encounter between magnetic field and solidification

As the most popular method to prepare metallic materials, solidification process determinates their solid strucuture and then the mechanical properties. Therfore, it is a longterm desire to precisely control such process. Enlightened by magnetohydrodynamics (MHD) theory that dealing with the problems of fluid flow under magnetic field, an idea to control the melt flow during solidification by applying magnetic field comes to people's mind. Verification of such idea leads to the encounter between magnetic field and solidification. Further, applying the MHD to metallurgy process gives the birth to a newly and rasing research field neamed electromagnetic processing of materials (EPM) that aiming at taking all the advantages of various types of magnetic fields in different material preparsions or processes. Therefore, it is better to introduce how MHD theory forms in advanced if we intend to know how the encounter between magnetic field and solidification happens.

1.1.1 Step from Magnetohydrodynamics to Electromagnetic Processing of Materials

Magnetohydrodynamics, a branch of the hydromechanics, specially deals with how the electrically conducting fluids behave under an external magnetic field. It is the combination of two classical disciplines that electromagnetism and fluid mechanics [1-3]. A Swiss astrophysicist named Hannes Alfvén is known as the establisher of MHD theory because he firstly proposed the term "Electromagnetic-hydrodynamic" in 1942 [3] and won the Noble prize on the benefit of this work. Actually, the earliest MHD related event happened in 1832. In that year an English scientist Michael Faraday stood on the Waterloo Bridge in London and attempted to measure the electric signal when the salty Thames water ebbed back to the sea. Although Faraday did not detect any signals probably becaue of the poor ammeter, he had must been realized that solid or fluid subject should experience an electromotive force when it cutting the magnetic field lines [4, 5]. Further, if this subject is electrically conducting the electric currents can appear and lead to two consequences [6]:

1. These currents induce a new magnetic field that perturbs the original one;
2. These currents interacting with the original magnetic field produces an electromagnetic force, and this force perturbs the subjects' motions.

For the sake of illustrating the two consequences, a simple situation is considered. As shown in figure 1.1, a metal sheet dropping through a gap of magnet. The electromotive force will be induced in the sheet's immersed part as soon as it enters the magnetic field. At almost the same time, electric current loops should appear as indicated in the figure 1.1 (b), because the sheet is conducting. And then, those currents induce a magnetic field to deform the

original one as shown in figure 1.1 (a). In another aspect, an electromagnetic force oppose to the sheet's moving direction is produced via interacting between those currents and the original magnetic field. It is easy to image that if replace the moving metal sheet by the flowing melt the electrcomagnetic force (consequence 2) must influnce the melt's flows that play critical role in strucuture formation during solidification.

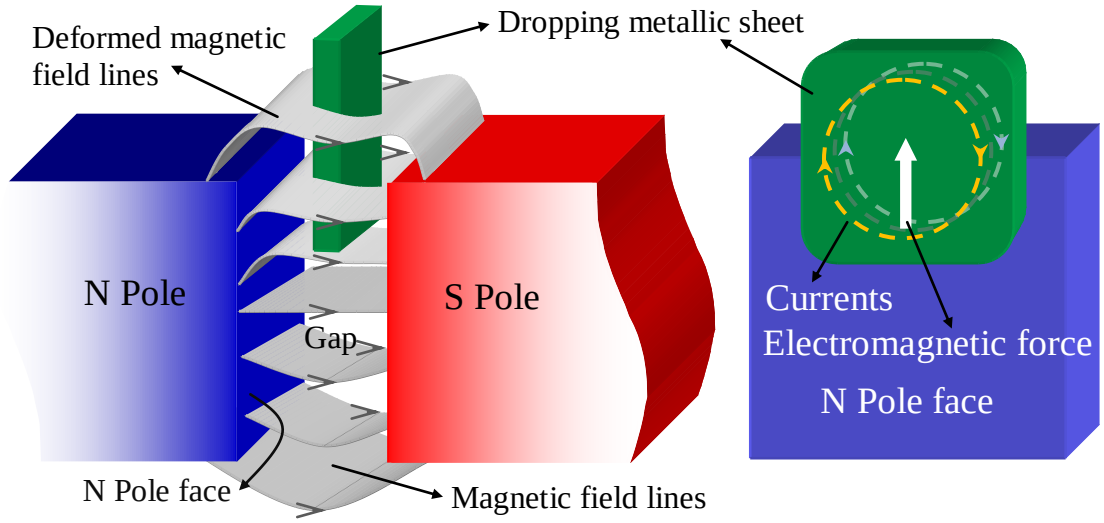

Figure 1.1 An example of basic MHD phenomena.

In order to know the view at the other side of the ocean, sail was chosen by our ancestors to discover this curiousness. Therefore how the seawater flows was eagered to know for the safety consideration. Based on a widely accepted view that magnetic field exists in a set of astronomic objects included earth [7], Faraday thought that the motions of ocean might be attributed to the perturbations of earth's magnetic field by consequence 1 [1], on the contrast, William Ritchie counted the movements of ocean to the consequence 2 [5]. It does not matter who is correct, the passion to figure our how the seawater flows motivated the initial development of MHD theory [8]. Table 1.1 briefly lists some remarkable events in astro- and geophysical fields that promoted the grwoth of MHD theroy before Hannes Alfvén pubished his electromagnetic-hydrodynamic wave theory in 1942. Once the theroy is established, it application should naturally attract peoples' attentions. But sometimes the practical applications can run ahead to the theroy, and this did happen in MHD related cases. Table 1.1 also lists some industrial and technological events based on MHD principles happend before 1942 that is considered as the birth year of MHD theroy. It can find that just when Faraday investigated the theory aspect of electromagnetic induction phenomenon, Rithchie had successfully pumped the water electromagnetically. In fact, Rithchie's experiment is the rudiment of the electromagnetic pump that firstly patented in 1910s'. Figure 1.2 simply

illustrates a case that pumping conducting liquids with vertical current and satic transverse magnetic field.

Table 1.1 MHD related events in Astrophysic, geophysic, industry and technology.

Year	Astrophysical & Geophysical	Industrial & Technology
1831	Michael Faraday discovered the electromagnetic induction [9].	
1832	Michael Faraday tried to detect the currents generated when Thames river water ebb tide [10].	William Ritchie electromagnetically pumped the water when he studied the voltaic electricity [5].
1889	Bigelow guessed that there were magnetic fields on the sun and hale, and Babcocks confirmed this later [11].	
1906		First patent for the induction heating appeared in UK [12].
1910s'		Electromagnetic pump & inductive cold crucible were invented [13].
1912		Emile Bachelet awarded a USA patent "levitating transmitting apparatus" for electromagnetic suspension system [14].
1917		The electromagnetic stirring was firstly attempted to modify the final solid structure in Europe [15].
1918	Larmor suggested the magnetic field of the sun and other heavenly bodies might be due to dynamo action, whereby the conducting material of the star acted as the armature and stator of a self-exciting dynamo [16].	
1919		Petersen converted the electromagnetic pump and invented the MHD generator using ionized gas as an armature [17].
1937	Hartmann & Lazarus theoretically and experimentally investigated the laminar flow of an electrically conducting liquid in a homogeneous magnetic field [18].	
1939	Walter Elsasser began to investigate the origin of earth's magnetic field [19].	
1942	Hannes Alfvén published the classical paper remarked the born of MHD [3].	

After the second word war, utilization of the nuclear energy in a peaceful and safe way caught lots of attentions. In order to control the thermonuclear fusion magnetic field must be applied to confine the ionized deuterium away from all walls. This is just the MHD case that conducting gases moving in a magnetic field and intensively studied until now [20]. Moreover, transferring the heat generated by nuclear reaction to the genset is another typical MHD

phenomenon because the liquid metal coolants should flow under external magnetic field as well [21]. From the steelmaking inductrial aspect, there should be burst demands on the steels because destroyed constructions are earger to be rebuilt after the wordwide war. Motived by this, many methods had been found by the metallurigists during those years to optimal the quality of iron and steel products. In which, applying an external magnetic field to influence the melt flows is one of their excellent achievements. It can image that such idea must be proposed by a metallurigist who was familiar with the newly MHD theory at that time. In the following years, MHD theory made another great progress under the exploration of applying it to the metallurgy processes [22-24].

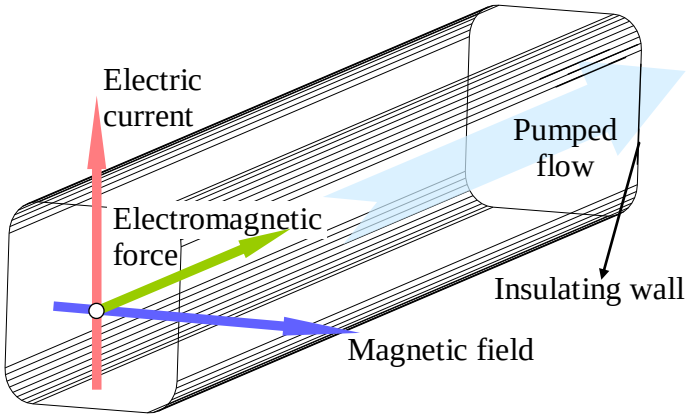

Figure 1.2 Simplest principle of the electromagnetic pump.

The first laboratory in the word aiming at applying MHD in metallurgy was offically established in Grenoble (France) in 1986, which was named MADYLAM at the beginning and the SIMAP/EPM now [15, 25 and 26]. The first international symposium specially focusing on applying MHD to metallurgy was hold by the International Union of Theoretical and Applied Mechanics (IUTAM) at Cambridge University in 1982. In a certain extends, this symposium foreboded the birth of a new research field named Electromagnetic Processing of Materials (EPM) [27]. In fact, just three years after the Iron and Steel Institute of Japan (ISIJ) found a aommittee of electromagnetic metallurgy [25, 27]. In another aspect, before the metallurgists noticed the charm of applying magnetic field, some material scientists had successfully employed the magnetic field to control the motion of the conducting solutiosn in electro-deposition process in 1975 [28-30]. This widens the application range of MHD theory in the field of material science and extends the content of EPM field. Finally, an international conference specially aiming at the newly progresses on the application of MHD to various material processes emerged in 1994 and was held every three years from then on. The term 'EPM' firstly used in the 6th international Iron and Steel Congress in 1990 was chosen to be the name of this newly research field [31-35].

1.1.2 Brief introduction of Electromagnetic Processing of Materials

Electromagnetic Processing of Materials is a broad concept, which contains subjects that related to applying various magnetic fields to different material processes, for example solidification, electro-deposite, heat treatment and sintering etc. [36]. The corresponding international conference was held alternatively in France and Japan only at the early stage. But now it has become a more worldwide academic event due to it had been held in German in 2009 and in China in 2012. Because there are lots kinds of material processes and as well as the types of magnetic fields, combinations between them provide numerous topics. Here, according to the chronological order of the topics' appearance, the main ones are introduced to give a general glance of the EPM research field.

- **Induction heating & Cold crucible electromagnetic melting**

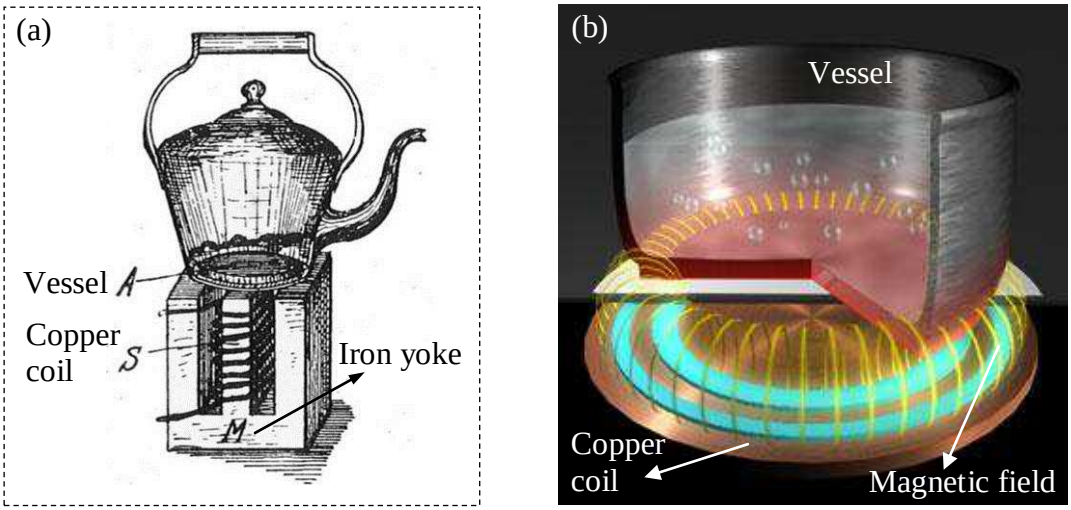

Figure 1.3 Induction cooker introductions appearing on the newspaper more than 100 years ago (a) and brief illustration the principle of the induction cooker (b).

The induction heating is introduced firstly because it is the earliest practical application of electromagnetic phenomenon. Thanks to Faraday and Joule, who found the time-changing magnetic field can induce eddy currents wthin the conducitng substance and electric currents flowing in the resistance can release heat respectively [37]. The self-heated feature gives the induction heating a number of intrinsic advantages, such as high electro-heating transfer efficiency, localized and shape changeable heating etc. [38-40]. These advantages enhance a wide application of induction heating, in which, the one closely related to people's live is induction cooker as shown in figure 1.3. Figure 1.3 (a) is the induction cooker firstly appeared on the newspaper 100 years ago [12, 41]. The principle of such cooker is briefly inllustrated in figure 1.3 (b). The copper coils supplied with alternate currents produce the time-changing magnetic fields, and such fields induce eddy currents in the vessel. Because the conducting

vessel must have resistance the flowing of those eddy currents release heat in accordance to the Joule's law, this heats the vessel.

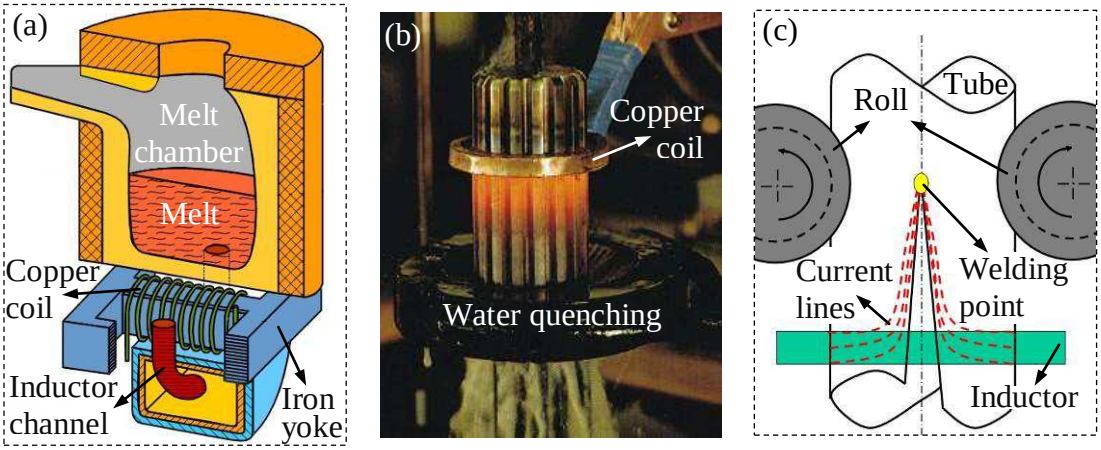

Figure 1.4 (a) Induction channel furnace; (b) Induction heating surface harden; (c) Induction welding.

Induction heating has wide application in industry as well and is mainly used in three processes, which are induction channel furnace in iron reserver tank or continuous casting tundish, surface quenching harden and induction welding [42-45]. In order to reduce the energy cost during the steel making process, an external heating is applied during transporting the iron or steel melts. Figure 1.4(a) shows the typical channel furnace with induction heating used by the iron reserver tank [46]. Moreover, because the electromagnetic stirring accompanies the induction heating all the time this channel furnace can also purify and homogenize the melts during transportation [47]. Because the copper coil can be easily shaped, the subject with complex shape can be heated. Further, take the advantage of skin effect of high frequency magnetic field surface hardened of complex shape products can be realized by high frequency induction heating coupling with water quenching as shown in figure 1.4 (b) [48, 49]. The third magic technology based on the principle of induction heating is induction welding. As illustrated in figure 1.4 (c), eddy currents induced by the inductor would gather at the yellow point because the currents always flow along the path with the lowest resistance. Therefore, the local current density at the yellow point is dramatically increased and make there remelted. And then, while the tube is transmitting by the two rolls the disconnected parts can be welded [50-52]. Although a lot of applications in accordance to the induction heating had been achieved, researches on the relevant topics are still active. This is because the complex intereaction between the accompanying electromagnetic stirring, heat and mass transfer is far from thoroughly understood. Moreover, how to more precisely control the induction heating is a longterm aspiration [53].

Induction heating provides another attactive application that melting the ultrahigh materials. Theoretically, if the material is conductivity it can be melted by induction heating

no matter how high melting temperature it is. But what kind of the crucible can be used blocks the further development of this application. Acctually, such obstacle motivates another great invention that the well known cold crucible electromagnetic melting. This smart solution was figured out in early 1910s' [54], and the first patent was obtained by a Germany company named Simens und Halske in 1931 [55]. The cold crucible is a water-cooled copper crucible made by a number of separated sectors to reduce the shield effect of the conducting crucible. In operation, a skull made by the melting object itself forms between the crucible and the melt and avoids the reaction between them. This makes melting the reactive materials become possible [56]. Figure 1.5 (a) gives a photo of real cold crucible electromagnetic melting device and figure 1.5 (b) shows its corresponding sketch. Except melting the reactive and ultrahigh melting point meterials cold crucible electromagnetic melting provides more possibilities, such as fabricating the ultrahigh purity materials and growing the single crystal [57-59]. Moreover, another good example of using the cold crucible electromagnetic heating in high efficient material preparing technology is the cold crucible continuous casting (C.C.C.C or 4C) process that illustrated in figure 1.5 (c). 4C process was developed initially by cooperation between the CEZUS company and MADYLAM (now SIMAP/EPM) laboratory in Grenoble (France) and patented in 1989 [60]. Similar to induction heating, it can find that a number of brilliant works related to cold crucible electromagnetic melting have been done. However, because the relationship bwteen flows and mass or heat transfer in melt contained in the cold crucible are not clearly undertood until now, massive investigations on this topic carry on with the aids of numerical simulations [61-63].

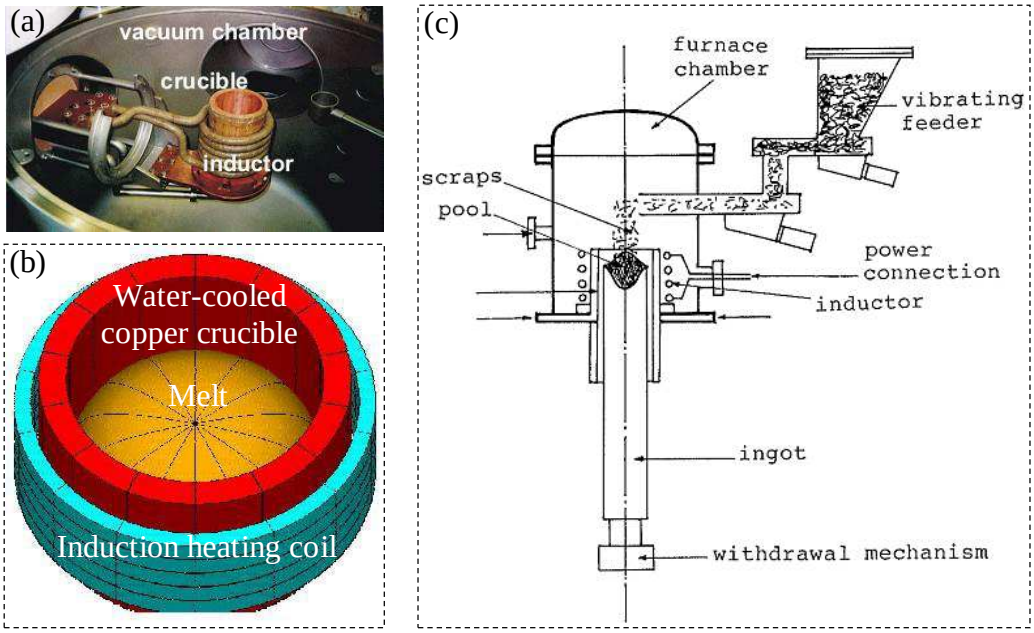

Figure 1.5 (a) Photo of real cold crucible electromagnetic melting device; (b) Sketch of cold crucible electromagnetic melting; (c) Sketch of cold crucible continuous casting device.

➢ **Electromagnetic levitation**

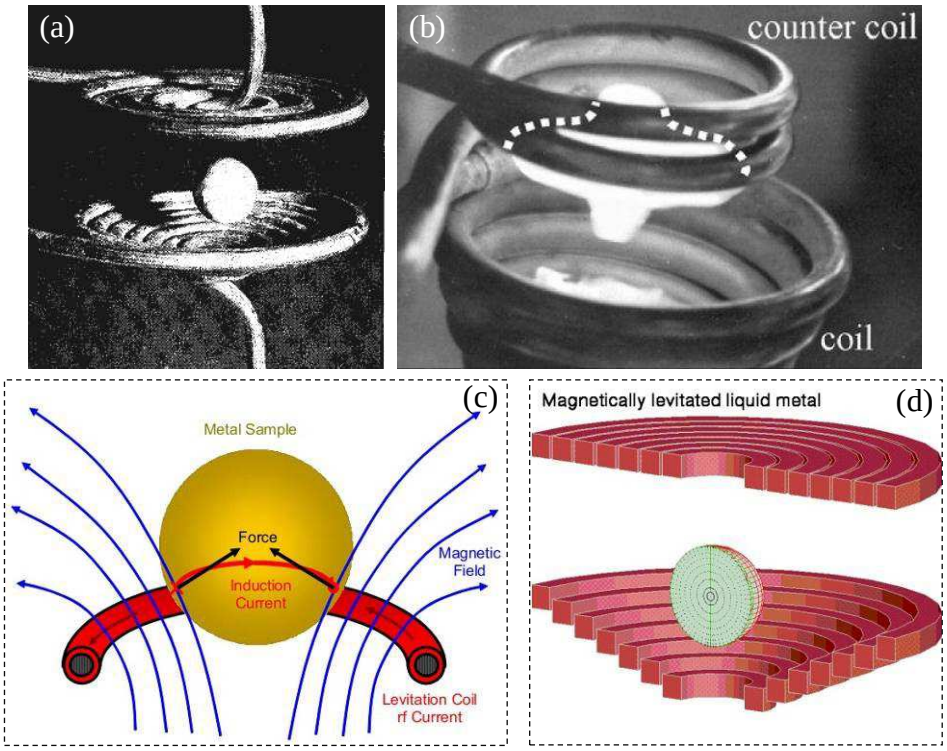

Figure 1.6 (a) Levitation of solid Al sphere; (b) Levitation of Al melt; (c) Illustration of levitating a melt droplet by AC magnetic field; (d) Example of numerical simulation of electromagnetic levitating.

When time stepped into 20th century's second decade, another fascinating phenomenon, electromagnetic levitation, was invented by perfectly utilizing the MHD principle as described in chapter 1.1.1 and patented in 1912 [64]. As one kind of magnetic levitation, electromagnetic levitation is realized via a time-changing magnetic field. This kind of field can induce the eddy currents in the conducting object and intereacts with them to produce the electromagnetic forces. If the electromagnetic forces are oppsite to and big enough to counterbalance the gravity under a certain conditions the conducting objectcan be levitated [65]. According to the baisis of the electromagnetic levitation, many applications had been achieved, for example the maglev train. In the same time, the advantages of such levitation were noticed and used by some material scientists, such as the examples given in figure 1.6. Figure 1.6 (a) shows the first experimental attempt of electromagnetic levitation in 1952 by Okress [66], figure 1.6 (b) gives the image of levitating aluminum melts by an alternating current magnetic field at EPM laboratory in France [67], the simply illustration of the levitation principle is in figure 1.6 (c), and figure 1.6 (d) provides an example of numercal simulation of electromagnetic levitation [68]. Moreover, it is worthy to point out that deep undercooling, ultrahigh pure material preparation and measurement of materials' high

temperature thermophysical paramenters can be realized with the aid of electromagnetic levitation as well [69, 70].

➢ **Electromagnetic stirring**

Electromagnetic stirring is another classical example of application of MHD principle and main subject in EPM field. This smart inventation was reported in a literature published in 1917 [71], and it is reasonable to believe that its appearance must be under the strong expectation of controlling the melt's flows in the metallurgical process.

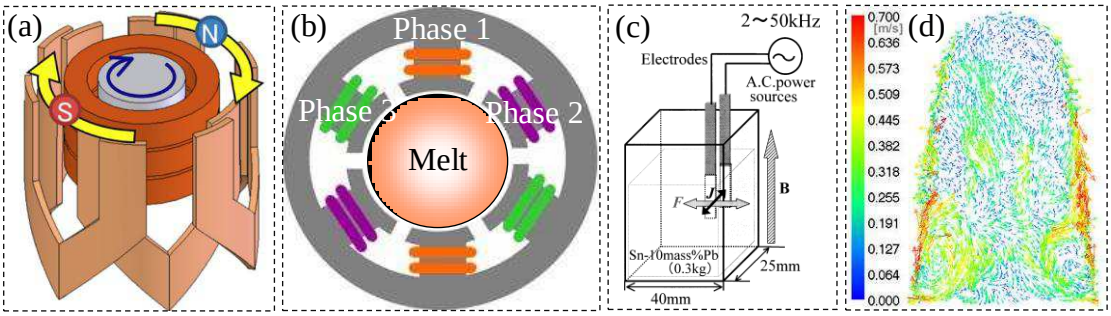

Figure 1.7 (a) Mechanically rotating magnetic field; (b) Rotating magnetic field realized by phase different currents; (c) Sketch of electromagnetic vibration device; (d) Numerical simulation of melt flows field during cold crucible electromagnetic melting.

According to the type of applied magnetic fields, melt can be stirred by the following approaches: 1) melt is stirred by an alternating current magnetic field, for example the melt can be stirred during of induction heating, cold crucible electromagnetic melting and electromagnetic levitation; [72]; 2) melt is stirred by an pulsed magnetic field [73]; 3) melt is stirred by a moving magnetic field such as melt can be stirred by a rotating magnetic field [74, 75]; and 4) melt is stirred by imposing the non-parallel magnetic field and electrical current simultaneously (sometimes called electromagnetic vibration) [76-78]. In order to gain some perceptual knowledge, figure 1.7 (a) gives an example of realizing the stirring by a mechanically rotating magnetic field. Figure 1.7 (b) shows the top view of the device stirring melt by imposing phase different currents. Figure 1.7 (c) simply illustrates the method commoly called electromagnetic vibration. It should be noticed that such method combines the advantages of stir and vibration, but the inserted electrode blocks the widely application of this method [79-81]. Because relationship between the input conditions and the corresponding flow field of stirred melt has not been thoroughly understood, researches on electromagnetic stirring are still rising. Moreover, due to the difficulties in observing flow field in melt, numerical simulation is a main and surfficient way used in the investigations on this topic [82-84]. Figure 1.7 (d) is an example of numerical simulation of flow field in melt during clod crucible electromagnetic melting [85].

➢ **Electromagnetic braking**

Controlling the fluid flow should at least contain two aspects that promote and suppress. If saying the electromagnetic stirring can be regarded as promoting melt flow, to fulfill the demands of control, there must be a method to suppress the flows in melt. It seems easy to realize the suppress purpose visa producing an electromagnetic force has opposite direction to melt flows [15]. Besides, beause the direction of electromagnetic force can be easily managed though modify the applying electromagnetic field. This method should be operable. However, suppressing flows by an opposite electromagnetic force is not so successful in reality. This is because stronger other than weaker motions will be led when the opposite force acts on the flowing melt. Nevertheless, even melt flows are slowed down by the opposite force, which are not stable [86].

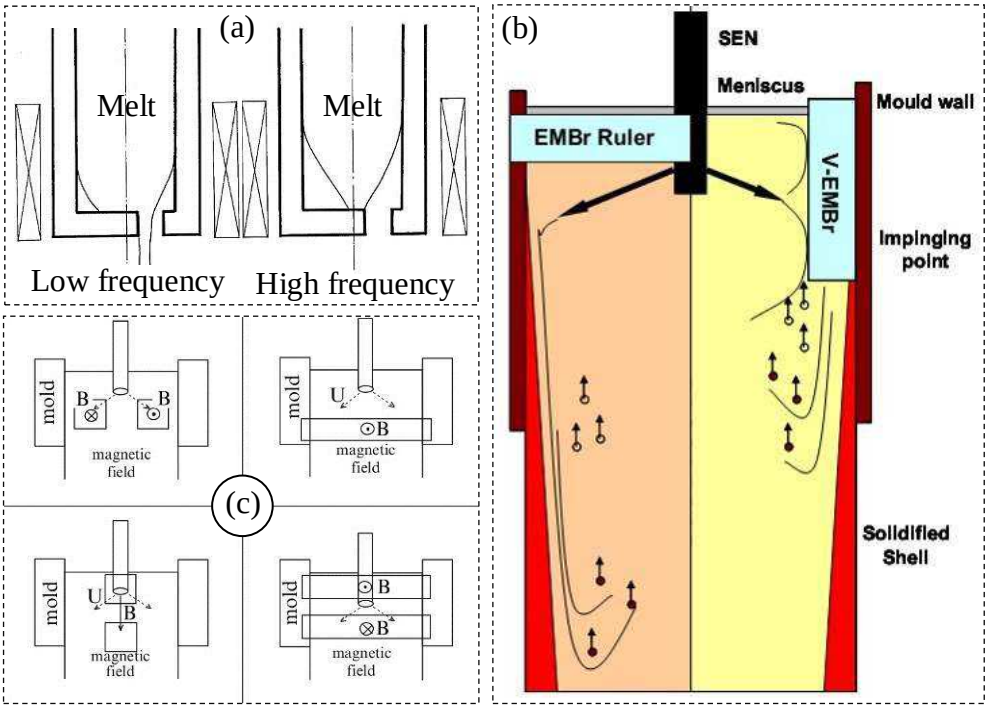

Figure 1.8 (a) Electromagnetic braking realized by induction coil around nozzle; (b) Electromagnetic braking used to suppress jet flow in continuous casting mold; (c) Four different types of electromagnetic braking realized by static magnetic field.

Therefore, more efficient method is desired to realize the truely control of melt flows. Motivated by this, another way was figured out that is using the induced electromagnetic pressure to balance the hydrostatic pressure of melt flows. As shown in figure 1.8 (a), a simple induction coil around the circular nozzle with a decentered hole can control the downward melt stream based on the similar principle of electromagnetic levitation [87]. However, the hole of nozzle cannot be placed in the center due to the alternating magnetic field with axisymmetric distribution is impossible to entirely stop the cylindrical flows or levitate them [88]. Figure 1.8 (b) gives the most commonly method used to suppress jet flow in the continouse casting mold by static magnetic field, which is based on the MHD theory

related effect 2 as illustrated by figure 1.1 [89]. For this method, if the static magnetic field is not situable arranged unwanted counter flows can appear near the nozzle jet [90-92]. So that, there are still many works worthy to do on this topic and numerical simulation can be the best choice to optimize the magnetic field and then to avoid the unwanted counter flows [93-95]. Figure 1.8 (c) shows some solutions to perfect the electromagnetic braking effect [96].

- **Electromagnetic shaping**

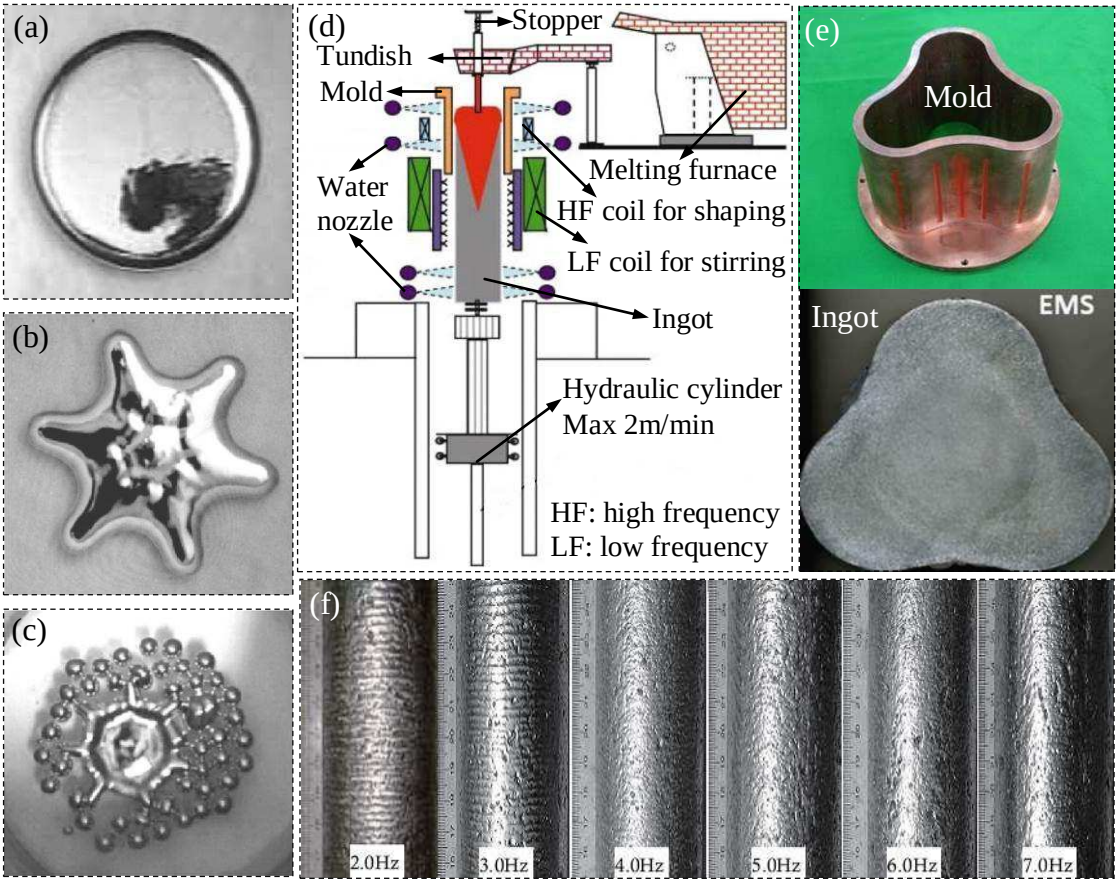

Figure 1.9 (a) Mercury drop is at rest; (b) Mercury drop is shaped by magnetic field with frequency of 2.1Hz; (c) Gallium drop is emulsified by magnetic field with frequency of 6.2 Hz; (d) Equipment for the near-net shape continuous casting; (e) Mold of equipment shown in (d) and the ingot; (f) Products of soft-contact continuous casting under different electromagnetic field frequencies.

Taking advantage of the electromagnetic pressure, another main subject of EPM, electromagnetic shaping is invented to control or modify the shape of liquid metal [97]. Because the electromagnetic pressure accompanies all electromagnetic related process, it is difficult to clearly tell the precise time when the electromagnetic shaping is invented. However, it must be a scientist with an art heart inside firstly noticed and treated this fascinating phenomenon as an individual research subject. Because, as shown in figure 1.9 (a) to (c), shaping the liquid melt just likes creating an artwork. These artworks are caused by the electromagnetic instabilities that related to both amplitude and frequency of the imposing magnetic fields [98-100]. Except creating artworks, electromagnetic shaping provides two

important industrial applications. One is the near-net shape continuous casting as shown in figure 1.9 (d) and (e) that the equipment, mold, and produced ingot respectively [101, 102]. The other is soft contacting continuous casting that had been successful used to fabricate the aluminum based alloys with high surface quality as shown in figure 1.9 (f) [103, 104]. Meanwhile, electromagnetic shaping is able to modify the meniscus in continuous casting mold, which can improve the surface quality of continuously casting products [105, 106].

- **Magneto-Electrochemistry**

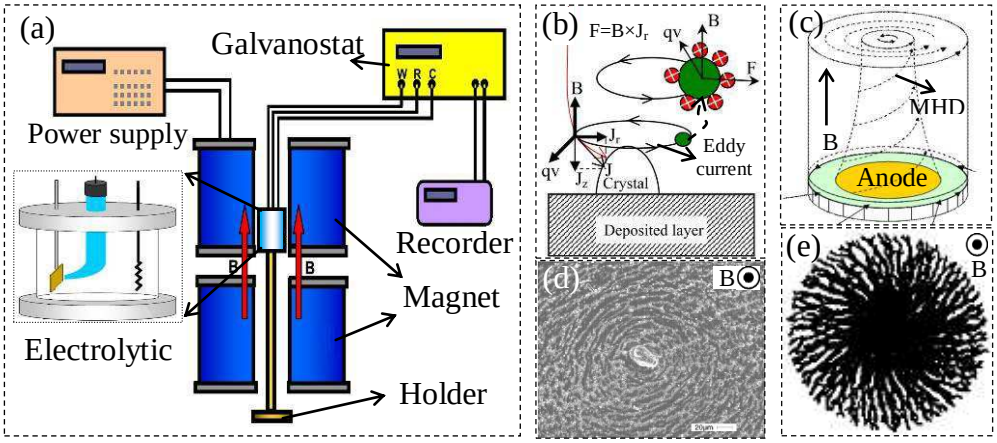

Figure 1.10 (a) Magneto-electrochemistry device; (b) Illustration of micro-MHD flows in composite magneto-electrodeposition; (c) Illustration of MHD flows in electroless deposition; (d) Micro-chiral structure of Ni/nano-particle-Al_2O_3 achieved under influence of micro-MHD flows; (e) Macro-chiral structure of Ag metal-leaves under influence of MHD flows.

Emergence of magneto-electrochemistry extends the application range of MHD theory and enriches the content of EPM research field [107]. Chemistry reaction is another efficient method to preparaing advanced materials [108-110]. Therefore, whether or not the magnetic field can affect during such process is worthy to investigate. Electrochemistry process was firstly choosed to investigate the influence of imposing an external magnetic field due to electric currents exists inherently [111-113]. Magneto-electrochemistry specially refers to the electrochemical process taking place in the presence of magnetic field, as shown in figure 1.10 (a) [114]. Because Lorentz force should be produced by the imposing magnetic field and the inherent electric currents, flows caused by such force appear in solutions and affect the key factor of such process that the mass transport [115]. Two kinds of flows involved in magneto-electrochemistry are defined, one is micro-MHD flow that produced by interaction between magnetic field and deformed current at the vicinity of crystal, and the other called MHD flow is generated by the non-parallel magnetic field and electric currents in the diffusion layer [116, 117], as illustrated by figure 1.10 (b) and (c). Under the influence of such flows, the micro- (figure 1.10 (d)) and macro- (figure 1.10 (e)) chiral structure were

obtained in composite electrodeposition of Ni/nano-particle-Al_2O_3 [118] and electroless deposition of Ag metal-leaves respectively [119].

Until now, main subjects of EPM have been introduced briefly, but which must be far from to get the fully view of EPM because some other topics are not mentioned such as velocimetry of liquid melt [120-122], electromagnetic field controlling plasma process [123-125], microwave heating [126], and application of electromagnetic field to environment problems [127, 128]. Particularly, topic the most closely related to the present thesis has not been introduced, which is a rising branch of EPM that applying static magnetic field to solidification process.

1.1.3 Influence of static magnetic field on solidification

As an important section in metallurgy and the widest method to prepare metallic materials, solicification was consciously treated as an independent discipline from late 1950s' to early 1960s' [129-131]. Although electromagnetic fields had been used in several metallurgical processes at that time, most of them were time-changing or mechanically moving magnetic fields [132-134]. First attemption of applying static magnetic field was inspired by the expectation to damp flows in melt that may result in solute segregation and banding in solidification process [135-137]. After that, rising interests on studying the influence of static magnetic field on solidification were waked up. Meanwhile, numerous interesting and meaningful phenomena were uncovered, particularly when the solidification is conducted under high static magnetic field [138-140].

- **Static magnetic field affects the thermodynamics of solidification**

Thermodynamics determinates the possibility of occurance of phase transformation, which is represented by the Gibbs free energy difference between parent and producing substances [141]. Just like temperature and pressure, magnetic field is another essential thermodynamic parameters and able to change the internal energy of system [142]. So that, if the phase transformation takes place in magnetic field, the Gibbs free energy of both parent and producing substances may be shifted because of their different magnetism properties [143]. In order to express this shift, additional item standing for the magnetization Gibbs energy difference is added to the expression of total Gibbs free energy difference of the system [142]:

$$\Delta G=\Delta G_0-(\mu_0/2)H^2\Delta(\chi V) \qquad (1.1)$$

where, ΔG_0 is free energy difference in the absence of magnetic field. The second item at right is the magnetization Gibbs energy difference, in which μ_0 is magnetic permeability ($4\pi\times10^{-7}$ $H\cdot m^{-1}$), H is imposed magnetic field strength, χ denotes magnetic susceptibility and

V represents molar volume of the substance. It can see that the bigger the magnetic susceptibility difference of the substances is the more apparent change of total free energy is. For this reason, inchoate investigations on this topic were almost focused on the ferromagnetic materials [144]. Murgaš and Biacovska applied a magnetic field during cooling the pure iron from melt and found that both temperatures of *l* to δ and δ to γ phase transformations were shifted to high region as indicated by figure 1.11(a) [145]. Similar investigations were also taken on solid phase transformation processes, such as austenite to pearlite, austenite to bainite and austenite to ferrite transformations. It was found that the bainite was dramatically promoted when applied a 10T magnetic field during bainite transformation process as shown in figure 1.11 (b) [146-148]. Additionally, phase diagram calculation suggested that magnetic field changed both γ-α and γ- Fe_3C transformation as revealed by figure 1.11(c) [149].

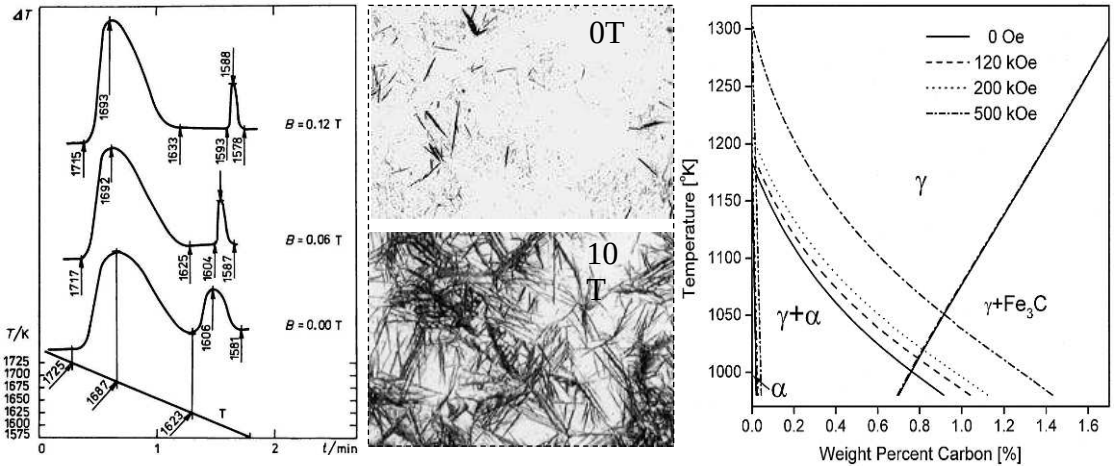

(a) (b) (c)

Figure 1.11 (a) Differental thermal analysis of cooling iron from melt without and with different magnetic fields; (b) Bainite transformation at 1275K for 10 min without and with a 10T magnetic field; (c) Fe-C phase diagram associated with the γ-α and γ- Fe_3C transformation under various magnetic fields.

Although the magnetization Gibbs energy difference between liquid and solid of non-ferromagnetic systems is negligible, the change of solidification temperature is detectable when an ultrahigh magnetic field is applied [150]. For example, Ren and Li et al. experimentally demonstrated that 10T magnetic field can increase the temperature of peritectic phase transformation, BiMn1.08 + L = BiMn, by about 20K [151]. If saying there is still a ferromagnetic phase involved, another experiment performed by Li, Fautrelle and Ren provided strong evidence. They found that 12T magnetic field is capable to increase the solidification temperature of Bi by about 6K [152]. Furthermore, Chuanjun Li invented a specially designed device to perform the differential thermal analysis under high magnetic field. He found that the high magnetic field can shift the solidification temperature of Al-Cu

binary system as well [153]. Meanwhile, he proposed another possibility that may respond to the solidification temperature shifting, which is the physical properties but not only the internal energy are changed under high magnetic field, surface tensions and wettability between the melt and the nuclei for instance [154].

➢ **Static magnetic field affects the orientation during solidification**

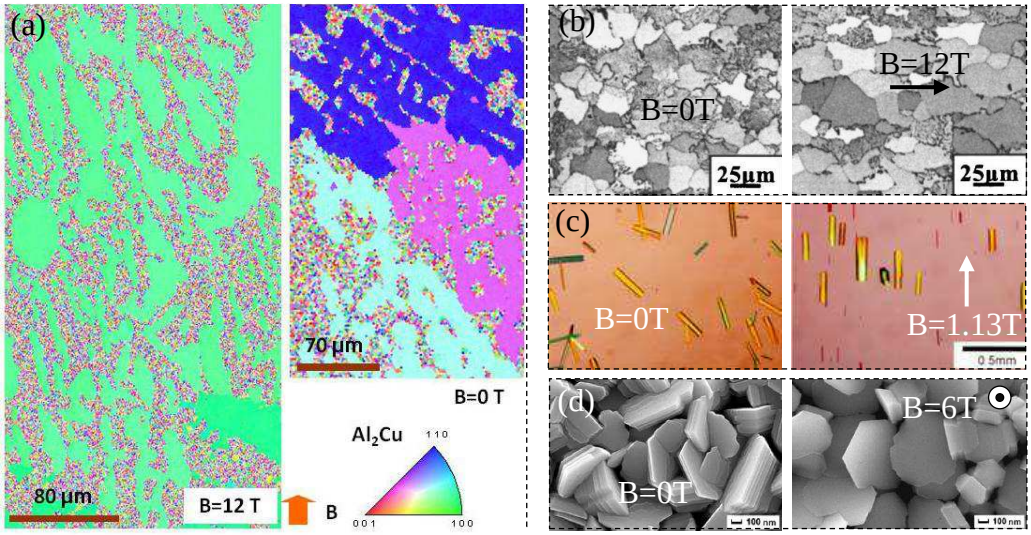

Figure 1.12 (a) Orientated Al-Al_2Cu alloy fabricated via solidification under a 12T magnetic field; (b) Oriented medium plain carbon steel obtained through austenitized under a 12T magnetic field; (c) Oriented egg white lysozyme under a 1.13T magnetic field; (d) Oriented Zn film achieved via vapor deposition under a 6T magnetic field.

When the thermodynamical demands are achieved solidification steps in the second stage that is the growth of nuclei. For this stage, which orientation should be selected is another core problem of solidification [155]. Moreover, because orientated or textured structures can dramatically increase products' physical and mechanical properties preparing the materials with aligned structure is desired, particularly, with the specified crystal orientation [156]. Inspired by this, some methods had been invented by numerals efforts paid, such as directional solidification. However, the crystallographic isotropy materials are always hard to be orientated because the small difference between the preferential growth direction and the others [157]. Thanks to magnetic susceptibility and shape anisotropy of crystals, the aligned structure of such materials may be achieved by applying an external magnetic field during solidification [158], electrodeposition [159], vapor deposition [160], solid transformation [161], and the protein synthetize process [162]. Figure 1.12 gives some examples of oriented structure obtained via applying magnetic field during different processes. Just as mentioned above, the magnetic susceptibility and shape anisotropy of crystals should respond to such alignment behaviors. The magnetic susceptibility is various in crystals' different axes [163], and the magnetic energy of each axis induced by the external magnetic field is expressed [164]:

$$G_{Mi} = -\mu_0 \chi_i H^2 / 2 \qquad (1.2)$$

where, G_{Mi} is magnetic energy of *i*-axis, μ_0 is magnetic constant ($4\pi\times10^{-7}$ $H\cdot m^{-1}$), H is the imposed magnetic field strength, χ_i denotes magnetic susceptibility of *i*-axis and *i* stands for the direction of crystal. It has been well know that crystal alway grows along the direction that bears minimum system energy. The growth of *c*-axis should be enhanced in the presence of external magnetic field if G_{Mab} is bigger than G_{Mc}, and then the orientated structure is achieved. In the case that magnetic axes correlate to the symmetry of crystal, for example the tetragonal crystal structure, the crystal receives a magnetic torque $T(\theta, H)$ [165] expressed as:

$$T(\theta, H) = \mu_0 \Delta\chi_{\parallel -\perp} H^2 V (\sin 2\theta) / 2 \qquad (1.3)$$

where, $\Delta\chi_{\parallel -\perp}$ is the susceptibility difference between two perpendicular axes, V is volume and θ is the angle between applied magnetic field and the axis with maximum $|\chi|$. Expression 1.3 reveals that the easy magnetization axis of the paramagnetic crystal should rotate along the applied magnetic field [166]. Because the induced demagnetizating field dependents on the shape of crystals and the magnetizating direction, the crystal has unsymmetrical structure can be orientated by the external magnetic field based on the shape anisotropy of crystals. In these cases, crystals should grow along the direction having lower demagnetizing field to ensure the minimum total magnetic energy of the sysem [167].

- **Static magnetic field affects the distribution of primary phases**

Other than the orientation of crystals, where are they placed is another crucial factor in determining metallic materials' properties [168]. Because the position of primary phases are decided by the nuclei, the inclusions and the local melts' condition (content of solutes for instance), if there is a method to affect these factors primary phasess' position may be controlled [169]. Fortunately, the magnetic property difference between the nuclei, the inclusions, the solutes and their surrounding melts permits the uniform or gradient static magnetic field to modify their distribution [170]. It shold be pointed oput that different from the electromagnetic levitation introduced in 1.1.2 the gradient static magnetic field is another approach to levitate substance, which is called magneto-Archimedes levitation [171]. The remarkable difference between these two levitations is the former realized by a time-changing magnetic field but the latter levitates substance by the static magnetic field [172].

In 1991, Beaugnon et al. levitated some diamagnetic substances by a high gradient static magnetic field and named such phenomenon as diamagnetic levitation [173]. This should be categorized to magneto-Archimedes levitation. The substance in gradient magnetic field is subjected to a magnetic force expressed as [174]:

$$F_M = \frac{\chi}{\mu_0} B \frac{\partial B}{\partial z} V \qquad (1.4)$$

where, μ_0 is magnetic constant ($4\pi\times10^{-7}$ $H\cdot m^{-1}$), B is magnetic field flux intensity, χ refers magnetic susceptibility and V is volume. Because both object and its surrounding medium are are subjected to this force, the object can be levitated if the resultant magnetic force acting on it is opposite and equal to its gravity. It can find that there should be only one position for a specified object to be stably levitated. Therefore, different objects must locate at different positions if put them in the same magnetic field. This provides an approach to separate the mixed objects via imposing a suitable magnetic field. As shown in figure 1.13 (a), the feeble magnetic particles are separated by a 12T magnetic field [175]. By using the gradient static magnetic field, Tagami et al. in-situ observed the solidification of a levitated water droplet and investigated the containerless crystal growth [176]. Wang Qiang et al. utilized a high gradient magnetic field to grade the Mn solutes in Mn-Sb melts and achieved the compositional gradient composites as shown in figure 1.13 (b) [177]. As shown in figure 1.13 (c), Ren Zhongming et al. studied the effect of magnetic field on the migration of primary MnBi phase in the melt and found that distribution of primary phase can be controlled via modifying magnetic fields and varying the holding time during solidification [178].

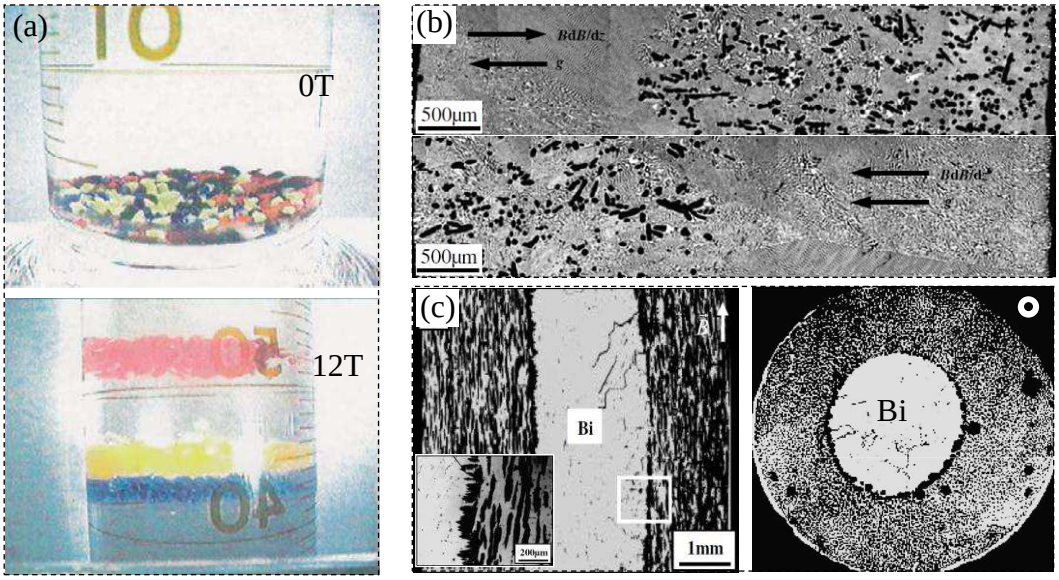

Figure 1.13 (a) Feeble magnetic particles with different magnetic susceptibilities in 6wt%$MnCl_2$ aqueous solution are separated by a 12T magnetic field; (b) Compositional gradient Mn-Sb alloy obtained by bulk solidification under a high gradient magnetic field; (c) Radial migration and alignment of primary phase in Mn-Bi alloy under gradient static magnetic field.

- **Static magnetic field affects the flows in melt during solidification**

Just like the storm can destroy everything when it passes, although the thermodynamical permission has been achieved, the selection of growth direction of crystal has been dicieded

and the position of primary phases has been redistributed, all these can be changed if severe engouth flows in melt appear during solidification [179]. Unlucky, flows in metl exist in almost cases if solidification conducted under terrestrial because the thermal and compositional gradient are always present [180]. Reducing or suppressing the flows in melt is desired in most crystal growth and solidification process [181]. However, not all the electromagnetic braking methods introduced in section 1.1.2 are suitable except the one using static magnetic field.

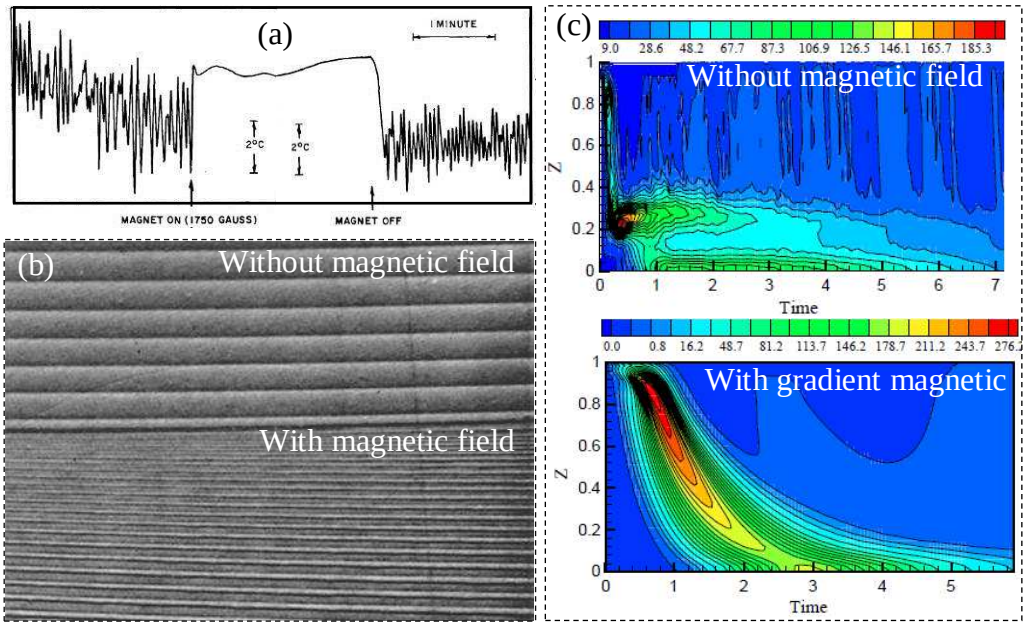

Figure 1.14 (a) Thermal fluctuations during crystal growth with and without a magnetic field; (b) Etched (211) surface of InSb single crystal without and with transverse magnetic field; (c) Simulation of the composition near solid-liquid interface without and with gradient magnetic field.

The theoretically analysis of damping flows in melt had been treated in 1952 by Chandrasekhar [182]. In 1966, Chedzey et al. published their experimental results that imposing a static magnetic field during growing the semiconductor crystal can eliminate the solute banding, or saying growth-striae. Curve shown in figure 1.14 (a) is the thermal fluctuations obtained by them. It can see that flows in melt were damped in the presence of a 0.175T staic magnetic field [135, 136]. After that, intensive numerical and experimental researches have been performed to understand the role of various magnetic fields in optimizing the quality of crystals [183-185]. Like showing in figure 1.14 (b), which is the InSb single crystal obtained without and with a transverse magnetic field by Witt et al. [186]. Figure 1.14 (c) is the numerical simulation of composition near solid-liquid interface during growing SbGe crystal in the absence and presence of the gradient magnetic field. Oreper and Szekely numerically investigated the influence of external magnetic field on the buoyancy driven flows in a rectangular cavity and stated that the damping effect of applied magnetic

field was related to the its flux intensity and the geometry of studying system. Additionally, they pointed out that flows cannot be damped entirely [187]. Reports of damping flows in melt by a gradient static magnetic field also can be found [188-190]. This has the similar principle of magneto-Archimedes levitation, but the magnetic forces produced by the gradient static magnetic field are opposite to the melt flowing direction rather than the gravity direction.

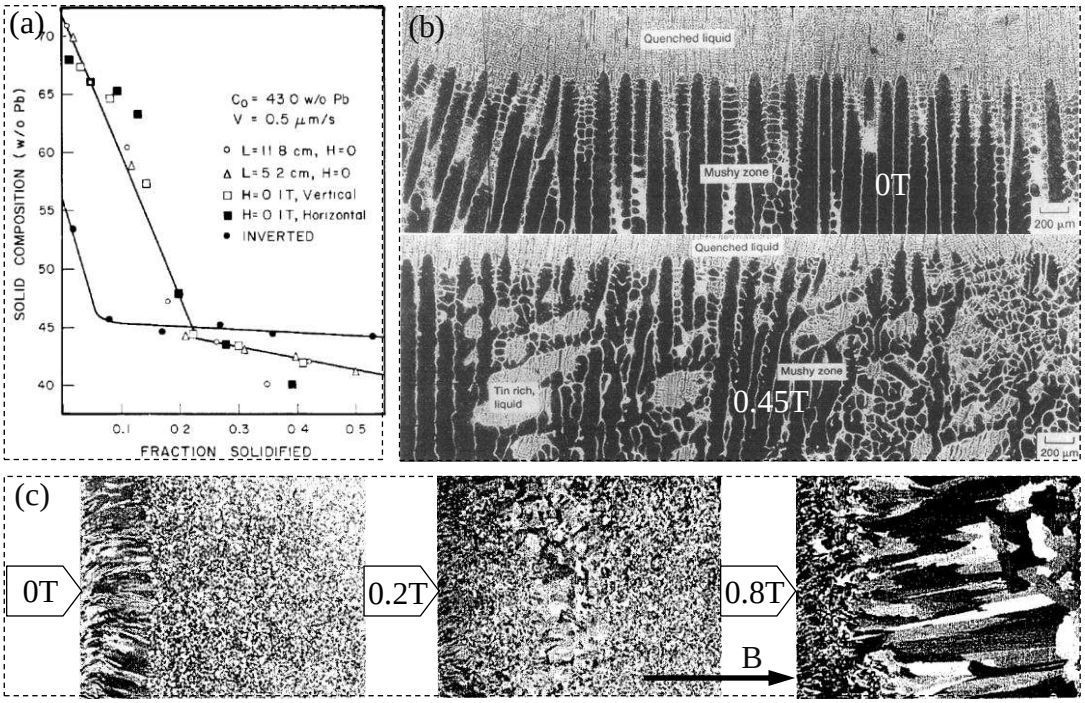

Figure 1.15 (a) Average solid composition *vs* solid fraction of Sn-43wt%Pb alloy fabricated with and without magnetic field; (b) Cellular microstructure of Pb-Sn alloys solidified without and with a 0.45 transverse magnetic field; (c) Macrostructure of Sn-Pb alloys solidified under different static magnetic fields applied parallel to the solidifying direction.

But the damping effect of static magnetic field does not always work, which was awared when some unexpected results emerge in directional solidification of metallic alloys under a static magnetic field. The first voice saying the invalid of the damping effect rose in 1981 [191], when Bottinger et al. investigated the relationship between solute convection and the macrosegregation in Sn-43wt%Pb alloy. They initially planed to suppress the convections by applying a 0.1T magnetic field, but they finally found that the static magnetic field cannot reduce macrosegregation at all (figure 1.15 (a)). To investigate this further, 13 years later, Tewari et al. applied a higher magnetic field during directional solidification of Pb-Sn alloys [192]. They also found that the 0.45T static transverse magnetic field has no influence on the bulk convections. In addition to, a strange phenomenon was uncovered. They found that 0.45T magnetic field led to new freckles in cellular arrays as shown in figure 1.15 (b) and attributed this to the magnetic field causing thermosolutal convection's anisotropy. Because

the appearance of freckles or saying the distortion of cellular arrys suggests convections exist in the mushy zone, such strange phenomenon should indicate that applying a static magnetic field may lead to new flows in melt during solidification. In fact, this is not role case, the indications for static magnetic field produceing new flows in melt can be aloso found in some other studies with different purposes. For instance, with the purposed to investigate the anisotropic effect of MHD on metal solidification Kinshida et al. solidified Sn-Pb alloys under different magnetic fields [193]. As shown in figure 1.15 (c), it can find that compare to the solid structure obtained without magnetic field the equiaxed crystal region was enhanced under in the sample solidified under 0.2T magnetic field. This indicates the existence of severer flows in melt when a 0.2T static magnetic field is applied because the increasing of equiaxed crystal region is commonly caused by intense flows in melt [194]. Nowadays, more indications of static magnetic field being able to produce new flows in melt during directional solidification emergy [195], but the systematic research is lack. This is one of the main reasons for making the present thesis.

1.2 Encounter between thermoelectric magnetic effect (TEME) and solidification

Similar to the encounter between magnetic field and solidification, before TEME officially comes across with solidification a relevant theory named thermoelectric MHD is proposed [196]. Therefore, it is better to begin the story from the meet between thermoelectric currents and magnetic field to the appearance of thermoelectric MHD theory, and then we can gradually step into the following encounter between TEME and solidification.

1.2.1 Meet between thermoelectric currents (TEC) and magnetic field

TEC refers the currents that caused by heat and is one aspect of the thermoelectric (TE) effect. Three phenomena make up the TE effect, which are Seebeck effect that converting temperature difference directly into electricity, Peltier effect that heat absorbing or releasing at an junction of two dissimilar metals when elecrtric currents flowing across, and Thomson effect that heating or cooling of a current-carrying conductor with thermal gradient [197]. These three phenomena were discovered respectively in 1821 by Thomas Johann Seebeck, in 1834 by Jean-Charles Peltier, and in 1851 by Lord Kelvin [198]. Although the TEC was discouvered early in 1820s', the meet between it and the external magnetic field happened almost a century later. This was realized by a smart invention that pumping the liquid metal by the Lorentz force produced via TEC interacting with magnetic field. In order to transfer the heat from fusion reactor blanket to the hot engine and then to generate electricity, the coolant

should be carefully chosen. Because the low solidification and high evaporation temeperature, liquid metal is the best candidate. Otherwise, how pump such the liquid melt coolant should be sovled as well. At that time, because the MHD theory and related effects had been widely known, people tried to find a method in accordance to the principle of electromagnetic pumping. It should be clear that temperature difference along the heat exchanging tube inherently exists and the liquid metal and the tube must have dissimilar physical properties. This gives rise to the appearance of TEC in case the liquid meltal coolant flowing within the heating exchanging tube. Moreover, the magnetic field must exist to protect windings from neutron bombardment in the fusion reactor blanket [199].Therefore, the problem of pumping liquid metal coolant in nuclear fusion generator was solved by the interaction between the inherent TEC and the static magnetic field [200]. This solution made TEC meet the magnetic field. After that, under intensive demands on developing fusion reactor generator, studies on optimizing the utilization of the interaction between TEC and magnetic field were boom. For this reason, several progresses and patents had been made as listed in table 1.2 that the events happened before Shercliff published the thermoelectric MHD theory in 1979 [196].

Table 1.2 Experiments and patents that utilize interaction between TEC and magnetic field

Year	People	Events
1951	W. Murgatroyd	Improvements in or relating to heat transfer systems. *U.K. Patent Appl.* 20911/51 [201]
1954	E. Luebke L. B. Vandenberg	Compact reactor power plant with combination heat exchanger thermoelectric pump (also *U.S. Patent* 2.748.710, 1956) [200]
1956	K. F. Schoch	An experimental liquid metal thermoelectric electro-magnetic pump – heat exchanger [202]
1961	D. von Rex	Thermoelectric pump for liquid metal [203]
1964	J. F. Osterle S. W. Angrist	The thermoelectric hydromagnetic pump [204]
1964	S. R. Rocklin	Thermoelectric pump *U.S. Patent* 3.116.693 [205]
1965	M. A. Perlow K. A. Davis	The development of the SNAP-10 thermoelectric pump (also *U.S. Patent* 3.288.070, 1966) [206]
1969	M. de Cachard P. Caunes	Fuel elements of sodium thermosyphon for irradiation cell [207]
1969	V. S. Makarov A. Kh. Cherkasskii	Pressure-consumption characteristic and efficiency of a thermoelectromagnetic pump [208]

Just like the paper published by Hannes Alfvén in 1942 marking the establishment of fully-fledged MHD theory, the paper published by J. Arthur Shercliff in 1979 [196] is regarded as the birth of thermoelectric magnetohydrodynamics (TEMHD) theory. Although this paper mainly dealt with the fluid flow problems involved in heat exchanging process in the nuclear fusion generator, he proposed the idea of applying TEMHD to metallurgy. This

lighted the enthusiasm of studying TEMHD phenomena in metallurgy process and provided a reasonable explanation to how new flows in melt appear when the solidification is conducted under external magnetic field. After that paper, J. Arthur Shercliff applied his TEMHD theory to some specific phenomena such as the pipe end problems in TEMHD and TEMHD with walls parallel to the magnetic field [209, 210]. Although these topics are still related to the heat exchanging system of nuclear fusion generator, his brilliant works made the TEMHD theory gradually mature. So that let us go together with the material researchers who had got Shercliff's inspiration to discover the TEMHD phenomena in the metallurgy, particularly in solidification process.

1.2.2 Review on researches of TEM flows in melt during solidification

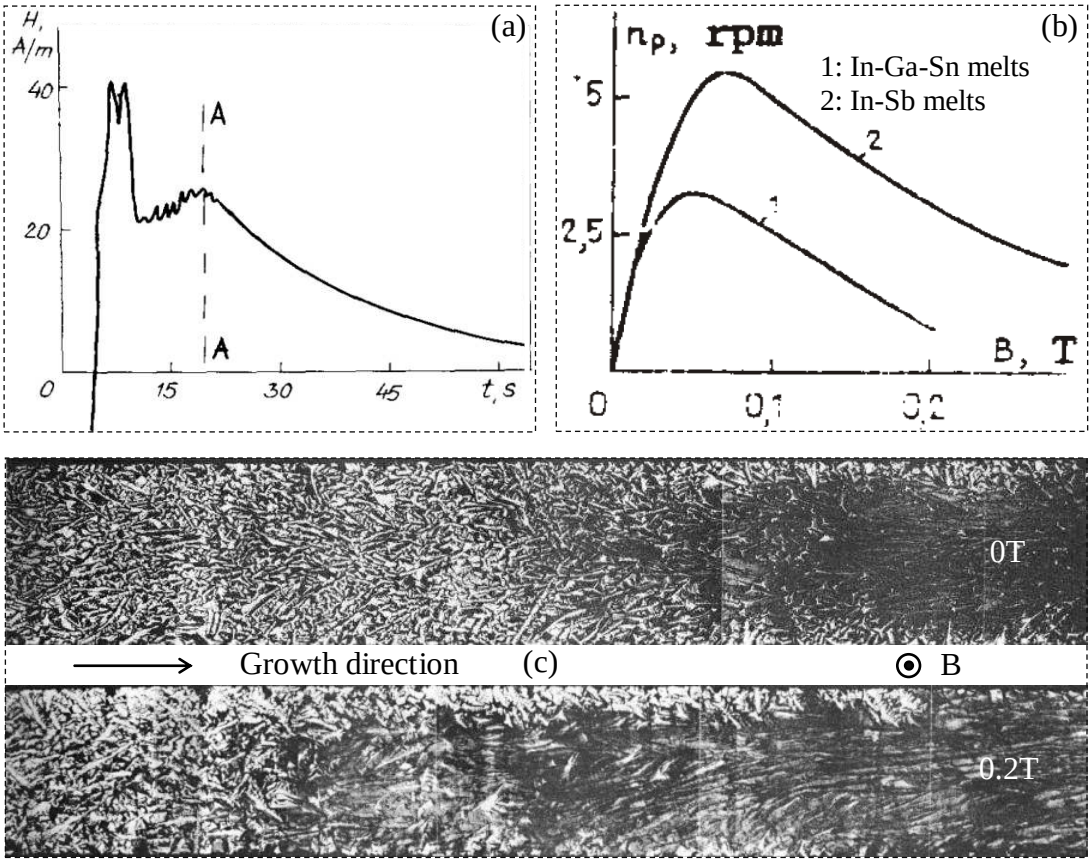

Figure 1.16 (a) Curve of magnetic field strength (H) close to crystallizing cadmium specimen versus the time (A-A corresponds to the moment that the solidification of the specimen finished); (b) Rotating velocities of liquid meltal veries with increasing magnetic field; (c) Bi-40at%Sn alloys solidified without and with a transvers magnetic field.

We call TEMHD flows thermoelectric magnetic (TEM) flows here in order to emphasize their original that interaction between TEC and magnetic field. The attempt of investigating TEM flows in metallurgy was made by some former Soviet Union scientists in the crystal growth process [211-213]. In 1981, when Michelson and Karklin investigated how the

magnetic field control the crystallization processes they found that currents generated by thermal electromotive force in the crystallizing body might affect the crystal growth via interacting with the magnetic field [211]. Further, they proved the existence of TEC by recording the changing of magnetic field that close to the vessel because the changing TEC should induce a fluctuation magnetic field near the crystallizing body. Figure 1.16 (a) is the curve of magnetic field strength versus time made by them. An explicitly evidence for the existence of TEM flows in melt during crystal growth was provided by Gorbunov in 1987 [212]. By applied only thermal gradient and vertical static magnetic field to liquid In-Ga-Sn contained in a copper crucible, he observed the motion and measured the rotaing speed from the surface under different magnetic fields as shown in figure 1.16 (b). It can find that TEM flows firstly speed up to the maximum and then slow down with the continuously increasing magnetic fields. Seven years later, the similar change tendency of the speed of TEM flows was pointed out by Kaddeche et al. in their numerical simulation works as well [217]. Furthermore, Gorbunov and Lyumkis argued that TEM flows should respond to the deformation of crystal shape and the remained periodic striations in doped silicon single crystal (figure 1.14 (b)) fabricated under a static magnetic field [213].

TEM flows in solidification of metallic alloys were noticed in the early 1990s' [214-216]. In 1991, Alboussière and Moreau et al. [214] solidified Bi-Sn and Pb-Sn alloys without and with magnetic field and found that solutal convection under magnetic field was more severe than the field is absent for Bi-Sn alloy as shown in figure 1.16 (c). Whereas, for Pb-Sn alloy, the solutal convection did not change a lot no mater the magnetic field is present or not. They concluded that the more severe convection appearing in Bi-Sn alloys should be TEM flows because Bi-Sn has much higher absolute thermoelectric power (70μV/K) than the Pb-Sn (0.1μV/K). After that, they built a numerical model to estimate the velocity of typical interdendritic TEM flows in 1994 [218]. By analyzed the influence of both Seebeck and Peltier effects on solidified microstructure they found that such effects can destabilize the liquid-solid interface [215]. They introduce a new dimensionless parameter *Se* to characterize the influenc of Seebeck and Peltier effects, which is expressed:

$$Se=\frac{\sigma_S\sigma_L}{\sigma_S+\sigma_L}\frac{(S_S-S_L)^2\theta}{\kappa_S+\kappa_L} \qquad (1.5)$$

where, σ is electrical conductivity, κ stands for the thermal conductivity, S is absolute thermoelectric power, θ denotes typical temperature at interface, subscripts S and L represents solid and liquid state respectively. SI units are used by the above physical quantities. Furthermore, Moreau and Lehmann et al. used TEM flows to modify interdendritic convections, introduced a simple model to simulate TEM flows in the mushy zone and

validated it by comparing the computing results to the experiment [219-221]. Figure 1.17 (a) to (c) show the typical structures obtained under different types of TEM flows.

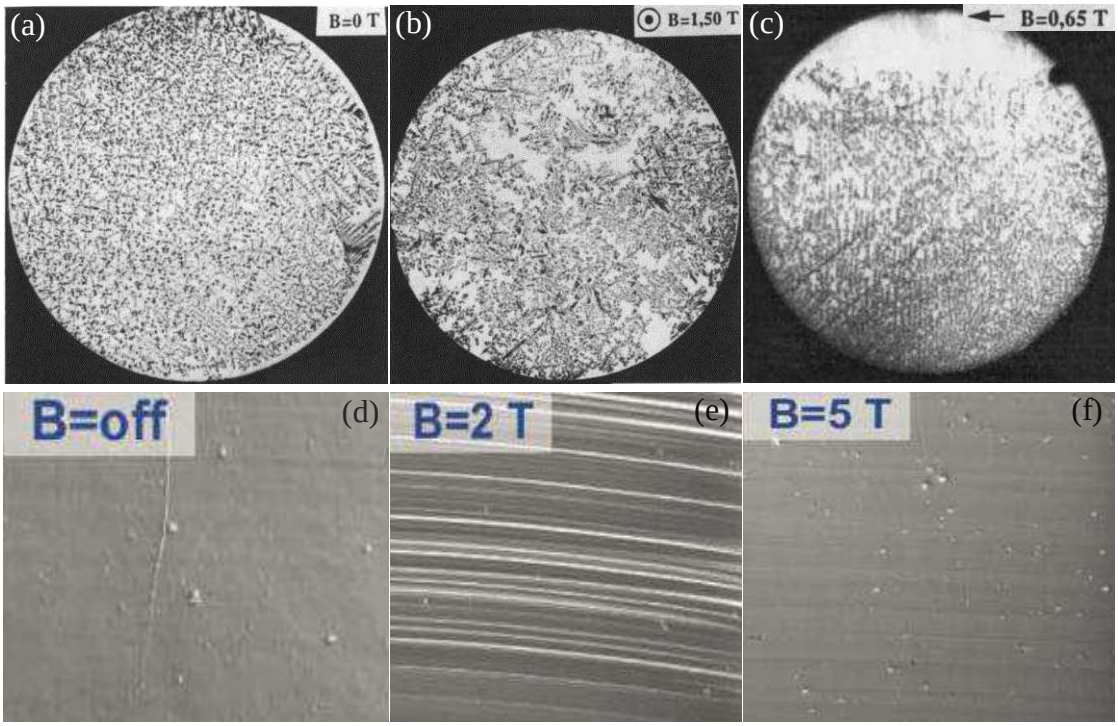

Figure 1.17 Transverse structures of Cu-Ag alloys directionally solidified without magnetic field (a), under a 1.5T axial magnetic field (b) and under a 0.65T transverse magnetic field (c). GeSi crystal grown under different axial magnetic fields: (d) 0T; (e) 2T; (f) 5T.

In 1990s', studies on TEM flows in crystal growth process developed as well, but this is after a little bit long stagnate from the pioneer exploration made by Gorbunov et al. It was 1998 when Cröll et al. found a new type of pronounced dopant striations quite different from the ones caused by buoyancy or surface tension driving convections. They thought this should be attributed to the occurrence of TEM flows during growing silicon under a strong static axial magnetic field [222]. In the same year, Khine and Wallker studied TEM flows in semiconductor crystal growth [223] and found the same change tendency of speed of TEM flows with imposing magnetic fields as the one measured by Gorbunov and numerically computed by Kaddeche. Further, they estimated the azimuthal component speed of TEM flows and found that the maximum speed can be several micrometers per second. This is able to cause the rotational-like striations during crystal growth. Moreover, they studied TEM flows in crystal growth under different moderate magnetic fields to find out how TEM flows vary with the imposing magnetic fields and the thermal gradient at crystal-melt interface [224]. Yesilyurt et al. numerically simulated the influence of TEM flows on Bridgman growth of $Ge_{1-x}Si_x$ [225] and found that the meridional convection altered the composition of melt in front of the crystal/melt interface then changed its shape. At the beginning of 21st century, they optimized their model and predicted TEM flows under varying gravity levels [226]. In

2001, Cröll et al. deeply studied the explanation used in their previous paper published in 1998 via numerical simulations [227]. The latest research of TEM flows in crystal growth we can find was taken by Dold, Szofran, and Benz in 2006 [228]. They experimentally proved that TEM flows reach the maximum speed under a unique magnetic field for the given condition, over such threshold, TEM flows slow down under higher magnetic field. This can be indicated by the periodic striations in the crystal as shown in figure 1.17 (d) to (f).

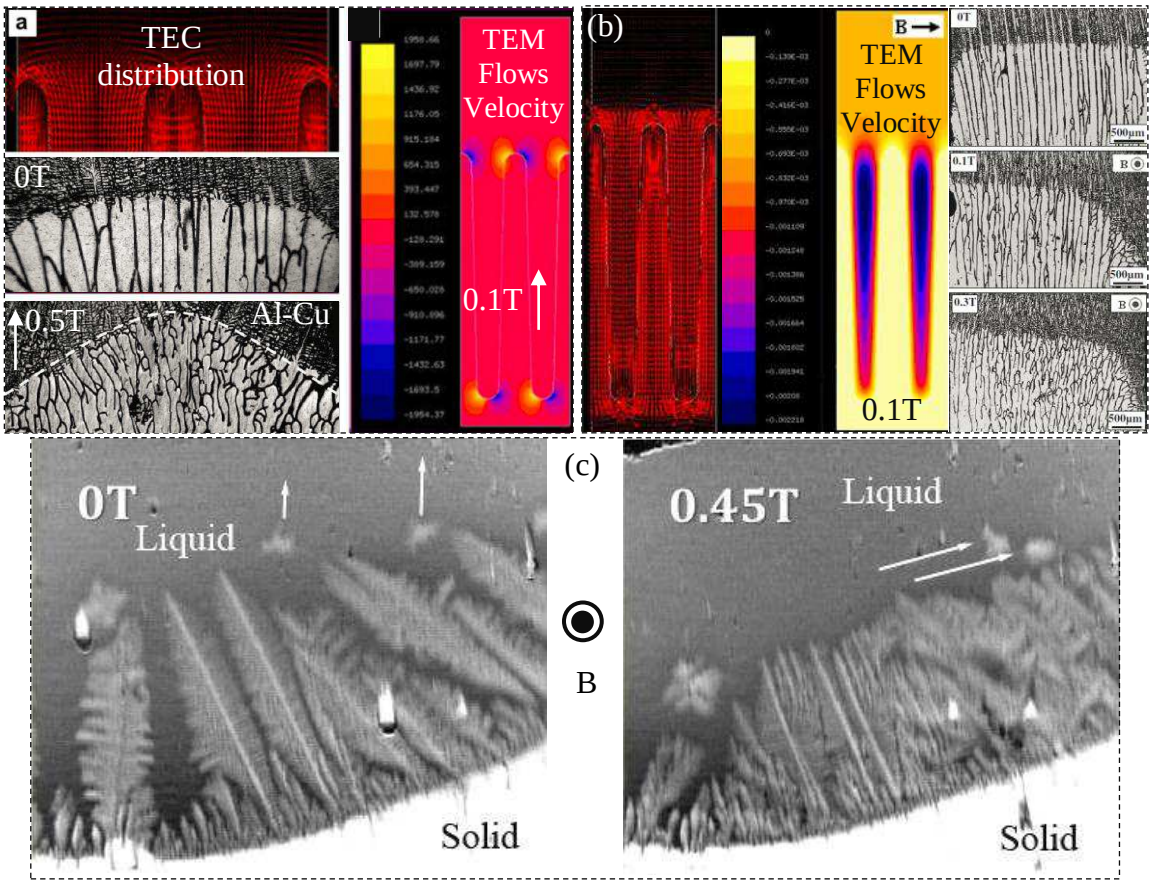

Figure 1.18 Computed TEC distribution, TEM flows and their corresponding experimental results under axial (a) and transverse (b) magnetic field; (c) In-situ observation of TEM flows generated by a transverse 0.45T magnetic field.

The researches of TEM flows in solidification of metallic alloys in this new millennium began with two master's work from Liaoning Technical University, China, published respectively in 2002 and 2006 [229, 230]. They investigated the influence of TEM flows on the formation of microstructure of Al-Cu and Al-Si alloys. This put forward a question that should we control the microsture by TEM flows during solidification? It is pity that no more publishing works from them could be found from then on. Fortunately, a raising and active group noticed this interesting topic and insisted the related study till now. This group is based on the successful cooperation between SIMAP/EPM laboratory in France and key laboratory of metallurgy of Shanghai University in China. Prof. Yves Fautrelle and Prof. Zhongming Ren respectively represent these two loboratories. In 2007, their first co-supervised Ph. D

student, Prof. Xi Li now, qualitatively evaluated the TEM flows in different typical scale lengths and compared with experimental results obtained under different axial magnetic fields [231, 232]. He concluded that effect of magnetic field varies for different typical scale lengthes, indeed, the smaller the structure is the larger the magnetic field is needed to produce the apparent TEM flows. In 2009, Li, Ren and Fautrelle thoroughly investigated TEM flows and its influences on solidification under a low axial magnetic field [233]. They computed the distribution of TEC along liquid-solid interface and the velocities of TEM flows around the cells/dendrites (figure 1.18 (a)) with help of Dr. Gagnoud. In the same year, a group from Germany published their numerical and experimental investigations on a pure TEM flows problem. They found that TEM flows can be vigorous and may be able to stir melt in some metallurgical processes [234]. In order to extend the previous studies, Li and Gagnoud treated the phenomenon similar to the one published in 2009 but under lower transverse magnetic field [235]. They found a perfect agreement between the simulation and the experimental results (figure 1.18(b)). During this period, a distinguished work was taken by a Japanese scientist Prof. Yasuda. He should be the first one to attempt to in-situ observe the TEM flows during directional solidification of metallic alloys [236] although his results seems wrong. Figure 1.18 (c) shows two pictures from him that captured by the synchrotron X-ray imaging technology during solidification of Al-Cu alloy. Because more and more material researchers have noticed and began to study TEM flows in solidification TEM flows in different systems was uncovered. For instance, Ren et al. found that TEM flows can result in a dramatic increased dendrite number in superalloys DZ417 [237], and Shen et al. found TEM flows should respond the modification of mushy zone length when directionally solidifying the hypereutectic Al-Al_2Cu alloy under different magnetic fields [238].

1.2.3 Review on researches of TEM force in solid during solidification

It has been well known that TEM flows are driven by the Lorentz forces induced by the interaction of TEC and magnetic field in melt. In fact, such forces should act on solid as well because TEC flow through liquid and solid [239]. Similarly, we name such forces as TEM forces to emphasize their origin. According to the literatures, it can find that the influence of TEM forces in solid are nearly ignored at the early stage of studying on the interaction of TEC and magnetic field in solidification. This is because forces in solid are always hard to detect comparing to the flows in melt. Besides, TEM flows can be apparent even if the imposed magnetic field is moderate or weak but the influence fof TEM forces in solid can be aware only when the magnetic field is relatively high [240]. Moreover, blocked by the limitation of high magnetic field generating technique, researches on influence of TEM forces

in solid during solidification are rare before recent [241]. Thanks to the fast development of superconducting materials, utilization of high, even ultrahigh, magnetic field in solidification or industrial metallurgy is realizable nowadays [242]. Because TEM forces in solid can be very strong under high magnetic field their influences should be paid attention to if the solidification is conducted under a high magnetic field. Indeed, performing solidification under high magnetic field is a rising research topic because many unexprected and meaningful phenomena have been uncovered in the past decade. Even though, the specialized studies on the influence of TEM forces in solid during solidification process appear till very recently.

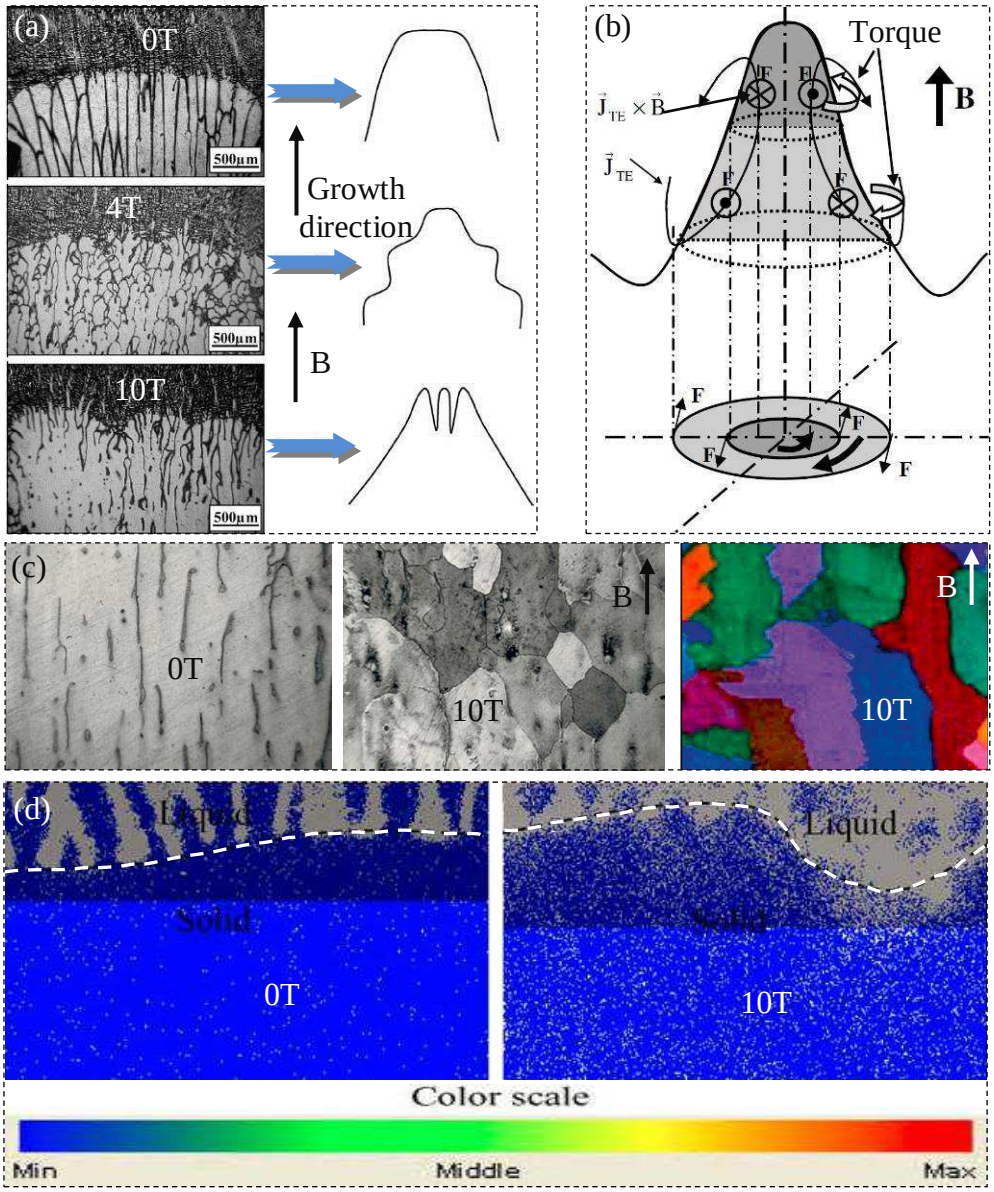

Figure 1.19 (a) Cell branching when Al-0.85wt%Cu alloy solidified at 5μm/s under different magnetic fields; (b) Illustration of torque caused by TEM forces on the top and the bottom of cell or dendrite; (c) Microstructure and EBSD map of Al-4.5wt%Cu alloy solidified at 5μm/s without and with 10T magnetic field; (d) Local crystal misorientation map of samples solidified without and with a 10T magnetic field (white dotted line refers the liquid-solid interface shape).

It was 2007 when Li, Fautrelle and Ren tried to validate their analysis on TEM flows [232] they found that cells were broken and liquid-solid interface became uneven under a 10T magnetic field. Further calculation suggested that TEM flows should be mostly suppressed under such high field. This makes they realize that the breaking of cells and the uneven interface might be caused by TEM forces in solid. They continuously investigated these novel phenomena and uncovered two important effects that TEM forces in solid can cause Columnar to Equiaxed Transition (CET) and liquid-solid interface instability [243, 244]. Regarding on the breaking of cells or dendrites, they studied the morphological instability of cells and dendrites during directional solidification under a high magnetic field [245]. They found that cells or dendrites twisted and deflected from the solidification direction at lower growth rates and side-branching and tip-splitting of cells appeared at moderate growth rates as shown in figure 1.19 (a). They thought that TEM forces changed the surface chemical potential of solid and shifted the surface tension of cellular or dendritic tips. After that, with the aids of numerical simulations done by Gagnoud, Li et al. confirmed the existence of a torque in a cell or dendrite as illustrated in figure 1.19 (b). Moreover they pointed out the posibility of TEM forces causing CET in directional solidification. In order to prove this, they directionally solidified various alloys, such as Al-Cu, Pb-Sn, superalloys, Zn-Cu, Al-Si, and Al-Ni, without and with high magnetic fields [246]. Electron back-scattered diffraction (EBSD) examination of the microstructure obtained from those experiemnts revealed that CET did occur under a sufficient high magnetic field as shown in figure 1.19 (c). Upon the uneven interface, with the help of Yudong Zhang and Claude Esling, Li et.al examined the local misorientation map of samples and found that the crystal mismatch of sample solidified under 10T magnetic field was more severe than that without magnetic field (figure 1.19 (d)) [240]. This demonstrated that TEM forces did exist in the solid when magnetic field was present. Moreover, concerning the changing of interface shape and the splitting of planar interface, it is reasonable to argue that TEM forces in solid may cause the interface instability. This argument was validated in Zn-Cu alloy by their following paper [247].

1.3 Purposes and organization of present thesis

It should be clear from the above introductions that electromagnetic fields have been widely used in metallurgical processes as an efficient flow field or microstructure controlling method. Therefore, investigation of ultilization of the magnetic field to optimize the solid structure of metallic materials will catch more and more attentions. Concerning TEC inherently exists in solidification process, TEM forces and TEM flows must appear once the external magnetic field is present. So that, how they affect the solidification and the

relationship between them and the magnetic field are desired to know. Although many studies on TEM forces and TEM flows in solidification have been made they are fragmentary. Therefore, it is the time to have a systematic investigation from the mechanism of how TEM forces and flows appear to their influences in solidification of metallic alloys. This motivates us to do the works in the present thesis that consists of six chapters.

In chapter 1, introduction of two important crossovers that making the TEME in solidification aware is given. Story begins with the emergence of magnetohydrodynamics (MHD) theory becasue its applications in metallurgy permits the first crossover between magnetic field and solidification. Besides, this crossover gives the birn to a rising research field namend electromagnetic processing of materials (EPM). Works on this crossover are generally introduced as well. After that, we begin another trip to see the second corssover between TEME and solidification. Because TEME is resulted from the interaction of TEC and magnetic field, the introduction of how TEC meets magnetic field is given in advanced. TEME should exist and affect in the metallurgy process was pointed out by Prof. Shercilff. More indications of TEM flows in solidification process have been reported because appying magnetic field during solidification has become popular. Certainly, these pioneer attempts on studying the TEME in crystal growth and solidification of metallic alloys are also reviewed.

In chapter 2, thermoelectric (TE) effect is introduced firstly, and then their corresponding phenomena in the solidification process are illustrated. Comparsion of the influence of different TE effects on solidification is taken and shows that TEC in accordance to Seebeck effect should be paid more attentions. Further, how TEM forces and TEM flows happen is phenomenologically described. Moreover, numerical simulations of TEC and TEME at the liquid-solid interface during solidification are taken after deducing the formulas of them to give a more intuitional view.

In chapter 3, TEME is confirmed by in-situ and real time observation during directionally solidifying the Al-Cu alloys. TEM forces are confirmed by comparing the analytical calculating velocities of TEM forces driving movement of particles to the velocities of the movement of crystals observed in directional solidification of Al-4wt%Cu alloys under a transverse magnetic field. In the other side, because TEM flows being capable to transport the rejected solutes are demonstrated by simulations and the shape of liquid-solid interface is sensitive to the solute concentration of melt ahead, TEM flows are confirmed via observing the shape evolution of panar liquid-solid interface.

In chapter 4, influence of TEM flows are examined with larger samples. Directional solidification of Al-Cu alloys under different axial and transverse magnetic fields is taken. Preliminary evaluation of the velocities of TEM flows are made before performing the

experiments. Results show that TEM flows are capable to change the liquid-solid interface shape whatever the morphology is. Numerical simulations of TEM flows with the same conditions used by experiments are taken and show reasonable agreement with the experimental results. The velocity evalutions, the experiments, and the simulations of TEM flows are consistent, and particularly, change tendency of the velocities of TEM flows with increasing magnetic fields that achieved from those three methods is perfectly consistent.

In chapter 5, whether TEME can influence the solidification of near-eutectic alloys or not is examined. Hypoeutectic Al-26wt%Cu and hypereutectic Al-40wt%Cu alloys are directionally solidified under different axial static magnetic fields. It is found that TEM flows exist and modified the mushy zone length dring solidification of both hypo- and hypereutectic alloys. Becides, dramatic growth enhancement of faceted Al_2Cu phase is found in Al-40wt%Cu alloys solidified under high magnetic field. This is becasue the defect multiplication in faceted phase can be caused by TEM forces acting on it. Defects in solid are benefit to the growth of faceted phase. Moreover, coupled growth structure is found in the hypoeutectic Al-26wt%Cu alloy solidified under a 4T axial magnetic field. Because in the absence of high magnetic field the dendrite-plus-eutectic structure is prevailing under the given conditions, such discovery may provide a novel method to extend the composition range for hypoeutectic Al-Cu alloys forming coupled growth structure. Differential thermal analysis (DTA) test sugguests that high magnetic field changing the solidification temperature of the α-Al and the eutectic phases shoud respond to the formation of coupled growth structure in this case.

In chapter 6, conlusions and prospects are given.

Chapter 2: Thermoelectric (TE) and thermoelectric magnetic effect (TEME) in solidification

2.1 Thermoelectric (TE) and thermoelectric magnetic effect (TEME) in directional solidification process

Considering thermal gradient at liquid-solid interface and the different physical properties of solid and liquid phases, such as thermal and electrical conductivities and absolute thermoelectric powers (ATP), it can be known that conditions at the liquid-solid interface naturally meet all the demands for the occurrence of TE currents in accordance to the Seebeck effect [248]. Therefore, TEME takes place once an external magnetic field is imposed. In order to more precisely and separately control the process conditions, directional solidification has been widely used in the investigations of solidification related problems [249]. Moreover, because the information of liquid-solid interface can be esealy obtained by such method this thesis uses directional solidification to study TEME in solidification as well.

2.1.1 TE effect

TE effect is an umbrella term used to describe the phenomena that direct conversion of temperature difference to electric voltage and vice-versa, which contains three separated effect that Seebeck, Peltier and Thomson effect [250]. About 200 years ago, with limited knowledge on the law of transition between heat and electric, it took 34 years from the first discovery of Seebeck effect related phenomenon to uncover the inner-relationship between these three separated effect [251]. However, at the atomic scale these effects and their relationship can be easily understood nowadays. Because charge carriers in material tending to diffuse from the hot to the cold part, electromotive force would appear if thermal gradient exists in a material [252].

- **Seebeck effect**

Seebeck effect was firstly discovered by a German physicist, Thomas Johan Seebeck, in 1821 [253]. He found that a circuit consisting of two dissimilar metals with junctions at different temperatures would deflect a compass magnet. He named such phenomenon ‘thermomagnetic effect’. A Danish physicist Hans Christian Ørsted reconsidered Seebeck’s discovery and found that electromotive force existing in two dissimilar materials. Therefore, he rectified the ‘thermomagnetic effect’ to ‘thermoelectricity effect’ [254]. It can image that if the dissimilar materials are conducting electric currents can appear in the circuit, and this should be the real reason for the deflecting of the compass observed by Seebeck. In order to memorize the first discover ‘Seebeck effect’ was used to represent this heat to electric

transition phenomenon. Figure 2.1 graphically illustrates the story from Seebeck's experiment to the measurement of thermoelectromotive force in a circuit and then the schematic of how TE currents flow in a circuit consisting of two dissimilar metals.

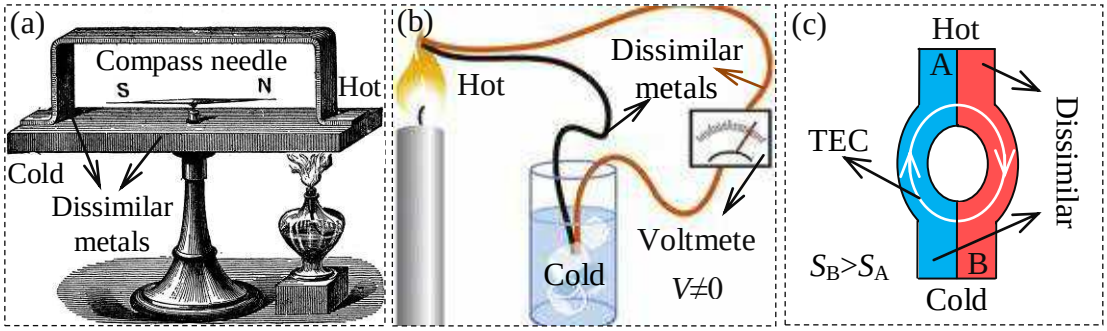

Figure 2.1 (a) Instrument used by Seebeck when he discovered the deflection of compass needle; (b) Illustration of 'thermoelectricity effect', V represents voltage; (c) TE currents flow in a circuit consisting of two dissimilar metals, S_A and S_B stands for ATP of metal A and B respectively, when $S_B>S_A$, TE currents flow from metal A to B at the hot junction.

➢ **Peltier effect**

Peltier effect refers to the phenomenon that heating or cooling happens at the junction of two dissimilar metals when there are electric currents flowing through. It was discovered by a French physicist named Jean Charles Athanase Peltier in 1834 [255]. 4 years later, relationship between the heating or cooling and the direction of electric currents was pointed out by Lenz [256]. Because the magnitude of heating or cooling at junction is proportional to the density of electrical currents flowing through, a proportionality coefficient named Peltier coefficient was defined [257]. Figure 2.2 (a) illustrates Peltier effect diagrammatically.

➢ **Thomson effect**

TE effect was full-fledged after the Thomson effect was predicted in 1854 and observed in 1855 by a British mathematical physicist William Thomson (later Lord Kelvin) [258]. Thomson effect was uncovered when Thomson attempted to establish a relationship of Seebeck and Peltier coefficient via introducing thermodynamics. Finally, Thomson relationships that describing the interdependency of these three separated phenomennon were found [259]:

$$\pi = S \cdot T \tag{2.1}$$

$$\tau = \frac{d\pi}{dT} - S \tag{2.2}$$

where, τ (V/K) is Thomson coefficient, and π (V) and S (V/K) is same as defined in figure 2.1 and figure 2.2. Based on this theory, Thomson believed that there must be a third phenomenon existing in the homogenous conductor, which was the later well-known Thomson effect. This phenomenon reveals that heat can be absorbed or emitted when electric

currents flow in a material with thermal gradient. Thomson coefficient was defined to link heat with both electric currents and thermal gradient. The illustration of Thomson effect is shown in figure 2.2 (b).

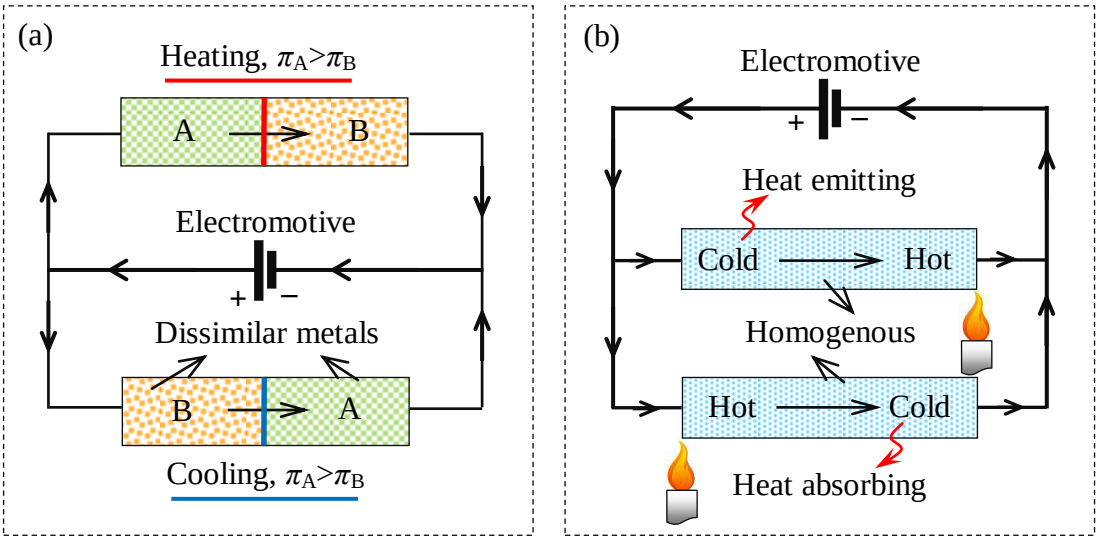

Figure 2.2 (a) Illustration of Peltier effect, π_A and π_B represents the Peltier coefficient of metal A and B respectively; (b) Illustration of Thomson effect, two conductors have the same Thomson coefficient.

Apart from TE effect, there is another phenomenon related to the conversion of heat and electric, which is Joule Heating. A British physicist and brewer James Prescott Joule studied and proposed such phenomenon in 1840s' [260]. Joule pointed out that electric currents flowing through a conductor can generate heat. However, Joule heating is not categorized to TE effect because it is not a thermodynamics reversible process. In the case of solidification, Joule heating is neglectable if there are no electric currents being imposed externally. This is because the density of TE currents is weak in most solidification process. Correspondingly, the electromigration of solutes caused by only TE currents can be neglected as well.

2.1.2 TE effect in directional solidification process

It must be found that the first step of TE effect is the appearance of TE currents, and this requests the circuit consisting of two dissimilar conductors and the temperature difference existing between the junctions. It is so happen that liquid-solid interface in directional solidification inherently meets the above requests. Generally, liquid and solid phase of alloy has different ATP and physical properties, so that they can be regarded as two dissimilar conductors. Bsides, solid and liquid phase must connect with each other at interface during the directional solidification proceeding. Moreover, thermal gradient exists at liquid-solid interface naturally. TE currents can appear at the vicinity of liquid-solid interface because the applied thermal gradient and the interface must not be perfectly orthometric in reality.

Take the typical morphologies of interfaces commonly obtained by directional solidification of metallic alloys (Figure 2.3 (a) to (c)), how TE effect takes place is illustrated. Select a small but representative element from each kind of interfaces as circled by the red rectangles, it can find that a simple geometry as drawn in figure 2.3 (d) can represent all the typical morphologies. In these cases, because upward thermal gradient provides a temperature difference between junctions and the different ATP and physical properties of solid and liquid phases TE currents can appear and flow as indicated by the dotted circle in figure 2.3 (d). Once there are electric currents flowing through the junctions between solid and liquid Peltier heating or cooling as indicated by the red or blue spot happens. Looking at the individual solid or liquid phase, heat absorbing or emitting occurs in accordance with Thomson effect.

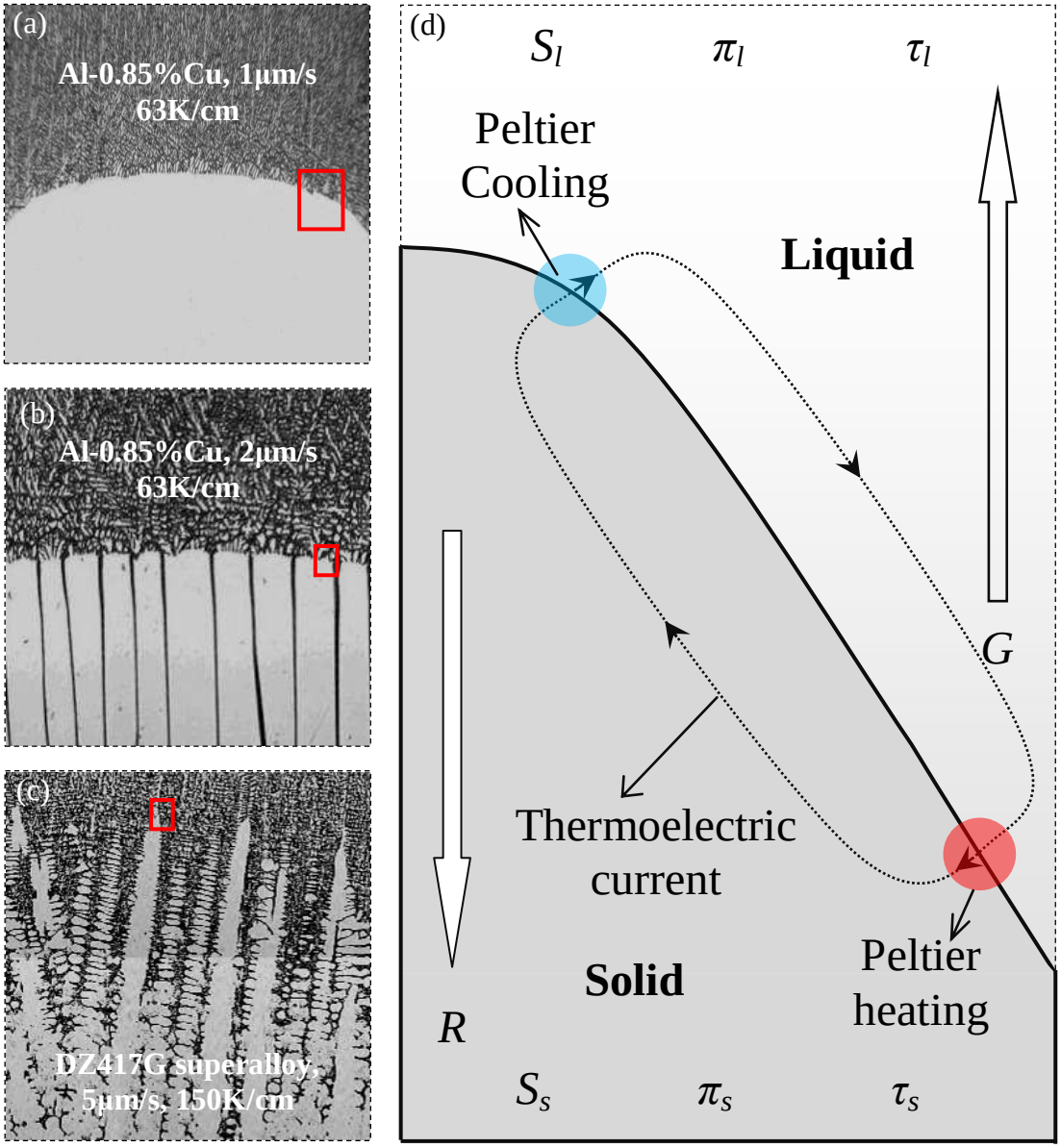

Figure 2.3 (a) Planar interface; (b) Cellular interface; (c) Dendritic interface; (d) Illustration of TE effect taking place at liquid-solid interface, G is thermal gradient and R is the growth velocity. S, π and τ are the same as defined in figure 2.1 and 2.2.

2.1.3 TEME in directional solidification process

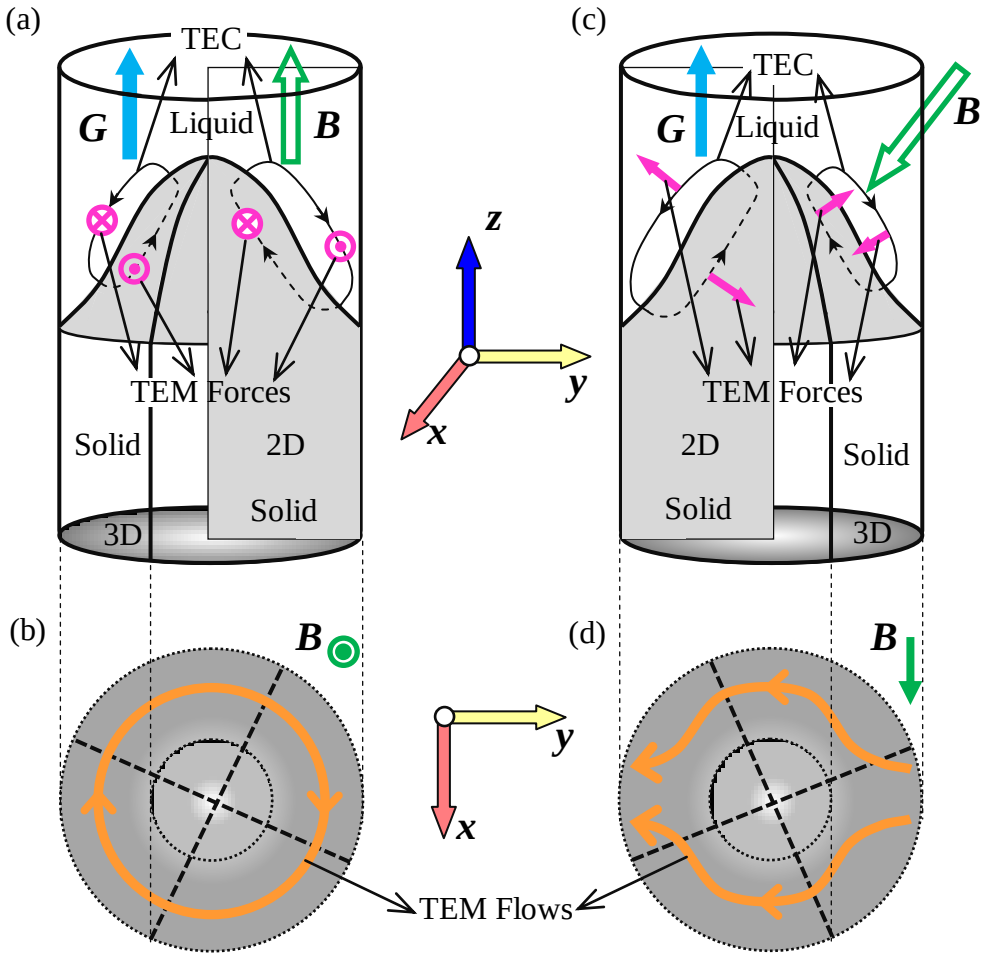

Figure 2.4 Graphically illustration of TEME at the vicinity of liquid-solid interface. (a) Illustration of TEM forces and its direction under axial upward magnetic field; (b) Top view of TEM flows in a horizontal plane; (c) Illustration of TEM forces and its direction under transverse magnetic field; (d) Top view of TEM flows in a horizontal plane.

As a non-contact method of controlling flows in melt, applying external magnetic fields has become a popular approach in metallurgy. In fact, the fast development of magnet manufacturing technique has permit to apply high magnetic field (>1T) in some industrial metallurgy process. Therefore, the influence of the interaction of TE currents and applied magnetic field should be paid more attentions because TE effect inherently exist in solidification or crystal growth processes. We name the Lorentz forces cause by interaction between TE currents and applied magnetic field TEM forces in this thesis. As introduction in chapter 1, TEM forces have a number of influences in solidification of metallic alloys, such as TEM forces in liquid can result in TEM flows and in solid they may trigger the fragmentation of dendrites or change the total chemical potential [261]. Therefore, in order to intuitively explain the interaction between TE currents and applied magnetic in solidification, typical cases are graphically illustrated in figure 2.4. Similar to the illustration of TE effect at liquid-solid interface, the structure drawn in figure 2.4 (a) and (c) can represent the planar, cellular

or dendritic morphology. Under the processing conditions given in figure 2.4 (a), TEM forces in liquid are swirling and result in TEM flows rotating around the solid front as indicated in figure 2.4 (b). Replace the axial upward magnetic field by a transverse one, TEM forces in liquid are pointing to the same direction as marked by the red arrows in figure 2.4 (c) and drive the one-way TEM flows at the adjacent of solid front as shown in figure 2.4 (d).

2.2 Thermoelectric currents (TEC) in directional solidification process

2.2.1 Neglect of Peltier and Thomson effects

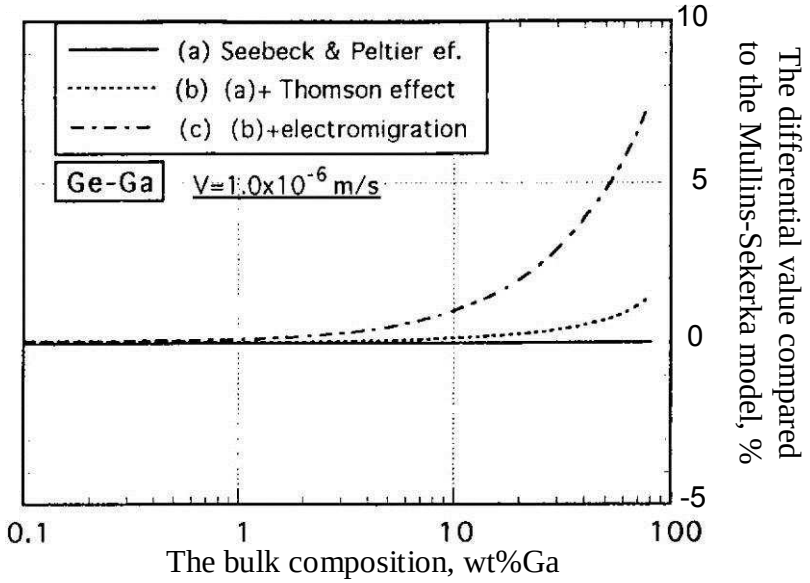

Figure 2.5 Comparison of interface instability considered the influence of TE effect and electromigration with that considered only the Mullins-Sekerka model for different initial compositions in the bulk.

Although above descriptions show that all the three phenomena of TE effect can exist at liquid-solid interface during directional solidification, Peltier and Thomson effects are neglectable in most cases [262]. Without any externally imposed electric field, Seebeck effect is the sole source of electric currents. Therefore, the magnitudes of the influences of Peltier and Thomson effects depended on the density of TEC. Generally, ATP of metals is about 10^{-6} *V/K*, electrical conductivity is about 10^{7} $(\Omega m)^{-1}$ and given the thermal gradient is 10^{3} *K/m*, the density of the resulting TEC is about 10^{3} A/m^2 during directional solidification of metallic alloys. Consequently, the flux of Peltier heating or cooling and heat production in accordance to Thomson effect is about 1 W/m^2. This is negligible because the solidification is always conducted under the temperature of several hundreds degree, particularly for the metallic alloys. Except this approximate estimation, Dr. Matoko TANAKA had precisely investigated the influence of TE effect on the interface instability [263]. He also found that Peltier and Thomson effects can be neglected as revealed by curves in figure 2.5. It can be seen that, compared to the Mullins-Sekerka (MS) interface instability analysis, the interface instability

was almost not affected by Peltier and Thomson effects for the Ge-Ga alloys with composition less than 10wt%Ga. Even for the high composition alloys, the influence of these two effects on the interface instability was less than 2%. Take both analyses above into account we consider only TEC in the flowing studies on the influence of TEM effect in solidification. And more, TEC should not be neglected when magnetic field is present can be proved by a simple estimation that the TEM forces caused by intereaction between a 10T magnetic field and the TEC estimiated just now is about 10^4 N/m^3. It is obvious that a 10^4 N/m^3 cannot be neglected no matter it acts in liquid or solid.

2.2.2 Formulation of TEC

Consider both the thermoelectric potential caused by temperature difference and the electromotive force induced by conducting substance moving through the magnetic field lines Ohm's law should be modified as [196]:

$$\vec{j} = \sigma\ (\vec{E} + \vec{u} \times \vec{B} - S\ \vec{\nabla} T) \tag{2.3}$$

in which σ is electrical conductivity, E denotes electrical field, u is velocity of moving substance in a magnetic field B, $\vec{\nabla} T$ stands for temperature difference and S is ATP. Assume the applied thermal gradient is upward, the temperature difference can be written as:

$$\vec{\nabla} T = G\vec{i}_z \tag{2.4}$$

here, G is constant thermal gradient and $\vec{i}_z$ is unit vector along z-axis. An effective scalar potential $W_i=V_i+S_iT$ should be defined before we formulate TEC in both liquid and solid, in which the subscript i stands for the state of concerning subject (s means solid and l means liquid). Further, it can set the thermoelectric potential as:

$$U(T) = \int S_i dT \tag{2.5}$$

that integrated for the datum temperature. Because S is assumed as constant, then it has:

$$U_i = S_i T \tag{2.6}$$

Considering TEC (Neglect $\vec{u} \times \vec{B}$) only and using the effective scalar potential, $W_i=V_i+S_iT$, expression 2.3 becomes:

$$\vec{j}_i = -\sigma_i \vec{\nabla}(V_i + U_i) = -\sigma_i \vec{\nabla} W_i \tag{2.7}$$

This togethers with the continuity of currents:

$$\vec{\nabla} \bullet \vec{j}_i = 0 \tag{2.8}$$

then it has:

$$\nabla^2 W_i = 0 \tag{2.9}$$

and, accordingly, W_i is harmonic.

Considering boundary condition, continuity of normal component of TEC must be satisfied at liquid-solid interface that can be expressed as:

$$-\sigma_l \frac{\partial V_l}{\partial n} - \sigma_l S_l G = -\sigma_s \frac{\partial V_s}{\partial n} - \sigma_s S_s G \tag{2.10}$$

where, G stands for the normal component of the thermal gradient. Moreover, the scalar potential V_l should equal to V_s at interface in the meantime.

In practice, ATP of materials is difficult to directly measure, but the ATP difference of a pair of dissimilar materials is easier to obtain. For the sake of showing how to use ATP difference, thermoelectric potential in a bimetallic thermocouple is calculated. As shown in figure 2.1 (c), TEC flows in the circuit can be described:

$$\zeta_{hot-cold} = \oint \frac{j}{\sigma} \cdot dr \tag{2.11}$$

which integrated through that circuit and along the TEC flowing direction, it gets:

$$\zeta_{hot-cold} = \int_{T_{cold}}^{T_{hot}} S_B \nabla T \bullet dr - \int_{T_{cold}}^{T_{hot}} S_A \nabla T \bullet dr = \int_{T_{cold}}^{T_{hot}} (S_B - S_A) dT = \int_{Tcold}^{T_{hot}} \Delta S_{BA} dT \tag{2.12}$$

Because S is constant, then it has:

$$\zeta_{hot-cold} = \Delta S_{BA} T \tag{2.13}$$

Considering the continuity of currents gives:

$$\nabla^2 \zeta_{hot-cold} = 0 \tag{2.14}$$

It can be seen that, for a given system, ATP difference of two dissimilar materials can be achieved by measuring the voltage in their circuit with a constant temperature difference. Correspongdingly, given the ATP difference is known, the corresponding thermoelectric potential can be calculated as well. It is just the later relationship permitting us to quantitively investigate TE and TEM effect in magnetic field assisting solidification process.

2.2.3 Simulation of TEC at liquid-solid interface

In order to show TEC in directional solidification process more intuitively, such currents at the vicinity of liquid-solid interface were simulated by the commercial code COMSOL Multiphysics (version 4.2.0.228). This code solves physics-based systems of partial or ordinary differential equations via using the finite element method for spatial discretization [264]. COMSOL can conveniently perform the multiphysics simulations through selecting the predefined physics/engineering modules or specifying a series of user-specific partial differential equations [265]. Here, we select the predefined stationary electric currents module

to perform the 2D axisymmetric simulations of TEC at a curved planar liquid-solid interface. Such interface shape is typical and widely obtained, therefore it is only drawn but not from computation. The drawing in 2D *r*-*z* work plane and the 3D topography achieved by revolving the 2D work plane around the *z*-axis were shown in figure 2.6 (a) and (b) respectively. This geometry corresponds to a cylinder sample of 5mm in height and 3mm in diameter, which are the same diamensions of samples used in the following real experiments.

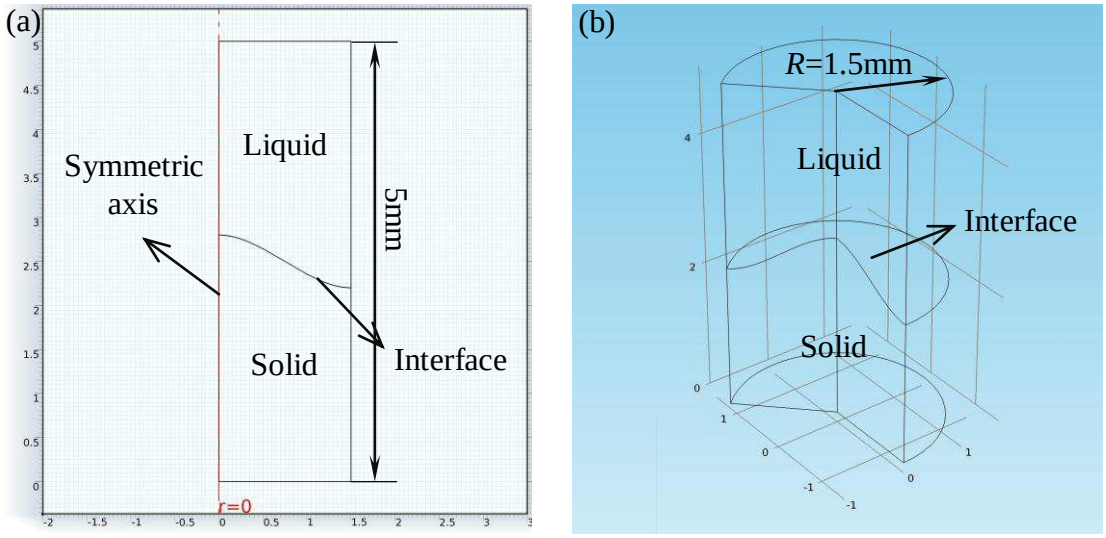

Figure 2.6 Geometry used in simulation of TEC at liquid-solid interface. (a) Drawing of the configuration in the 2D *r*-*z* work plane; (b) 3D topography of geometry.

Continuity of currents as described by expression 2.8 is applied in both solid and liquid and acts as the basic equation to describe the TEC. Based on the finite element method, projecting expression 2.8 in the basis of functions α_i on domain Ω has:

$$\iiint_{\Omega} \alpha_i \vec{\nabla} \bullet \vec{j} d\Omega = 0 \tag{2.15}$$

because

$$\vec{\nabla} \bullet (\alpha_i \vec{j}) = \vec{\nabla}\alpha_i \bullet \vec{j} + \alpha_i \vec{\nabla} \bullet \vec{j} \tag{2.16}$$

expression 2.15 becomes:

$$\iiint_{\Omega} \alpha_i \vec{\nabla} \bullet \vec{j} d\Omega = \iiint_{\Omega} \vec{\nabla} \bullet (\alpha_i \vec{j}) d\Omega - \iiint_{\Omega} \vec{\nabla}\alpha_i \bullet \vec{j} d\Omega = 0 \tag{2.17}$$

and then, follow the theorem of divergence:

$$\iiint_{\Gamma} \alpha_i \vec{j} \bullet \vec{n} ds - \iiint_{\Omega} \vec{\nabla}\alpha_i \bullet \vec{j} d\Omega = 0 \tag{2.18}$$

where, Γ is the boundary of domain. The first term at left of expression 2.18 represents boundary condition, which is zero for the isulating walls, so that the second term should be zero as well. Moreover, consider *j* that expressed by 2.7 it gets:

$$\iiint_{\Omega} \vec{\nabla}\alpha_i \bullet (-\sigma\vec{\nabla}V - \sigma S\vec{\nabla}T) d\Omega = 0 \tag{2.19}$$

This is the programing equation used in the simulation of TEC. Compare to equations 2.20 that governing the electric current module in COMSOL, TEC is set as an external current density J_e and wrriten in the same form of expression 2.7 in both liquid and solid. Q is set as zero to ensure the continuity of currents.

$$\begin{aligned} \vec{\nabla} \bullet \vec{J} &= Q \\ \vec{J} &= \sigma \vec{E} + \vec{J}_e \\ \vec{E} &= -\vec{\nabla} V \end{aligned} \qquad (2.20)$$

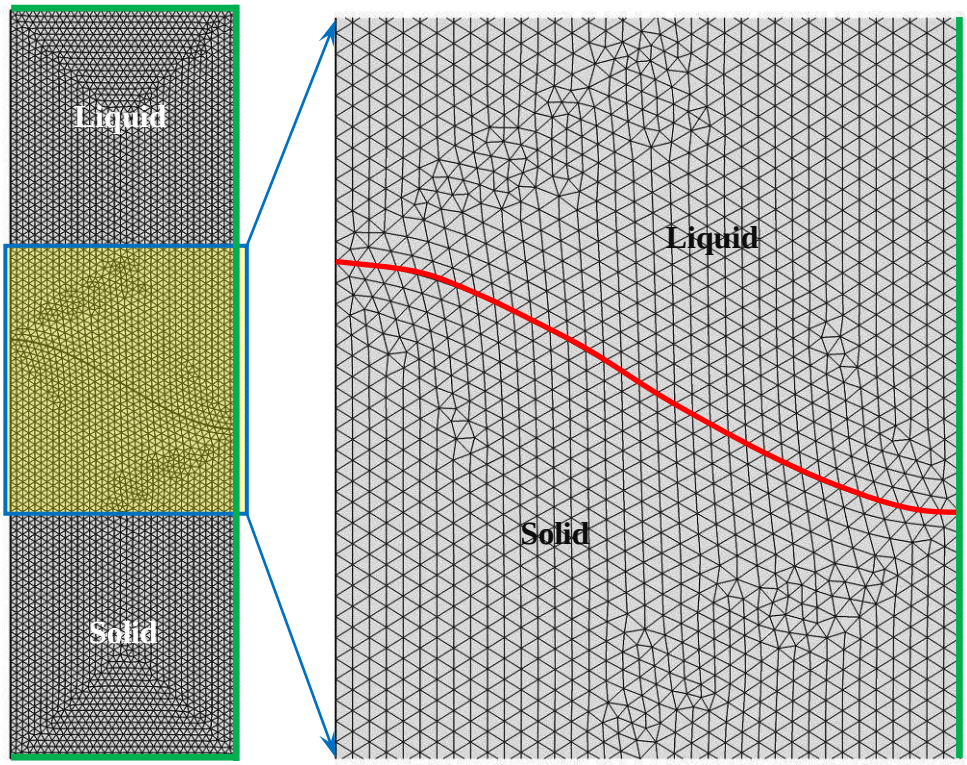

Figure 2.7 Mesh and boundary conditions used in simulation of TEC at liquid-solid interface with a 2D axisymmetric electric current module.

The 'extremely fine' triangular mesh as shown in figure 2.7 was used in simulation and created automatically under the control of physical phenomena. Electric insulating conditions are applied for the walls indicated by the green lines in figure 2.7. As the parameters list in table 2.1, simulations were performed for the Al-4wt%Cu alloy system because it is used in experiments as well, and a constant thermal gradient of 6000K/m is used. As shown in figure 2.8 (a), the computed thermoelectric potential increases gradually from the solid (cold) to the liquid (hot). Contours of both *r* and *z* components TEC densities are given in 2D plane as shown in figure 2.8 (b) and (c) respectively, which shows that the desity of both componets of TEC increase from the cold to the hot region as well. Figure 2.9 (a) shows the streamlines of norm TEC, and red arrows in figure 2.9 (b) indicates their flowing directions. It can be seen that TEC circuit forms around the liquid-soid interface. Further, the magnitudes of red arrows obtained in accordance to norm TEC density show that TEC is big at the region near to the

symmetry axis and gradually decrease in the regions that departing from the center. This can be more clearly seen in figure 2.9 (c) that the magnified figure of region near interface.

Table 2.1 Relevant physical properties of Al-4wt%Cu alloys used for simulation of TEC

Symbol	Unit	Solid	Liquid
S	V/K	-1.5×10^{-6}	-2.25×10^{-6}
σ	$(\Omega\cdot m)^{-1}$	7.9×10^{7}	4.0×10^{6}

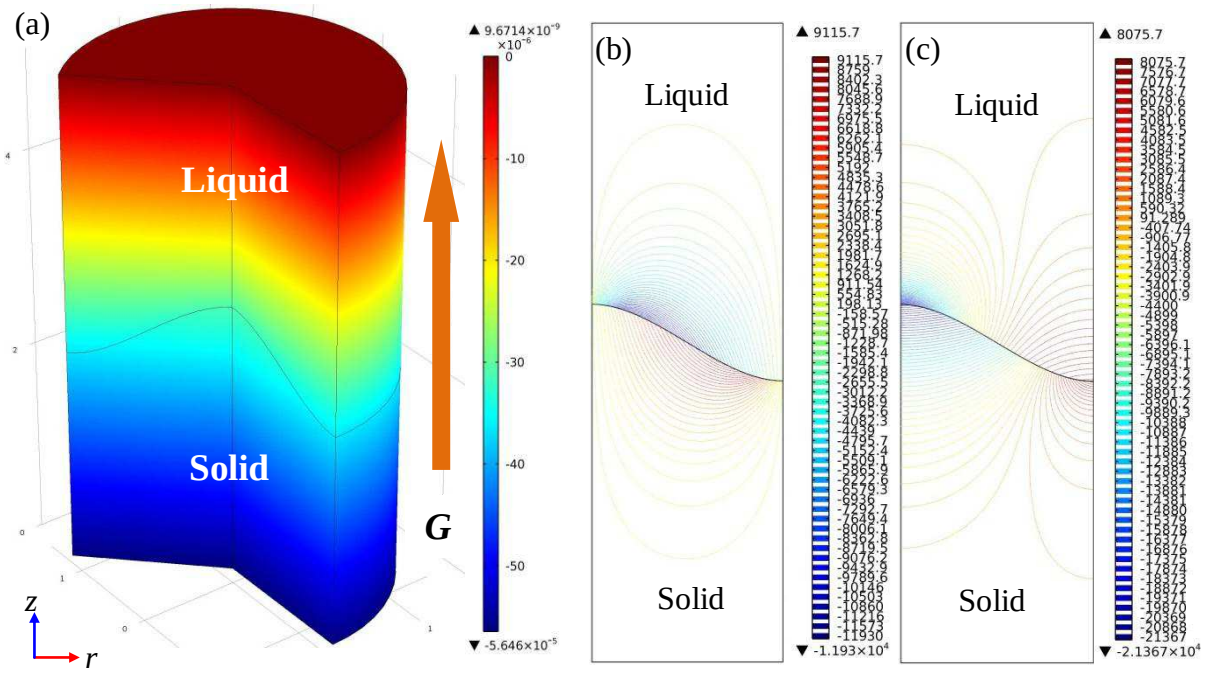

Figure 2.8 (a) Computed thermoelectric potential (V) represented by colored surface (thermal gradient, *G*, of 6000K/m); (b) Desitiy of the *z* component of computed TEC density (A/m^2); (b) Desitiy of the *r* component of computed TEC density (A/m^2).

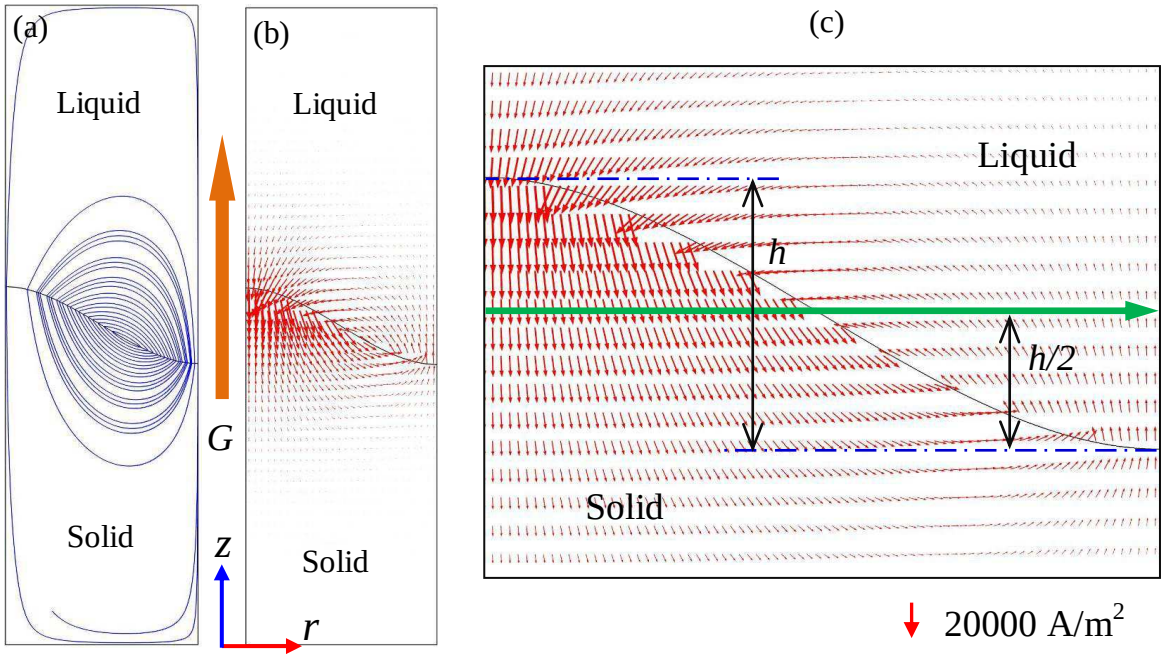

Figure 2.9 (a) Streamlines of norm TEC density; (b) Norm TEC's flowing direction. (c) Magnified view of the region near liquid-solid interface.

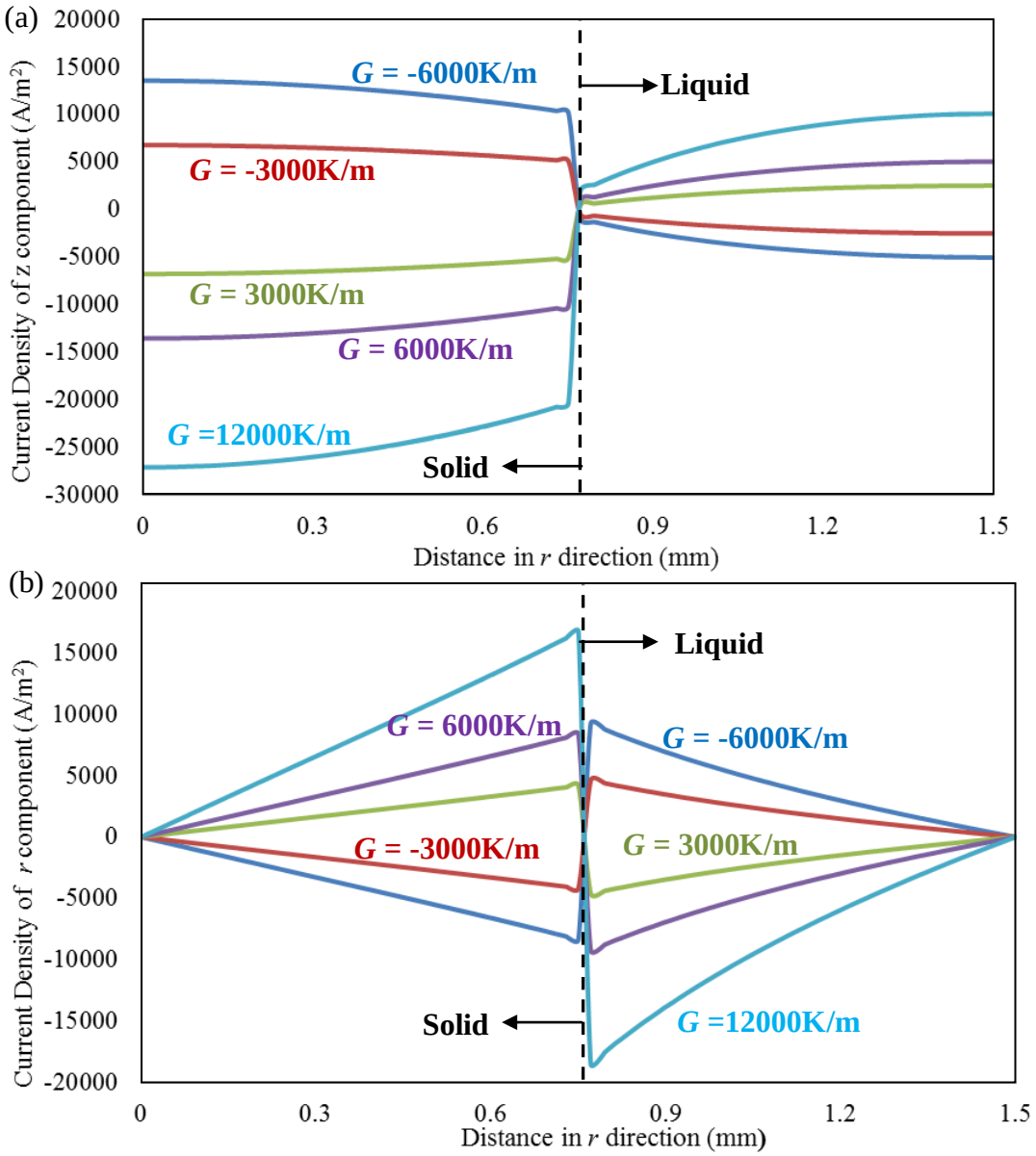

Figure 2.10 Curves of currents densities of *z* (a) and *r* (b) component of computed TEC varying with distance in *r* direction along the line at the middle height of curved interface under different thermal gradients.

Based on equations 2.7 and 2.19, it can be concluded that direction and magnitude of TEC dependent on the thermal gradient only if other conditions are fixed. In order to reveal this dependence, simulations of TEC at liquid-solid interface are performed under various thermal gradients. Current densitiy of both *z* and *r* components of TEC were detected along the green line as indicated in figure 2.9 (c) are taken and plotted versus the distance from the center to the crucible wall for each thermal gradient. As shown in figure 2.10, the magnitudes of TEC increase with the absolute values of thermal gradients increasing, and their direction reverses once the thermal gradient is imposed in an opposite direction. Moreover, in order to give a more clearly view of the dependence of direction of TEC on the direction of imposed thermal gradient, figure 2.11 gives the thermoelectric potential and corresponding norm TEC

generated by the thermal gradient of 3000 K/m and -3000 K/m respectively. It is obvious that direction of both thermoelectric potential and TEC reverse once the thermal gradient changes from positive to negative. In additions, one thing should be noticed that both *r* and *z* components of TEC rapidly decrease to zero at just the liquid-solid interface. This satisfies the currents continuity boundary conditions at interface and agrees with the physical reality, therefore, which can prove the validity of simulations performed above to a certain extent.

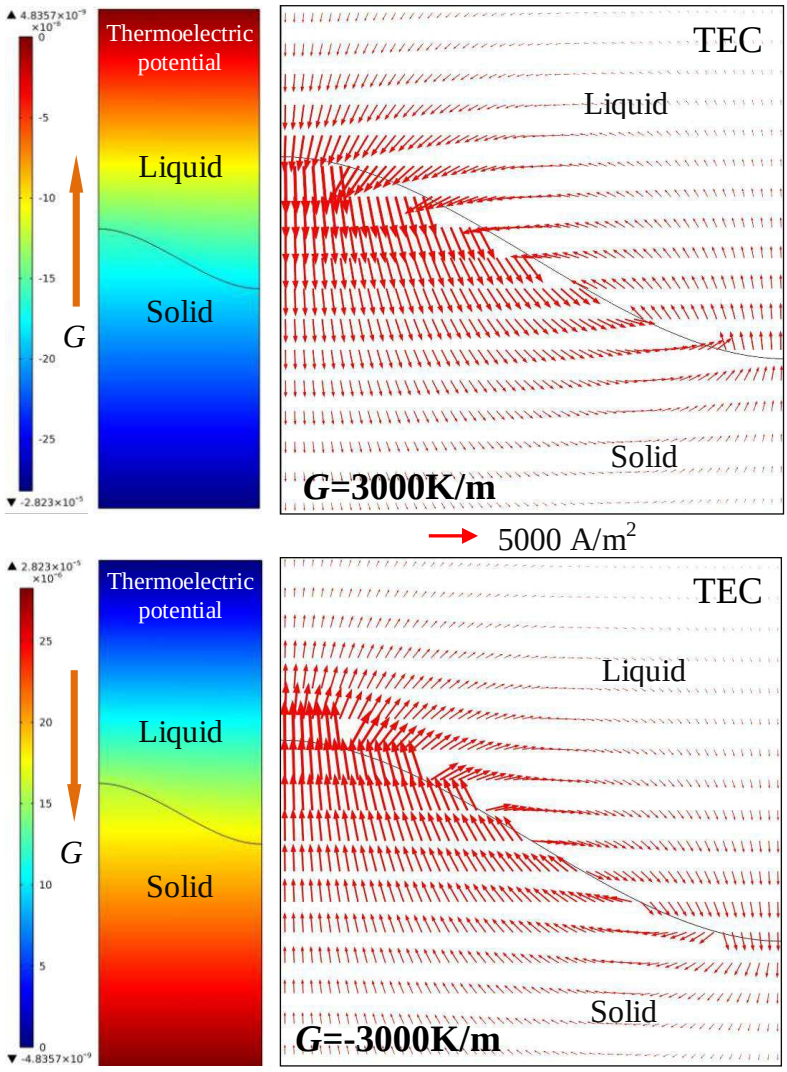

Figure 2.11 Thermoelectric potential and corresponding norm TEC densities generated by the thermal gradient of 3000K/m and -3000K/m.

Because liquid and solid has different thermal conductivites, different thermal gradients in liquid and solid should be achived if the imposed termperature difference is constant. This is the common case in most directional solidification process [266]. For this reason, the thermal transfer module is coupled in the following simulations of TEC. Set the top wall as 983.15K and the bottom wall as 953.15K, which gives a 6000K/m thermal gradient for the thermal conductivity uniform medium. Simulations containing both electric current and heat transfer modules are performed with the same geometry shown in figure 2.6. In order to get a reference, simulation of temperature fields in the thermal conducitivity uniform medium is

perform in advance. Compare the one in thermal conducitivity nonuniform media or saying the real case that setting different thermal conductivities to liquid and solid (95 W/mK for liquid and 150 W/mK for solid), as shown in figure 2.12 (a), no apparently influence from coupling heat transfer module is detected if the temperature difference is constant. However, when look at the magnified region near interface, change of both temperature field and thermal gradients are detectable as shown in figure 2.12 (b). This means that temperature field is not modified a lot by coupling heat transfer module and using the real materials parameters. However, because TEC at the liquid-solid interface is closely related to the temperature field, how such modified temperature field affects the distribution and magnitude of TEC should be determined. Therefore, magnitude of TEC densities computed without and with coupling heat transfer module were measured and shown in figure 2.13. Curves in figure 2.13 (a) are *z* component densities of computed TEC plotted along the horizontal line as indicated in figure 2.9 (c), and figure 2.13 (b) shows the curves of *r* component dendities of computed TEC plotted along the vertical line as indicated in figure 2.12 (a).

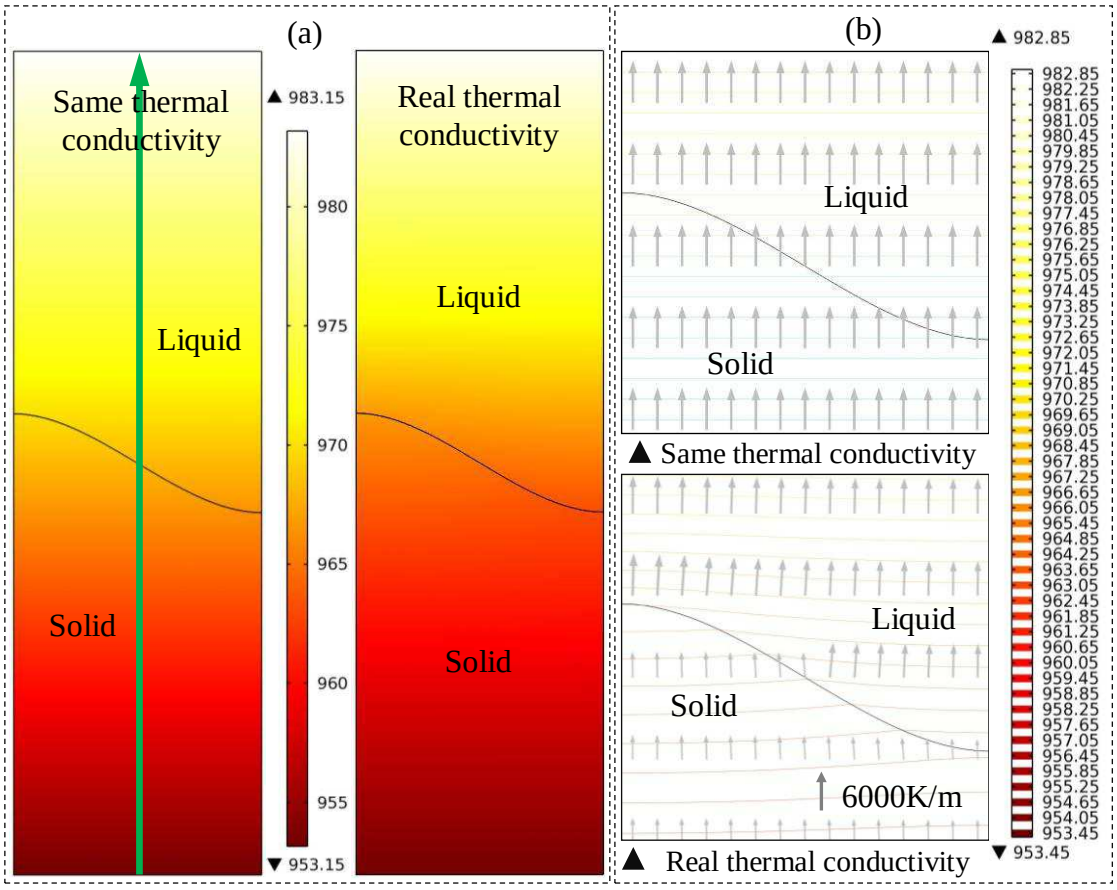

Figure 2.12 (a) Temperature fields obtained by simulating with the constant and the real thermal conductivities for solid and liquid; (b) Contours of temperature (*K*) and arrows of thermal gradient (*K/m*) obtained by simulating with the same and the real thermal conductivities for solid and liquid.

It can find a tiny deviation as emphasized by the green circle in both figure 2.13 (a) and (b). Compare the deviations to the changes of temperature field and thermal gradient near

interface, it can conclude that coupling heat transfer module and using real materials properties in simulation of TEC at liquid-solid interface have a neglectable influence. Indeed, the change tendency of TEC with the given temperature difference has not altered at all. This suggests that when performing only the qualitative analysis of TEC the heat transfer may not be necessary to take in consideration, on the contrary, if make the quantitative investigation the influenc of heat transfer should be paid more attentions to. Moreover, in addition to reveal the deviation of TEC at the vicinity of liquid-solid interface, figure 2.13 (b) provides another evidence for the validity of present simulations. It must have been found that TEC rapidly decreases in the region far from the interface both in liquid and solid. This just satisfies the far field conditions that no currents out of domains and agrees with the physical reality that Seebeck effect weakens quickly in the thermophysical property uniform medium [267].

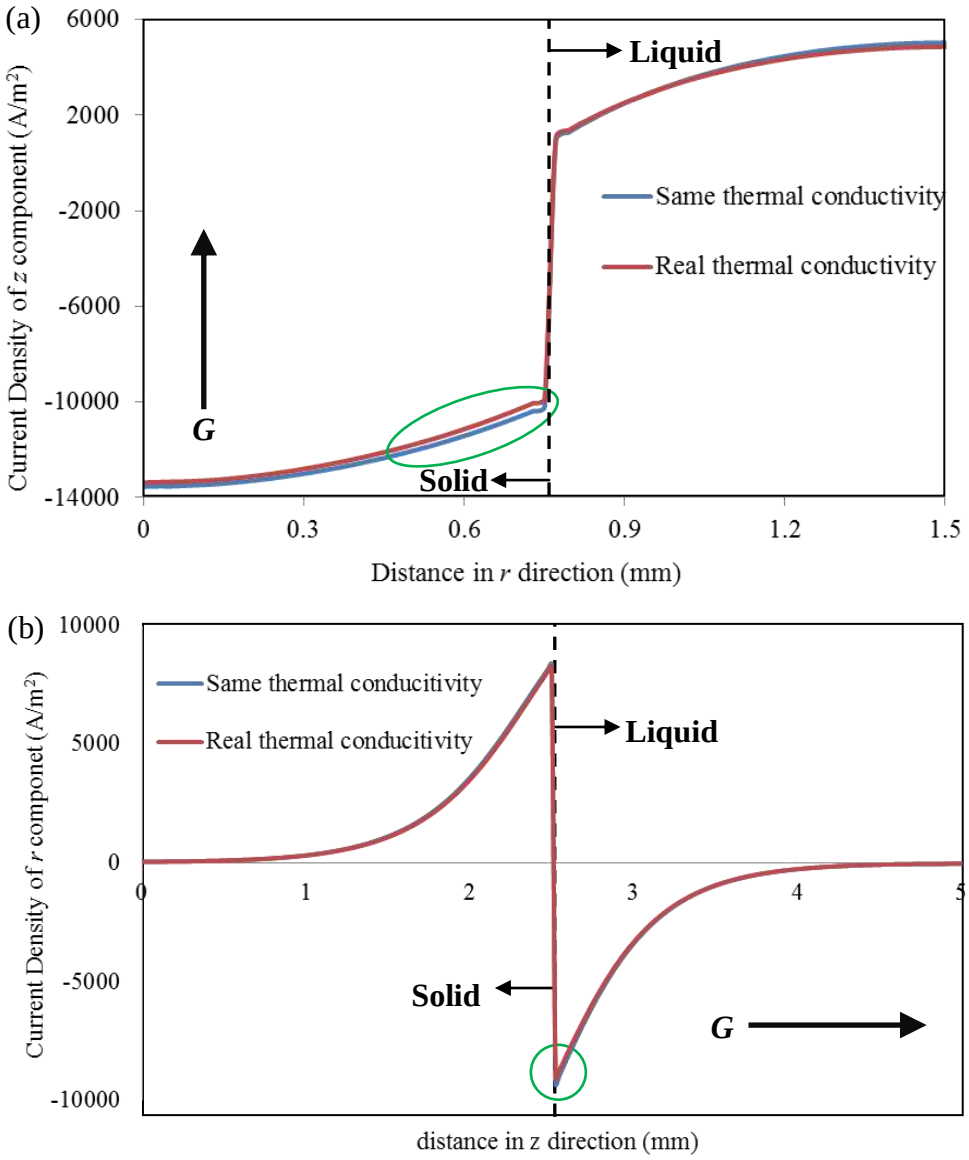

Figure 2.13 Computed TEC with the same and the real thermal conductivities for liquid and solid. (a) Computed *z* component densities of TEC plotted along the horizontal line as indicated in figure 2.9 (c) ; (b) Computed *r* component densities of TEC plotted along the vertical line as indicated in figure 2.12 (a).

2.3 Thermoelectric magnetic effect (TEME) in directional solidification process

As explained in chapter 2.1, once the external magnetic field is present it must interact with the internal TEC to casue TEME in the directional solidification process. Here, a preliminarily view of TEM forces and TEM flows will be unfolded by numerical simulations. Before simulations, TEME is formulated in the context of solidification, and the simulation method is verified after that.

2.3.1 Formulation of TEME

Interacting between electric current and magnetic field results in a body force named Lorentz or Laplace force, similarly, the major premise of TEME is a kind of Lorentz force that resulted from the interacting btween the internal TEC and the imposed magnetic field. According to the rule of electric current continuity, TEC at liquid-solid interface should flow cross both solid and liquid, consequently, TEM forces exist in both of them as well. Similarly to Lorentz force, TEM forces can be expressed by the classical formulation as well:

$$\vec{F} = \vec{j} \times \vec{B} \tag{2.21}$$

that togethers with discussions in section 2.2.2, TEM forces acting on solid and liquid are expressed respectively as:

$$\vec{F_s} = -\sigma_s S_s \vec{\nabla} T \times \vec{B} \tag{2.22}$$

$$\vec{F_l} = -\sigma_l S_l \vec{\nabla} T \times \vec{B} \tag{2.23}$$

According to the definition of fluid, existence of TEM forces in liquid can drive flows that the TEM flows. Insert an external volume force term to Navier-Stokes (N-S) equation, TEM flows can be described as:

$$\frac{\partial(\rho\vec{u})}{\partial t} + \rho(\vec{u} \bullet \vec{\nabla})\vec{u} = -\vec{\nabla} p + \rho\vec{g} + \mu\nabla^2\vec{u} + \vec{j} \times \vec{B} \tag{2.24}$$

It should be noticed that $\vec{u} \times \vec{B}$ must be taken into account when calculate the electric currents *j*, because TEM flows must induce electromotive force once they appear in melt. Conseqently, it has:

$$\vec{j} \times \vec{B} = \vec{F_l} + (\vec{u} \times \vec{B}) \times \vec{B} \tag{2.25}$$

with assumption that metl are incompressible Newton fluid, the conservation of mass becomes:

$$\vec{\nabla} \bullet \vec{u} = 0 \tag{2.26}$$

Two approaches can be used to get the flow field of TEM flows governed by expressions 2.24 to 2.26. One is directly solving the equations with several assumptions and approximations, and the other is numerical simulation. Here, we employ the latter one to display TEM forces and TEM flows in directional solidification process.

2.3.2 Verification of the simulation method

Before taking simulations of TEM effect, the using method should be verified. In order to do this, a simple case is considered. Assume an infinite-long cylinder immersed in its corresponding melts and a vertical constant thermal gradient exists in such system, TEM forces acting on the cylinder are both analytically calculated and numerically simulated. Comparing the consistency of TEM forces separately achieved by these two methods can provide the opinion on whether the simulation method is valid or not. The case of infinite-long cylinder immersed in its metls can be treated as a pure 2D problem. Figure 2.14 shows the dimensions and geometry used by both analytical calculation and numerical simulation.

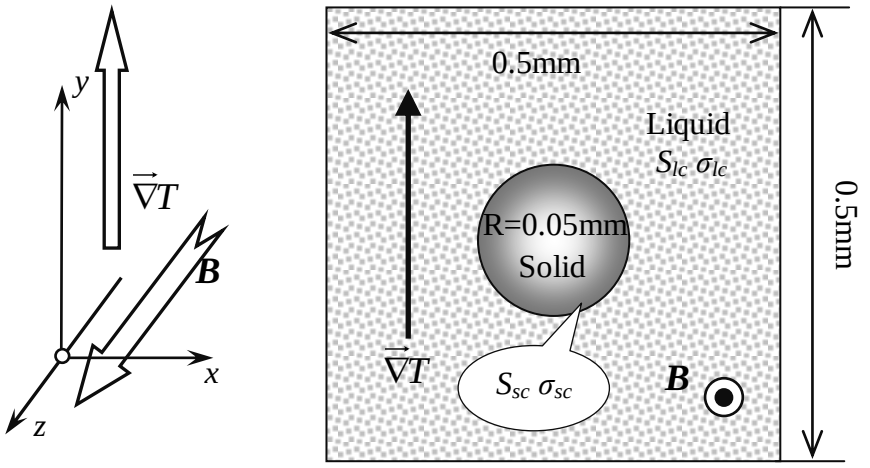

Figure 2.14 Dimensions and geometry used by both analytical calculation and numerical simulation and the coordinate. S_{lc} and S_{sc} are the ATP of liquid and solid respectively. σ_{lc} and σ_{sc} respectively presents electric conductivity of liquid and solid.

Solve both expressions 2.7 and 2.22 in this case TEC forces acting on the cylinder can be expressed as:

$$\overrightarrow{F_{sc}} = -\sigma_{sc} B_0 (\nabla V_{sc} \times \vec{i}_z + S_{sc} G \vec{i}_y) \qquad (2.27)$$

with

$$\vec{B} = B_0 \vec{i}_z \qquad (2.28)$$

and

$$\vec{\nabla}T = G\vec{i}_y \qquad (2.29)$$

where, B_0 and G are constant and applied magnetic field flux intensity and thermal gradient respectively, $\vec{i}_z$ and $\vec{i}_y$ are unit vectors along z-axis and y-axis respectively, ∇V_{sc} is the scalar potential in solid cylinder, S_{sc} and σ_{sc} respectively presents ATP and electrical conductivity of the solid cylinder. Project expression 2.27 in three unit vectors, the corresponding components of TEM forces in the Cartesian frame can be achieved:

$$F_{scy} = F_{scz} = 0 \tag{2.30}$$

and

$$F_{scx} = -\frac{\sigma_{sc}\sigma_{lc}GB_0(S_{sc} - S_{lc})}{\sigma_{lc} + \sigma_{sc}} \tag{2.31}$$

where, F_{scx}, F_{scy}, and F_{scz} respectively stands for TEM forces' x, y and z component acting on the solid cylinder, S_{lc} is ATP of cylinder's corresponding melts, and σ_{lc} is its electrical conductivity, which are the same sa illustrated in figure 2.14. Further, becasuse TEM forces are constant within the cylinder, the total force of x component is:

$$\overline{F_{scx}} = -\frac{\sigma_{sc}\sigma_{lc}GB_0(S_{sc} - S_{lc})}{\sigma_{lc} + \sigma_{sc}} vol \tag{2.32}$$

vol is the cylinder's volume.

It should be found that two aspects can be examined to validate the simulation method in accordance to the analytical solution. One is dependence of the direction of TEM forces' x component on the given conditions, such as the thermal gradients or imposed magnetic fields. The other is the exactly magnitude of TEM forces acting on the cylinder. In another aspect, considering the assumption that material properties are unique in each medium, examining whether or not TEC and TEM forces distribute uniformly within the solid can judge the valid of simulations to a certain extent.

Because TEC is the only source of electric currents, simulation of TEC should be taken before TEM forces. TEC is simulated without coupling the heat transfer module in this pure 2D case, because the analytical calculation did not take heat transfer into account as well. Figure 2.15 shows the computed TEC generated by a constant thermal gradient of 3000K/m. The gradually increasing thermoelectric potential with smoothly rising temperature (Figure 2.15 (a)) agrees with the previous simuations of TEC at curved liquid-solid interface. Free of arrows in the region far from the cylinder as shown in figure 2.15 (b) suggests that TEC is nearly zero there, which satisfies the far field conditions and can validate this simulation method to a certain extent. Figure 2.16 is the view of magnified region near the solid cylinder, in which, (a) shows the streamlines of norm TEC, and (b) indicates the direction of norm TEC by red arrows. Parallelly arranged streamlines and arrows within the solid cylinder reflect the

uniformity distribution of TEC, which agrees with the assumption that thermophysical properties with each medium are unique. Further, simulations of TEC were performed under several thermal gradients in order to confirm their uniformity wthin the soid. Figure 2.17 shows the curves *y* component densities of computed TEC plotted along the horizontal line as indicated by the white arrow in figure 2.15 (a) under different thermal gradients. The flat segments of each curve represent TEC within the solid cylinder. Combine the results shown in figure 2.16 (a) and (b), it can confidently say that TEC within the solid distributes uniformly. This uniform distribution can verify the validity of this simulation method in another aspect.

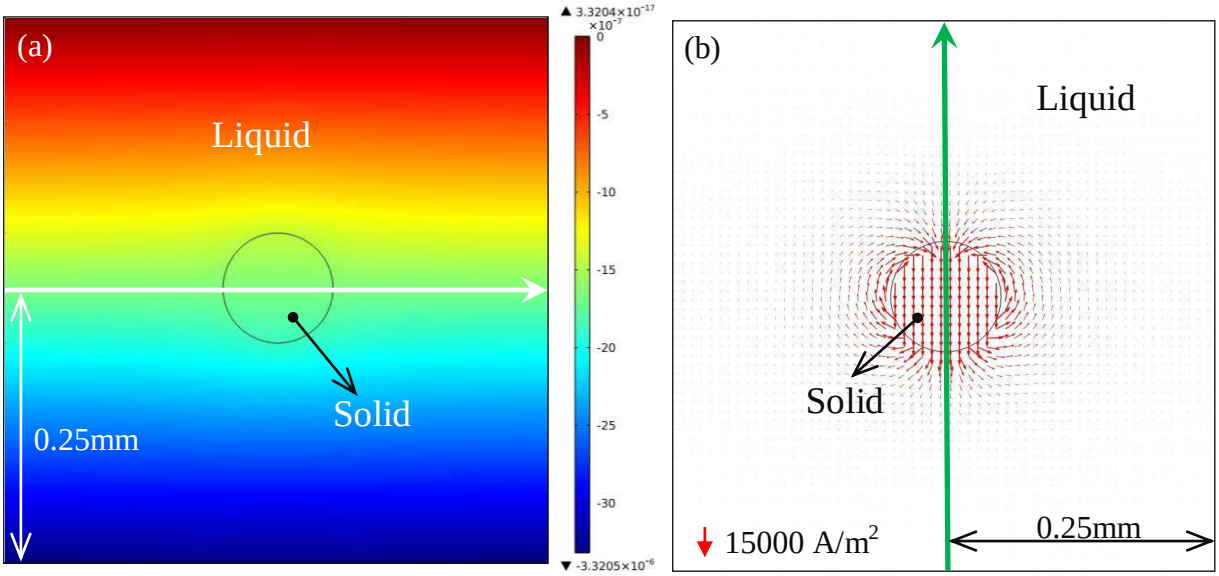

Figure 2.15 Computed TEC (a) Thermoelectric potential generated by a constant thermal gradient of 3000K/m and (b) its corresponding TEC flowing direction indicated by red arrows.

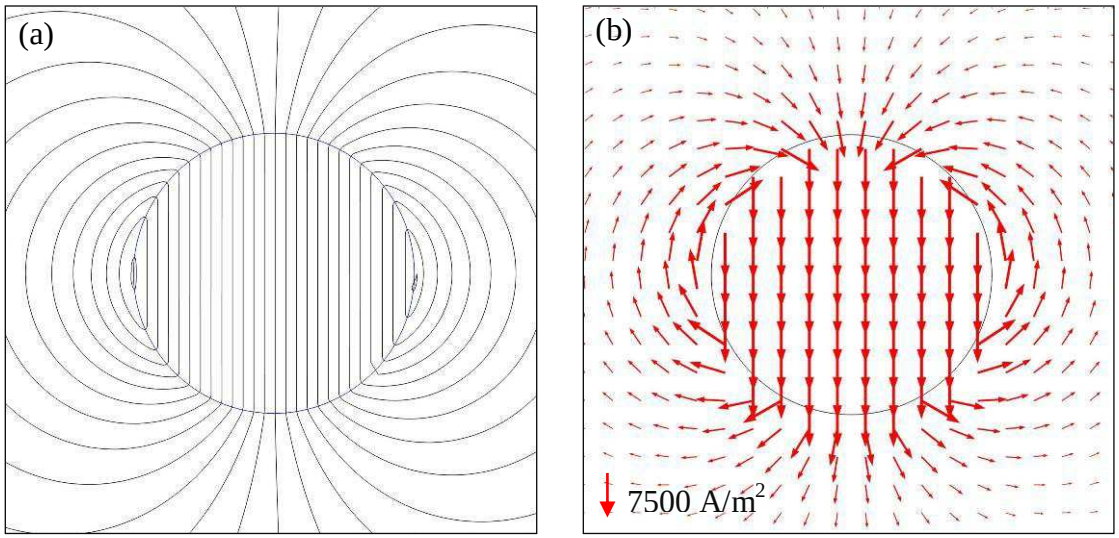

Figure 2.16 (a) Streamlines of norm TEC in region within and near the solid cylinder and (b) its corresponding TEC flowing direction indicated by arrows.

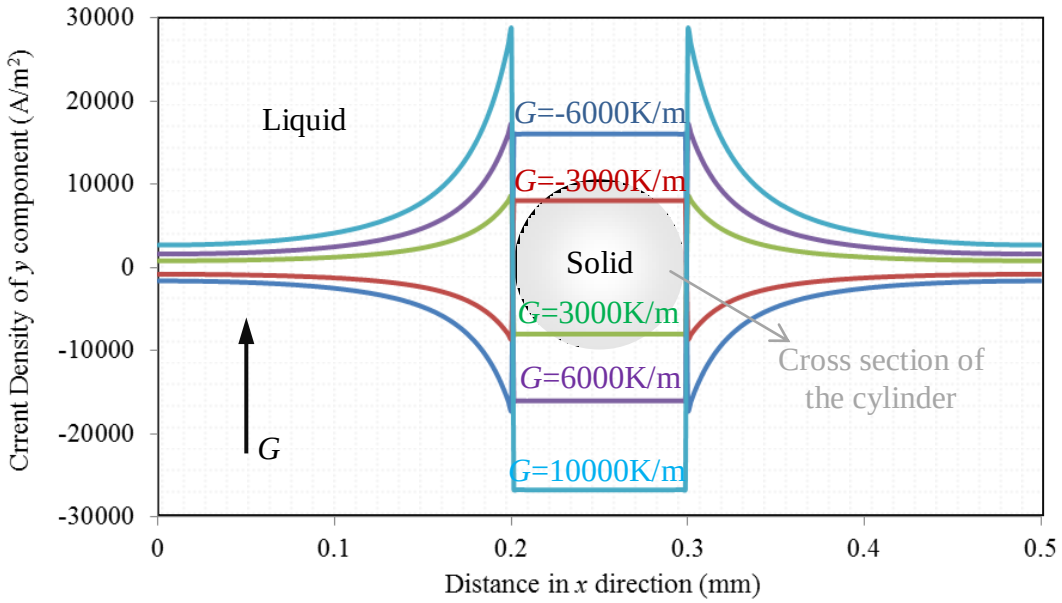

Figure 2.17 Profiles of *y* component densities of computed TEC along the horizontal line indicated in figure 2.15 (a) for different thermal gradients.

When TEC has been known, simulation of TEM forces acting on the cylinder can be done. Because TEM forces act as the external volume forces in the N-S equation that governing TEM flows, such forces can be obtained via solving the TEM flows field. Moreover, because there is no physical module in COMSOL suitable to compute $\vec{j} \times \vec{B}$ only, TEM forces acting on cylinder are achieved by solving expression 2.24 in both liquid and solid. By setting an ultrahigh viscosity to solid, 10^6 *Pa*·*s* for instance (the viscosity of melts is about 10^{-4} *Pa*·s), the computed flow field in solid is almost zero, and the solution of flow field in liquid (melts) is not affected. Therefore, simulations of TEM flows field in both liquid and solid are performed for this pure 2D case by combining the COMSOL predefined electric current and fluid flow modules. The direct linear solver is used to solve the modified N-S equation. Figure 2.18 shows the computed TEM forces caused by TEC interacting with a 0.08T magnetic field imposed in *z* direction, in which, red arrows have the same direction with TEM forces and their sizes suggest the magnitude of TEM forces. According to the coordinate defined in figure 2.14, positive thermal gradient and TEM forces mean they are in the same direction of positive *y*- and *x*- axis respectively. Because we use the same coordinate in both calculation and simulation, the comparison of their results can be taken directly. It can be found from the analytical calculation that the sign of F_{scx} should be opposite to that of the thermal gradient under a fixed magnetic field and vice versa. Highlighted by the big blue arrow at cylinder's centre, the same relationshipt between the direction of *x* compnent of computed TEM forces in solid and thermal gradient is obtained from the computed results. This perfect consistency verifies the validity of the using simulation method in one aspect.

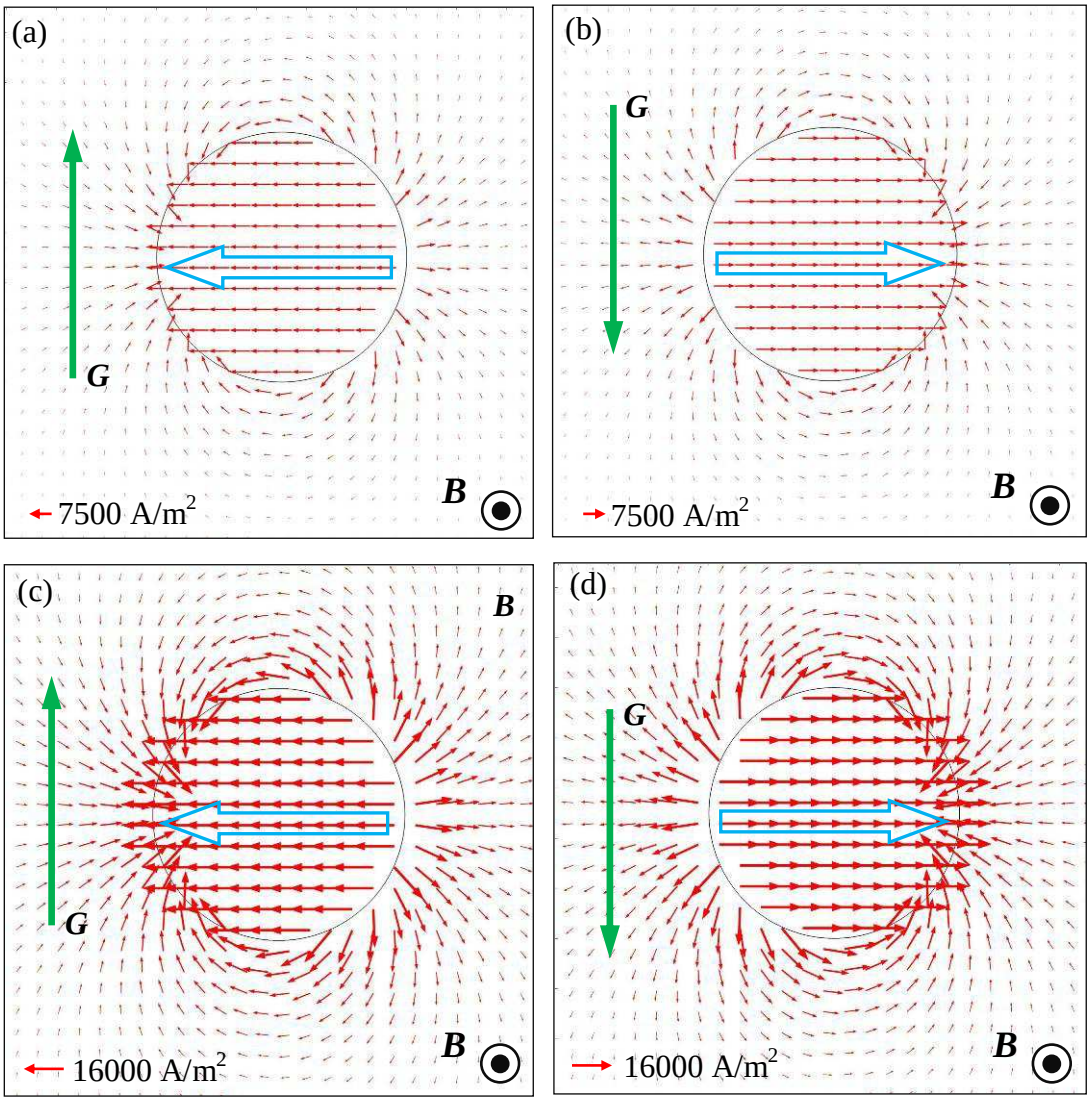

Figure 2.18 Arrows of computed TEM forces resulted by different thermal gradients and a 0.08T magnetic field imposed in *z* direction. (a) *G*=3000K/m; (b) *G*=-3000K/m; (c) *G*=6000K/m; (d) *G*=-6000K/m.

In another aspect, the exact magnitude of TEM forces obtained from both analytical calculation and numerical simulation should be compared. For this reason, simulations of TEM flows in both liquid and solid are performed under several thermal gradients and magnetic fields. Further, the magnitudes of *x* component of computed TEM forces are profiled along the vertical line as indicated in figure 2.15 (b). Figure 2.19 shows the corresponding curves. It can be seen that flat segment in each curve confirms the uniform distribution of TEM forces. As discussed previously, this agrees with the unique thermophysical property assumption and is able to verify the simulation method to a certain extent. Moreover, it can also find that inverse correspondence between the direction of TEM forces and the thermal gradients is revealed, and the magnitude of TEM forces in solid increases with the increasing of magnetic field and the absolute value of tha applied thermal gradient. All these features can be found from the analytical solution, and these consistencies

validate the simulation method. Even though, let us make the comparison of exact magnitude of TEM forces obtained from both analytical calculation and numerical simulation anyhow.

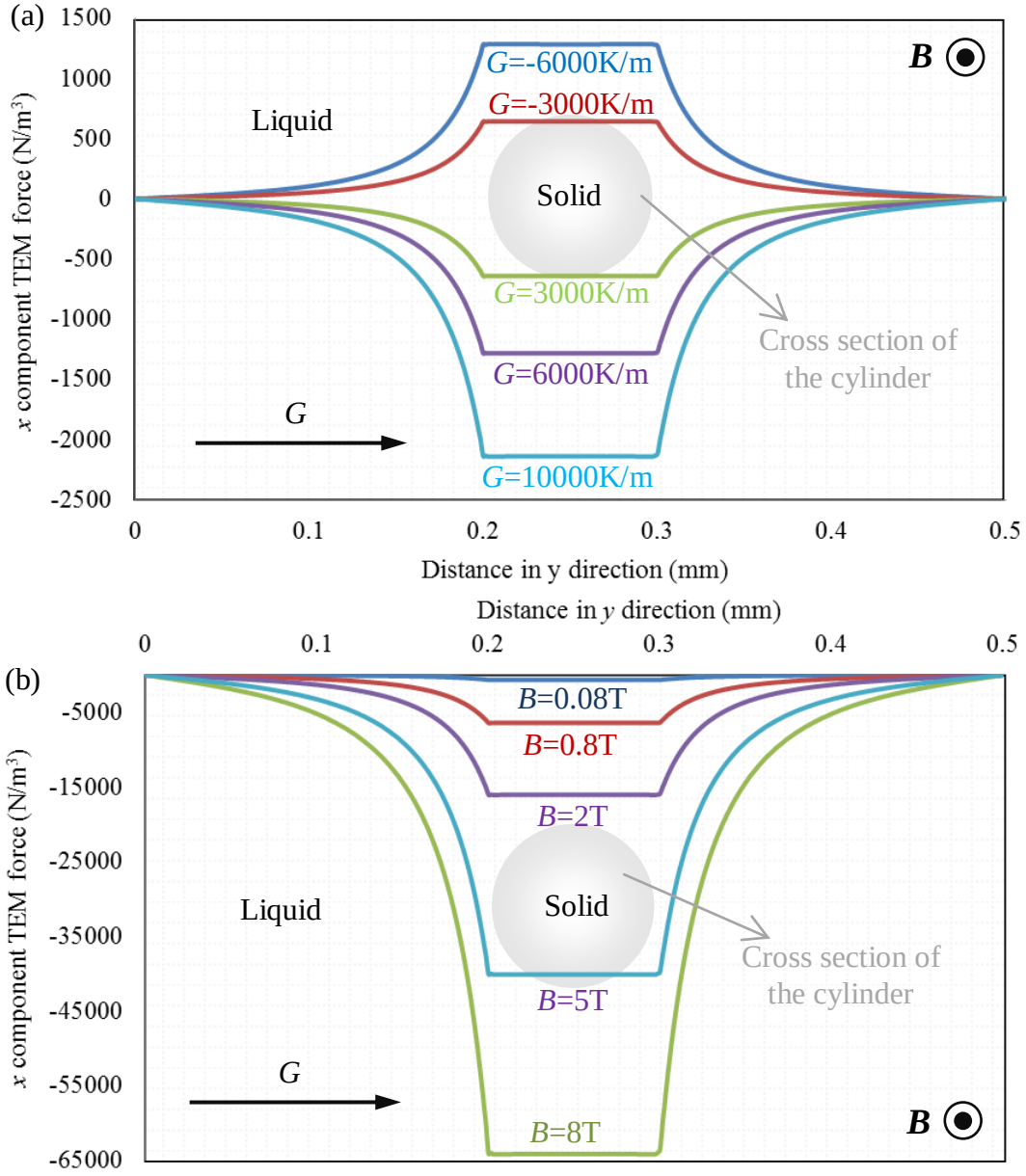

Figure 2.19 Curves of *y* component desities of compited TEC plottd along the vertical line indicated in figure 2.15 for different thermal gradients (a) with same magnetic field of 0.08T and different magnetic fields (b) with fixed thermal gradient of 3000K/m.

Because magnitude of computed TEM forces acting on solid is the one corresponding to flat segment of each curve in figure 2.19, there are several results can be used to compare with the analytical solutions. In another aspect, the analytical calculation can provide a continuous curve of F_{scx} as the function of thermal gradient or magnetic field. Therefore, as shown in figure 2.20, the comparison of exact magnitudes of TEM forces can be made by inserting the points standing for computed results to the continuous curve achieved by analytical calculation. Finally, it can conclude that computed results perfectly agree the analytical

calculations, which then definitely verifies the validity of the simulation method used here. This enables us confidently to employ such method to uncover the TEM effect in the following section.

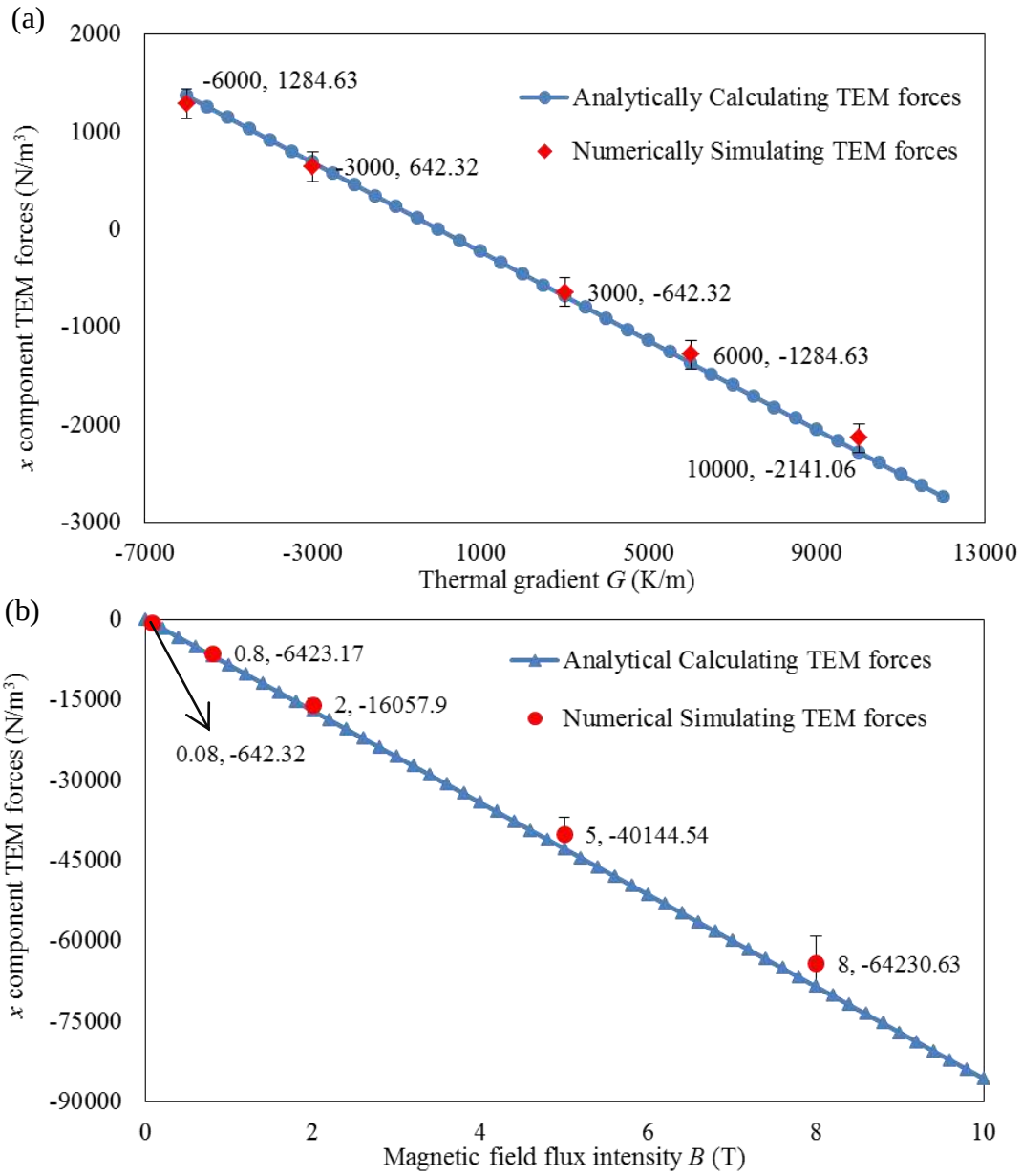

Figure 2.20 Comparison of the exact *x* component magnitudes of TEM forces acting on the cylinder obtained by analytical calculation and numerical simulation. (a) TEM forces plotted under various thermal gradients with 0.08T magnetic field; (b) TEM forces plotted under different magnetic fields with constant thermal gradient of 3000K/m.

2.3.3 Simulation of TEM effect in directional solidification process

Use the same method that has been verified in chapter 2.3.2, and couple the fluid flow and electric current modules predefined in COMSOL, simulations are performed to uncover TEM effect in directional solidification process. Similar to the one used in chapter 2.2.3, 2D axisymmetric geometry is used as well. Moreover, in order to investigate the influence of heat

transfer on TEM effect, both results of simulations without and with coupling the heat transfer module are examined. Consequently, simulations of TEM effect in this section should involve three physical phenomena that electric current, fluid flow and heat transfer. Consider so, the related material properties of Al-4wt%Cu alloy are given in table 2.2.

Table 2.2 Materials properties of simulation system for TEM effect

Symbol	Unit	Solid	Liquid
S	V/K	-1.5×10^{-6}	-2.25×10^{-6}
σ	$(\Omega\cdot m)^{-1}$	7.9×10^{7}	4.0×10^{6}
μ	Pa·s	2.0×10^{6}	2.9×10^{-3}
κ	W/mK	150	95
C	J/KgK	0.9×10^{3}	1.08×10^{3}
ρ	Kg/m^3	2.7×10^{3}	2.4×10^{3}

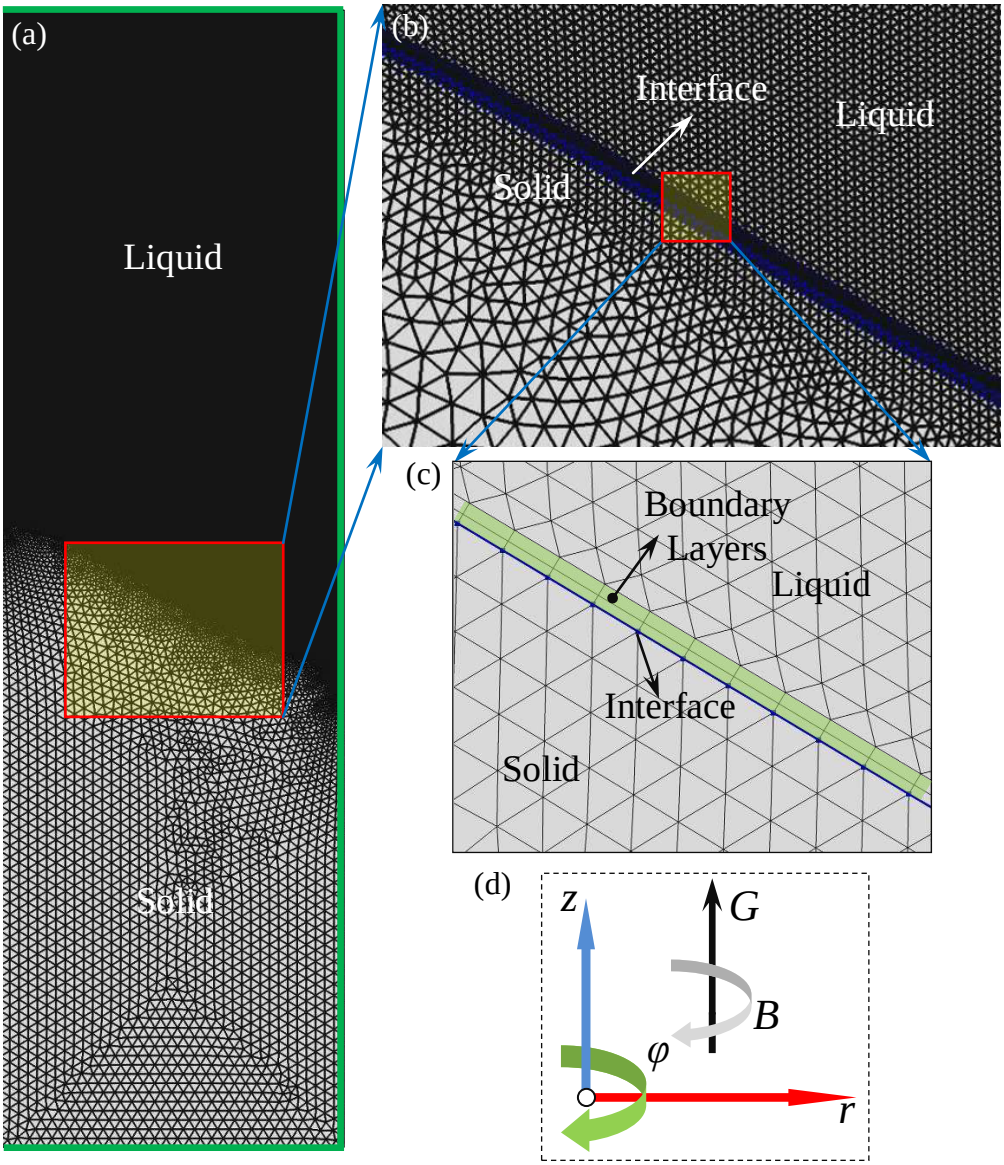

Figure 2.21 (a) Mesh and non-slipping and insulating conditions (Green lines) used in simulation of TEM effect in solidification process; (b) Magnified region indicated by the red box in (a); (c) Magnified region indicated by the red box in (b) showing the boundary layers along interface; (d) Coordinate used in these 2D axisymmetric simulations.

Geometry, its dimensions and meshes are the same as used in chapter 2.2.3. But meshes in liquid should be refined because flow flied involved in this case. The refinement of meshes is realized by applying fluid flow phenomena controlling mesh in liquid. Meshes of the whole domain after refinement is shown in figure 2.21 (a). It should be noticed that how the meshes in liquid like is hard to tell from figure 2.21 (a) because they are extremely fine. Therefore, figure 2.21 (b) gives a magnified view of meshes near the liquid-solid interface. Moreover, as shown in figure 2.21 (c), two boundary layers along interface are added at the liquid side because the complex flow field always appears very close to interface. Non-slipping conditions are applied to the walls indicated by green lines in figure 2.21 (a) for fluid flow module and insulating conditions are also set to these walls for electric current module. Based on the coordinate defined in figure 2.21 (d), COMSOL permit input only *r* and *z* component external volume forces in 2D axisymmetric case. This limits the direction of applied magnetic field that must be in φ direction, which is because only φ direction magnetic field can produce the *r* and *z* component TEM forces with a *z* direction thermal gradient. Fortunately, although the constant φ direction magnetic field is not realistic, such setting does not affect the purpose of showing TEM effect in directional solidification process at all.

It has been clearly that TEC is one of the premises for TEM effect. Therefore, simulations of TEM effect in solidification should begin with TEC as well. Moreover, considering that TEM flows in melt can induce an electromotive force described by $\vec{u}\times\vec{B}$, how this influences the finally TEC is shown in advanced. Add the $\vec{u}\times\vec{B}$ term to the expression governing the electric currents, simulation of TEC with considering the influence of induced electromotive force can be achieved by computing TEM effect but not TEC only. Apparently changes of TEC in liquid region can be observed via comparing the TEC without and with the influence of TEM flows inducing electromotive force as shown in figure 2.22.

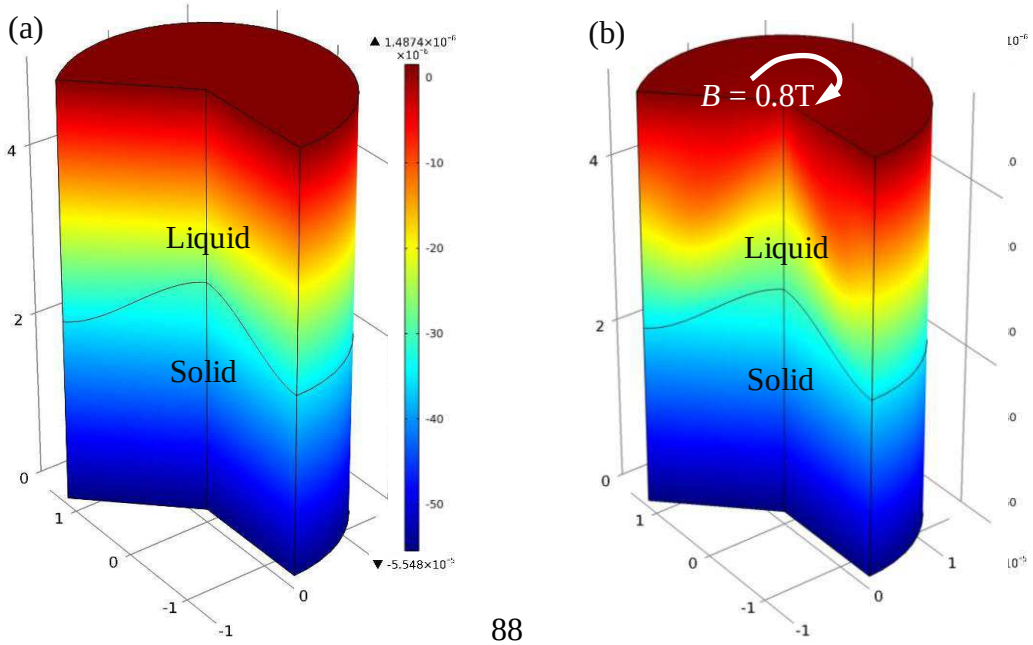

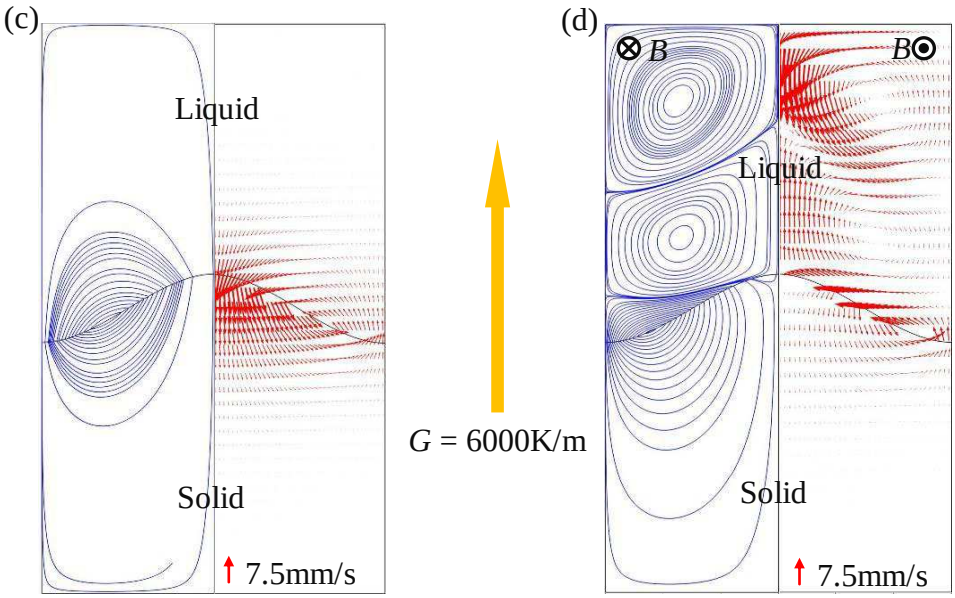

Figure 2.22 Thermoelectric potential obtained without (a) and with (b) coupling the fluid flow module, streamlines and arrows of norm TEC obtained without (c) and with coupling the fluid flow module (d). Constant thermal gradient G of 6000K/m is used for both cases. A 0.8T magnetic field B is imposed in φ direction. Unit of the legend is V.

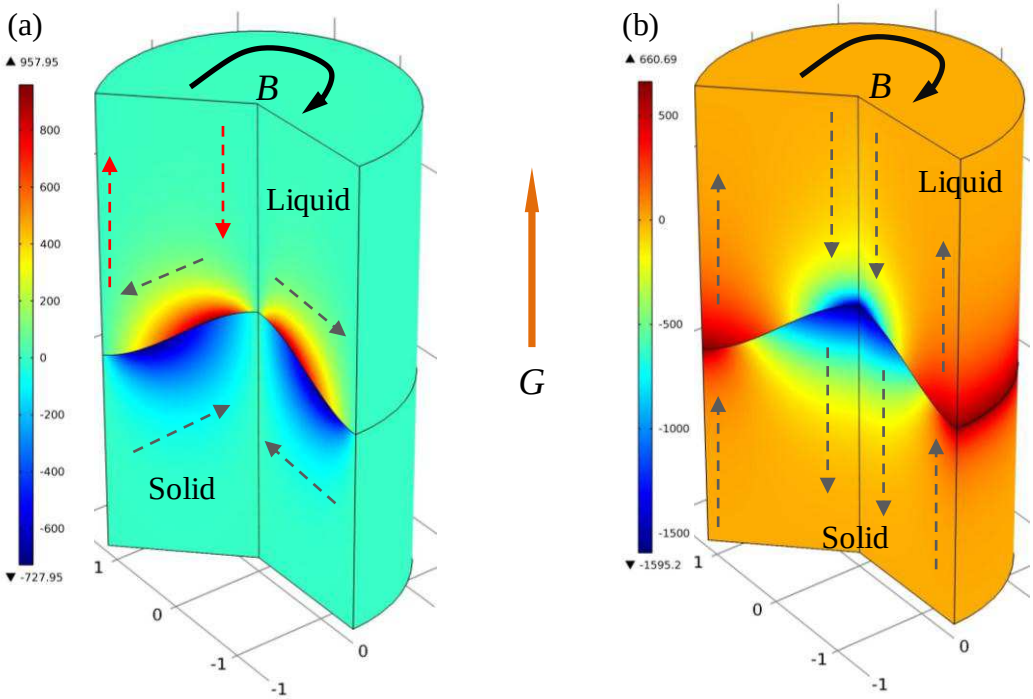

Figure 2.23 (a) r component and (b) z component of Computed TEM forces achieved under a constant temperature gradient G of 6000K/m and a 0.08T magnetic field B. Unit of the legend is N/m^3

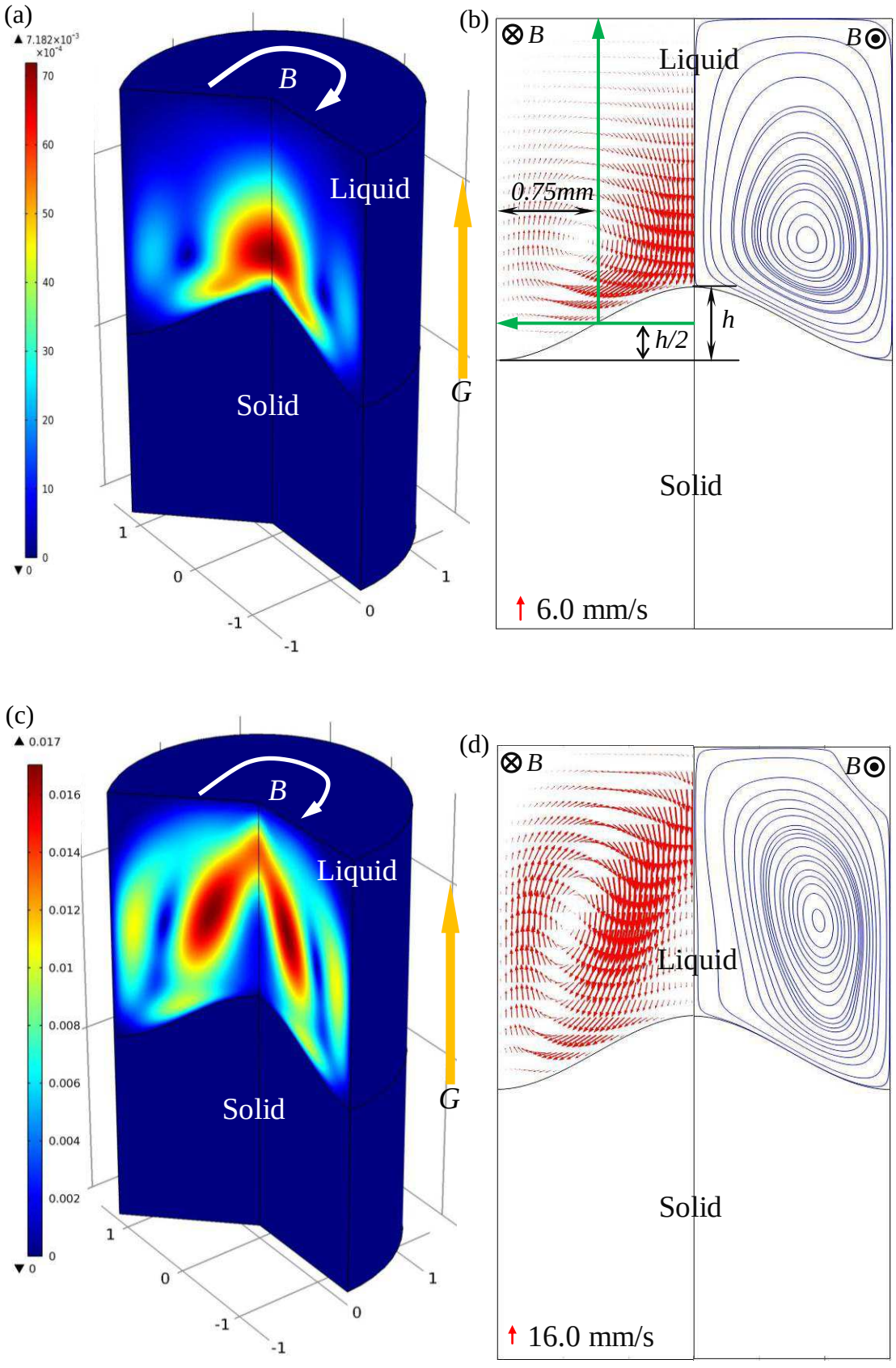
(a)
B
Liquid
Solid
G
(b)
B
B
Liquid
0.75mm
h
h/2
Solid
6.0 mm/s
(c)
B
Liquid
Solid
G
(d)
B
B
Liquid
Solid
16.0 mm/s

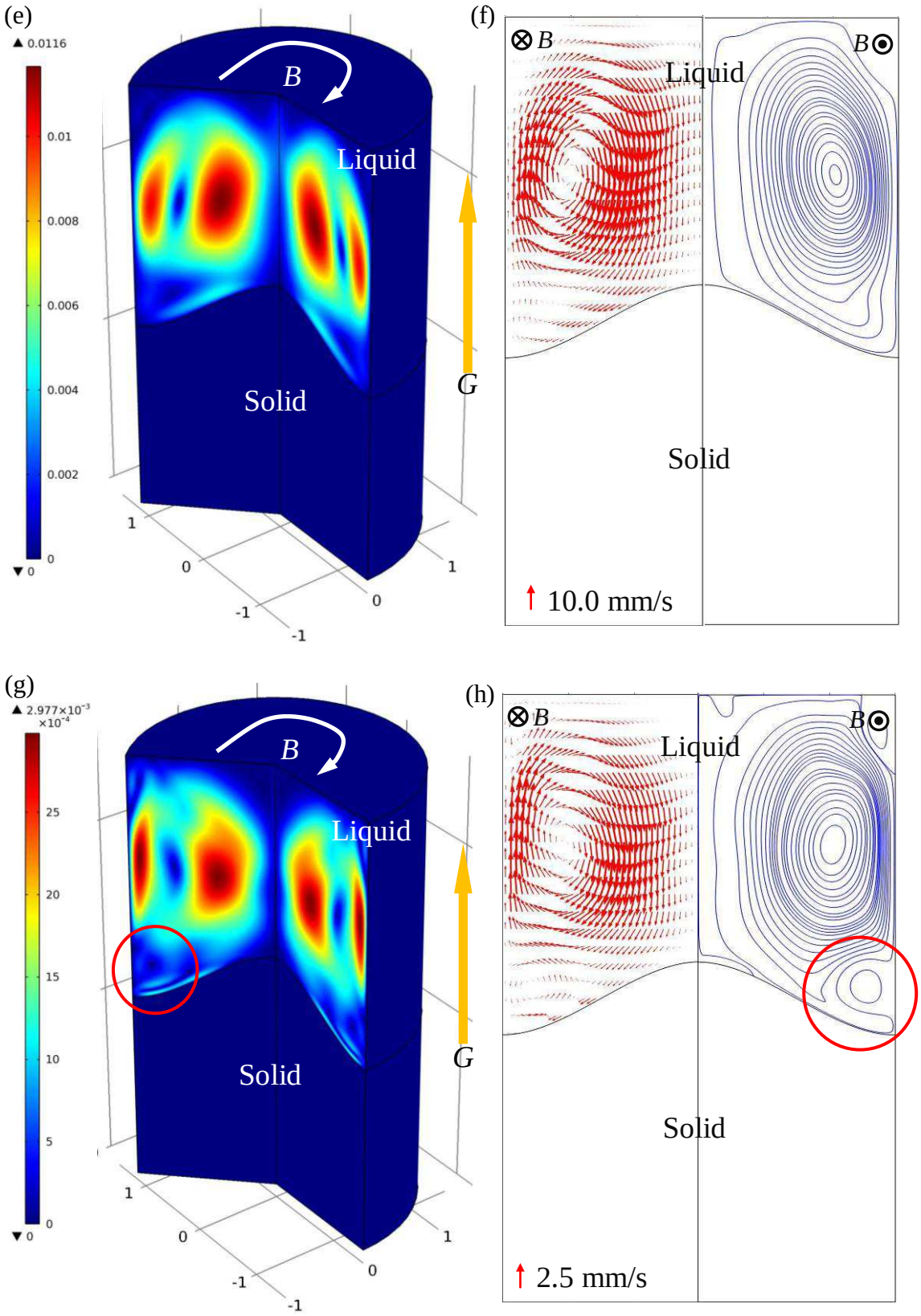

Figure 2.24 Computed TEM flows fields, arrows and streamlines are norm velocities of TEM flows under a constant thermal gradient G of 6000K/m and different magnetic fields that (a) and (b) B=0.08T; (c)and (d) B=0.8T; (e) and (f) B=1.6T; (g) and (h) B=8T. Color surfaces stand for the magnitude of velocities of computed TEM flows. Unit of the legends is m/s.

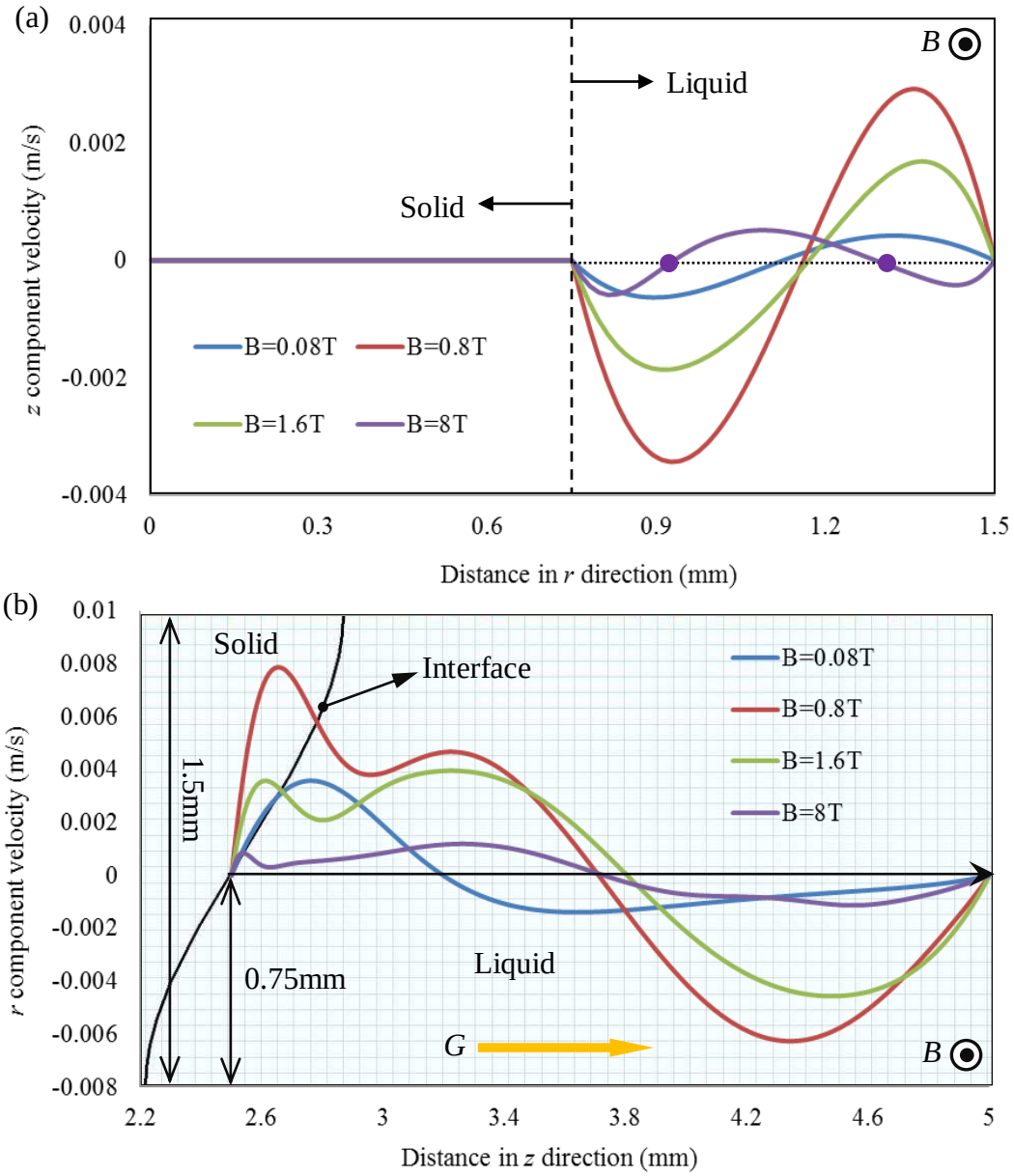

Figure 2.25 Curves of *z* (a) and *r* (b) components velocities obtained under different magnetic fields and respectively plotted along the horizontal and vertical lines indicated by the green arrows in figure 2.24 (b).

Step to TEME, TEM forces should be shown in advance. Both *r* and *z* components of TEM forces achieved under a constant thermal gradient of 6000K/m and a 0.08T imposed magnetic field are displayed in figure 2.23. It can be seen that whatever the component is TEM forces exist near the liquid-solid interface only. This agrees with the distribution of TEC that regions departing from the interface in both liquid and solid are free of currents. Based on the coordinate defined in figure 2.21 (d) and magnitudes of TEM forces represented by colored surface in figure 2.23, the general direction of *r* and *z* components of computed TEM forces are pointed out by gray dotted arrows in figure 2.23 (a) and (b) respectively. It can find that the *r* component of TEM forces are outward from center in liquid and inward from periphery in solid, and the *z* component of TEM forces are downward at center and upward at

periphery in both liquid and solid. In other words, in solid, a torque along the interface can be produced by the *z* component of TEM forces. Image the dimensions of geometry used in these simulations are small enough to represent a tip of cells or dendrites, the torque in solid may break their arms when TEM forces become sufficient big. Moreover, in liquid, indicate the *z* component of TEM forces by the dotted red arrows on the figure showing the *r* component of TEM forces, as shown in figure 2.23 (a), it can be known that a vertical vortex can be driven by such TEM forces in liquid.

In order to prove the discussion about vertical vortex in liquid above, TEM flows under various magnetic fields are simulated and shown in figure 2.24. Meanwhile, in order to illustrate the flow field more precisely, magnitudes of *z* and *r* components velocities of TEM flows are measured and plotted respectively along a horizontal and vertical line as indicated in figure 2.24 (b). Figure 2.25 shows the corresponding curves. Just like predication based on the TEM forces in liquid shown in figure 2.23 (a), a vertical vortex appear as demonstrated in figure 2.24 (a) and (b). This suggests that, with a constant thermal gradient of 6000K/m, even such week magnetic field (0.08T) is able to drive detectable flows. It can also find that TEM flows slow down rapidly in the region far from the liquid-solid interface because the arrows and streamlines of their norm velocities are rare. This rapid velocity decreasing can be proved by the blue curves shown in figure 2.25 (b) as well. Another phenomenon should be noticed is that the vortex is small and locates at the region near to both the liquid-solid interface and the symmetric axis when the magnetic field is 0.08T. Increase the magnetic field, both the range and the center of vortex in liquid are changed. As shown in figure 2.24 (c) and (d), the vortex is enlarged and locates at the region near to the top and the periphery when the magnetic field is 0.8T. This can be proved by the red curve in figure 2.25 (b) as well because the period of this curve occupies almost the liquid region. When the magnetic field is 1.6T, the center of vortex is closer to the periphery than that achieved unde 0.8T magnetic field. Further, much higher magnetic field that 8T does not dramatically change the range and the position of the vertical vortex a lot. But a new phenomenon should be noticed in this high field case that new vortex very close to the liquid-solid interface and the very periphery wall appears as indicated by the red circle in figure 2.24 (g) and (h). This may be a special phenomenon occurring under high magnetic field (High hartmann number case) only, for example the Hartman layer problem. Because this new phenomena relates to another research topic and is out of the concerning range of the present thesis, here, no more discussions will be given. Regarding the magnitude of the velocities of TEM flows achieved under different magnetic fields, it can conclude from the curves in figure 2.25 that the absolute values of both *z* and *r* component

velocities of TEM flows increase with the increasing magnetic field until 1.6T and then are apparently suppressed when the magnetic field is over the thredhold value, 8T for instance.

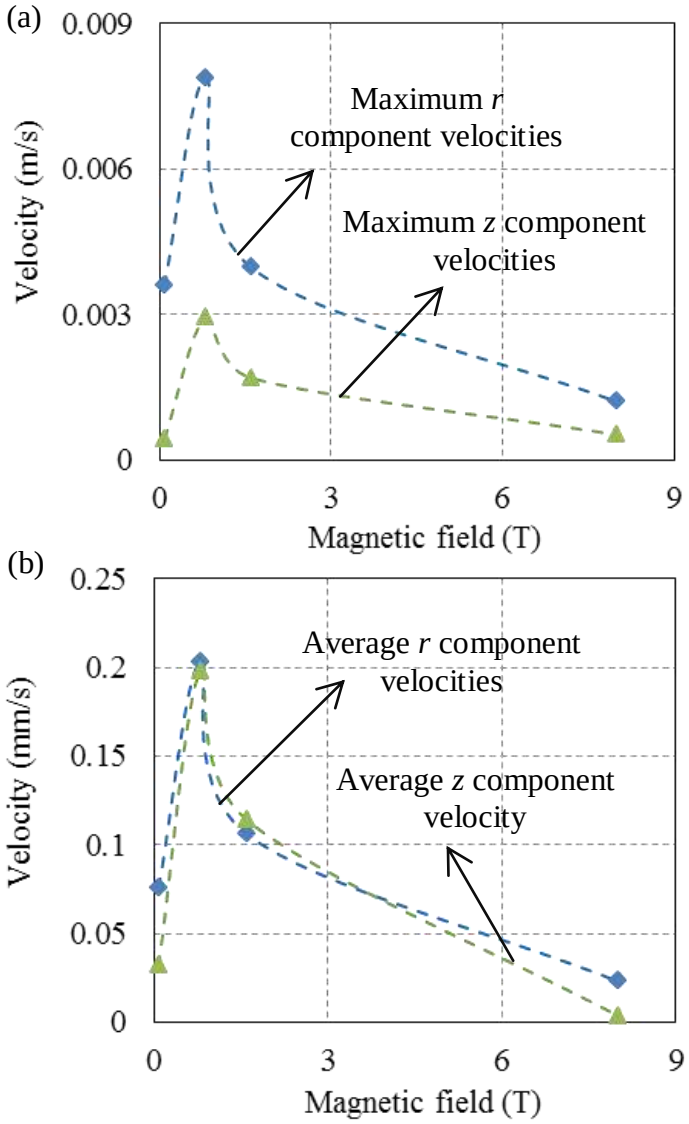

Figure 2.26 Curves of maximum (a) and average (b) *r* and *z* component velocities of TEM flows varying with different magnetic fields.

In order to investigate how the velocities of TEM flows vary with the imposed magnetic fields, the maximum velocities of TEM flows, as well as the average, are plotted versus magnetic fields as shown in figure 2.26. These curves suggest a unique change tendency of TEM flows with constantly increasing magnetic fields, which is TEM flows firstly speed up to a maximum velocity under a crtical magnetic field and then slow down when magnetic field increases further. Indeed, this should be resulted from the competition between TEM forces in liquid and magnetic damping forces that expressed as $(\vec{u}\times\vec{B})\times\vec{B}$. It can be known from the expression 2.23 that TEM forces in liquid are proportional to *B*, on the contrast, the magnetic damping forces are proportional to B^2. Conseqently, the competition between these two kinds of forces must lead to a critical magnetic field under which the velocities of TEM flows reach the maximum.

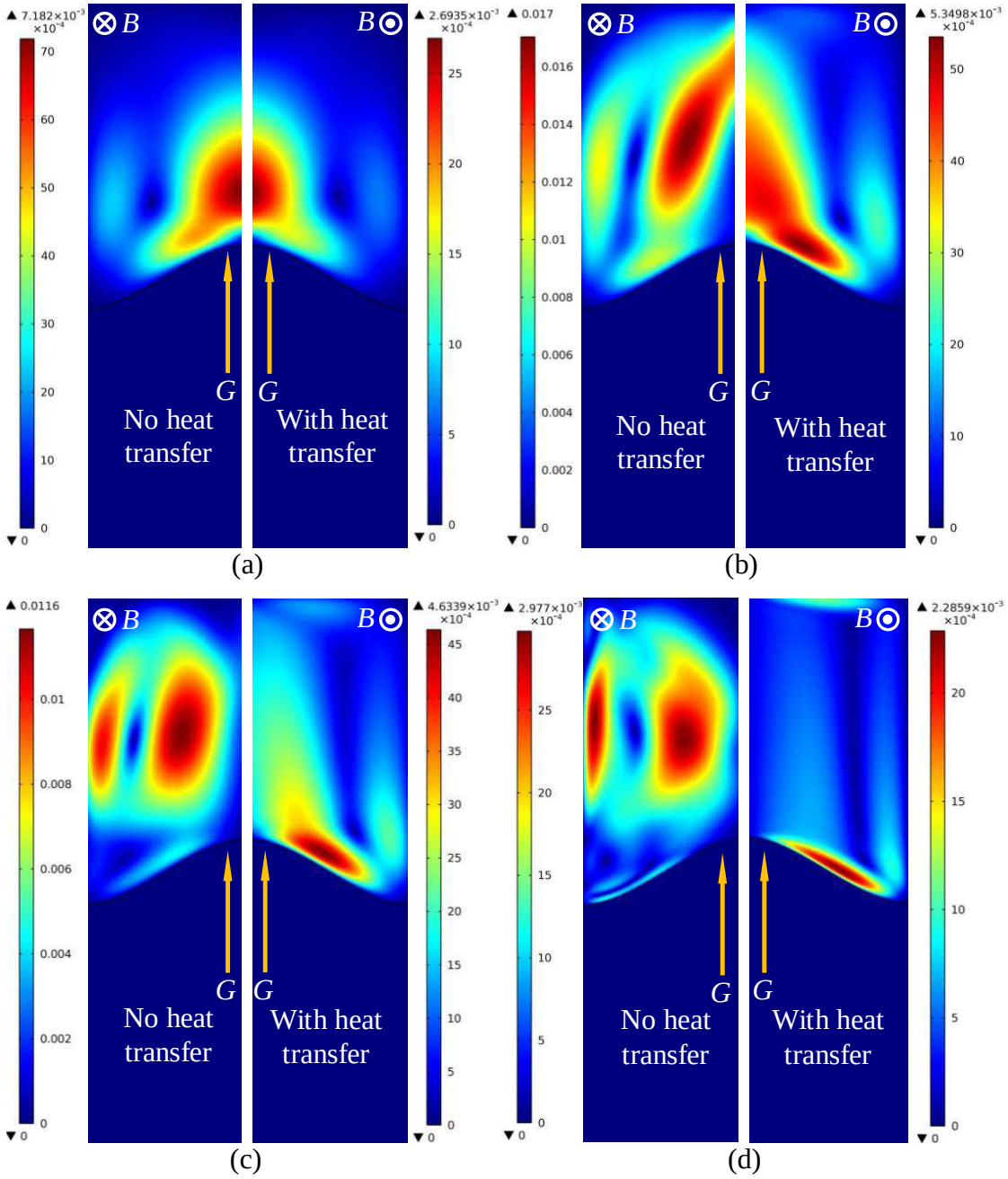

Figure 2.27 TEM flows fields simulated without and with coupling heat transfer under different magnetic fields. (a) *B*=0.08T; (b) *B*=0.8T; (c) *B*=1.6T; (d) *B*=8T. Unit of legend is m/s.

For the sake of coming closer to the reality and investigating the influence of coupling heat transfer in simulation of TEME, the heat transfer module predefined in COMSOL is added to the simulations coupling both the electric current and the fluid flow modules. Because there are two phases involved in simulation, the governing equations of heat transfer in liquid and in solid are defined separately. In liquid, the initial values of flow field and pressure are set to use the calculating results from the previous stpe of computing TEM flows. In solid, governing equations of heat transfer in solid state predefined by the COMSOL are

used. Meshes are kept the same as described in figure 2.21, and materials properties used in simulations can be found in table 2.2.

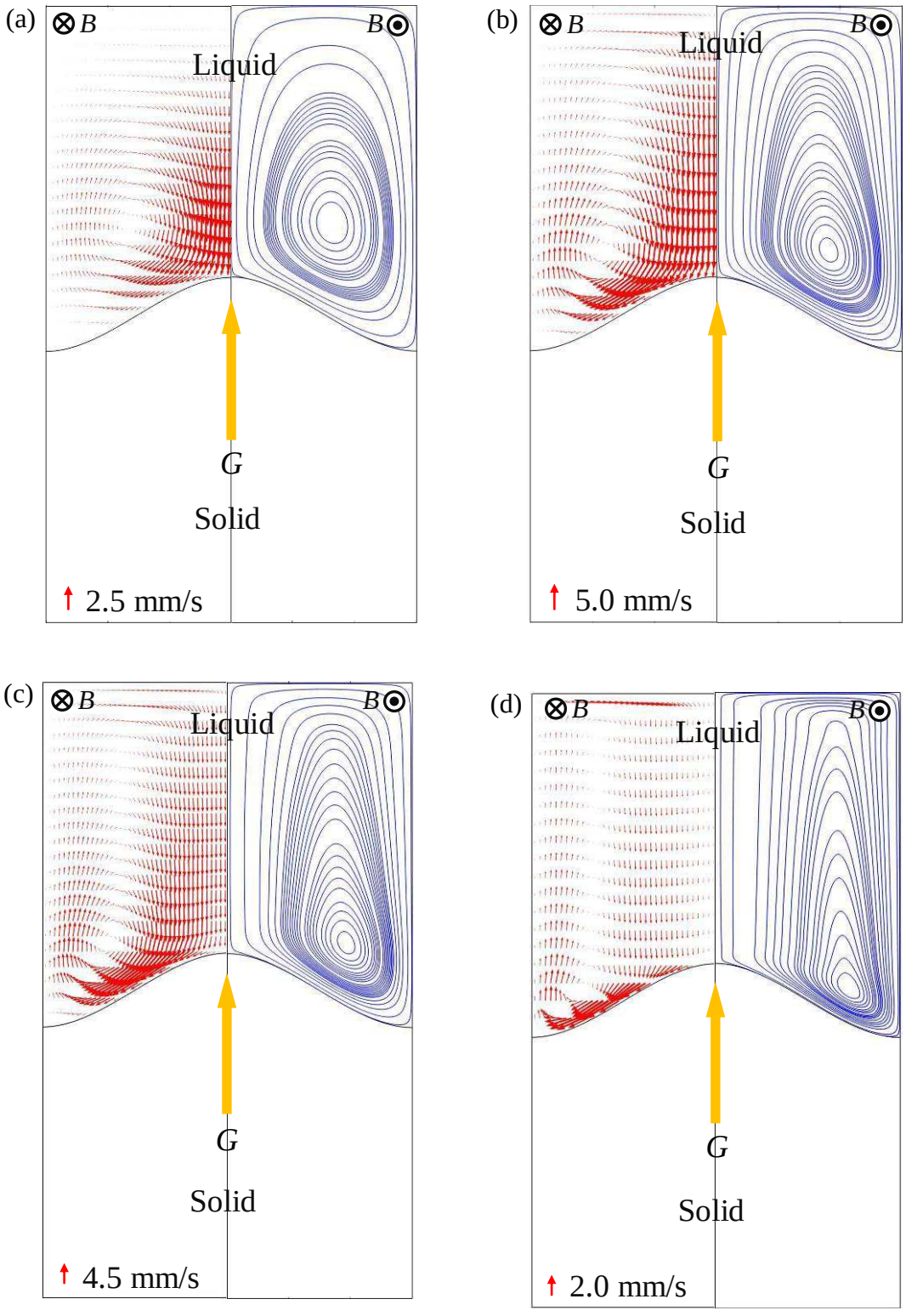

Figure 2.28 Arrows and streamlines of TEM flows simulated with heat transfer under different magnetic fields. (a) B=0.08T; (b) B=0.8T; (c) B=1.6T; (d) B=8T.

Comparisons of TEM flows fields obtained without and with coupling the heat transfer module under different magnetic fields are shown in figure 2.27, from which dramatic changes are uncovered. With the help of figure 2.28 that the arrows and streamlines of TEM

flows simulated with heat transfer module under different magnetic fields, it can see that the general flow field one vertical vortex occupying the almost liquid region is not changed whaterver the heat transfer is coupled or not. However, differerent from the simulations without coupling heat transfer the center of the vortex obtained with coupling heat transfer module become closer and closer to the liquid-solid interface with increasing magnetic fields. Moreover, the lower part of the vortex becomes very thin and near to the interface when the magnetic field is 8T as indicated by the red region in figure 2.27 (d) or the gathered streamlines in figure 2.28 (d). Because the flows in liquid vastly affect the heat transfer, and TEC is partly decided by the temperature field, TEM flows fields are dramatically changed by coupling the heat transfer module should be reasonable and understandable.

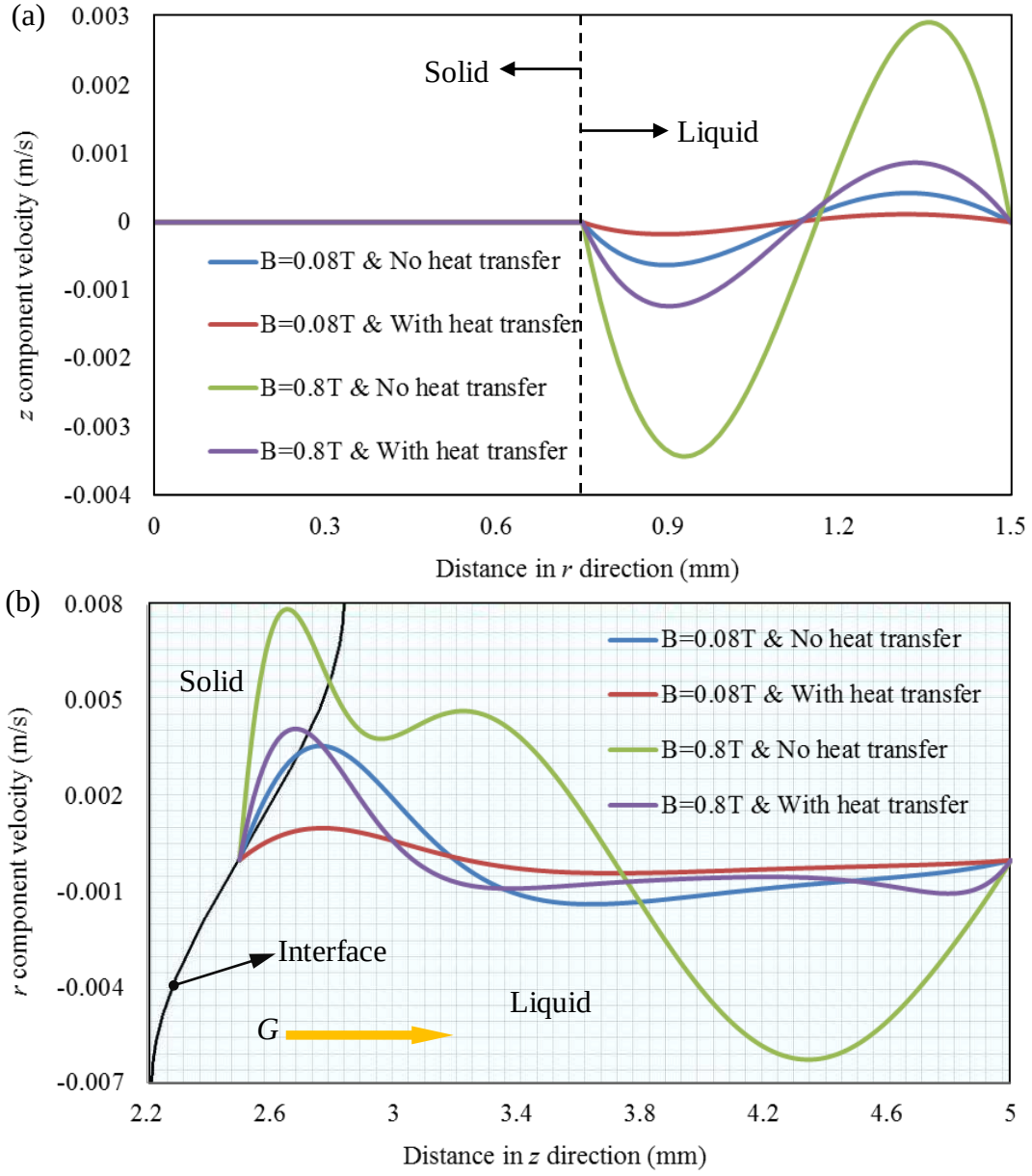

Figure 2.29 Curves of *z* (a) and *r* (b) component velocities of TEM flows simulated without and with heat transfer module respectively plotted along the horizontal and vertical lines indicated by green arrows in figure 2.24 (b).

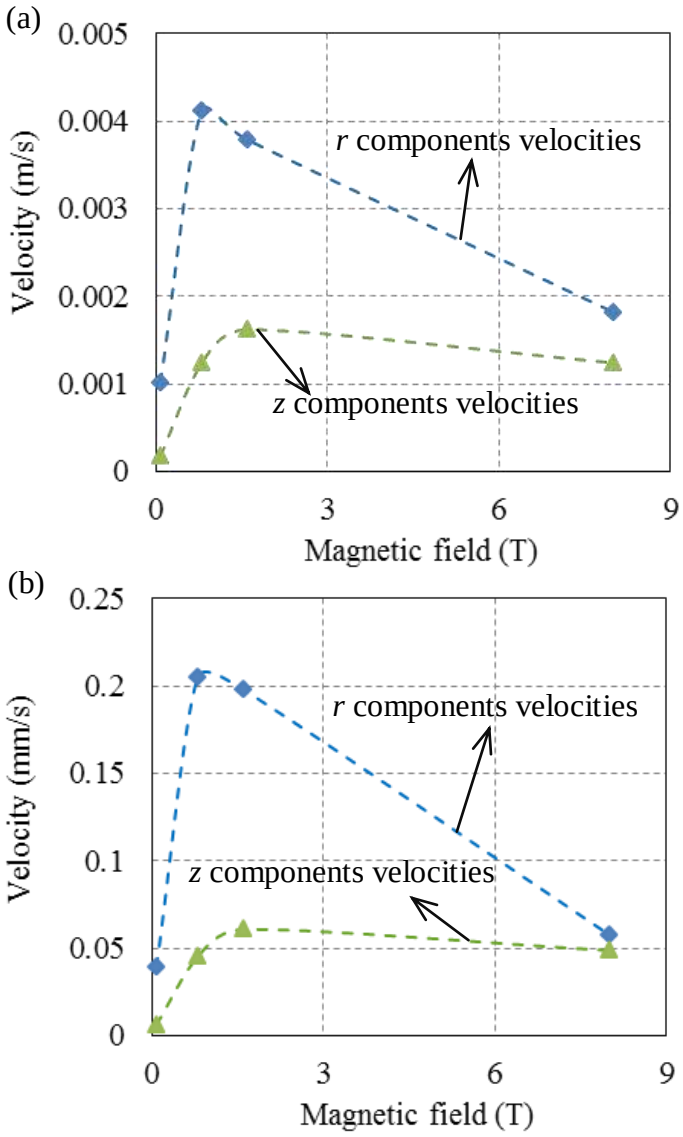

Figure 2.30 (a) Curves the maximum velcoties of TEM flows computed with coupling heat transfer module varys with different magnetic fields; (b) Curves the average velcoties of TEM flows computed with coupling heat transfer module varys with different magnetic fields

Except TEM flows fields, influence of heat transfer on the magnitudes of its velocities is examined as well. Both *z* and *r* components velocities of conmputed TEM flows are ploted and respectively shown in figure 2.29 (a) and (b). Because the minimum and maximum velocities of TEM flows appear respectively under 0.08T and 0.8T magnetic field, the influence of heat transfer on the magnitudes of velocities of TEM flows is compared for these two cases only. It can find that taking heat transfer into account decreases the velocities of TEM flows, which should be attributed to the homogenization effect of flows in liquid on the temperature field. Once heat transfer in liquid is considered, the temperature field of liquid must be homogenized by TEM flows, and the homogenized temperature field reduces the temperature difference that one of the determining factors for producing TEC. Conseqently, the reduced TEC slows down the TEM flows. In another aspect, as shown in figure 2.29,

curves obtained by simulations coupling heat transfer module are smoother than those without considering influence of heat transfer, which can prove the homogenous effect as well. Moreover, it can find that the influence of heat transfer is more apparent under a 0.8T magnetic field than that under 0.08T. This can be another evidence for the homogenous effect of TEM flows on the initial temperature field because TEM flows under 0.8T magnetic field are faster.

Similar to figure 2.26, how the velocities of computed TEM flows vary with different magnetic fields is worthy to investigate as well when the heat transfer module is coupled. Measure and plot the maximum and average velocities of TEM flows versus magnetic fields how the velocities of TEM flows vary with magnetic fields can be revealed by curves shown in figure 2.30. It can see that both maximum and average velocities increase to the maximum under a critical magnetic field and then decrease with further rising magnetic fields. This agrees with that obtained from simulations without coupling heat transfer module. Therefore, it can conclude that such tendency of how the velocities of TEM flows vary with imposed magnetic fields should be a general principle for TEM flows in directional solidification process.

Although the purpose of this section is unfolding TEM forces and TEM flows in directional solidification process, it would be also interesting to examine the influence of TEM flows on the temperature field. It can be known that maximum velocities of TEM flows appear under a 0.8T magnetic field from the simulations above. Therefore, the temperature fields obtained without and with TEM flows generated by a 0.8T magnetic field are simulated and shown in figure 2.31. Moreover, the contours of *r* component thermal gradients are also given in figure 2.31. It can be found that the modification of temperature field by TEM flows is undetectable as indicated by the colored surface. However, as shown in figure 2.31 (b), the contours of *r* component thermal gradients at the top of liquid region suggests that the thermal gradients in liquid are changed a lot. More precise, both *z* and *r* component thermal gradients obtained without and with considering the influence of TEM flows are measured and plotted along the vertical line indicated by the green arrow in figure 2.12 (a). Figure 2.32 shows the corresponding curves. It can see that the curves of thermal gradients obtained under influence of TEM flows are appreantly smoother than those without considering TEM flows. This enhances the conclusion that TEM flows are able to homogenize the intial temperature field. Moreover, deviation of *r* component thermal gradients as indicated by the blue circle suggests that TEM flows decrease the temperature difference in that region. This can explain, in another aspect, why slower TEM flows are obtained when simulations taken the heat transfer module into account.

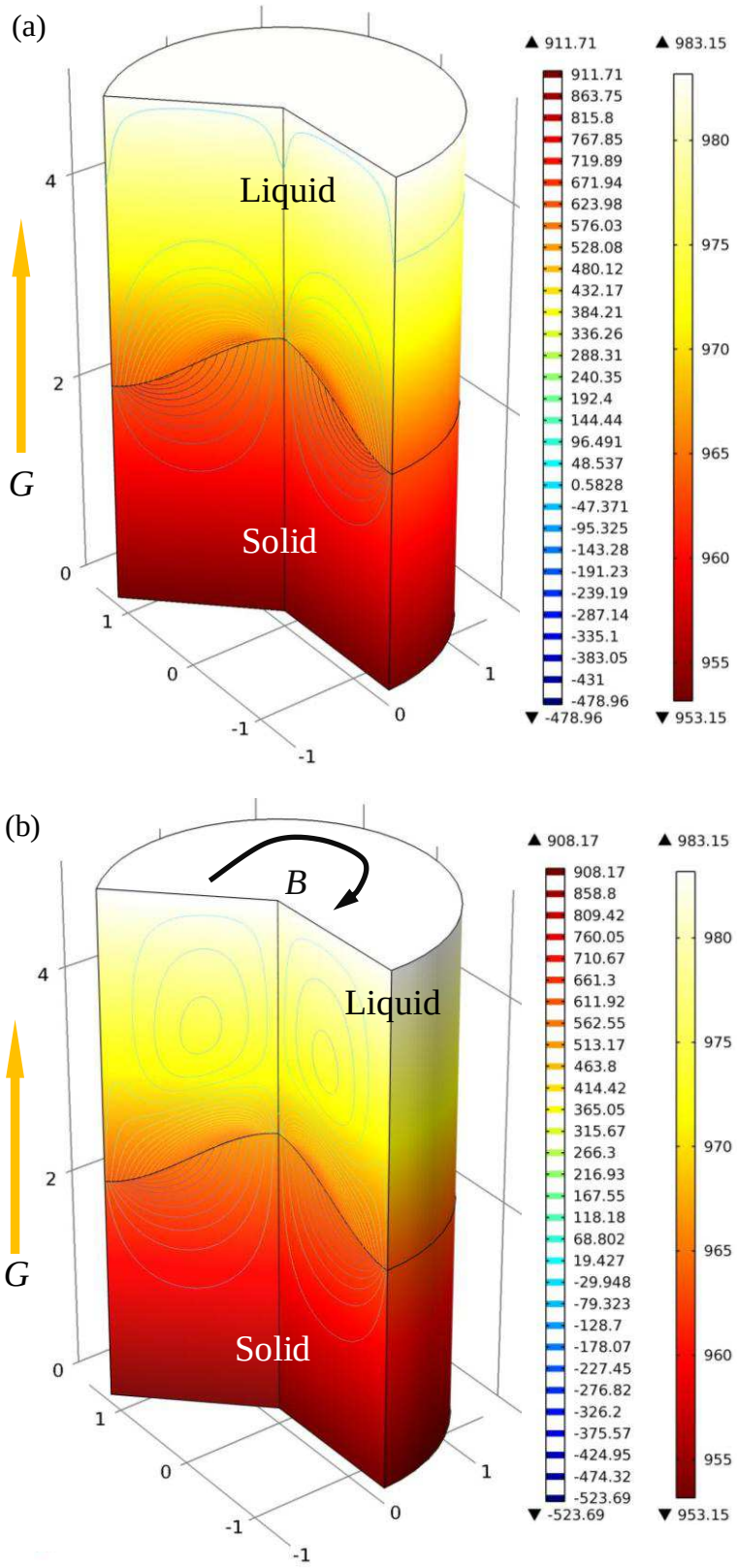

Figure 2.31 Computed temperature fields (colored surface, K) and *r* component thermal gradients (contours, K/m) without (a) and with (b) considering the influence of TEM flows produced by a 0.8T magnetic field *B* and a constant thermal gradient of 6000K/m *G*.

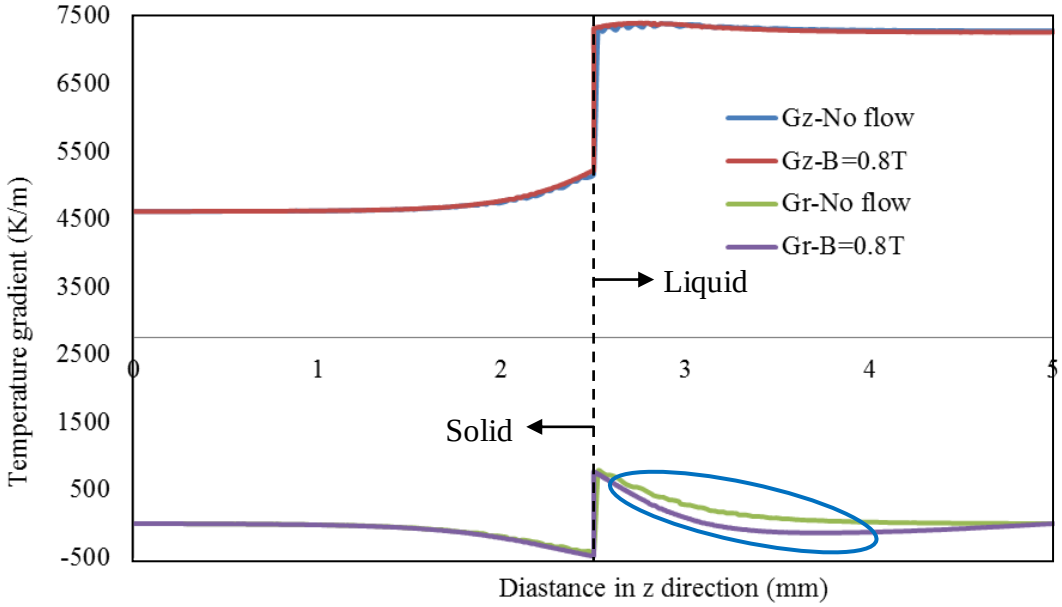

Figure 2.32 Thermal gradients computed without and with TEM flows generated by a 0.8T magnetic field plotted along the vertical line as indicated in figure 2.12 (a). G_z and G_r represent z and r component thermal gradients respectively.

2.4 Summary

Aim at unfolding TEM forces and TEM flows in solidification process, this chapter introduced the TE effect by the phenomenological analysis and the corresponding phenomena in directional solidification process in advanced. The approximate estimation of the influence of Peltier and Thomson effects on solidification showed these two effects are negligible. In fact, detail analyses about the influence of TE effect on liquid-solid interface instability made by Dr. Makoto Tanaka had proved that Peltier and Thomson effects can be neglected in solidification of metallic alloys neither. Therefore, considered Seebeck effect only, the governing equations and boundary conditions for TEC were formulated. Further, TEC at the liquid-solid interface in directional solidification was numerically simulated to intuitively display how it appears and acts. And then, TEME occurs when an external magnetic field was present. Phenomenological explanations of both TEM forces and TEM flows were given, and formulations of them closely followed. After that, numerical simulations of TEM forces and TEM flows in the context of directional solidification were performed to unfold how the TEME emergy and affect. Certainly, verification of the simulation method used here was taken prior to perform those simulations. Finally, comparisons of simulations of TEME without and with coupling the heat transfer module were made, which showed that the heat transfer cannot be neglected when dealing with the TEME problems. For this reason, simulations in the following chapters are performed by coupling three physical modules predefined in COMSOL that electric current, fluid flow and heat transfer.

Chapter 3: Visualization of thermoelectric magnetic effect (TEME) in directional solidification process

Thanks to the discovery of synchrotron radiation beam and the development of X-ray imaging techniques, in-situ and real time observing the process of solidification of metallic alloys comes true [268]. During the past twenty years, this method has provided numerous precise data for critical validation of solidification theories and for the optimization of numerical simulation predictions [269]. Consequently, it becomes an efficient and reliable method to characterize and confirm phenomena those appear in solidification process [270]. So that we also try to prove the TEM forces and TEM flows in directional solidification process by in-situ observation in this chapter. Moreover, analytical calculations of TEM forces driving movement of a sphere and numerical simulations of TEM flows with the same conditions used by in-situ observation experiments are taken. Combine the in-situ observation, analytical calculation and numerical simulation, TEM forces and TEM flows in directional solidification process are more clearly uncovered, and its influence on solidification structure are revealed to a certain extent.

3.1 Experimental apparatus

3.1.1 General view of in-situ synchrotron X-ray imaging setup

The in-situ and real-time observation of directional solidification of metallic alloys are taken in European Synchrotron Radiation Facility (ESRF) located at Grenoble, France. Based on the third generation X-ray beam, ESRF provides more than 40 beamlines to perform various scientific investigations. Beamline named BM05 is the one that provide in-situ synchrotron X-ray imaging facility. Indeed, experiments in the present thesis are all carried on this beamline. As shown by the photo taken before experiments and the corresponding sketch in figure 3.1, except the X-ray beam emitter main components of the setup used for in-situ synchrony X-ray imaging are ultrahigh vacuum Bridgeman furnace and fast readout-low noise (FReLoN) CCD camera that developed at ESRF. Sufficient high energy of synchrotron radiation source makes it possible to record images with enough contrast in a reasonable timescale (less than 1 second), which is fast enough to investigate some dynamic problems of solidification such as the growth and motion velocities of crystals or solute transportation driven by flows in melt. Moreover, the FReLoN can achieve a good compromise between larger field of view and satisfying spatial resolution (pixel size used is 7.47μm×7.46μm) that is sufficient for the concerned length scales in this thesis.

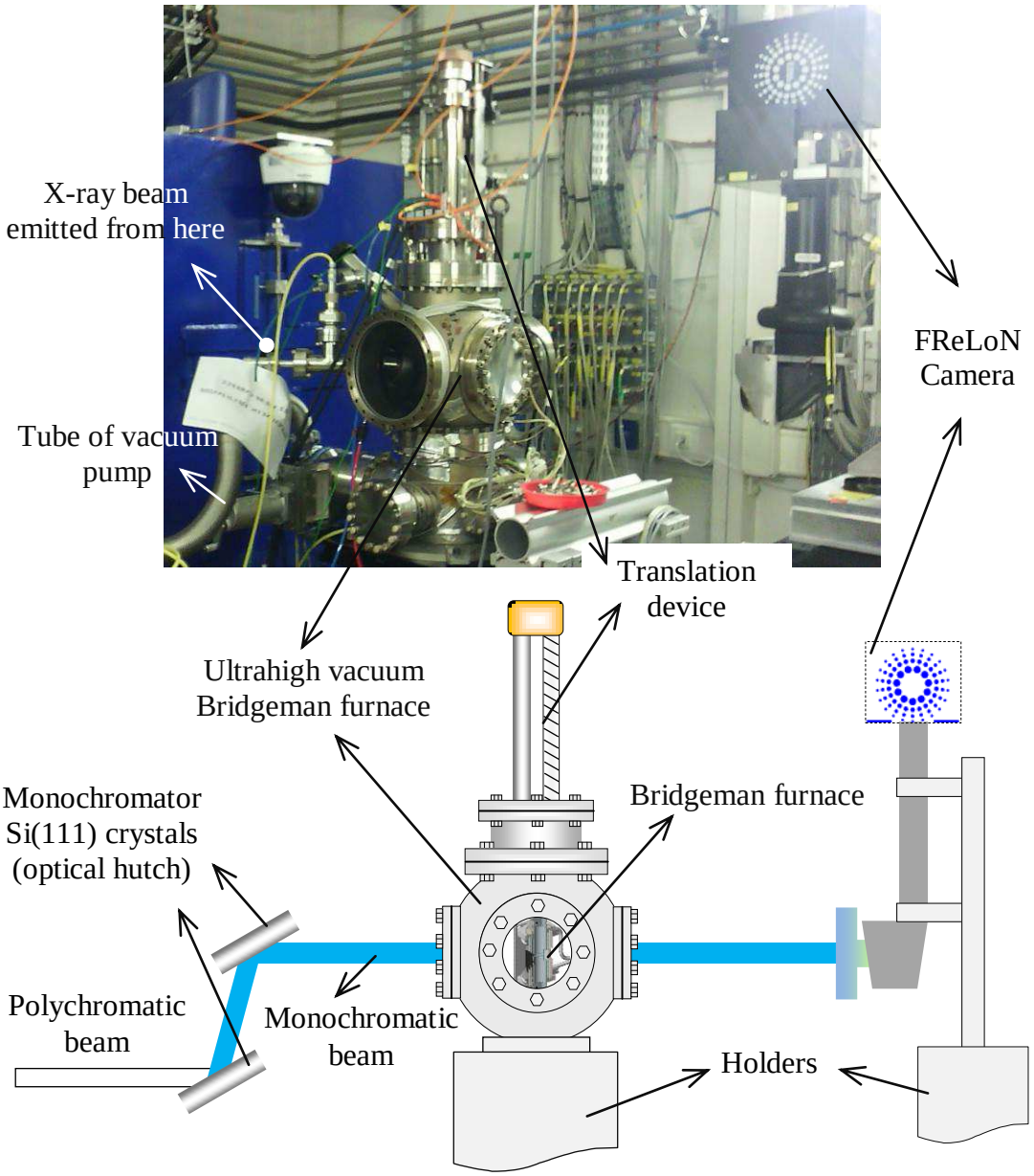

Figure 3.1 Photo and sketch of in-situ synchrony X-ray imaging setup.

3.1.2 Ultrahigh vacuum Bridgeman furnace and samples

In order to protect the heating elements and samples from oxidizing during experiments, an ultrahigh vacuum chamber made by stainless steels is used, which can subject to more than 10^{15} Pa pressure difference. Several windows with various sizes as shown in figure 3.2 (b) were reserved to meet different demands such as linking vacuum pump, fixing translation device and permitting synchrotron X-ray beam passing through. In which, there is a reservation for changing samples as indicated by red circle in figure 3.2 (a), and the view seen from this window is shown in figure 3.2 (c).

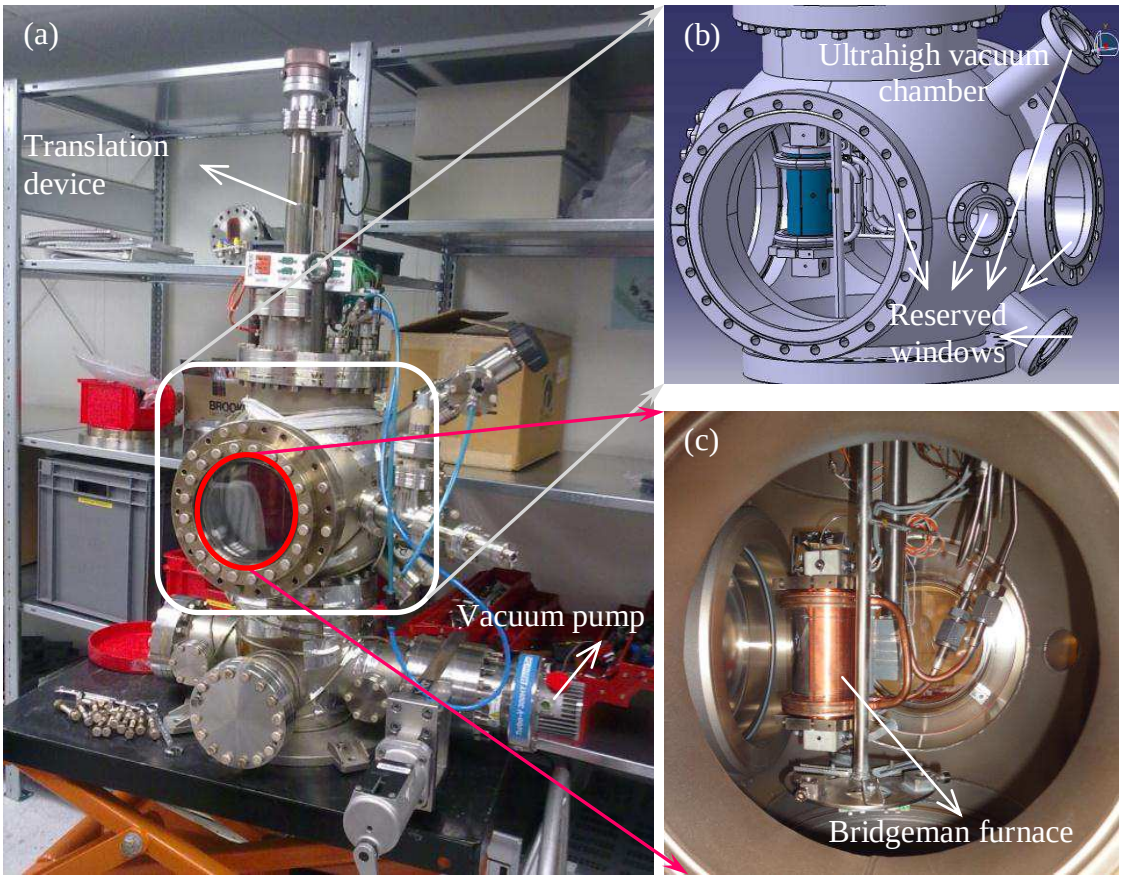

Figure 3.2 Photos and 3D drawing of ultrahigh vacuum Bridgeman furnace.

Figure 3.3 shows the furnace that placed inside the ultrahigh vacuum chamber, as shown by the 3D drawing, which consists of two separated heating elements. In order to protect the surrounding electric devices from high temperature two layer water cooling jets are placed outside the heaters. Directional solidification is realized by the power down method, which applies the same cooling rate on two separated heating elements during the entire experiment. In fact, suc two heating elements design permits not only the directional solidification but also the isothermal solidification by setting the same temperature and the same cooling rate to both heating elements. Adjustment of samples position is achieved by the translation device fixed at the top of vacuum chamber as shown in figure 3.1 and 3.2, which can realize both vertically up/down travelling and horizontally revolving. Sample holder is linked to this device by a stainless steel tube as marked in figure 3.3. Constrained by the request that samples must be perpendicular to the synchrotron X-ray beam, there are maximum three samples can be put for each time. In fact, when the magnet system is installed only one sample can be used for each time because the limitation of space.

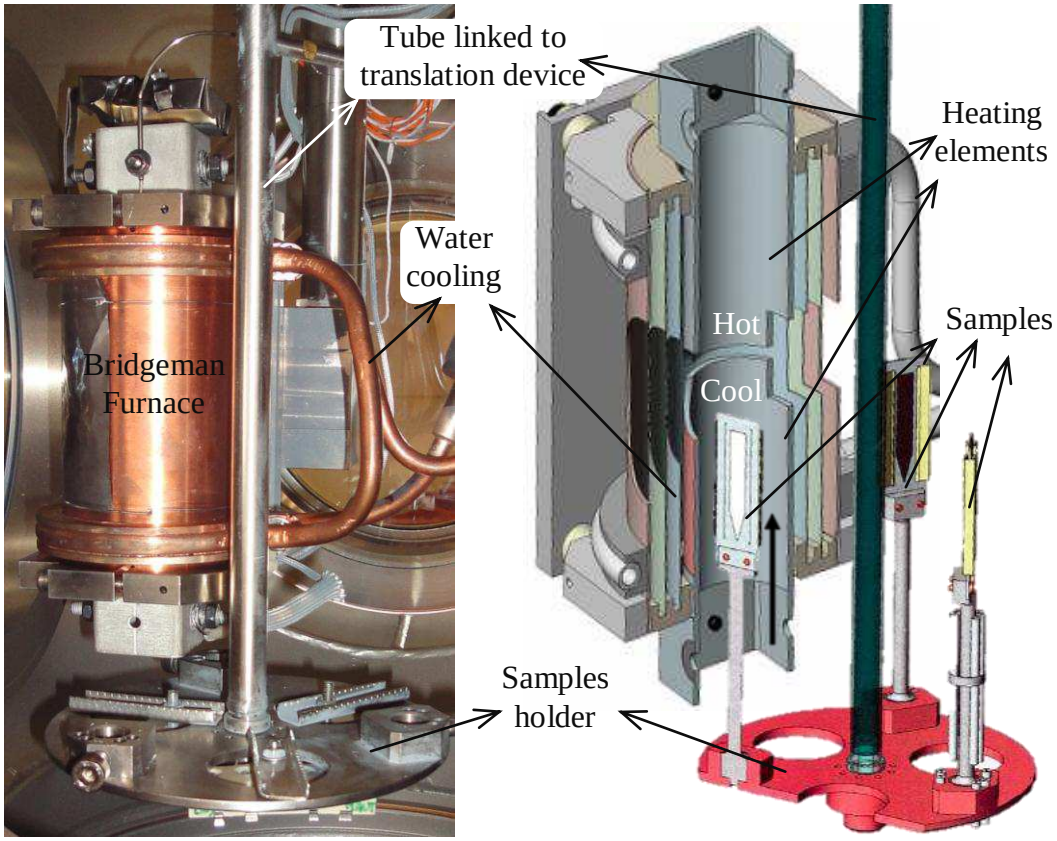

Figure 3.3 Photo and 3D drawing of Bridgeman furnace.

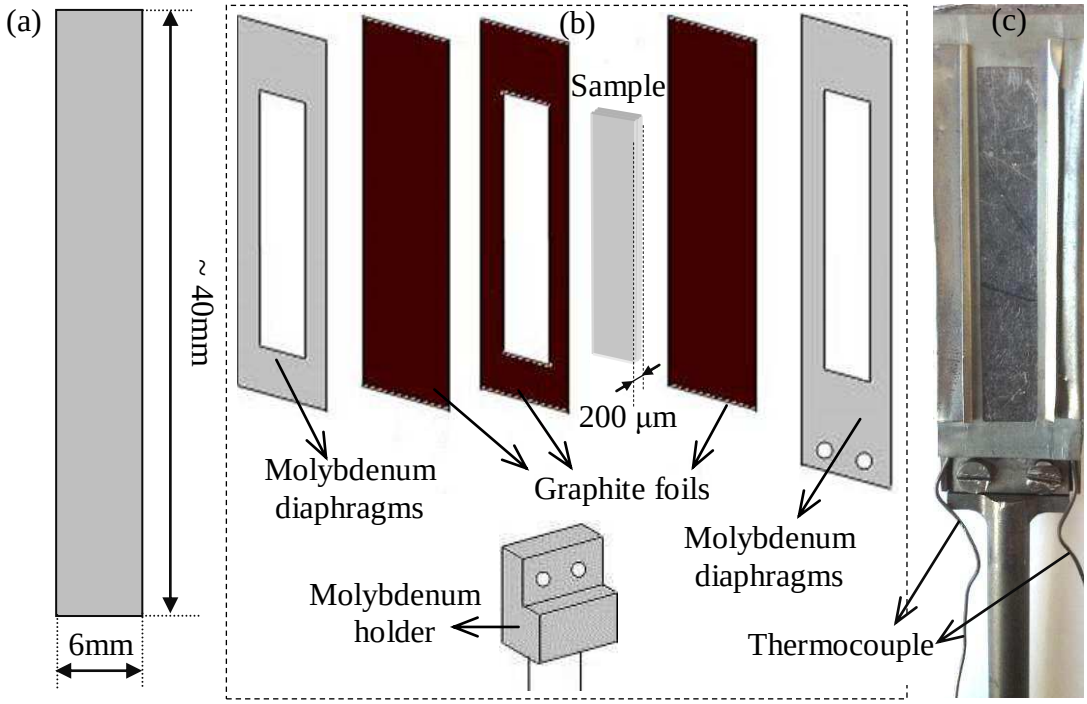

Figure 3.4 (a) Dimensions of samples; (b) Illustration of assembling the samples; (c) Photo of assembling sample used in experiment.

Because absorption was the main source of image contrast and depends on the atomic number of elements or solute content, there is a restriction on the thickness of samples to

permit synchrotron X-ray beam passing through. In the present experiments, samples are about 150 to 250μm in thickness, 40mm in height and 4 to 6mm in width as shown in figure 3.4 (a). The Al-Cu alloys used in this study are fabricated from pure Al and Cu elements. The prefabricated samples are sandwiched between two graphite foils and two molybdenum diaphragms, hold together with two clips and fixed to a holder as illustrated in Figure 3.4(b). Photo of the sample assemble used in experiments is shown in figure 3.4 (c).

3.1.3 External magnet system

In order to impose the magnetic field, an external magnet system should be installed. However, there are limited spaces left to do so because this ultrahigh vacuum Bridgeman furnace is intentionally designed to investigate solidification process without any external fields. For this reason, a samarium cobalt permanent magnet is chosen. The size of the magnet is 50mm×50mm×50mm. Figure 3.5 (a) and (b) show how it is mounted.

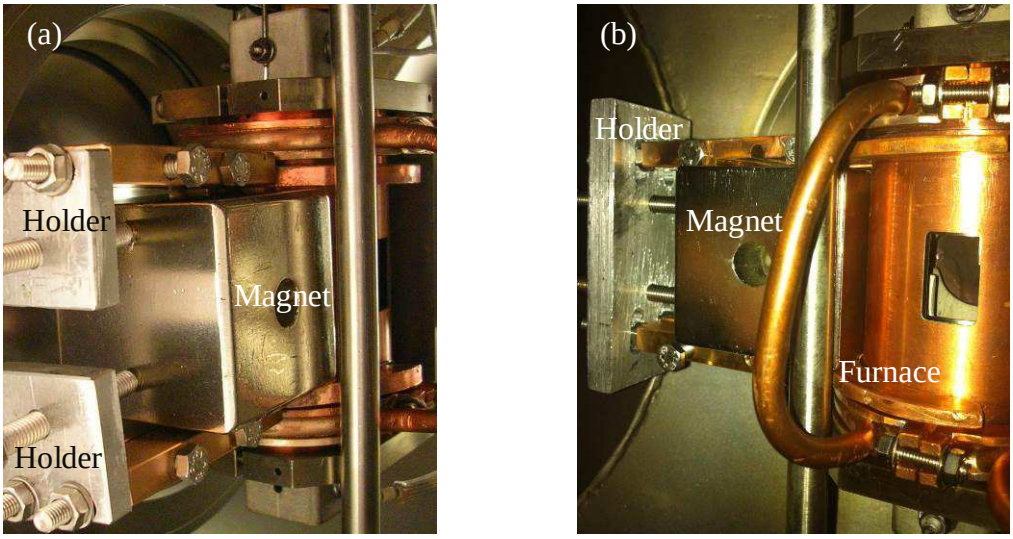

Figure 3.5 Photos illustrating how magnet system is mounted.

Magnetic fields generated by this permanent magnet are simulated by using the static magnetic field and no current module predefined by COMSOL with this magnet's real property parameters. Figures 3.6 (a) and (b) respectively shows the geometry and mesh used in these simulations. As displayed in figure 3.6 (c), simulations are constricted within the vacuum chamber, and the magnetic fields fulfill the vacuum chamber as indicated by the blue streamlines that representing the magnetic field lines. Magnify region that we are most interesting, magnetic fields inside the furnace are given by red arrows in figure 3.6 (d).

Further, near the furnace and the magnet, magnetic fields on both *x*-*y* and *y*-*z* planes were examined and displayed in figure 3.7 and 3.8 respectively. Based on the magnetic fields represented by arrows and contours, it can be reasonablly regarded that the magnetic fields

uniformly distribute within the sample region. More precisely, computed magnetic flux intensities varying along *y* and *z* direction as indicated by purple and green arrows respectively in figure 3.7 (b) and 3.8 (a) are profiled. The corresponding curves are respectively shown in figure 3.7 (c) and 3.8(c). In order to show the uniformity, the curve corresponding magnetic fields within the sample is magnified and inserted in figure 3.7 (c). Moreover, magnetic field flux intensities along y direction are measured and compared with the simulations in figure 3.7 (c) as well. The perfect consistent between the measurement and simulation verifies the validity of the simulations of magnetic field generated by that permanent magnet and the uniformity of magnetic field within the sample regions.

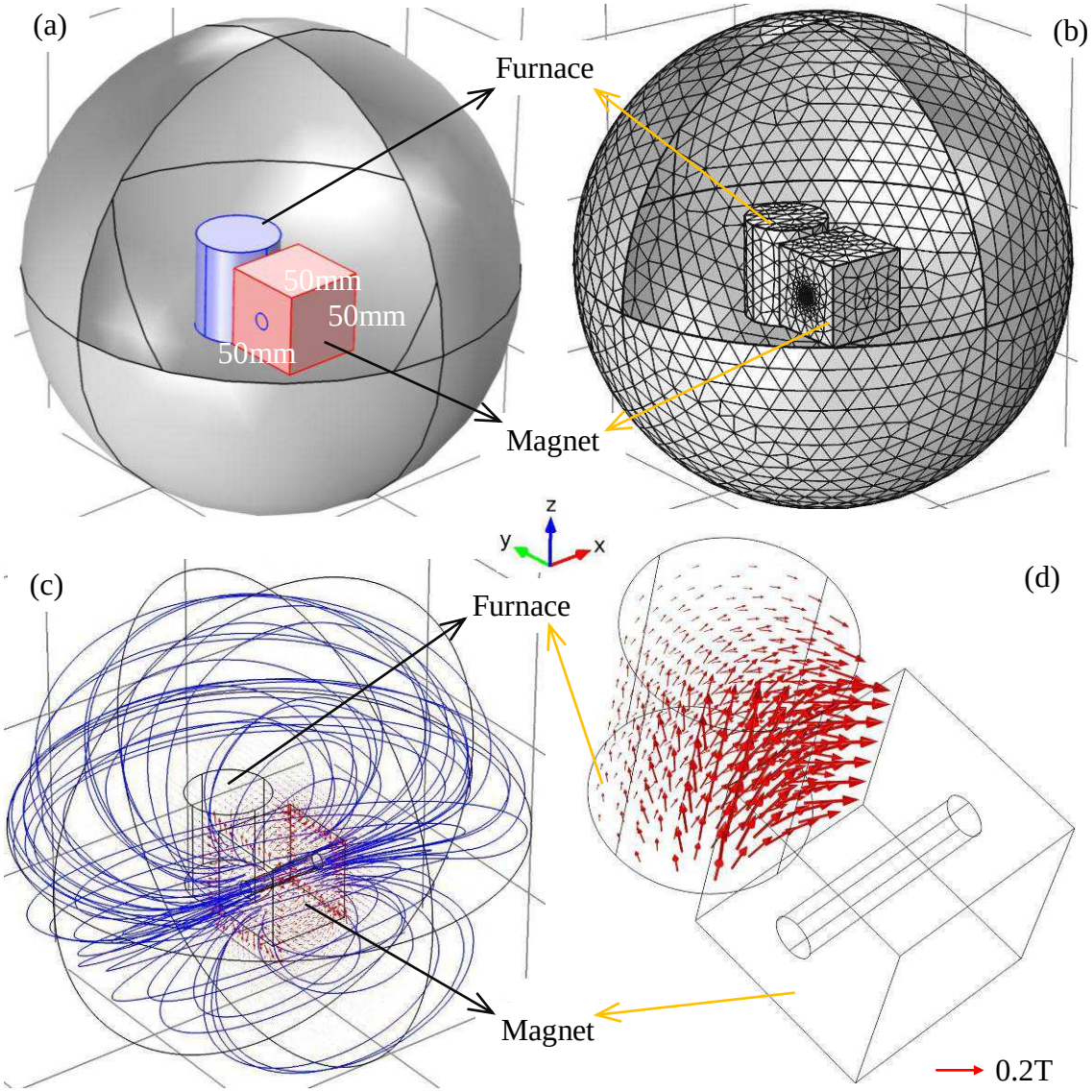

Figure 3.6 (a) Geometry used in simulation of magnetic fields; (b) Meshes used in simulation of magnetic fields; (c) Streamlines and arrows of magnetic field distribution; (d) Arrows of magnetic field near the furnace and magnet.

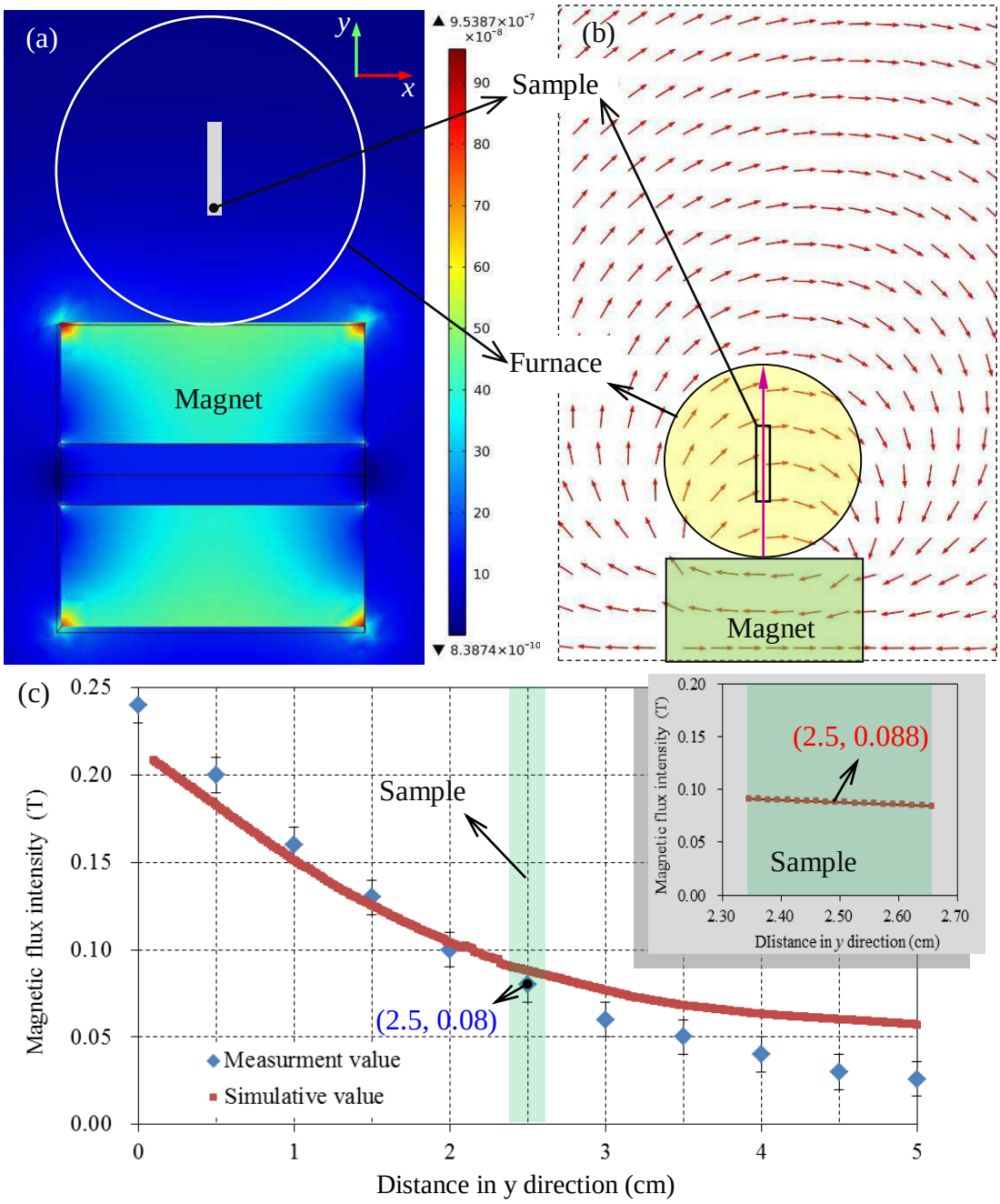

Figure 3.7 (a) Magnitudes of magnetic fields near the magnet and furnace in *x*-*y* plane, unit of legend is T; (b) Arrows of magnetic fields responding to (a), the arrows are normalized; (c) Curves of computed and measured magnetic field flux intensities varying along *y* direction as indicated by the purple arrow in (b).

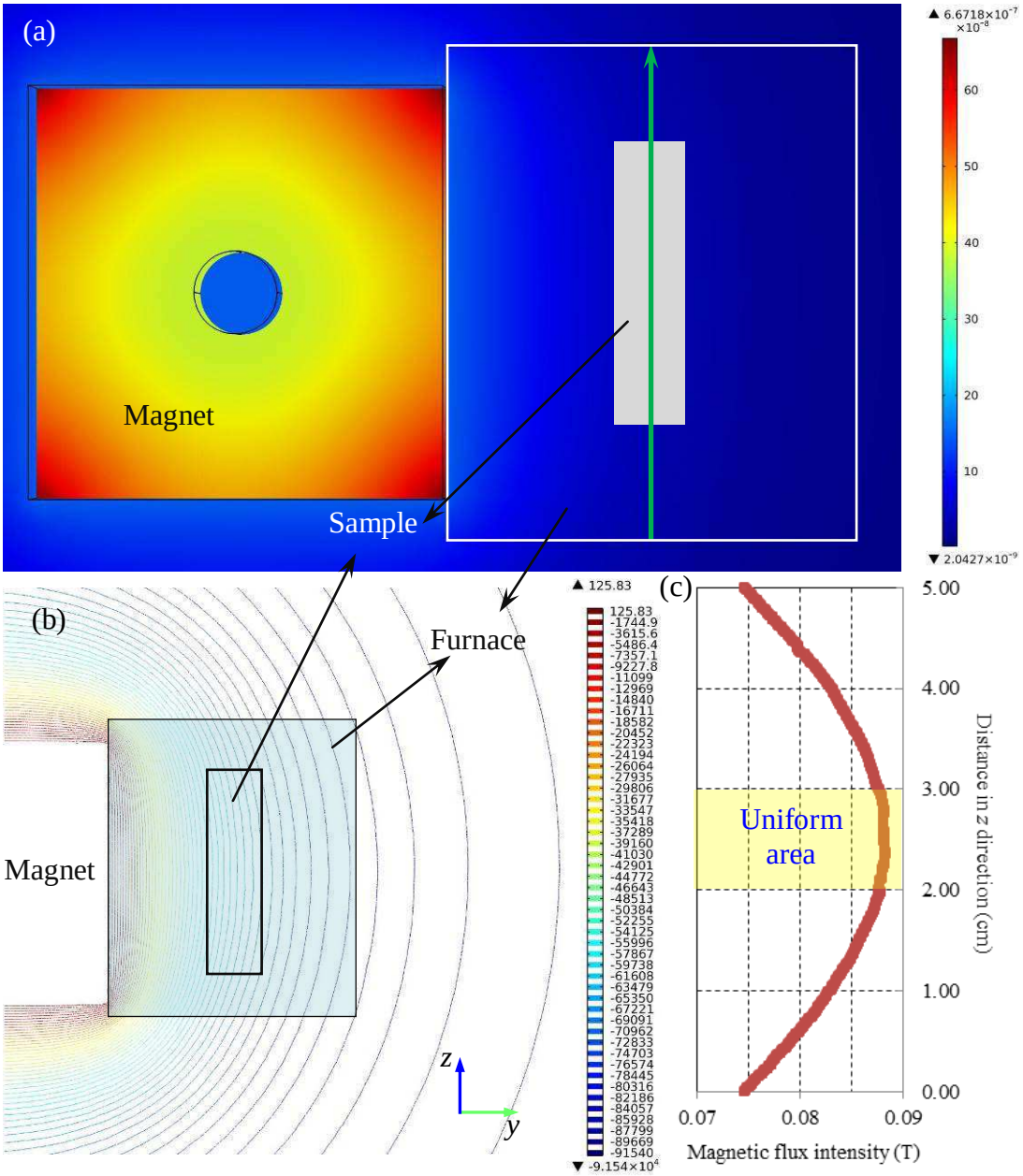

Figure 3.8 (a) Magnitudes of magnetic fields near the magnet and furnace in *y*-*z* plane, unit of the legend is T; (b) Contours of magnetic fields responding to (a); (c) Curve of computed and measured magnetic field flux intensities varying along *z* direction as indicated by the green arrow in (a).

3.2 In-situ observation of thermoelectric magnetic (TEM) forces

Considering it is hard to in-situ and real time observe or measure the stresses in solid, particularly during solidification process, TEM forces are thougth to be in-situ observed and proved if their directly resulting phenomenon is detected or recorded. The movements of crystals during directionally solidifying Al-Cu alloys under a transverse static magnetic field are observed and analyzed to uncover the TEM forces acting on the solid. Moreover, because the movements of crystals can be also driven by the flows in melt analytical calculations of TEM forces driving movements of sphere particles are taken. TEM forces in solid are confirmed by comparing the real movement velocities of crystals measured in the in-situ observation to the analytical calculating velocities of TEM forces driven movements of sphere particles. Indeed, for these in-situ observation experiments, flows in melt should be very week because the thickness of the sample is very thin that only about 200μm and thermal-solutal stable configuration (upward thermal gradient with heavier rejected solutes) [271] is used.

3.2.1 Analytical calculations of TEM forces driving movements of sphere particles

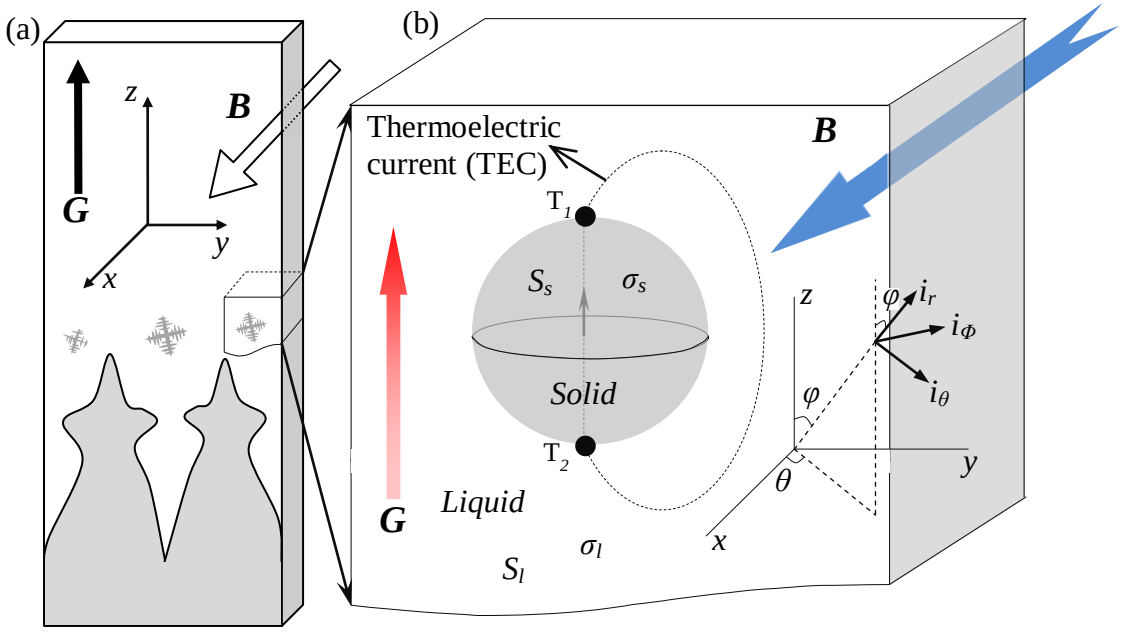

Figure 3.9 (a) Illustration of conditions used in analytical calculating the TEM forces driving movement of sphere particles immersed in its melts with a constant thermal gradient and under a static transverse magnetic field; (b) The model and spherical coordinates (r, ϕ, θ) used in analytical calculations and schematic of TEC.

The calculations of TEM forces driving movements of sphere particles are taken by assuming the thermal conductivity and the other physical properties being unique within liquid and solid respectively. Moreover, it is supposed that the size of particles is small enough to avoid any influences from the container walls. The external magnetic field B is applied in x-axis direction, and liquids around the particle are considered as infinite. The velocities of TEM forces driving movements of sphere particles can be simply estimated by

balancing the TEM forces to the Stokes drag forces. Therefore, TEC and TEM forces should be calculated before that estimation. The temperature difference is prescribed as:

$$\vec{\nabla}T = G\,\vec{i}_z \tag{3.1}$$

where G is the thermal gradient and $\vec{i}_z$ is a unit vector along the z-axis. Neglect electromotive force induced by liquids moving across the magnetic field lines and apply Ohm's law, the equation governing the electric current density is:

$$\vec{j}_i = -\sigma_i \vec{\nabla} V_i - \sigma_i S_i G \vec{i}_z = -\sigma_i \vec{\nabla} W_i \tag{3.2}$$

where σ_i and S_i respectively denotes the electrical conductivity and the ATP, subscript i can be replaced by l for the liquid or s for the solid phase, and W_i is defined as an effective scalar potential:

$$W_i = V_i + S_i T \tag{3.3}$$

here, V_i is the scalar potential. Regarding the continuity of electric current density:

$$\vec{\nabla} \cdot \vec{j} = 0 \tag{3.4}$$

the effective scalar potential W_i is harmonic.

The boundary condition at the liquid-solid interface requires the continuity of the normal component of electric current density:

$$-\sigma_l \frac{\partial V_l}{\partial n} - \sigma_l\, S_l\, G\, \vec{i}_z . \vec{n} = -\sigma_s \frac{\partial V_s}{\partial n} - \sigma_s\, S_s\, G\, \vec{i}_z . \vec{n} \tag{3.5}$$

and the scalar potential:

$$V_s = V_l \tag{3.6}$$

where, $\vec{n}$ is the normal component unit vector. Moreover, the normal component of current density should be zero at infinity. Because the liquid aroud the particle is regarded as infinity it has:

$$\vec{j}_l . \vec{n} \equiv -\sigma_l \frac{\partial V_l}{\partial n} - \sigma_l\, S_l\, G\, \vec{i}_z . \vec{n} = 0 \tag{3.7}$$

Because we look at a sphere particle, TEC in this situation can easily be solved analytically in spherical polar coordinates. Based the spherical polar coordinates defined in figure 3.9 (b), the Laplace equation governing W_i can be:

$$\frac{1}{r^2}\frac{\partial}{\partial r}\left[r^2 \frac{\partial W_i}{\partial r} \right] + \frac{1}{r^2 \sin\varphi}\frac{\partial}{\partial \varphi}\left[\sin\varphi \frac{\partial W_i}{\partial \varphi} \right] = 0 \tag{3.8}$$

Because the thermal gradient is symmetric along z-axis, it can be assumed that the electric potential is axisymmetric in the form:

$$W_i = \tilde{W}_i(r)\cos\varphi \tag{3.9}$$

Replacing W_i in equation 3.8 by 3.9 leads to the following equation governing $\tilde{W}_i(r)$:

$$\frac{1}{r^2}\frac{d}{dr}\left[r^2\frac{d\tilde{W}_i}{dr}\right]-\frac{2\tilde{W}_i}{r^2}=0 \tag{3.10}$$

with the boundary conditions:

$$\tilde{W}_l(r=+\infty)=0 \tag{3.11}$$

$$\tilde{W}_l(r=R)=\tilde{W}_s(r=R) \tag{3.12}$$

and $\tilde{W}_s(r=0)$ is non-singular. R is the radius of the particle. The solution for $\tilde{W}_i(r)$ is:

$$\tilde{W}_l(r)=b\left[\frac{R^3}{r^2}\right] \tag{3.13}$$

$$\tilde{W}_s(r)=a\,r \tag{3.14}$$

with $b=-\dfrac{\sigma_s}{(\sigma_s+2\sigma_l)}(S_s-S_l)G$ and $a=-\dfrac{\sigma_l}{\sigma_s}\dfrac{2b}{R^3}$.

TEM forces acting on particle can be expressed:

$$\vec{F_s}=\vec{j_s}\times B\vec{i_x} \tag{3.15}$$

with $\vec{j}_s\equiv-\sigma_s\nabla W_s$. So that:

$$\vec{F_s}=-\sigma_s B\nabla W_s\times\vec{i_x} \tag{3.16}$$

In order to obtain the three components of TEM forces in Cartesian coordinates as defined in figure 3.9 (a), perform projections on the unit vectors ($\vec{i}_x,\vec{i}_y,\vec{i}_z$) it has:

$$F_{sx}=F_{sz}=0 \tag{3.17}$$

$$F_{sy}=2\sigma_s GB_0\left[\frac{\sigma_l}{2\sigma_l+\sigma_s}\right](S_s-S_l) \tag{3.18}$$

The single component of total TEM forces $\bar{F}_{sy}$ acting on the particle is simply because TEM forces are constant within the solid:

$$\bar{F}_{sy}=2\sigma_s\,G\,B_0\left[\frac{\sigma_l}{2\sigma_l+\sigma_s}\right](S_s-S_l)\,vol \tag{3.19}$$

where *vol* is the volume of the sphere particle.

The simple estimation of TEM forces driving movements of particles are taken by equaling TEM forces expressed by 3.19 to the Stokes drag forces acting on the same particle:

$$\overline{F}_{sy} = 2\sigma_s G B_0 \left[\frac{\sigma_l}{2\sigma_l + \sigma_s}\right](S_s - S_l)\, vol = 6\pi\mu RU \qquad (3.20)$$

here, U is the estimated velocity of particle, R is the radius of particle, μ is viscosity of the surrounding melt and vol is $\frac{4}{3}\pi R^3$. Consequently, velocity of the sphere particle can be expressed:

$$U = \frac{2}{9}\frac{R^2}{\mu}\overline{F}_{sy} \qquad (3.21)$$

It is clear that the comparison between the analytically calculated velocities of sphere particles and the directly measuring ones during in-situ observation experiments can be made in two aspects. One is the dependence of the main direction of crystals' movements on the direction of applied thermal gradients and magnetic fields. The other is the exact magnitude of the velocities of movements obtained by analytical calculation and direct measurement. Actually, if the movements of crystals are really driven by TEM foces acting on them the former comparison is easy to make by in-situ observation. This is because that the change of the main direction of movements should reverse when the magnetic field or thermal gradient changes to the opposite direction. In the other aspect, comparison of exact magnitude of velocities of movements must be made after the experiments because the velocity measurements of the movements of crystals need to trace each crystal image by image. In order to make the latter comparison, use the materials properties of Al-4wt%Cu alloy list in table 3.1 velocities of TEM forces driving movements of sphere particles were analytically calculated for different magnetic flux intensities and thermal gradients. Further, the calculating results are plotted versus the diameters of the sphere particles, and the curves are shown in figure 3.10. With respect to the coordinate defined in figure 3.9 (a), positive thermal gradient means the high temperature is at the positive *z*-axis, and positive magnetic field refers that the transverse field has the same direction with *x*-axis. It can be seen that the bigger the particle is the faster its TEM forces driving movement is. The TEM forces driving movements of sphere particles can be speeded up by increasing absolute value of thermal gradients, as well as the magnetic flux intensities. Moreover, sphere particles reverse the direction of their movements when the sign of thermal gradient or magnetic field changes to the opposite.

Table 3.1 Materials properties of simulation system for TEM effect

Symbol	Unit	Solid	Liquid
S	V/K	-1.5×10^{-6}	-2.25×10^{-6}
σ	$(\Omega\cdot m)^{-1}$	7.9×10^{7}	4.0×10^{6}
μ	Pa·s		2.9×10^{-3}

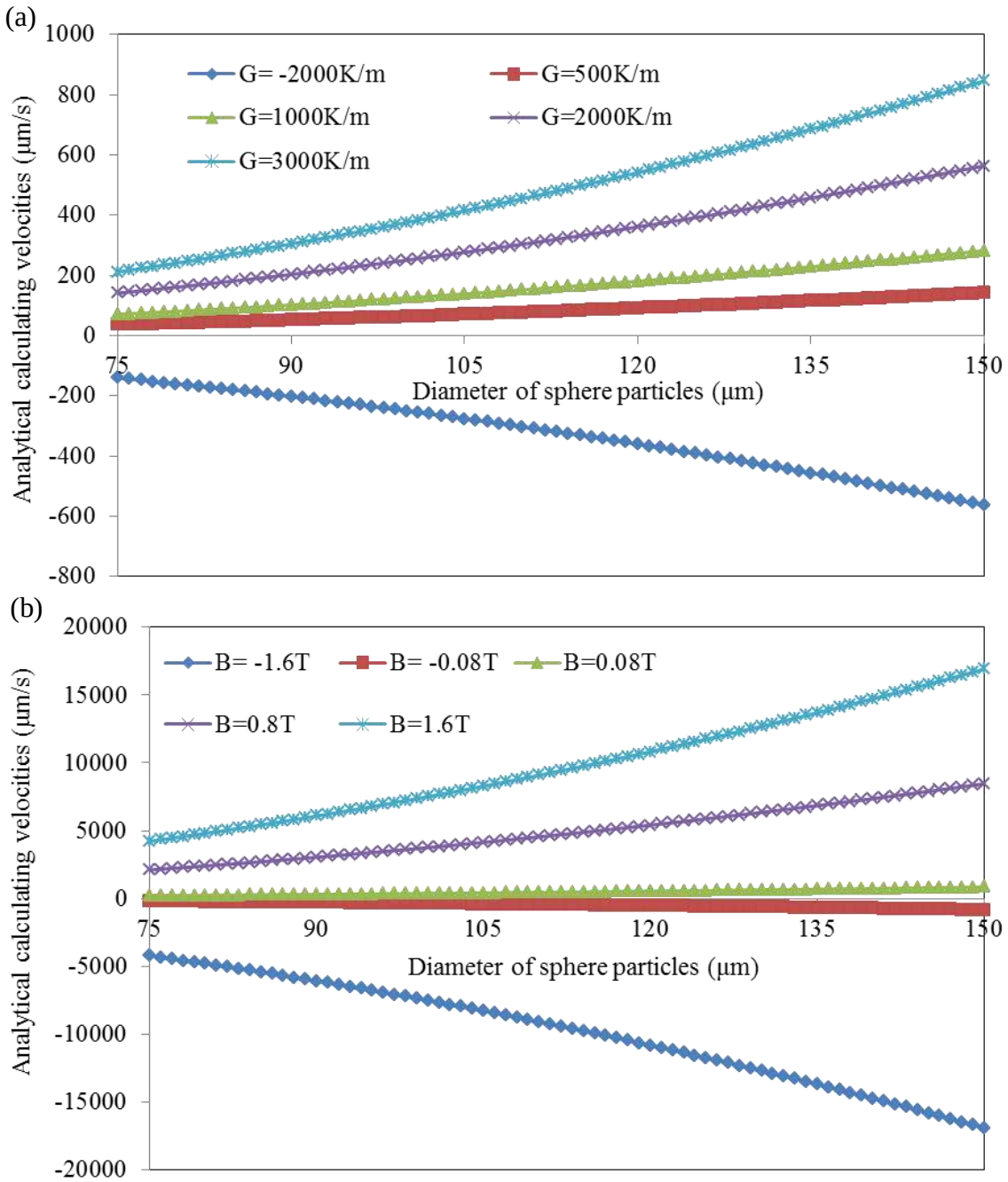

Figure 3.10 Analytical calculated velocities of particles plotted versus their diameters under different thermal gradients (a) under a 0.08T magnetic field and magnetic fields (b) under a thermal gradient of 3000K/m.

3.2.2 Velocity measurement of movements of crystals during in-situ observation experiments

According to discussions in the above paragraph, it must have been known that there are two aspects can be compared between the calculation and the in-situ observation experiments. They are the dependence of main direction of TEM forces driving movements on the direction of imposed magnetic fields or thermal gradients and the exact magnitudes of their velocities. Therefore, in-situ observation experiments are performed respectively under positive and negative magnetic fields with fixed thermal gradient of 3000K/m and with various thermal

gradients under a fixed magnetic field of 0.08T. Before give the measurement results, it should be necessary to explain how to determinate the typical diameter of crystals and measure the distance between two positions of crystal in two successive images. It will be easily understood with the help of illustrations shown in figure 3.11.

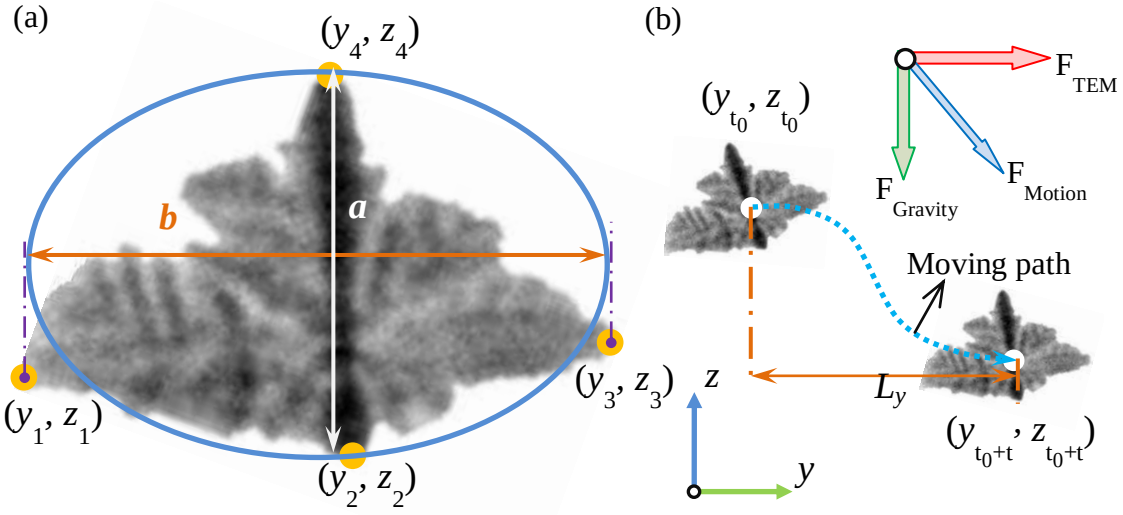

Figure 3.11 (a) Illustration of how to determinate the typical diameter of a crystal; (b) Explanation of how to measure the distance between two positions of crystal.

Figure 3.11 (a) shows a dendrite which is the common crystal observed during directional solidifications process. As shown in figure 3.11 (a), consider the two main arms of crystal as the long and the short axes of an ellipse and measure the length of these two axis to calculate the area of that ellipse as indicated by the blue solid line in figure 3.11 (a). Because the exact coordinate values of each pixel can be known by the free image analysis software named ImageJ the long and the short axis of the ellipse (*a* and *b*) can be calculated:

$$a = [(y_2 - y_4)^2 + (z_2 - z_4)^2]^{1/2} \tag{3.22}$$

$$b = [(y_1 - y_3)^2 + (z_1 - z_3)^2]^{1/2} \tag{3.23}$$

Calculate the area of this ellipse and equal it to the area of a circle:

$$\pi ab = \pi r^2 \tag{3.24}$$

Then we can assigned the typical diameter of the crystal shown in figure 3.11 (a) as 2*r*. Moreover, because the resolution used here is 7.46×7.46μm^2, the exact typical diameter can be obtained by 2*r*×7.46μm.

When the typical length of crystals has been decided, it it the time to measure the distance between two positions of the cyrstal recorded in two successive images. With respect to the coordinates defined in figure 3.9 (a), the field of view obtained during in-situ observation experiments is in the *y*-*z* plane as indicated in figure 3.11 (b). Appoint the geometrical center of crystals representing their positions, as marked by the white points in figure 3.11 (b), the precise distance between two positions of the crystal can be obtained

because the exact coordinate values of the geometrical centers of crystals can be given by ImageJ as well. The interval, *t*, between two successive images can be known automatically during experiments. Movement velocities of the crystal, *V* (μm/s), can be approximately calculated:

$$V = \frac{7.46[(y_{t_0+t} - y_{t_0})^2 + (z_{t_0+t} - z_{t_0})^2]^{1/2}}{t} \tag{3.25}$$

Indeed, only the *y*-axis direction speed of the movements of crystals can be compared because the total length of the moving path of a crystal like drawing by the blue dotted line in figure 3.11 (b) can not be got. Therefore, the *y*-axis direction speed should be calculated:

$$V_y = \frac{L_y}{t} = \frac{7.46(y_{t_0+t} - y_{t_0})}{t} \tag{3.26}$$

In another aspect, the previously analytical calculation of movement velocities of sphere particles are also *y*-axis direction speed only because the calculation did not take the effect of gravity into account as well.

The main movement direction of crystal can be revealed by a figure that is projected from several successive images containing the same crystal but at different positions as shown in figure 3.12. Figure 3.12 (a) is projected from 9 images, which displays the moving path of the crystal under a positive thermal gradient of 3000K/m and a 0.08T transverse magnetic field. More distinctly, region marked by a white rectangle in figure 3.12 (a) is magnified and shown in figure 3.12 (b), in which the white dotted line with arrows indicates the real moving path of the crystal, and the angle between the main direction of the movement marked by the yellow arrow and *y*-axis is defined as Φ. Similarly, moving path of the crystal under the same thermal gradient but a -0.08T transverse magnetic field is shown in figure 3.12 (c) that projected from 5 successive images. It can find that the angle between main direction of movement of this crystal and *y*-axis is π-Φ. These demonstrate that the crystals reversed their moving direction when the imposed magnetic fields changed to the opposite direction.

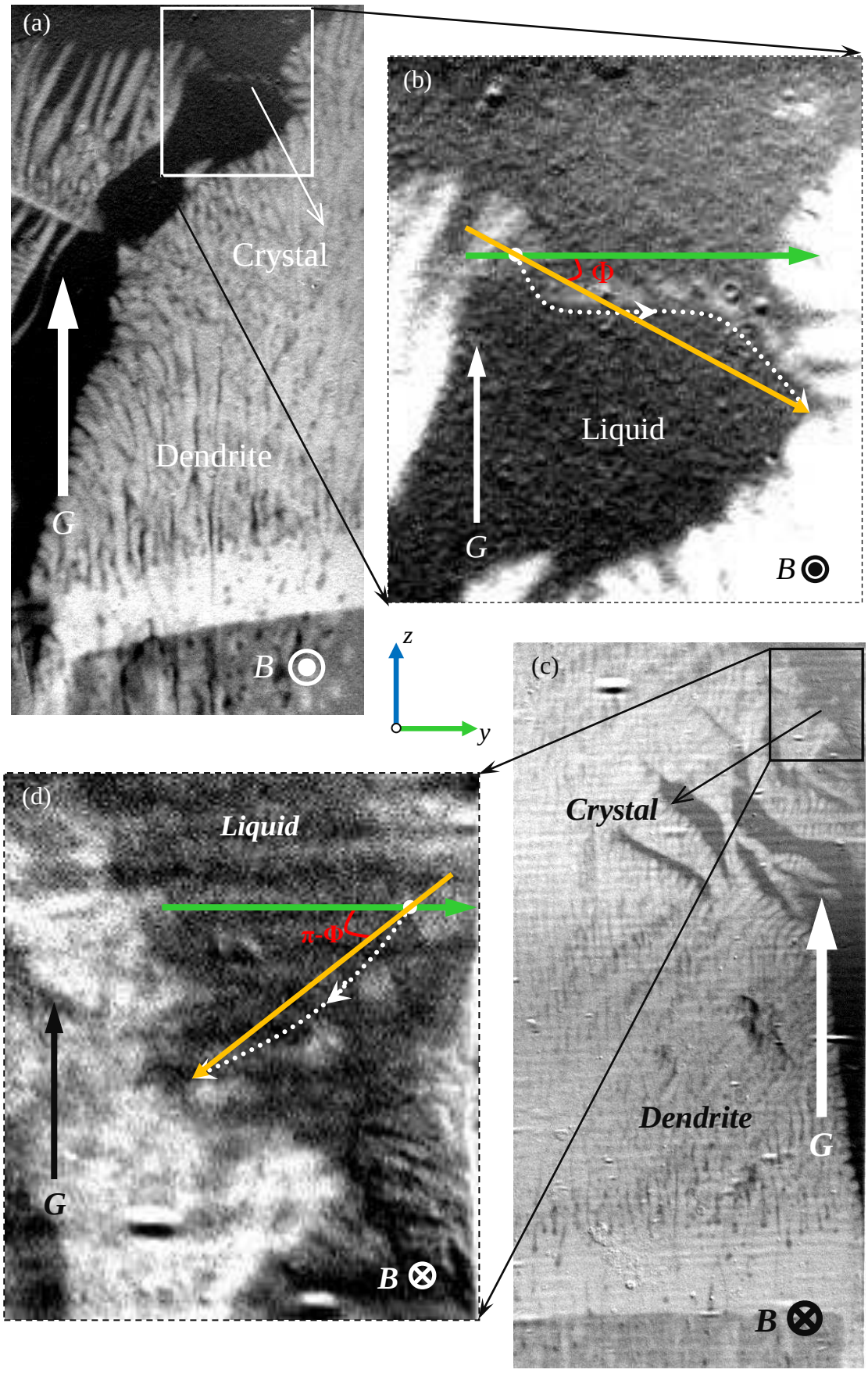

Figure 3.12 Pictures obtained by projecting successive images with the concerned crystal that captured during directionally solidifying Al-4wt%Cu alloys under (a) and (b) a 0.08T transverse magnetic field, (c) and (d) a -0.08T transverse magnetic field. (G=3000K/m, Cooling rates are the same that 2K/min)

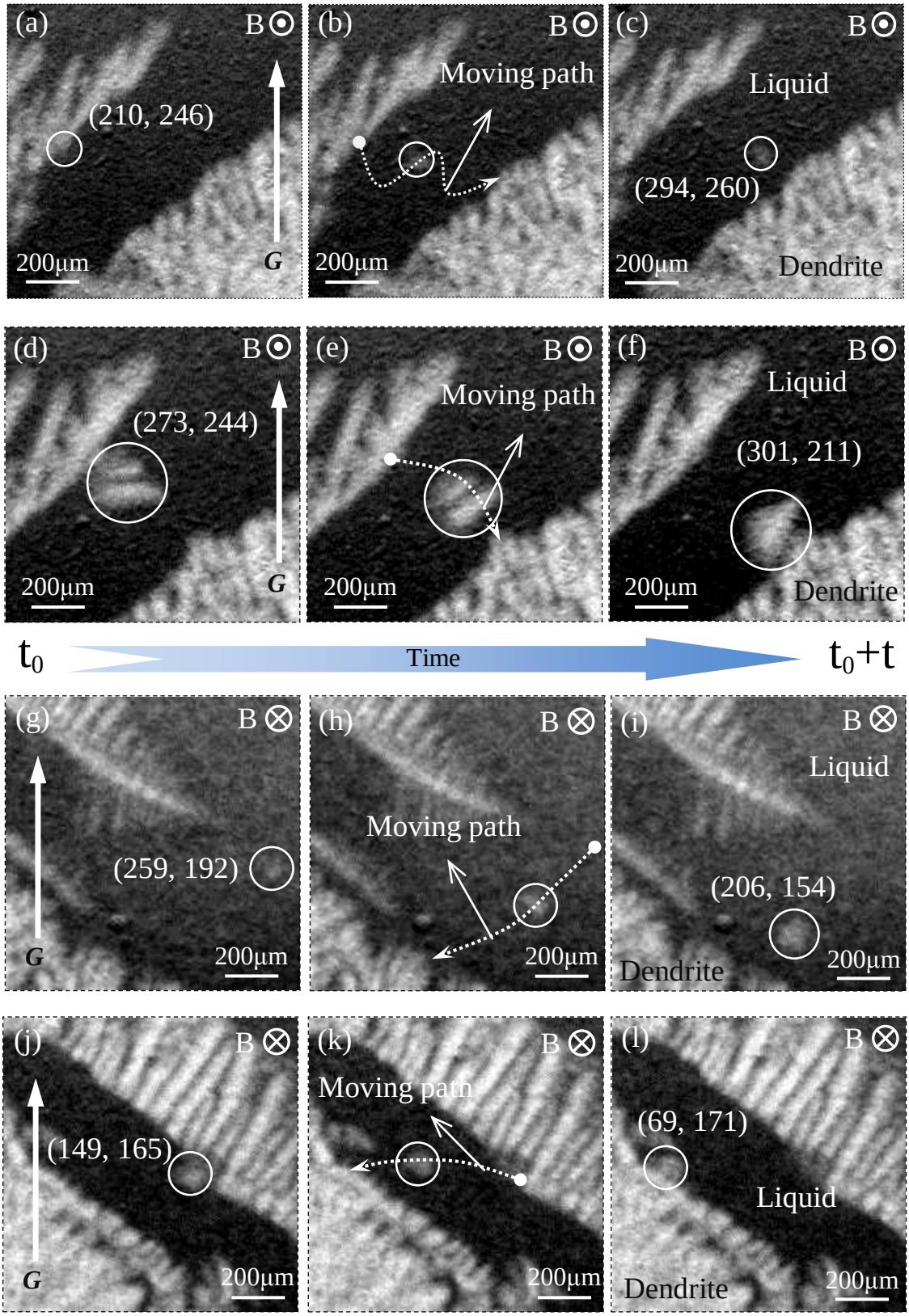

Figure 3.13 Examples of measuring the exact magnitudes of velocities of crystals' movements during directionally solidifying Al-4wt%Cu alloys under transverse magnetic fields. (a-c) B=0.08T, typical diameter is 93.2μm; (d-f) B=0.08T, typical diameter is 126.8μm; (g-i) B=-0.08T, typical diameter is 116.1μm; (j-l) B=-0.08T, typical diameter is 107.6μm. (*G*=3000K/m, Cooling rates are the same that 2K/min)

The exact magnitudes of movement velocities of crystals are carefully measured. Several free crystals were observed during experiments. Using the method introduced by figure 3.11, the velocity measurements were made on all of them. Upon each of the moving crystals, its final typical diameter is defined as the mean value of typical diameters obtained from all relevant images. Likewise, the mean value of velocities of a crystal achieved from every two successive images is regarded as its real velocity. Figure 3.13 (a) to (c) is the process of measuring a crystal with 93.2μm in diameter, and the crystal typical diameter is 126.8μm in (d) to (f). Reverse the magnetic field direction, figure 3.13 (g) to (i) show the crystal with 116.1μm in diameter, and the typical diameter of crystal in (j) to (l) is 107.6μm. Further, these measured movementvelocities of crystals are plotted versus their typical diameters and shown in figure 3.14. It can be concluded that the big crystals have higher velocities than the small ones. Moreover, whatever the size of the crystals their movement velocities seem proportional to about the square of their typical diameters, which agrees with the analytical solutions.

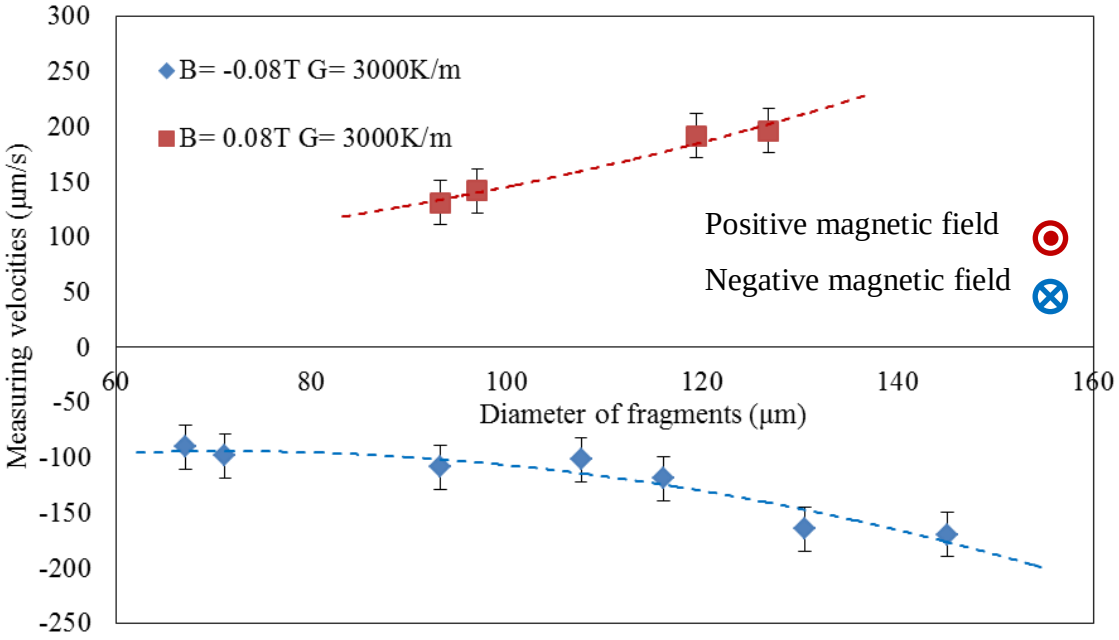

Figure 3.14 Curves of measured movementvelocities of crystals plotted versus their typical diameters under positive and negative transverse magnetic fields and fixed positive thermal gradient of 3000K/m.

Based on the introductions of TEM effect in chapter 2 and the analytical calculations in this chapter, it can been known that the main direction of TEM forces driving movements of sphere particles does not only depend on the direction of imposed magnetic fields but also the direction of applied thermal gradients. Al-10wt%Cu alloys were directionally solidified with thermal gradients applied in different directions in order to examine the dependence of main directions of the movements of crystals on the direction of applied thermal gradients. Projecting 35 successive images captured during experiment under a negative thermal gradient into a figure, the main direction of movements of the crystal is unfolded. As shown

in figure 3.15 (a), path of each crystal is pointed out by the red arrows, and their main direction is marked by the yellow one. Kept the other conditions fixed, similar experiment was conducted without any thermal gradients (figure 3.15 (b)), it can find that crystals vertically sink down because they are heavier than the surrounding melt. Moreover, it can be revealed from figure 3.15 (c) that positive thermal gradient makes crystals moving from the right of the sample to the left. According to these observations, it should be clear that once the direction of applied thermal gradient is reversed the main direction of the movements of crystals turns to the opposite as well, and more, the horizontal movements of crystals must be casued by the applied thermal gradient and the imposed magnetic field together. In fact, the only result of the interaction between thermal gradient and magnetic field is TEME in the context of the present experiments. Additionally, influences of the magnitude of thermal gradients were also investigated. Figure 3.16 (a) to (c) respectively gives the projected figures showing the movement paths of crystals under a -0.08T transverse magnetic field and thermal gradients with different magnitudes. In these cases, as indicated by red arrows in each figure, the main directions of the movement of crystals are the same that from the right of sample to the left. Further, the angle between the main direction and the *y*-axis can be obtained as indicated by the yellow arrows crossing over the green one in figure 3.16. Indeed, based on the balance of forces acting on a crystal as illustrated in figure 3.12 (b), such angle is capable to represent the magnitudes of TEM forces acting on crystals because this angle is the tangent function of the gravity of a crystal and the TEM forces acting on it. Therefore, it can find that TEM forces acting on the crystals increase when the magnitude of thethermal gradient is elevated as well.

Upon the velocity measurement of the movements of crystal, solidification of Al-10wt%Cu provides more data to make the comparison with the analytical calculations. Velocity measurements were made only on the crystals with small change of their size during the whole solidification process in order to enhance the accuracy. Similar to figure 3.13, figure 3.17 gives four examples of velocity measurements in four different experiments. Applied different thermal gradients these experiements were conducted under fixed transverse magnetic field of -0.08T and with the same cooling rates of 2K/min. For each case, three different positions of a crystal captured during the in-situ observation experiments are respectively shown in three successive figures. Figure 3.18 shows curves of the measuring velocities of the movements of crystals plotted versus their typical diameters. It suggests that the velocities of crystals increase with the increasing of the magnitudes of thermal gradients. Moreover, it can be found that the velocities of crystals seem approximately proportional to

the square of their typical diameters, which agrees with the conclusion revealed from figure 3.14 and the analytical calculations.

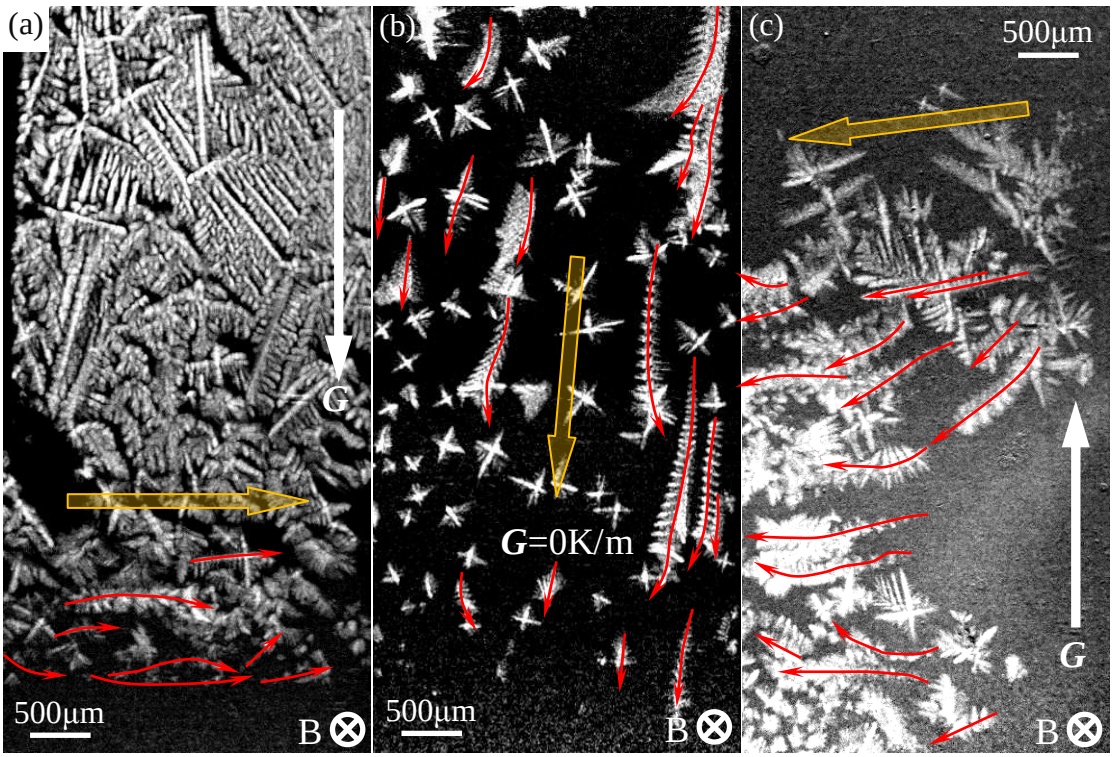

Figure 3.15 Projecting figures of crystals' movements with different directions thermal gradients. (a) *G*=-2000K/m; (b) *G*=0K/m; (c) *G*=2000K/m. (B=-0.08T; Cooling rates are the same that 2K/min)

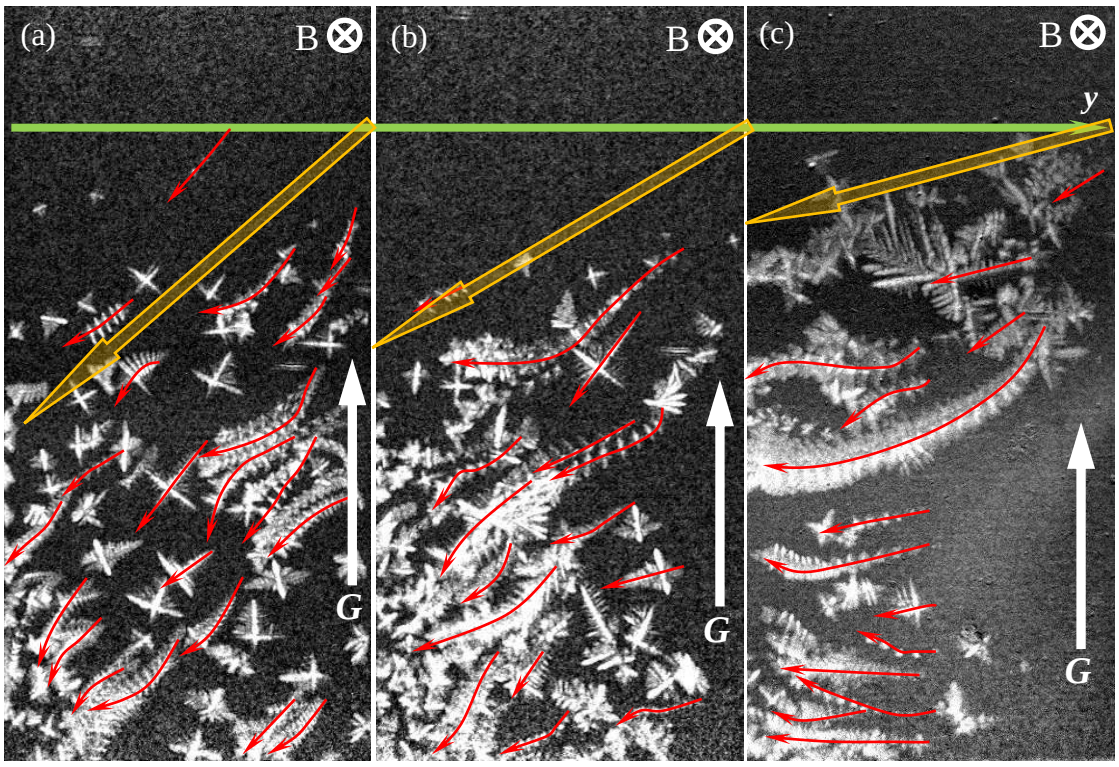

Figure 3.16 Projecting figures of crystals' movements with different magnitudes thermal gradients. (a) *G*=500K/m; (b) *G*=1000K/m; (c) *G*=2000K/m. (B=-0.08T; Cooling rates are the same that 2K/min)

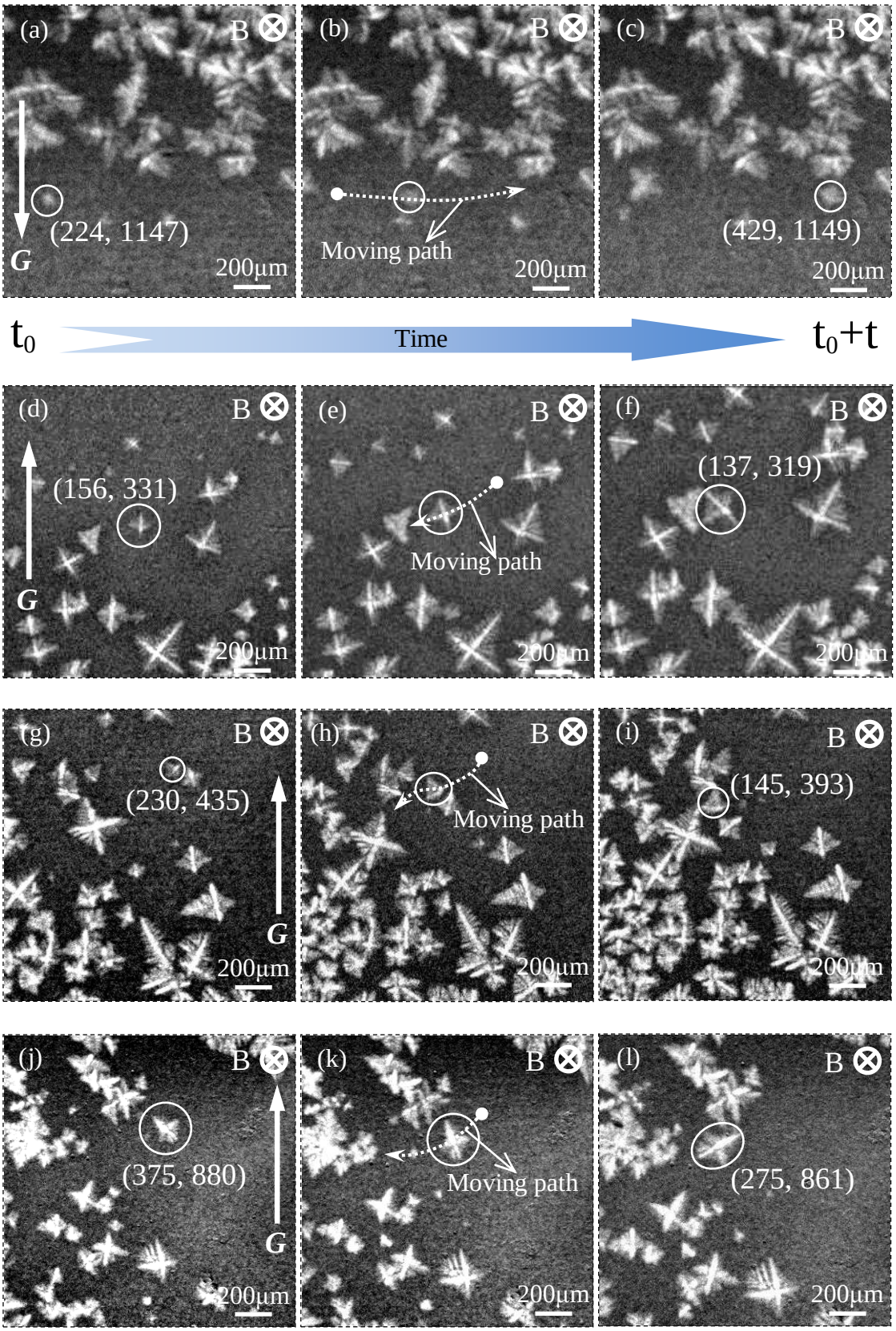

Figure 3.17 Examples of measuring the exact velocities of crystals' movements during directionally solidifying Al-10wt%Cu alloys with different thermal gradients and the same transverse magnetic field of -0.08T. (a-c) *G*=-2000K/m; (d-f) *G*=500K/m; (g-i) *G*=1000K/m; (j-l) *G*=2000K/m. (Cooling rates are the same that 2K/min).

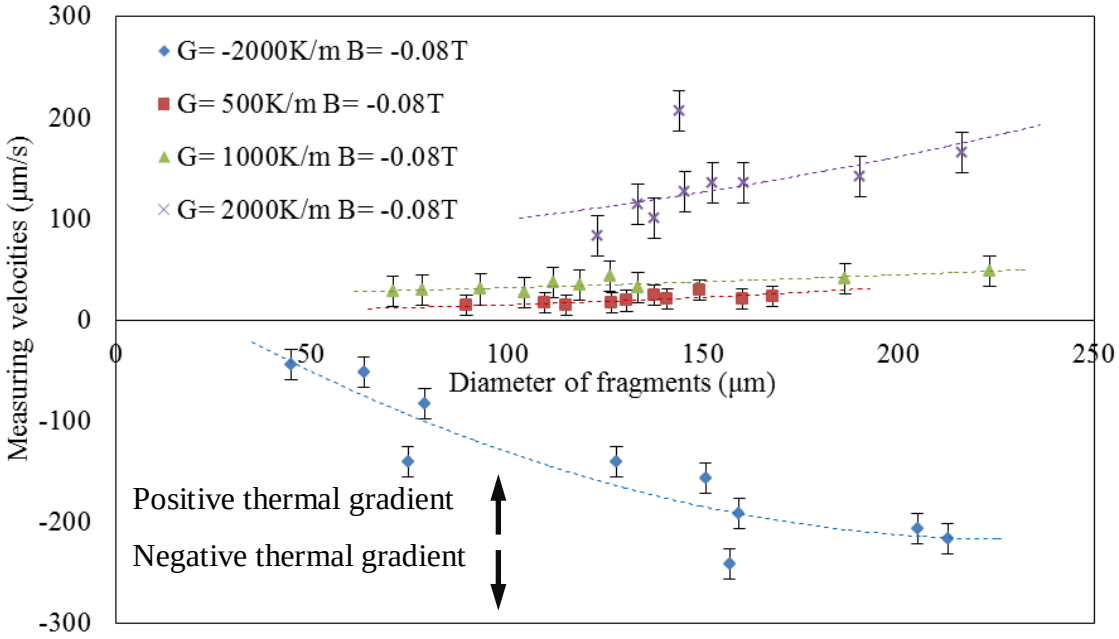

Figure 3.18 Curves of measuring velocities of the movements of crystals plotted versus their typical diameters under different applied thermal gradients and fixed transverse magnetic field of -0.08T.

3.2.3 Comparison of analytical calculations and in-situ measurement results

Because the analytical calculations of the movements of sphere particles are based on the assumption that the driving forces are only the TEM forces acting on them the existence of TEM forces in solid can be confirmed if the observed movemements of crystals perfectly are consistent with the analytical calculations. Further, we can argue that TEM forces are in-situ and real time observed as well. For these reasons, comparison between the analytical calculations and in-situ measurement results are made in two aspects. One is the dependence of main direction of the movements of crystals on the given conditions, such as the direction of imposed magnetic fields and applied thermal gradients. The other is examining whether or not the movement velocities of crystals obtained by measuring can be comparable to the calculated velocities of TEM forces driving movements of sphere particles. As shown in figure 3.19, the former comparison can be made by a new coordinate consisting of the velocity acting as *y* axis and thermal gradient acting as *z* axis. Besides, it should be pointed out that '*U*' in figure 3.19 refers to velocity obtained by analytical calculation and 'V_y' stands for velocity achieved by in-situ measurements, and both of them are represented by the velocity axis in the new coordinate. Based on this ccordinate, comparison of the calculated and measured main direction of the movement of crystals is easy to make. For example, under conditions given in the first quadrant that the applying magnetic field and thermal gradient are both positive, both of the calculated and measured main directions of the movement of crystals are the same and in positive *y*-axis direction. Similarly, look upon the cases belong to

the second and the fourth quadrant of this coordinate, it can draw the same conclusion that the main directions of the movements of crystals achieved by both analytical calculation and in-situ measurement are the same. In another aspect, comparison between the cases respectively belongs to the first and the second quadrant shows that the crystals turn their movement directions when the magnetic field is reversed. Comparison between cases respectively belongs to the second and the forth quadrant of this coordinate indicates that the crystals also reverse their movement directions when the thermal gradient is applied in the opposite direction. Therefore, it can say that the main directions of the movements of crystals and their dependences on the given conditions are consistent no matter they are achieved by analytical calculations or in-situ measurements. This ensures us to conclude that the movements of crystals during directional solidification of Al-Cu alloys under an external transverse magnetic field must be driven by the TEM forces acting on them.

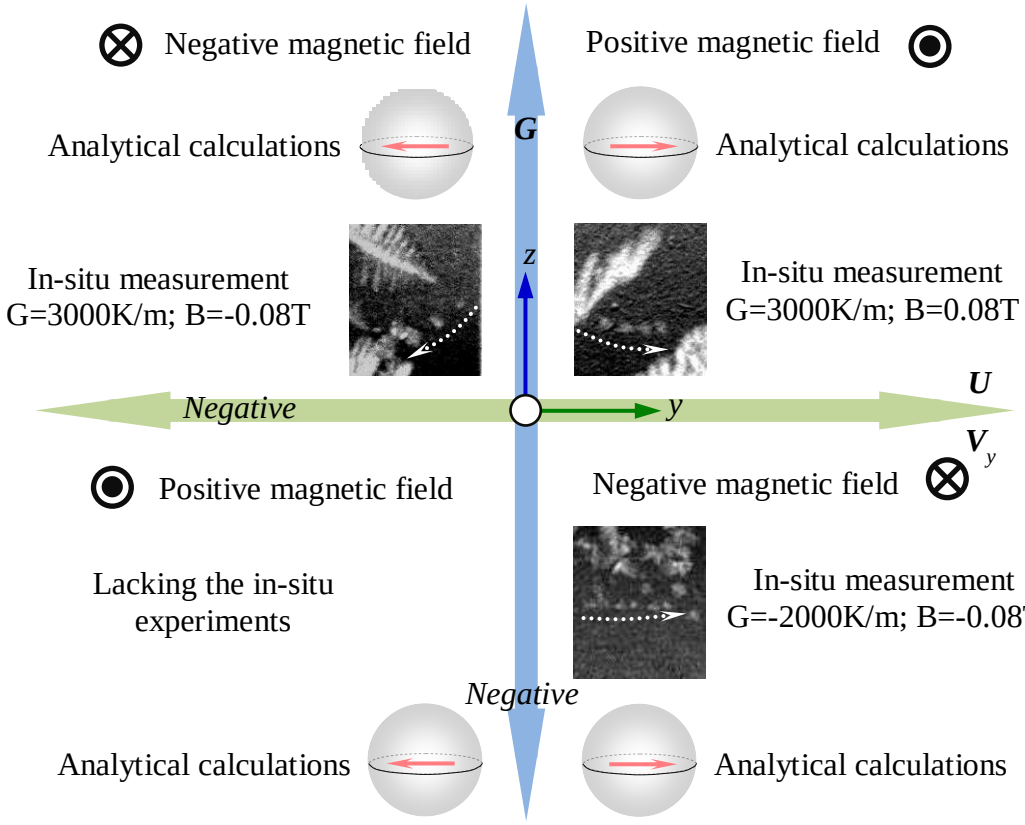

Figure 3.19 Comparisons of dependence of the main directions of crystals' movements on the direction of applied thermal gradients and magnetic fields obtained by analytical calculations and in-situ measurement.

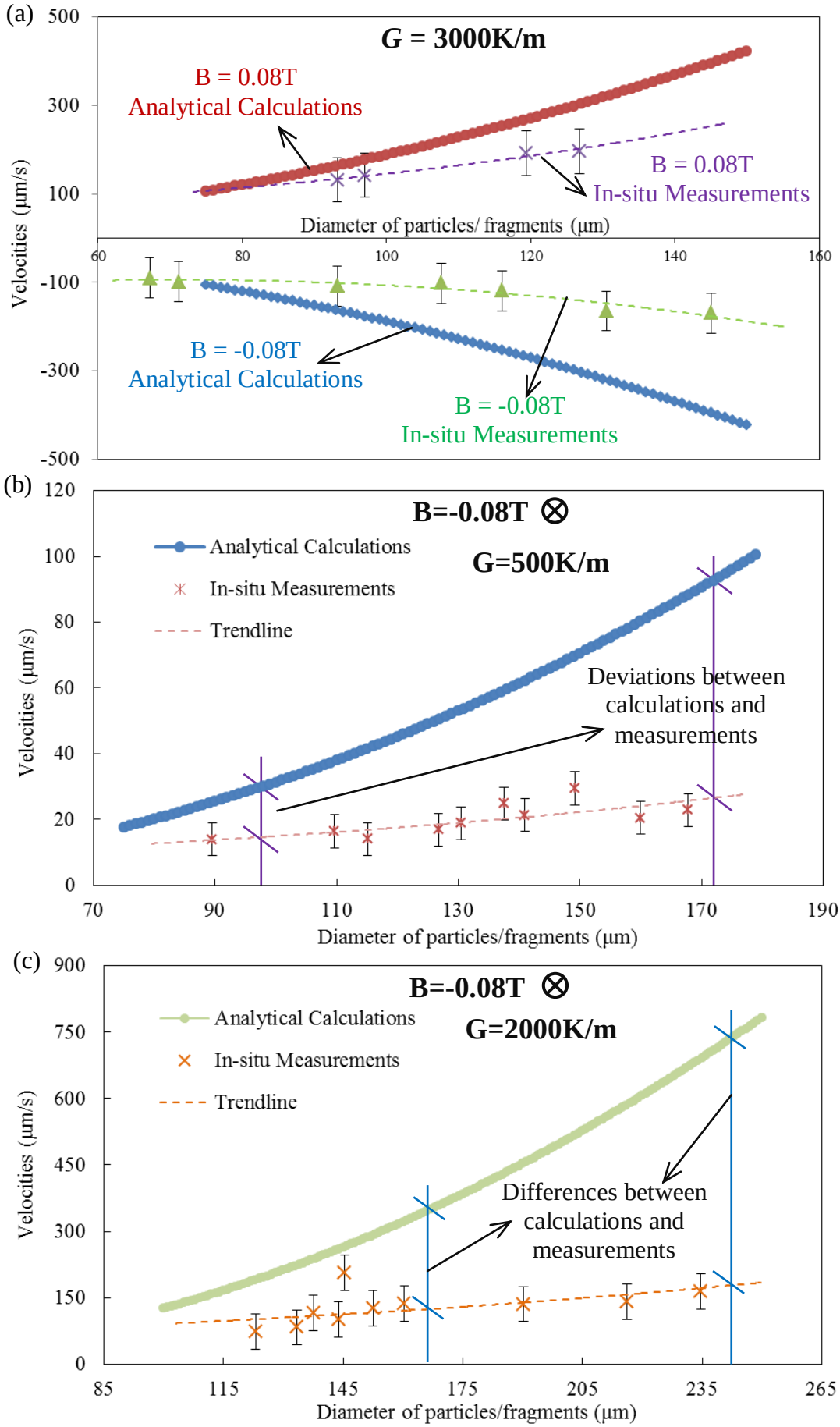

Figure 3.20 Comparisons of velocities obtained by analytical calculations and in-situ measurements under (a) transverse magnetic fields in opposite directions and various thermal gradients that (b) 500K/m and (c) 2000K/m.

On the other aspect, comparisons of velocities of crystals' movements were made. Figure 3.20 shows curves of both analytically calculating and in-situ measuring velocities plotted respectively versus the diameter of sphere particles and the typical diameters of crystals. Figure 3.20 (a) gives the velocities obtained under transverse magnetic fields in the opposite directions and with the fixed 3000K/m thermal gradient. Figure 3.20 (b) and (c) reveal velocities achieved under fixed transverse magnetic field of -0.08T and different thermal gradients of 500K/m and 2000K/m respectively. In figure 3.20 (a), positive velocities mean the sphere particles or crystals move toward to the positive *y*-axis direction, and negtive ones stand for they move to the opposite directions. Therefore, figure 3.20 (a) can manifest the dependence of main directions of the movements of crystals on the given conditions as well. The same conclusion as the one obtained from figure 3.19 can be drawn again. When look upon the velocity magnitudes of movements, deviations between analytical calculations and in-situ measurements must come to your eyes. More precisely, the velocities of crystals measured through the in-situ observation are slower than velocities of TEM forces driving movements of sphere particles obtained by analytical calculations. In fact, those deviations are reasonable because the very thin crucible (about 200μm) should more or less block the movements of crystals with the typical diameters of about 50μm to150μm but the analytical calculations did not take this into account. In another aspect, those deviations becoming bigger when the typical diameter is close to crucible's thickness as indicated in figure 3.20 (b) and (c) can also prove this wall blocking effect. For this reason, it can say that the movements of crystals observed during in-situ experiments have comparable velocities with the analytically calculated TEM forces driving movements of sphere particles. The conclusion that TEM forces in solid exist and drive the crystals to move during directionally solidifying the Al-Cu alloys under a static transverse magnetic field thus is confirmed further.

Up to now, based on the analytical calculations of TEM forces driving movements of sphere particles, the in-situ measurement of the movements of crystals during directionally solidifying the Al-Cu alloys under a static transverse magnetic field and the comparisons between them, it can be confident to conclude that TEM forces in solid do exist and respond to the movements of crystals. It can also say that TEM forces are in-situ and real-time observed.

3.3 In-situ observation of thermoelectric magnetic (TEM) flows

After directly seeing the effect of TEM forces in solid, it should step to the second phenomenon of TEME that TEM flows. Indeed, confirmation of TEM flows can be regarded as another evidence for the existence of TEM forces because TEM flows are produced by the

TEM forces in liquid. Similar to the forces, directly seeing the flows in melt by synchrotron X-ray imaging method is difficult as well. This is becaue the contrast used by X-ray radiography mainly comes from the different absorption abilities of the different compositions and densities of subjects. Although flows influence the mass transfer and then cause composition difference, such differences are not sufficient to achieve the clear contrast. Considering the solid and liquid phases can be distinguished clearly by synchrotron X-ray imaging, it is easier to detect if the liquid-solid interface are changed. Therfore, if some modifications of liquid-solid interface caused directly by the TEM flows during directional solidification can be seen, we can consider TEM flows to be in-situ observed as well. According to the widely accepted fact that the shape of liquid-solid interface during directional solidification is determined by the local solute distribution and temperature field [272-274], it can know that interface shape should be changed if the composition of nearby melt and temperature field is changed. Therefore, provided TEM flows appear near the interface the original composition and temperature field in front of the interface must be changed, and as well as the initial liquid-solid interface shape. Particularly, the shape change of interface can be apparently observed when it is planar. For these reasons, the directional solidification of Al-4wt%Cu with fixed thermal gradient in the presence and absence of a transverse magnetic field were taken and in-situ observed. However, whether TEM flows can appear or not under the available experimental conditions should be analyzed in advance.

3.3.1 Simulations of TEM flows in in-situ experiments

On account of discussions in chapter 2, TEC definitely exists during directional solidification of metallic alloys because most of their liquid and solid have different ATP. When these currents meet an external magnetic field, TEM forces can be produced and exist in both solid and liquid. However, based on the hydrodynamics theory, the flows can be driven only if the forces in fluid are not curl-free. Therefore, TEM flows cannot be driven at all if TEM forces in liquid are curl-free. Consider so, it is necessary to calculate the curl of TEM forces in liquid under the conditions that in-situ experiment can provide. Based on the introductions of experimental device in chapter 3.1, it can know that the imposed transverse magnetic field is parallel to *x*-axis and perpendicular to the *y*-*z* plane as shown in figure 3.6. Under this arrangement, the curl of TEM forces in liquid can be calculated:

$$\nabla \times \vec{F_l} = \nabla \times [\vec{j_l} \times B\vec{i_x}] = B\vec{i_x} \times (\nabla \times \vec{j_l}) \tag{3.27}$$

Since we have:

$$\vec{j_l} = -\sigma_l \vec{V_l} - \sigma_l S_l G\vec{i_x} \tag{3.28}$$

here, V_l is electrical potential in liquid, and the curl of $\vec{j_l}$ is zero, accordingly:

$$\nabla \times \vec{F_l} = 0 \tag{3.29}$$

Meanwhile, note that the TEM forces in liquid are divergence free as well:

$$\nabla \bullet \vec{F_l} = \nabla \bullet [\vec{j_l} \times B\vec{i_x}] = B\vec{i_x} \bullet (\nabla \times \vec{j_l}) = 0 \tag{3.30}$$

It can be concluded from above analysis that the curl of TEM forces would not be curl-free only if S_l is not constant. Although S_l varies with melt composition, it is almost neglectable within one melt. This seems to break our wish for directly observing TEM flows. However, before entirely deny this proposal, it would be better to numerically simulate the TEM flows fields and then to confirm the validaty of the conclusion that TEM forces in liquid under conditions in-situ experiments can provide are unable to produce TEM flows.

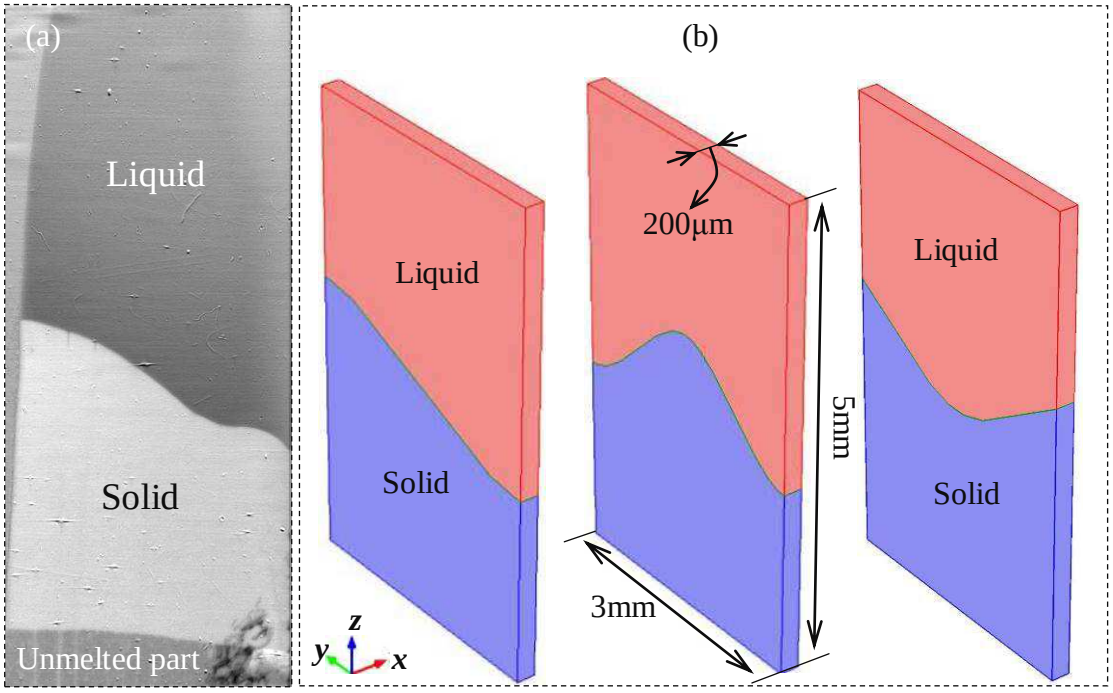

Figure 3.21 (a) Liquid-solid interface shape obtained during in-situ observation of directionally solidifying Al-4wt%Cu alloys without magnetic field; (b) Geometries of sideling, convex and concave interface and the dimensions.

Based on the shape of liquid-solid interface shown in figure 3.21 (a) that obtained by our collaborators during their no field experiments, three different interface shapes were chosen to cover as many kinds of shapes as possible. As shown in figure 3.21 (b), they are sideling, convex and concave interfaces, and the dimensions of the whole simulating domain are given in this figure as well. Mesh method used for these three different interface shapes is the same, so only the meshes for the sideling interface case are given in figure 3.22 as an example. These finer triangular meshes were created via selecting the fluid flow phenomenon as the controlling condition in COMSOL, and the region near liquid-solid interface was refined as shown in figure 3.22. More clearly, figure3.22 (b) gives the magnified view of the region

indicated by the green box in figure 3.22 (a), in which, red surface emphasizes the sideling liquid-solid interface. With the same parameters listed in table 2.2, the COMSOL predefined electric current, thermal transfer and fluid flow modules are selected and coupled to simulate the TEM flows field produced by the conditions that in-situ experiments can provide.

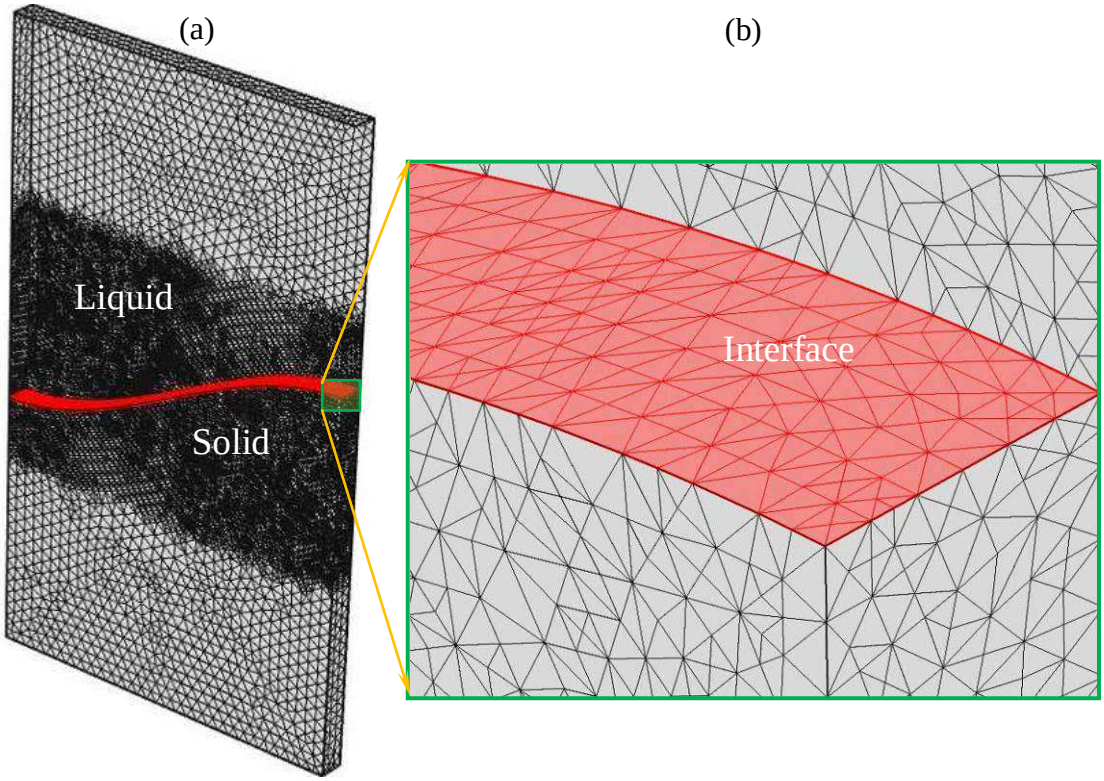

Figure 3.22 Example of meshes used in simulations of TEM flows field under conditions that in-situ experiments can provide.

The computed results obtained with three different interface shapes are shown in figure 3.23. In figure 3.23 (a), (c) and (e), colored slices give the thermoelectric potential generated by a thermal gradients of 3000K/m, gray streamlines reveal the corresponding TEC and red arrows denote the TEM forces produced by a transverse 0.08T magnetic field interacting with the TEC. The arbitrary distribution of red arrows suggests that TEM forces are curl-free. Colored slices shown in figure 3.23 (b), (d) and (f) give the magnitude of the velocities of TEM flows. Dark blue color in the solid domains means no flows there, which verifies the validity of the simulation method used again. According to the color legends, it can find that even the highest velocity is negligible because it is less than 1 μm/s. This indicates that TEM forces in liquid cannot drive any TEM flows under conditions that in-situ experiments can provide. In addition, the computed TEM flows fields represented by the random distributing red arrows in figure 3.23 (b), (d) and (f) also suggest that TEM flows do not appear under these conditions.

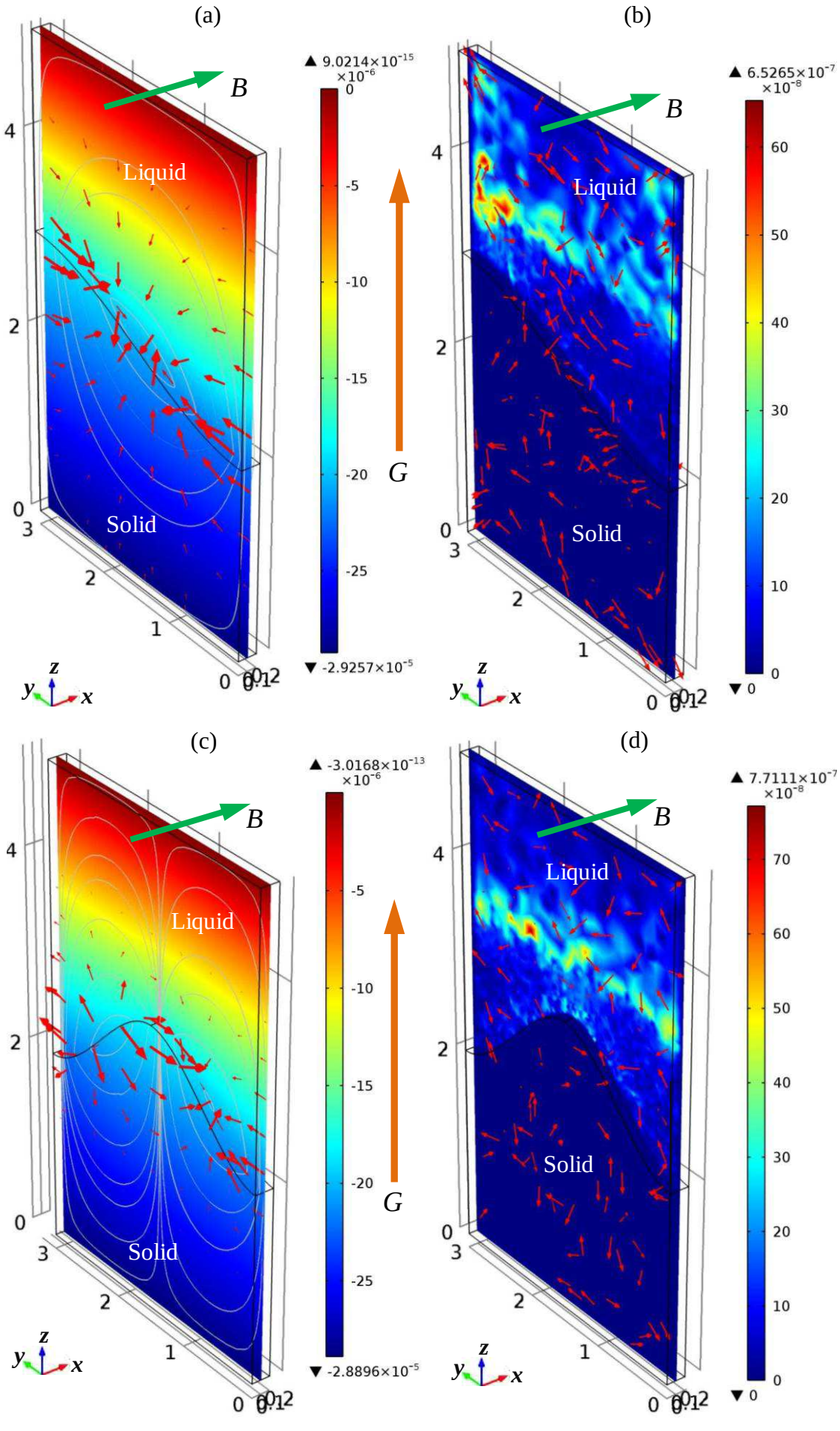
(a)
(b)
(c)
(d)
B
G
Liquid
Solid
▲ 9.0214×10⁻¹⁵
×10⁻⁶
0
-5
-10
-15
-20
-25
▼ -2.9257×10⁻⁵
▲ 6.5265×10⁻⁷
×10⁻⁸
60
50
40
30
20
10
0
▼ 0
▲ -3.0168×10⁻¹³
×10⁻⁶
▼ -2.8896×10⁻⁵
▲ 7.7111×10⁻⁷
×10⁻⁸
70
z
y
x

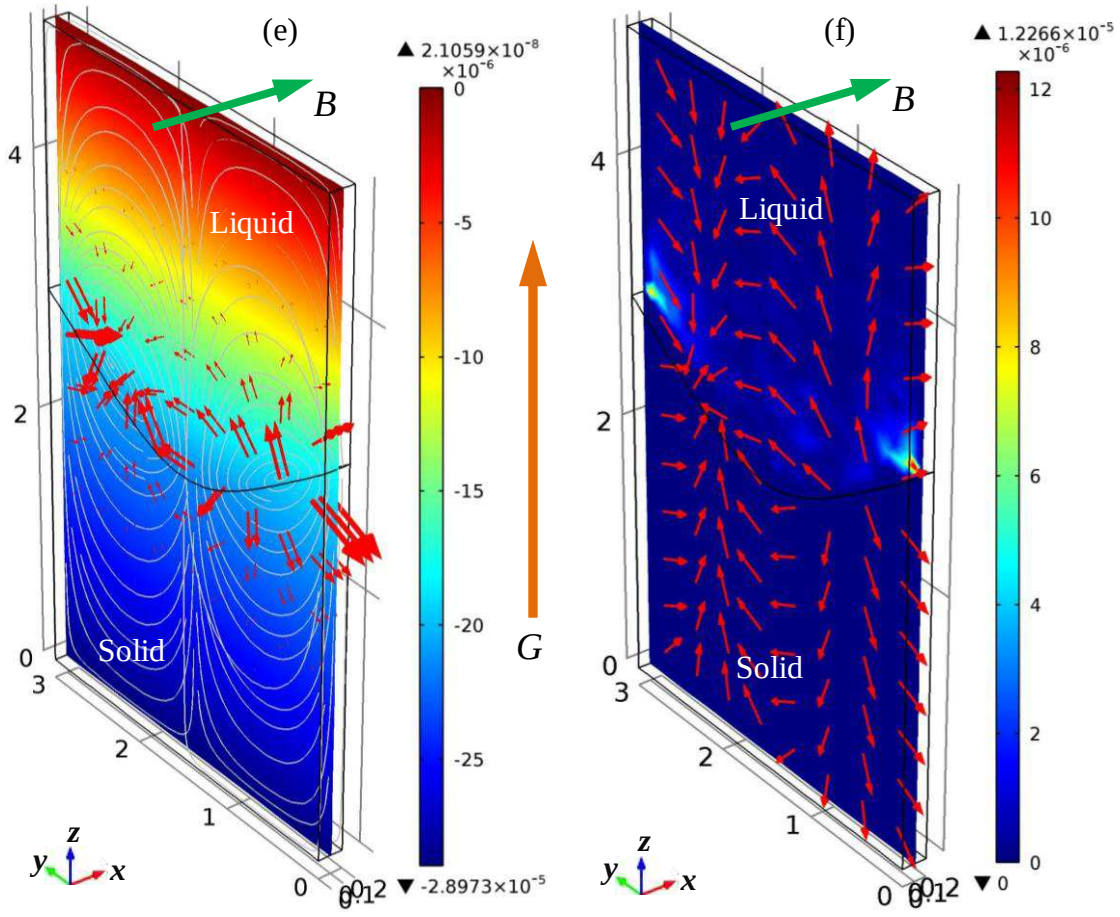

Figure 3.23 Computed thermoelectric potential denoted by colored slice, TEC represented by streamlines and TEM forces referred by red arrows: (a) Sideling interface case; (b) Convex interface case; (e) Concave interface case, and their corresponding TEM flows fields indicated by the colored slices and red arrows are respectively shown in (b), (d) and (f). Units for legends in (a), (c) and (e) are V, and those for legends in (b), (d) and (f) are m/s. (B=0.08T, G=3000K/m)

Until now, it seems that wish for in-situ observing TEM flows should be broken down because both the calculation of the curl of TEM forces in liquid and simulations of TEM flows with the conditions that in-situ experiments can provide show no flows can appear. Fortunately, the reality is always not so ideal, such as the liquid-solid interface cannot be perfectly flat in the *x*-axis direction as indicated in figure 3.22. Indeed, the calculation of the curl of TEM forces in liquid and the simulations of TEM flow fields are pure 2D problems if interfae is perfectly flat in *x*-axis direction as in figure 3.24 (a). Therefore, the uneven liquid-solid interface in *x*-axis as described in figure 3.24 (b) to (d) may provide us another possibility to have TEM flows under the present experimental conditions. In order to examine this idea, simulations using those more realistic interface shapes were taken. The interface shape in *x*-*z* plane cannot be known during in-situ experiment because the view field is in *y*-*z* plane. Moreover, because the experimental apparatus cannot realize the quenching process, interface shape in *x*-*z* plane cannot be revealed by post-mortem method as well. For these

reasons, three different interface shapes in *x*-*z* plane as shown in figure 3.24 (b) to (d) were used in order to cover all the possibilities.

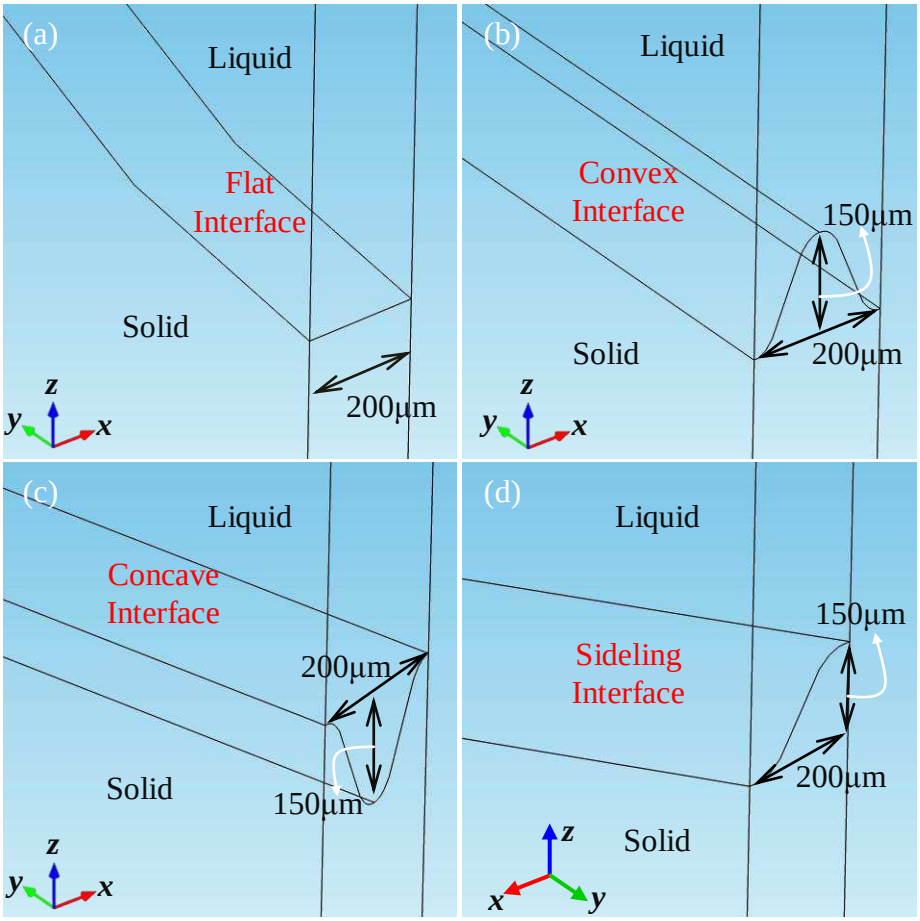

Figure 3.24 (a) Interface is flat in *x*-axis direction; (b) Interface is convex in *x*-axis direction and its dimensions; (c) Interface is concave in *x*-axis direction and its dimensions; (d) Interface sideling in *x*-axis direction and its dimensions.

Geometries with three different interface shapes in *x*-*z* plane were meshed with the same method. Therefore, only an example of them is given in figure 3.25. Fine triangular meshes were created under the control of fluid flow phenomenon, and meshes near the interface are refined as shown in figure 3.25 (b). Moreover, ten 5μm thickness boundary layers were added to the liquid-solid interface as revealed in figure 3.25 (c) in case the complex flow fields appear at the vicinity of the interface. Concerning the noises indicated from figure 3.23, simulations of TEC were performed with both normal and extremely fine meshes. Computed results show no apparent difference. Therefore, it is reasonable to neglect the system noises. Useing the same parameters listed in table 2.2 and combining the COMSOL predefined electric current, heat transfer and fluid flow modules, TEC, TEM forces and TEM flows were simulated with a thermal gradient of 3000K/m and a 0.08T transverse magnetic field. Figure 3.26 shows *z*-component of TEC in (a), *y*-component of TEM forces in (b) and the magnitude of the velocities of TEM flows in (c). It can find that TEME in these cases mainly concentrates in the region near liquid-solid interface. Therefore, in the following parts the

details of computed results are given in this region only. Figure 3.26 (d) shows how TEC distributes around the liquid-solid interface with convex shape in *x*-*z* plane, and (e) is the view seen from *x*-*z* plane. This figure shows that TEC circuit is in *x*-*z* plane at the vicinity of interface. TEM forces in solid and liquid are displayed respectively in figure 3.26 (f) and (g), which reveal that TEM forces in solid all point to negative *y*-axis direction and they are toward to the opposite direction in liquid. In addition, figure 3.27 shows the results that TEC and TEM forces simulated with liquid-solid interface being concave and sideling in *x*-*z* plane respectively. Together the results shown in figure 3.26, it can conclude that the shape of liquid-solid interface in *x*-*z* plane has no influence on the districbution of TEC and the direction of TEM forces, but uneven interface in *x*-*z* plane is indispensable for the occurence of TEME under the present experimental conditions.

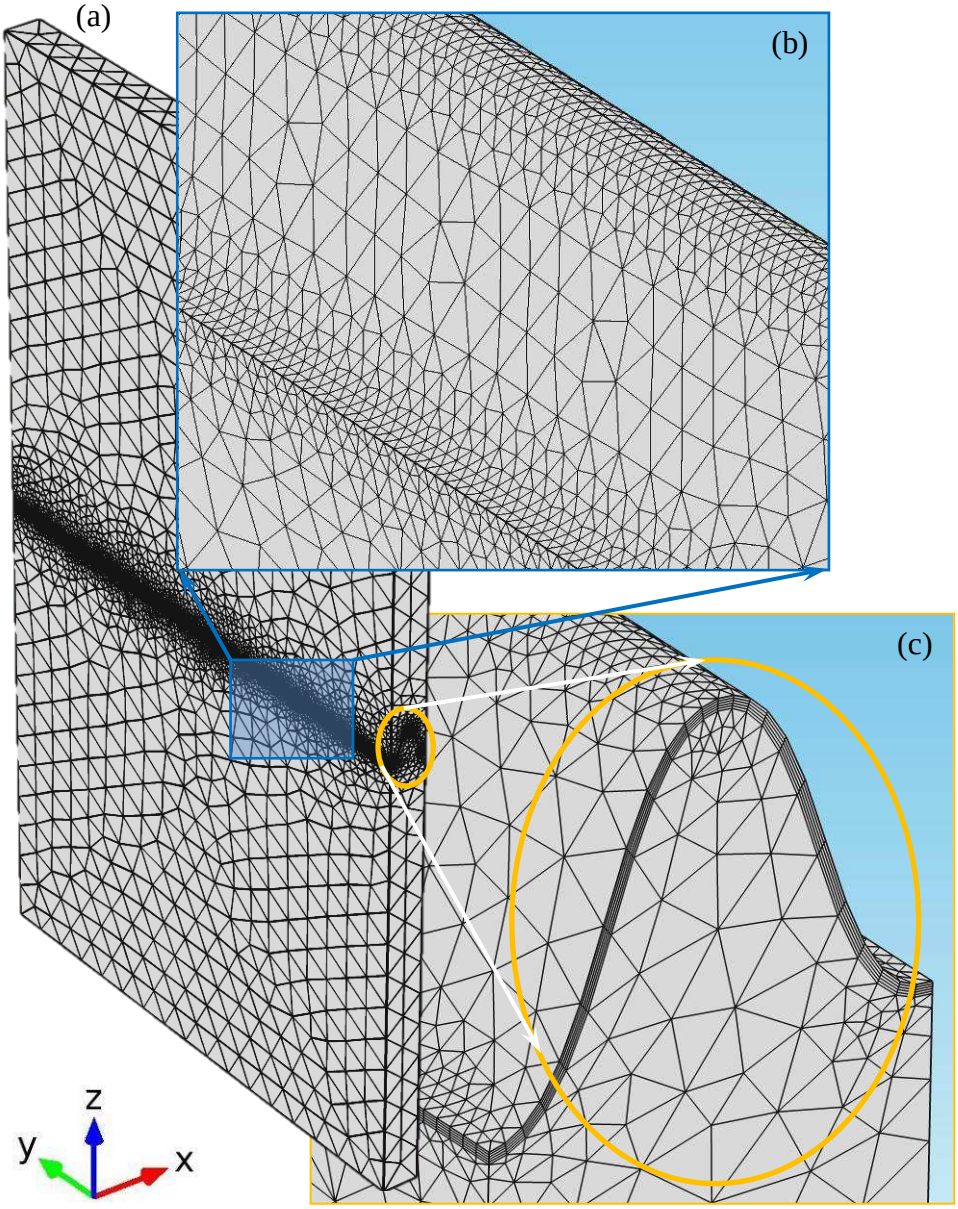

Figure 3.25 Example of meshes used in simulation of TEM flows with different interface shapes in *x*-*z* plane. (a) Fine triangular meshes used in all domains; (b) Meshes near interface are refined; (c) Ten 5μm thickness boundary layers are added to the liquid-solid interface.

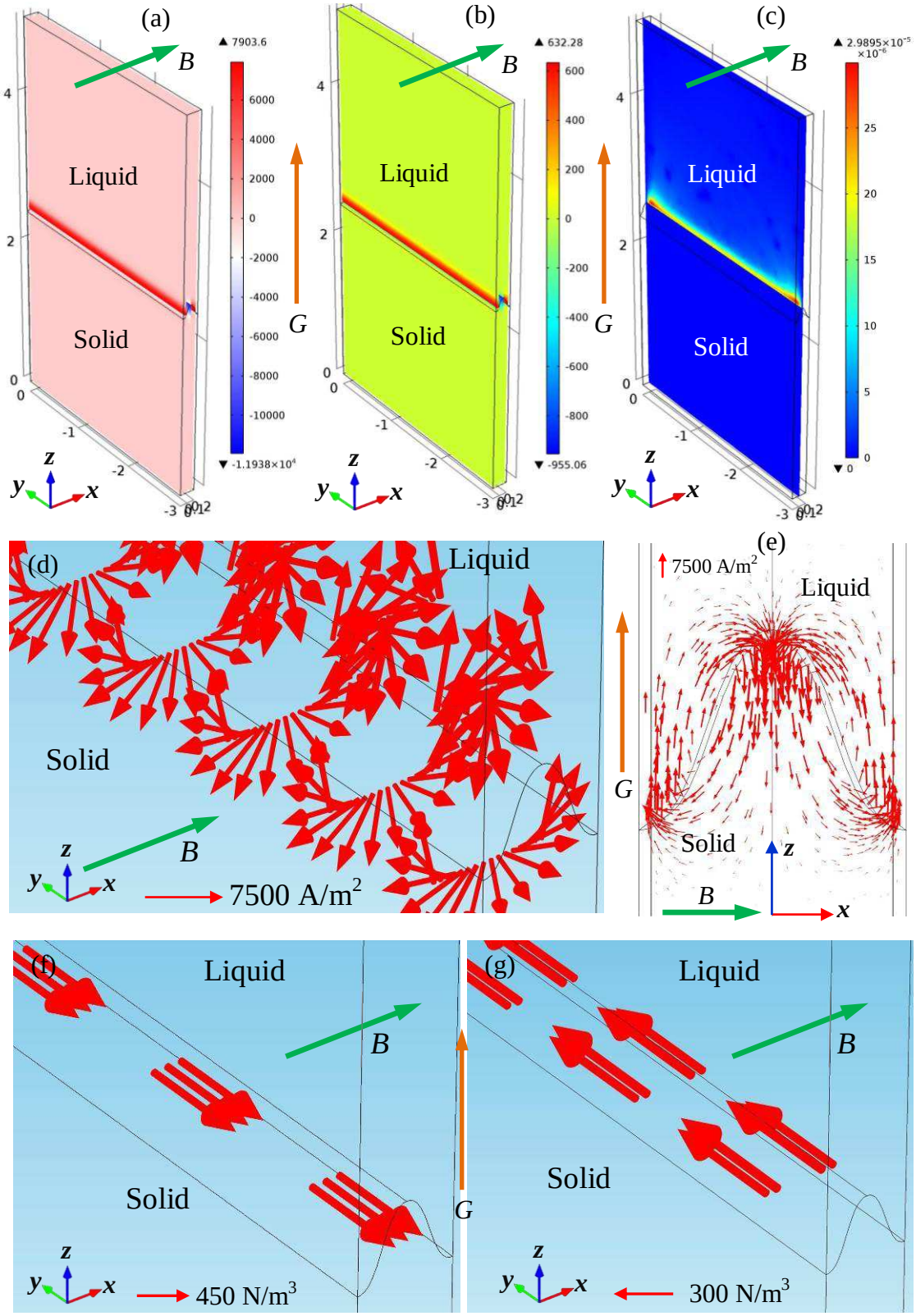

Figure 3.26 Computed results with liquid-solid interface being convex in *x*-*z* plane. (a) *z* component of TEC, and unit of the legend is A/m^2; (b) *y* component of TEM forces, and unit of the legend is N/m^3; (c) Velocity magnitude of TEM flows, and unit of the legend is m/s; (d) Arrows of TEC near interface; (e) Arrows of TEC around interface viewed from *x*-*z* plane; (f) Arrows of TEM forces in solid; (g) Arrows of TEM forces in liquid. (*B*=0.08T; *G*=3000K/m)

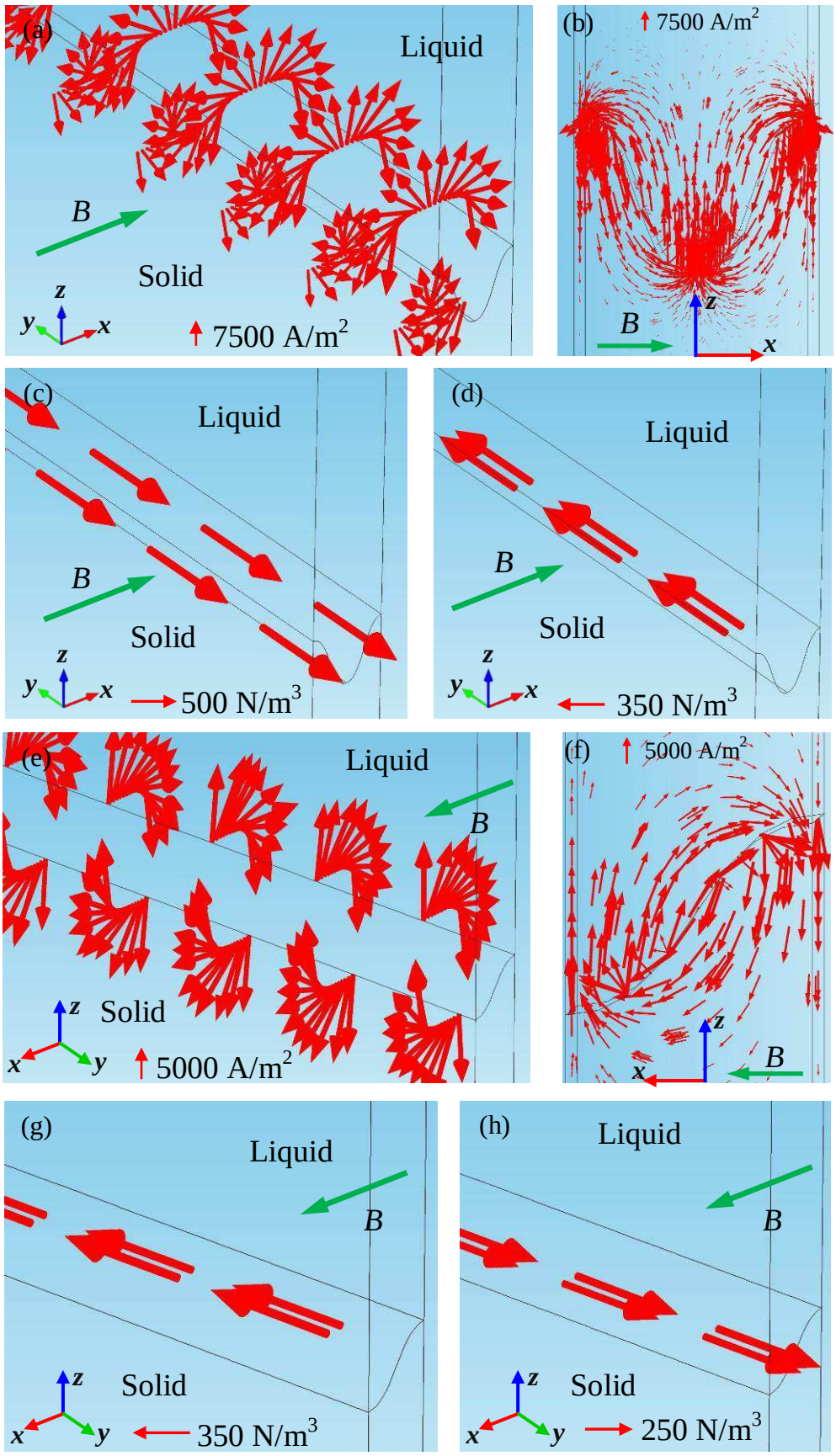

Figure 3.27 Computed results with liquid-solid interface being convex (a)-(d) and sideling (e)-(h) in *x*-*z* plane: (a) and (e) Arrows of TEC near interface; (b) and (f) Arrows of TEC around interface viewed from *x*-*z* plane; (c) and (g) Arrows of TEM forces in solid; (d) and (h) Arrows of TEM forces in liquid. (*B*=0.08T; *G*=3000K/m)

Further, how the TEM flows act is simulated for three different interfaces shapes in *x*-*z* plane. Figure 3.28 shows the case that interfae is convex in *x*-*z* plane, figure 3.29 gives the case that interfaces is concave in *x*-*z* plane and figure 3.30 displays the case that interface is sideling in *x*-*z* plane. In these three figures, figure (a) show the 3D view of computed TEM flows in liquid, in which the colored slices stand for the magnitudes of the velocities of TEM flows and arrows near interface reveal their flowing direction. Figure (b) are the *x*-*z* planes cut at the position *y*=1.5mm, in which the colored surfaces represent the magnitudes of the velocities of TEM flows as well. Moreover, in order to get the exact magnitudes of the velocities, their *y* component velocities of TEM flows are profied along vertical lines locating at three different positions as indicated by the white lines in figure (b), and the corresponding curves are shown in figure (c). According to these similuations, it can conclude that TEM flows do appear at the vicinity of liquid-solid interface under the present experimental conditions when the interface is not perfectly flat in the *x*-*z* plane (Indeed, the interface being uneven in *x*-*z* plane is the common case). Moreover, the directions of computed TEM flows are always flowing toward the positive *y*-axis direction whatever the shapes of interface in *x*-*z* plane are.

Concering the shape of the initial liquid-solid interface should be changed if the one-way flowing TEM flows are capable to transport and then redistribute the rejected solutes, the simulations of TEM flows with more realistic interface shapes relight our wish for in-situ observing TEM flows because the shape change of liquid-solid interface can be distinctly detected. However, not all the flows in melt can transport the solutes but only the ones are sufficiently intense. Whether the flows are sufficiently intense or not can be judged by a mass transfer characterizing dimensionless number P_{e_C}, which is named Peclect numer and expressed as:

$$P_{e_C} = \frac{UL}{D} \tag{3.31}$$

where, U is velocity of flows with the unit of m/s, L is the characteristic length with the unit of m (here, the thickness of sample 200μm is used), and D is diffusion coefficient of solute in melts that $4\times10^{-9}m^2/s$ [275]. Take the minimum velocities obtained in the three simulations as given in figure 3.28 (c), 3.29 (c) and 3.30 (c), 58.5μm/s, the Peclet number is 2.925. Because Peclect numer is bigger than unit even employing the minimum velocities of computed TEM flows, it can be concluded that TEM flows under the present experimental conditions are sufficiently intense to transport the rejected solutes.

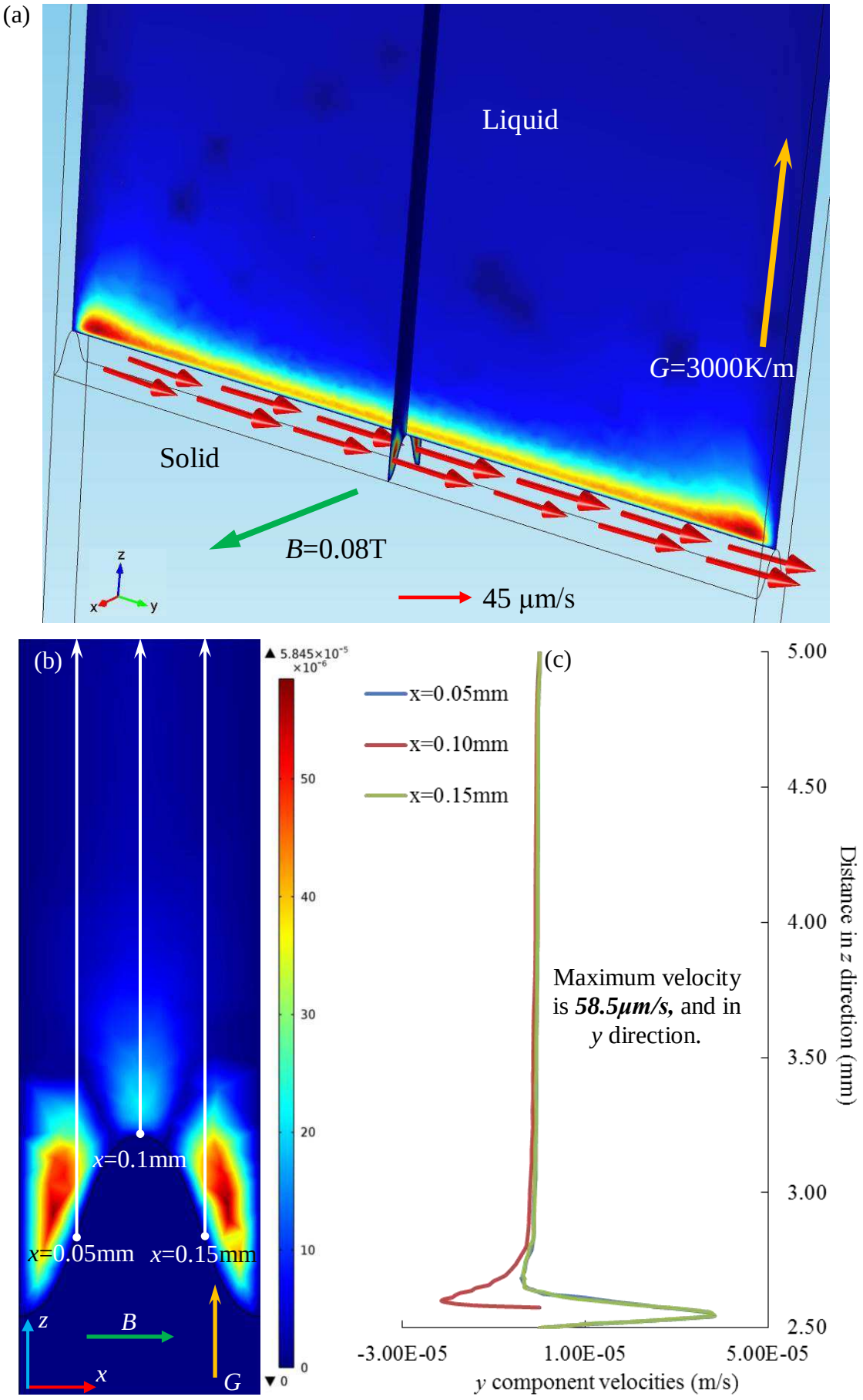

Figure 3.28 TEM flows simulated with an interface being convex in *x*-*z* plane. (a) Colored slices refer velocity magnitude and red arrows denote TEM flows fields; (b) TEM flows viewed from *x*-*z* plane cut at the position y=1.5mm, unit of legend is m/s; (c) How *y* component velocities varying along vertical lines as indicated in (b).

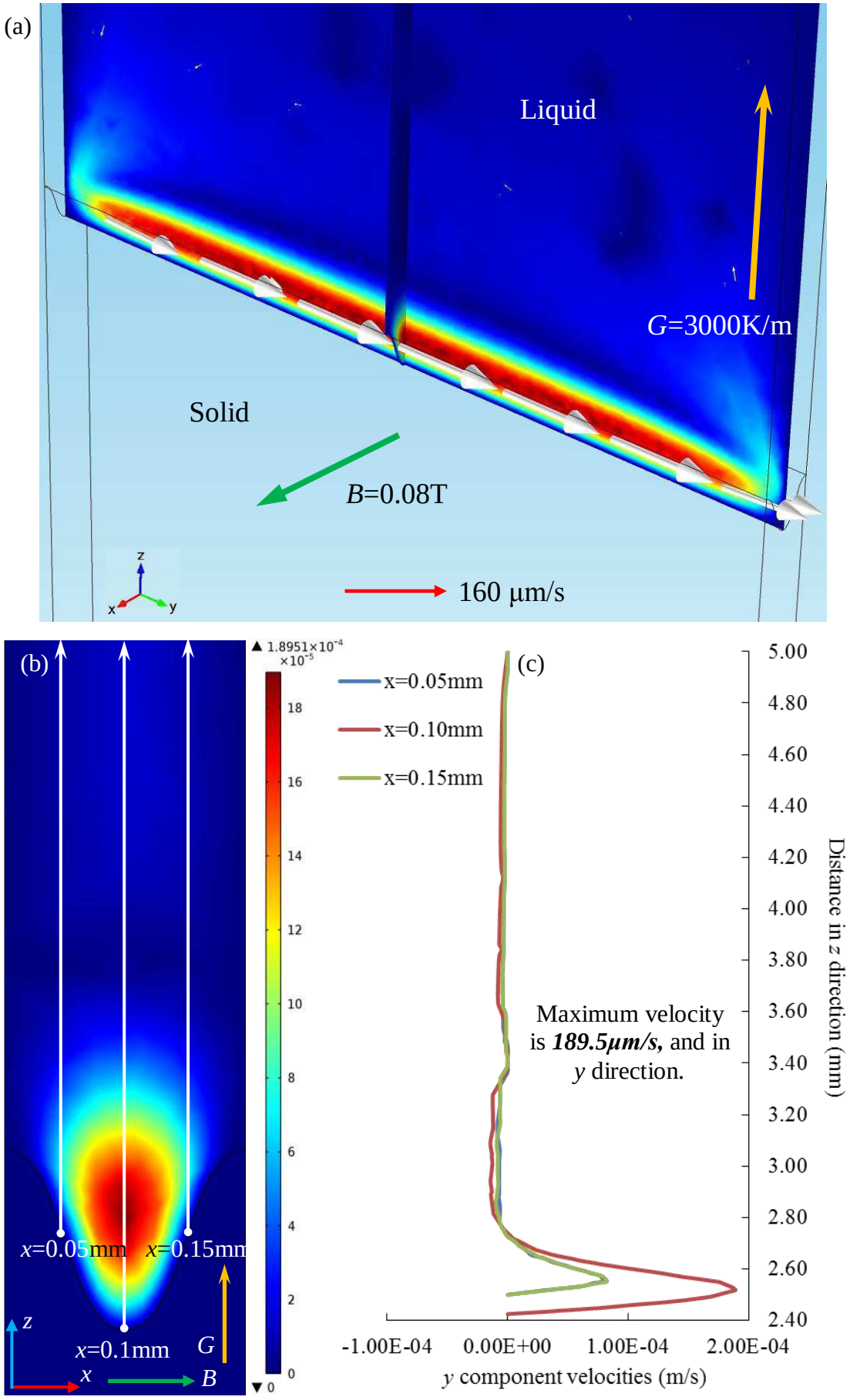

Figure 3.29 TEM flows simulated with an interface being concave in *x*-*z* plane. (a) Colored slices refer velocity magnitude and red arrows denote TEM flows fields; (b) TEM flows viewed from *x*-*z* plane cut at the position y=1.5mm, unit of legend is m/s; (c) How *y* component velocities varying along vertical lines as indicated in (b).

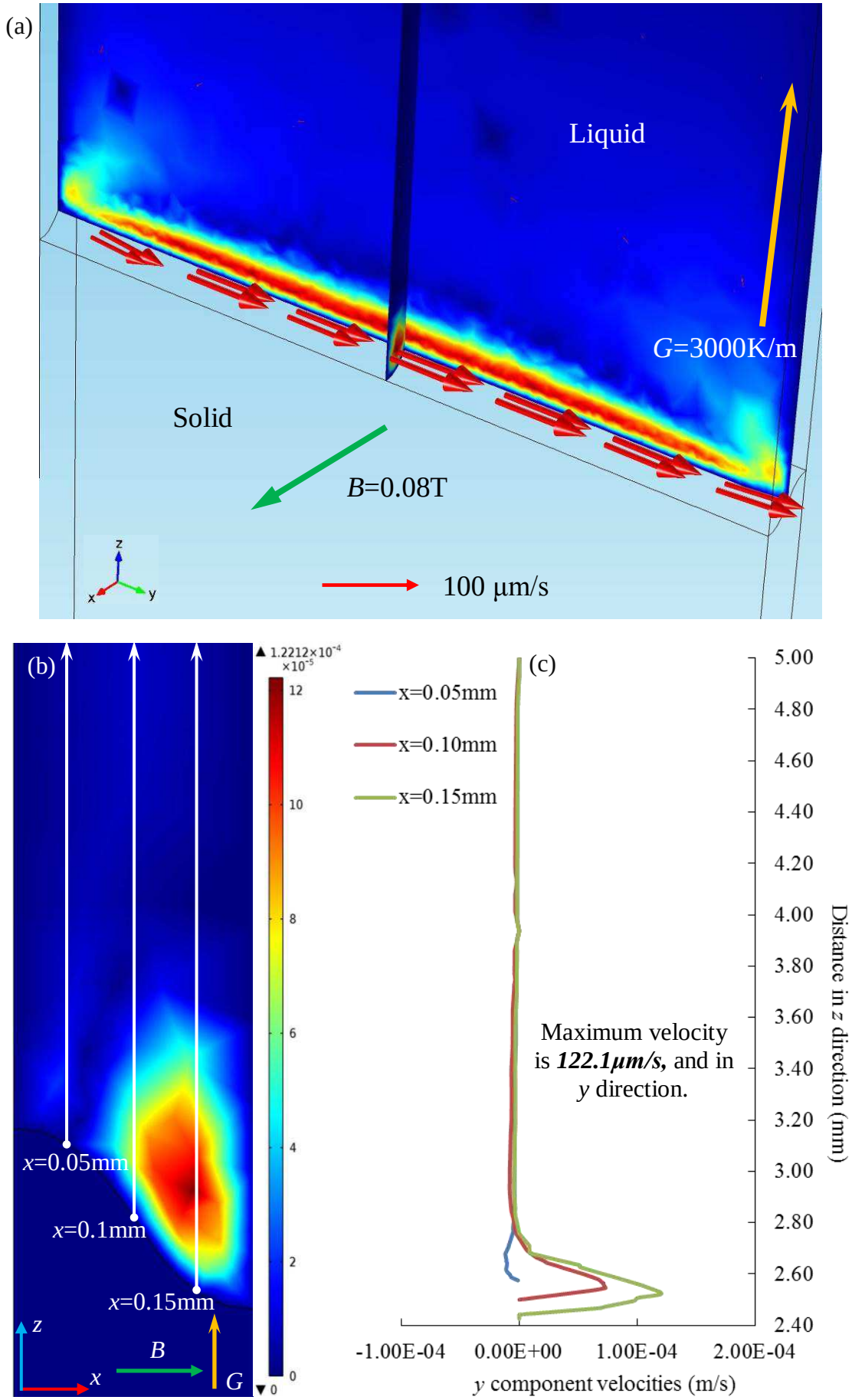

Figure 3.30 TEM flows simulated with an interface being sideling in *x*-*z* plane. (a) Colored slices refer velocity magnitude and red arrows denote TEM flows fields; (b) TEM flows viewed from *x*-*z* plane cut at the position y=1.5mm, unit of legend is m/s; (c) How *y* component velocities varying along vertical lines as indicated in (b).

3.3.2 In-situ observation of shape change of liquid-solid interface

Encouraged by the above simulations, the directional solidifications of Al-4wt%Cu alloy without and with external magnetic field were performed and in-situ observed. The no field experiment had been accomplished by our collaborators from Marseille University (IM2NP). Figure 3.31 shows 6 successive images captured during directionally solidifying the Al-4wt%Cu alloy with a thermal gradient of 3000K/m and in the absence of magnetic field. The cooling rate used in the no field experiment is 0.1 K/min that corresponds to the growth velocity of about 0.55μm/s. The view field is in *y*-*z* plane as indicated by the 2D coordinates in figure 3.31 (a). Because figure 3.31 (a) was captured at almost the beginning of cooling, it can be seen that the initial liquid-solid interface shape is sideling in *y*-*z* plane. Let us define the angle between interface and *y*-axis as the measure of the sideling degree of interface. It can find that the sideling angle increases with time as indicated by figures 3.31 (b), (d) and (f). This is attributed to the appearance of one-way flowing solutal convections flowing with the pattern as marked by the yellow loop in figure 3.31 (e). Moreover, the appearance of solutal convections in this experiment is easy to understand because the rejected heavier copper solutes must sink down to the any low-lying region of the initial sideling interface. As solidification proceeds, more and more copper solutes will gather at the hollow part of interface, which suppresses the growth of the corresponding region of interface. However, at the same time, melt concentration ahead the heave part of interface diminishes, which enhances the local growth velocity. Consequently, these two counteractive effects together make the initial interface become more sideling.

Figure 3.32 shows 6 successive images captured during directionally solidifying the Al-4wt%Cu alloy with a thermal gradient of 3000K/m and a 0.08T transverse magnetic field. Figure 3.32 (a) is the moment that the solidification just began and gives the coordinate of the view field. It can see that the initial liquid-solid interface is sideling as well, and the right part of the interface is hollow. According to simulations of TEM flows above, yellow loop in figure 3.32 (b) simply indicates the pattern of TEM flows under the conditions used in this experiment. If these flows are sufficiently intense, the rejected copper solutes can be transported from the front of the hollow part of interface to its heave part, and then the enriched solutes slow down the local growth velocity. At the same time, low concentration melt in front of the hollow part of interface increases the growth velocity. Consequently, the sideling degree of the initial interface should decrease, and finally, the liquid-solid interface became nearly flat. Moreover, one thing should be emphasized that there exists an region with less dark color as marked by the purple dotted lines in figure 3.32 (d) to (f). Based on imaging principle used by the synchrotron X-ray imaging, the less dark color means that this area is

thinner compared to the other regions. The abruptly narrowing thickness can block or saying greatly reduces the permeability of TEM flows and as well as the solutes. So that, when the liquid-solid interface enters in this region, for example at about 136.8mins as shown in figure 3.32 (d), solutes cannot be transported to the region with less dark color. Consequently, melt in the front of the middle of interface is greatly enriched by the solutes, and melt ahead the right side of interface become dilute at the same time. For this reason, the growth of the middle part of interface is depressed, and reversely, growth of the right side of interface is speeded up. Finally, the interface should slightly be concave in the middle and heave at the right side, which is just the case shown in figure 3.32 (e) and (f).

With purpose to confirming the discussions above, how growth velocities of different parts of liquid-solid interface vary with time were measured along three vertical lines locating at different positions as indicated in figure 3.32(c). Curves shown in figure 3.33 suggest that both the right and the middle parts of interface grown faster than the left part at the early stage of solidification that was about the first 120mins. As the time going, the growth velocity of the left part of interface ran ahead. And finally, the growth of the initial hollow part of interface became the fastest one about 130 minutes after the solidification began. This makes the initial sideling interface becoming into nearly flat. However, such flat interface may not be maintained because the growth of the left and the right parts of interface' will speed up whilist the middle part will slow down predicted by the trendline of each curve shown in figure 3.33. This is reasonable because the abruptly narrowing thickness in front of the right side of interface will prevent the nearby melt from being further enriched, meanwhile, the rejected solutes will be continuously transported from the left part of interface to the middle by the left-to-right flowing TEM flows.

Although the possibility of the occurence of TEM flows had been predicted by the simulation with the interface uneven in *x*-*z* plane, it is still necessary to check whether the left-to-right flowing TEM flows can or cannot appear with the observed initial sideling interface. To do so, used the same simulation method as stated in section 3.2.1 and parameters list in table 2.2, 3D simulations of TEM flows with the observed initial sideling interface were performed. Similarly, three different shapes of interface in *x*-*z* plane were all used. Results are shown in figure 3.34, in which, velocity magnitudes are represented by colored slice and velocity field are represented by red arrows. Besides, the mass transfer characterizing Peclet numbers were calculated for each case by using the maximum velocity given by the corresponding color legend. These simulations show that left-to-right flowing TEM flows do exist, and the corresponding Peclet number sugguests that these TEM flows are intense enough to transport the rejected solutes. Therefore, the shape change of liquid-solid interface

in directional solidification of Al-4wt%Cu alloy under a 0.08T transverse magnetic field is reasonably attribute to TEM flows. In another aspect, we can say that TEM flows are in-situ observed.

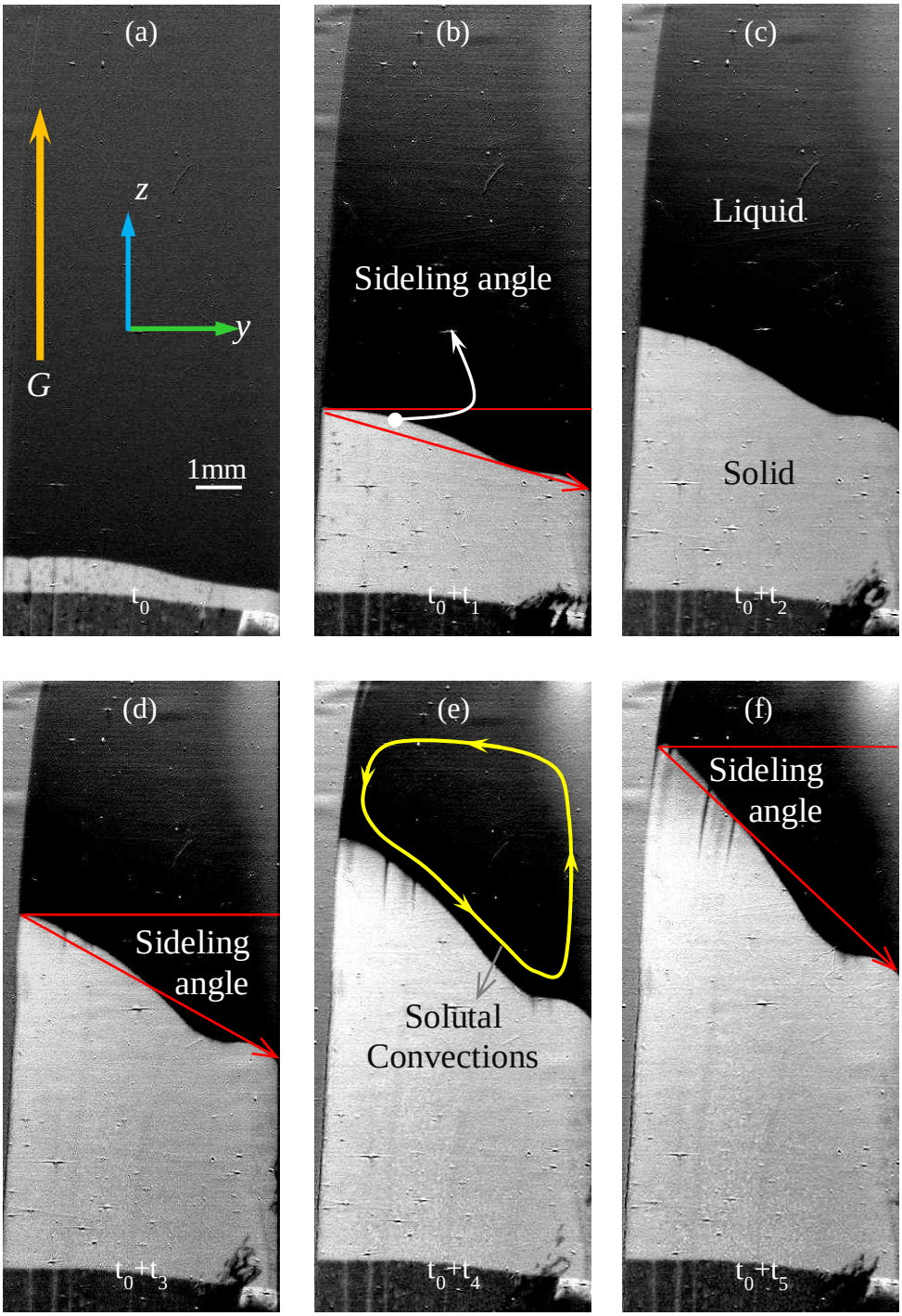

Figure 3.31 Six successive images captured during directionally solidifying Al-4wt%Cu alloy without magnetic field (G=3000K/m; Cooling rate is 0.1K/min). (a) The moment that solidification just began and the coordinate of the view field; (b) The moment at t_1 mins after beginning and the illustration of sideling angle; (c) The moment at t_2 mins after beginning; (d) The moment at t_3 mins after beginning; (e) The moment at t_4 mins after beginning and the illustration of the pattern of solutal convections; (f) The moment at t_5 mins after beginning.

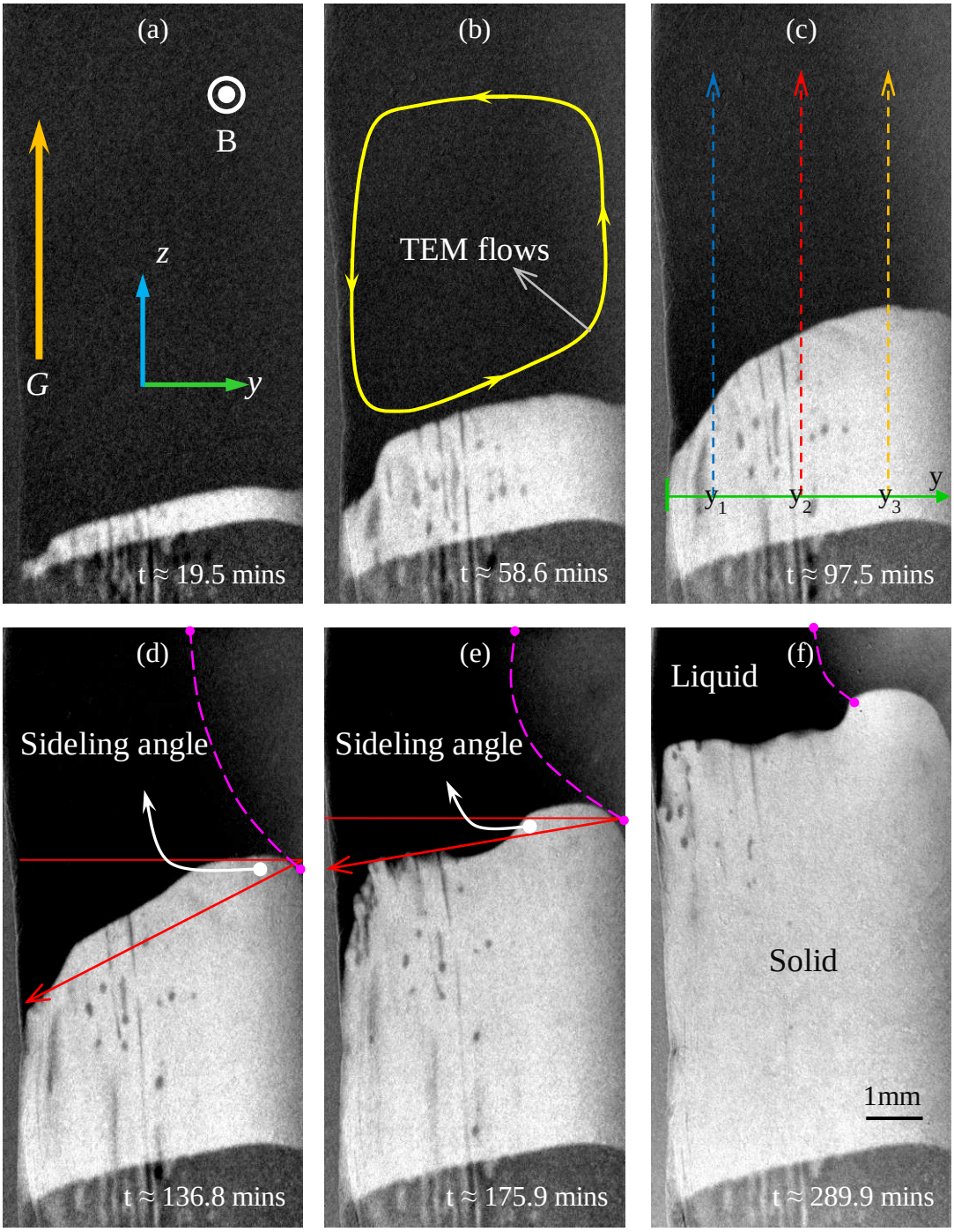

Figure 3.32 Six successive images captured during directionally solidifying Al-4wt%Cu alloy under a 0.08T transverse magnetic field (G=3000K/m; Cooling rate is 0.1K/min). (a) The t≈19.5mins moment that almost the beginning of solidification and the coordinate of the view field; (b) The moment at t≈58.6mins and the simply drawing of the pattern of TEM flows in accordance with simulations with similar experimental conditions; (c) The moment at t≈97.5mins and the indication of paths for measuring growth velocities; (d) The moment at t≈136.8mins and the mark of the thinner crucible region; (e) The moment at t≈175.9mins; (f) The t≈289.9mins moment that the solidification almost finish.

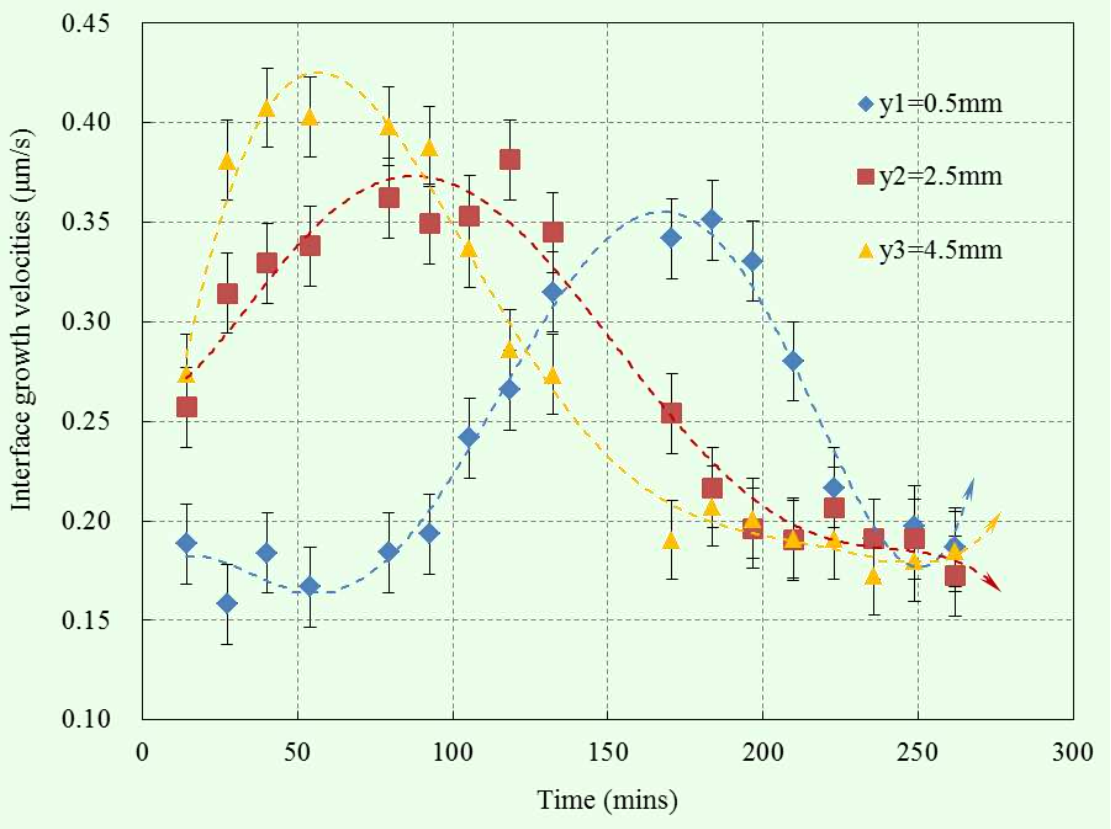

Figure 3.33 Growth velocities of different parts of liquid-solid interface varying with time plotted along three vertical lines as indicated in figure 3.32 (c). From the left to right, these three vertical lines are at y_1=0.5mm, y_2=2.5mm and y_3=4.5mm positions. (The width of the sample is 5mm.)

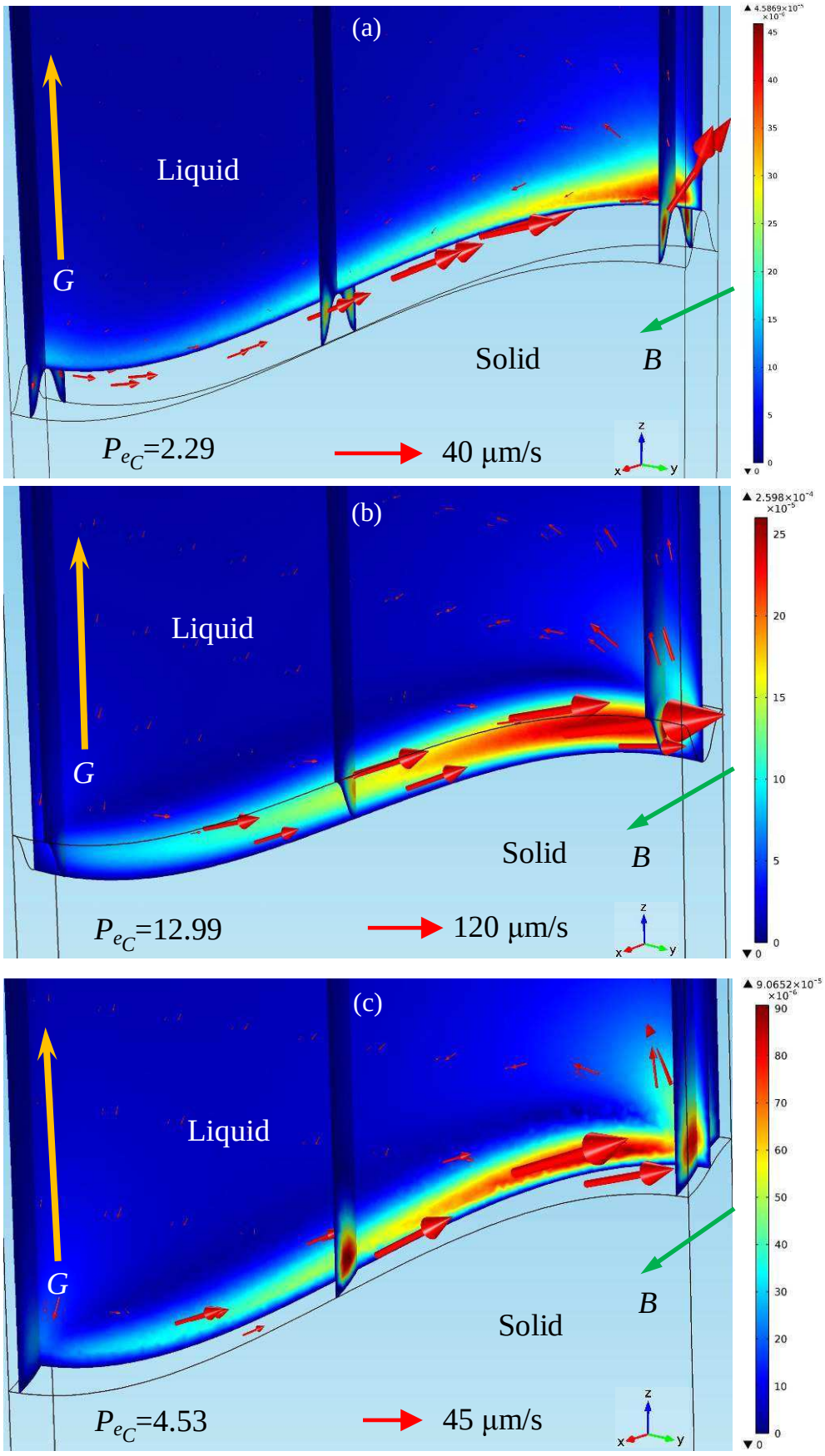

Figure 3.34 TEM flows simulated with the observed initial sideling interface and the same conditions used in the with magnetic field experiments. (a) Interface is convex in *x*-*z* plane; (b) Interface is concave in *x*-*z* plane; (c) Interface is sideling in *x*-*z* plane. (*G*=3000K/m, *B*=0.08T)

3.4 Summary

For the purpose of directly observing TEME during directionally solidifying the metallic alloys, the live observation of phenomena TEM forces and TEM flows were introduced in chapter 3.2 and 3.3 respectively. Experimental apparatus used for in-situ observing the directional solidification process was introduced in chapter 3.1. Because both of TEM forces and TEM flows are difficult to directly detect by the synchrotron X-ray imaging, we regard TEM forces and TEM flows are visualized if their directly resulting phenomena are seen. Upon the TEM forces, the movements of crystals during solidification were measured and compared to analytical calculated TEM forces driving movements of sphere particles. It found that the observed movements of crystals were the same as the calculated ones. This suggested that the movements of crystals were directly casued by TEM forces in solid when the directional solidification was conducted under a 0.08T transverse magnetic field. And then, it can be stated that TEM forces in solid were in-situ oberaved. About the TEM flows, whether they can appear or not under the conditions used by in-situ experiments was analyzed by simulations in advance. Fortunately, the answer was positive. Simulations showed that left-to-right flowing TEM flows near liquid-solid interface can be produced and sufficiently intense to transport the rejected solutes. It has been well known that the one-way flowing flows in melt can concentrate the solutes to one side of the sample, and then the enriched melt ahead the interface are able to change the liquid-sloid interface shape. Therefore, the shape change of interface observed during directionally solidifying the Al-4wt%Cu alloy under a 0.08T transverse magnetic field should be reasonable attributed to the left-to-right flowing TEM flows. And then, it can say that TEM flows were in-situ observed. At last, the 3D simulations with the same interface shape observed in the in-situ observation experiment were performed to further confirm the occurence and the direction of TEM flows.

Chapter 4: Influence of thermoelectric magnetic effect (TEME) on liquid-solid interface shape in directional solidification process

Considering the formulations of TEC and TEME have been given, TEM forces and TEM flows have been unfolded by 2D axisymmetric simulations and their direct resulting phenomena have been in-situ observed by synchrotron X-ray imaging, we can confidently say that the existence of TEME in directional solidification process has been proved. Therefore, for the next step, whether TEME can or not influence the formation of structure during directional solidification should be examined. Although the in-situ experiments in chapter 3 can indicate the possibility of TEME on modifying the solidified structures to a certain extent 200μm thickness metal ingots are rarely used in practice. So that, directional solidifications of Al-Cu alloys with bigger samples that millimeter size in 3 dimensions are conducted without and with different magnetic fields. This chapter experimentally examines the influence of TEM flows on the shape of liquid-solid interface because which strongly influences the generation and propagation of defects [276], the radial compositional uniformity [277], grain size and orientation of phases [278], and the flows play a crucial role in modifying the shape of interface [279]. Moreover, 3D simulations of TEM flows are performed to confirm the experimental results and display TEM forces in these cases. Before step into the experiments and the simulations, quantitative evaluation of TEM flows is made.

4.1 Evaluation of thermoelectric magnetic (TEM) flows

Although the formulas of TEC and TEM flows have been given in chapter 2 they are recalled here to make the evaluation of TEM flows coherent. Because the total electric currents considered here contain the currents caused by electric field $\sigma\vec{E}$, currents generated via liquid moving across the magnetic field $\sigma\vec{u}\times\vec{B}$ and the TEC $\sigma S\vec{\nabla}T$, the Ohm's law should be expressed as:

$$\vec{j}=\sigma(\vec{E}+\vec{u}\times\vec{B}-S\vec{\nabla}T) \tag{4.1}$$

with

$$\vec{\nabla}\bullet\vec{j}=0 \tag{4.2}$$

where, σ, S, $\vec{u}$ and $\vec{B}$ respectively denotes electrical conductivity, ATP, velocity of flows in melt and the imposed magnetic field, and the units of these parameters can be found in table 4.1. With the assumption that ATP within a single medium is constant and the liquid is incompressible, Navier-Stokes equations governing TEM flows can be written as:

$$\frac{\partial(\rho\vec{u})}{\partial t}+\rho(\vec{u}\bullet\vec{\nabla})\vec{u}=-\vec{\nabla}p+\rho\vec{g}+\mu\nabla^2\vec{u}+\vec{j}\times\vec{B} \tag{4.3}$$

with the continuity equation:

$$\vec{\nabla}\bullet\vec{u}=0 \tag{4.4}$$

where, ρ, μ and p is respectively the density, the dynamic viscosity and the pressure. The units of these parameters can be found in table 4.1 as well.

Table 4.1 Physical properties used in evaluations and simulations of TEM flows

Symbol	Unit	Solid	Liquid
S	V/K	-1.5×10^{-6}	-2.25×10^{-6}
σ	$(\Omega\cdot m)^{-1}$	1.3×10^{7}	4.0×10^{6}
μ	Pa·s	2.0×10^{6}	2.9×10^{-3}
ρ	Kg/m^3	2.7×10^{3}	2.4×10^{3}

It must have been noticed that intereaction between electric currents j and the magnetic field B produces two types of Lorentz forces even when no external electric field is applied. One is TEM forces, and the other is generated by the interaction between the inducing currents and the magnetic field expressed by the term $\sigma(\vec{u}\times\vec{B})\times\vec{B}$. The former in liquid drives TEM flows and are proportional to the first order of B and the latter ones act as the braker and are proportional to the square of B. Consequently, competition between the driving and the damping forces occurs, and it can know that the driving TEM forces dominate at the beginning and then the damping forces prevail as B constantly increases. Correspondingly, the resulting TEM flows in melt should firstly speed up to the maximum speed and then decrease with constantly increasing magnetic field. Therefore, let us evaluate TEM flows' increasing stage in advanced.

According to the theory of hydrodynamics, if there are forces in liquid the velocity of their driving flows can be estimated via balancing the driving forces to inertia or viscous forces. So that, it has:

$$\rho\frac{u_1^2}{\lambda}\approx\sigma SGB \text{ with } S=S_s-S_l \tag{4.5}$$

and

$$\mu\frac{u_2}{\lambda^2}\approx\sigma SGB \text{ with } S=S_s-S_l \tag{4.6}$$

where, G, S_l and S_s respectively denotes the applied thermal gradient, the ATP of liquid and solid, u_1 is the evaluated velocity via balance between TEM forces and inertia, u_2 is obtained by equaling TEM forces to viscous forces. Further, it gets:

$$u_1 \approx \sqrt{\frac{\sigma SG\lambda B}{\rho}} \tag{4.7}$$

$$u_2 \approx \frac{\sigma SG\lambda^2 B}{\mu} \tag{4.8}$$

However, we need to judge which velocity we should take. This can be judged by a dimensionless number named Reynolds number, *Re*:

$$Re = \frac{\rho\lambda u}{\mu} \tag{4.9}$$

where, u and λ represents the velocity of flows in melt and typical length scale respectively. The criterion used by the Reynolds number can varies from 1 to 4 for the different concerning conditions. For the present cases, it defines that balance between TEM forces and inertia is used when $Re > 1$, and balance between TEM forces and viscous forces is valid when $Re \leq 1$. Replace u in equation 4.9 by equations 4.7 or 4.8, it has:

$$Re_1 = \frac{\sqrt{\rho\sigma SG\lambda^3 B}}{\mu} \tag{4.10}$$

and

$$Re_2 = \frac{\rho\sigma SG\lambda^3 B}{\mu^2} \tag{4.11}$$

here, Re_1 and Re_2 is respectively the Reynolds number of u_1 and u_2. Considering the criterion defined for the present cases is whether *Re* bigger or smaller than 1 the magnetic field range for equations 4.8 being valid can be obtained via seting $Re_1>1$, and that for equation 4.9 can be obtained by seting $Re_2 \leq 1$. In fact, the threshold value of magnetic field for shifting using equiation 4.8 to using equation 4.9 to esitame the TEM flows can be calculated by equalling the equation 4.10 to 4.11. Correspondingly, it has:

$$B_{R_e} = \frac{\mu^2}{\rho\sigma SG\lambda^3} \tag{4.12}$$

where, B_{R_e} is the threshold magntic field over which the balance between TEM forces and inertia should be used to estimate the velocities of TEM flows, and below which balance between TEM forces and viscous forces should be used. It can be found from equations 4.12 that this threshold magnetic field depends on the typical length, λ, only when the system has been decided.Therefore, how select the suitable typical length should make clear. Based on the typical interface morphologies obtained in directional solidification as shown in figure 2.3 (a) to (c), 1mm is regarded as typical length of the planar interface because this kind of interface has the same scale with the diameter of using crucible which is usually about several

millimeters; for the cellular or dendritic interface the size of their primary arms are regarded as their typical lengths that respectively 0.1mm and 0.01mm.

Use the physical parameters in table 4.1 and the thermal gradient of 6000K/m that the same one used in the following experiments, the magnetic field ranges that respectively used to evaluate u_1 and u_2 were calculated for all the typical lengthes. The results are listed in table 4.2. It can find that only the magnetic field weaker than about 1.95×10^{-4}T should be used to evaluate TEM flows via balance between TEM forces and viscous forces when the typical length is 1 mm. Because 1.95×10^{-4}T nearly equals to the terrestrial magnetic field that about 10^{-4} to 10^{-5} T, the evaluation of TEM flows always use the balance between TEM forces and inertia for the 1mm typical length scale. Upon the case that typical length is 0.1mm, TEM flows should be evaluated by u_2 when the magnetic field is lower than 0.195T or by u_1 at higher magnetic fields. About TEM flows with the smallest typical length that 0.01mm, only the balance between TEM forces and viscous forces needs to care because the balance between TEM forces and inertia works when the magnetic field is higher than 194.6T that exceeds the highest static magnetic fields we can achieve on the earth [280].

Table 4.2 Evaluation mechanisms and their corresponding magnetic field ranges for different typical length scales (Primary step of the evaluation of TEM flows)

Typical length scales	**Force balance**	***Re***	***B* (T)**
λ = 1mm	TEM forces ≈ viscous forces, u_2	≤1	$0\sim1.95\times10^{-4}$
	TEM forces ≈ inertia, u_1	>1	$\geq1.95\times10^{-4}$
λ = 0.1mm	TEM forces ≈ viscous forces, u_2	≤1	0~0.195
	TEM forces ≈ inertia, u_1	>1	≥0.195
λ = 0.01mm	TEM forces ≈ viscous forces, u_2	≤1	0~194.6
	TEM forces ≈ inertia, u_1	>1	≥194.6

It must be emphasized that these evaluations are very preliminary because they did not take the damping forces into account. Therefore, let us consider influenc of the damping forces in the following evaluations. On the basis of MHD theory that has been simply introduced in chapter 1, the inducing electric currents governed by the second item at the right side of equations 4.1 should appear once the melt moves and cut the magnetic field lines. Interaction of such inducting currents and the magnetic fields produces a kind of Lorentz forces to damp the melt movements. In the present cases, because TEM flows cannot be parallel to the imposed magnetic fields all the time the inducing electric currents as well as the damping forces emerge once the TEM flows appear in melt. For this reason, TEM flows should speed up with a decreasing acceleration and then gradually slow down as soon as the damping forces are comparable to the TEM forces as:

$$\sigma SGB \approx \sigma u_3 B^2 \tag{4.13}$$

where, u_3 is the evaluated velocity of TEM flows when the damping forces prevailing. Further, it has:

$$u_3 \approx \frac{SG}{B} \tag{4.14}$$

Actually, equation 4.14 can be obtained from the MHD principle as well. It is because when the magnetic fields are sufficient high the viscous friction should be restricted within a layer named Hartmann layer that locate along the boundaries perpendicular to the magnetic fields. The thickness, δ, of Hartmann layer can be estimated:

$$\delta = \frac{1}{B}\sqrt{\frac{\mu}{\sigma}} \tag{4.15}$$

And then, balance of TEM forces and viscous forces is modified as:

$$\mu \frac{u_3}{\delta^2} \approx \sigma SGB \tag{4.16}$$

It can be seen that u_3 achieved from 4.16 has the same form as equation 4.14, which means the evaluation of u_3 is also valid from the view of MHD theory.

Schematically illustrate the evolution of these evaluated velocities that u_1, u_2 and u_3 with respect to magnetic fields in figure 4.1, it can find that the maximum velocity of TEM flows can be approximately estimated via equalling u_1 or u_2 to u_3. Either the former or the latter equivalence should be used depends on the typical length scale. Therefore, it is necessary to have the expression of the critical magnetic field $B_{\max}$ obtained by u_1=u_3 and $B_{\max'}$ achieved by u_2=u_3:

$$\sqrt{\frac{\sigma SG\lambda B_{\max}}{\rho}} = \frac{SG}{B_{\max}} \tag{4.17}$$

and

$$\frac{\sigma SG\lambda^2 B_{\max'}}{\mu} = \frac{SG}{B_{\max'}} \tag{4.18}$$

thus, it has

$$B_{\max} = (\frac{\rho SG}{\lambda\sigma})^{1/3} \tag{4.19}$$

and

$$B_{\max'} = \frac{1}{\lambda}\sqrt{\frac{\mu}{\sigma}} \tag{4.20}$$

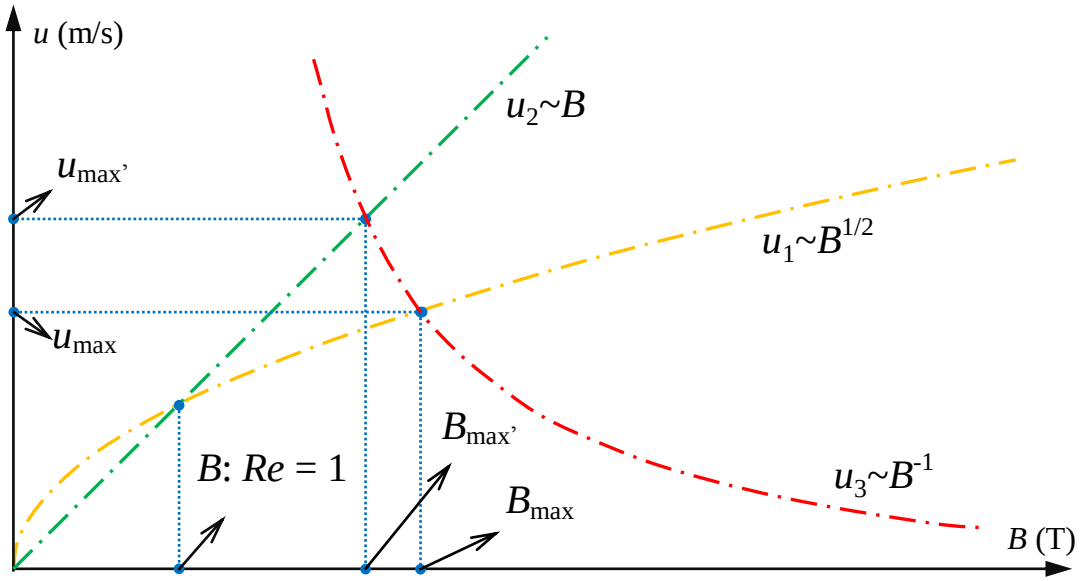

Figure 4.1 Illustration of the evolution of u_1, u_2 and u_3 with respect to imposed magnetic fields.

Based on table 4.2, it can know that evaluation of TEM flows for the typical length of 1mm should use u_1 until the imposed magnetic fields reach B_{max}, after that, u_3 should be employed. Upon the typical length of 0.1mm, both B_{max} and $B_{max'}$ should be calculated to judge the critical magnetic field over which TEM flows begin to slow down. Indeed, if $B_{max'}$ is higher than 0.195T that the upper limit of magnetic field range valid for u_2, the maximum TEM flows will appear under B_{max}. About the 0.01mm typical length scale, although u_1 is valid in an unrealizable magnetic fields range both B_{max} and $B_{max'}$ need be calculated as well because TEM flows will slow down when the imposed magnetic field is over $B_{max'}$ if B_{max} is lower than 194.6T. Table 4.3 lists the results of calculations in accordance to the discussions above. According to table 4.3, how TEM flows vary with the imposed magnetic fields is evaluated for the three typical lengths respectively and the the results are shown in figure 4.2.

Table 4.3 Critical magnetic fields corresponding to the maximum TEM flows and the regulations used to evaluate TEM flows

Typical length scales	B_{max} (T)	$B_{max'}$ (T)	Regulations for evaluating TEM flows
λ = 1mm	0.139	-	u_1 is valid from 0T to 0.139T u_3 is valid from 0.139T to infinite
λ = 0.1mm	0.300	0.269 (>0.195T)	u_2 is valid from 0T to 0.195T u_1 is valid from 0.195T to 0.300T u_3 is valid from 0.300T to infinite
λ = 0.01mm	0.646 (<194.6T)	2.692	u_2 is valid from 0T to 2.692T u_3 is valid from 2.692T to infinite

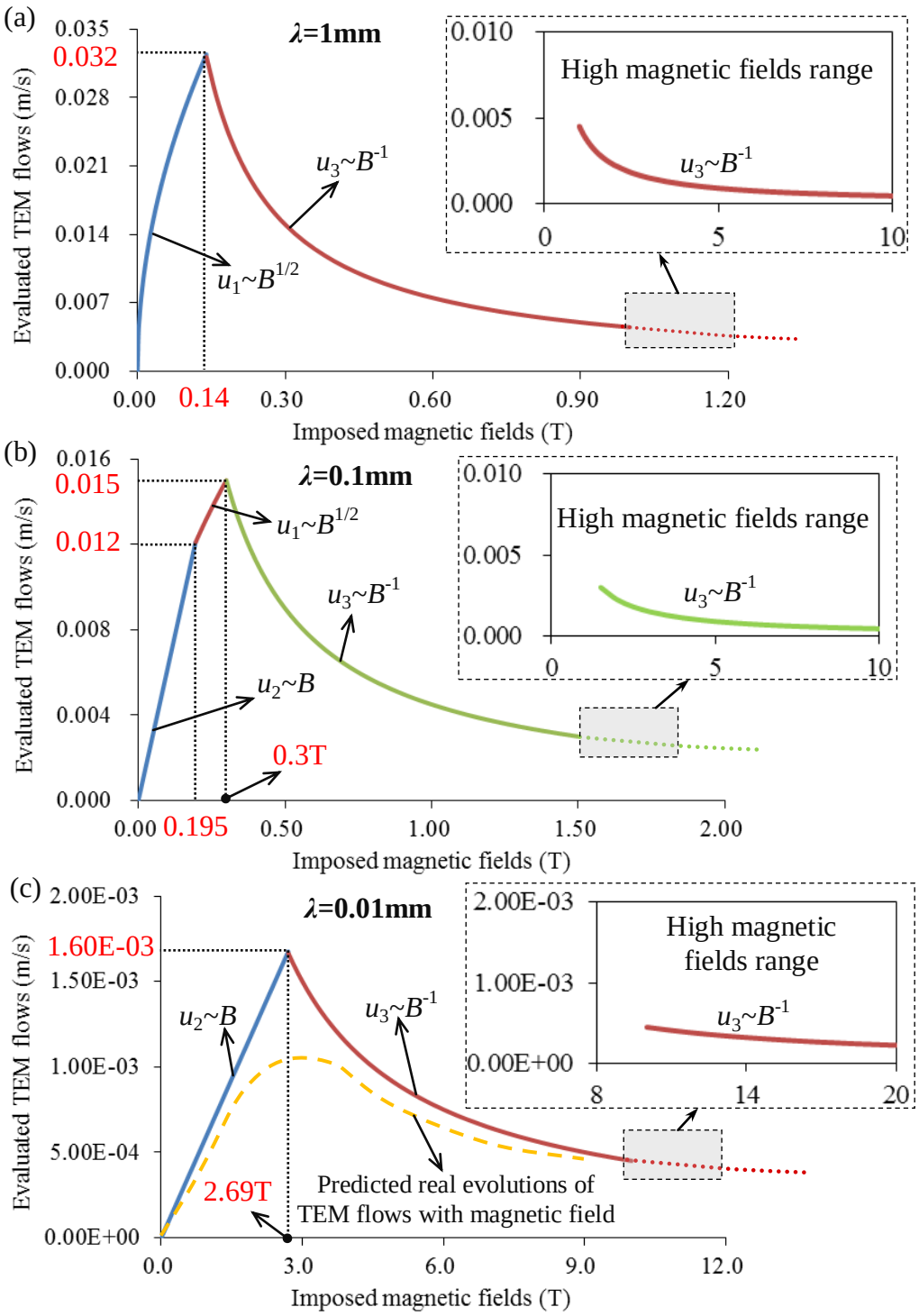

Figure 4.2 Curves of evaluating TEM flows varying with imposed magnetic fields for different typical scales: (a) λ=1mm; (b) λ=0.1mm (c) λ=0.01mm.

Figure 4.2 shows that no matter how long the typical length is TEM flows always speed up to the maximum and then slow down with the constantly increasing magnetic fields. Further looking at the speeding up period of TEM flows for each typical length, it can be found that the corresponding magnetic field range of the speeding up period is different for different typical length, moreover, the relationship between the velocities of TEM flows in the speeding up period and the magnitudes of imposed magnetic fields is different when the

typical length is changed. In the case of 1mm typical length, the velocities of TEM flows are proportional to the square root of the imposed magnetic field until it is about 0.14T as revealed by figure 4.2 (a). When consider cellular interface case that 0.01mm is the typical length, TEM flows linearly speed up with the imposed magnetic field until it is about 0.195T and then their velocities are proportional to a square root of the magnetic field until it is about 0.3T as shown in figure 4.2 (b). If the typical length is 0.01mm, TEM flows speed up linearly with the imposed magnetic field until they reach the maximum velocity under about 2.69T magnetic field (figure 4.3 (c)). At last, one more thing should be stressed for these evaluations that the realistic curve of how TEM flows vary with the increasing magnetic fields should be the one indicated by the yellow dotted line in figure 4.3(c). This is because that the present evaluations are based on the force balance with only one pair of reactive forces, such as the balance between TEM forces and viscous forces. Indeed, the magnetic field damping forces must be added to the balance between TEM forces and inertia or viscous forces even when they do not dominate because they can change the accelerations of TEM flows anyway. For this reason, the acceleration of TEM flows at their speeding up period should not be constant but gradually decrease to zero until TEM flows reach the maximum velocities. With such kinds of acceleration, curve of speeding up of TEM flows should act like the yellow dotted line in figure 4.3(c). Fortunately, these simplifications are acceptable because the evaluations above can still provide the correct evolution tendency of TEM flows with the imposed magnetic fields increasing and approximate critical magnetic field corresponding to the maximum velocity of TEM flows.

4.2 Experimental investigation of influence of thermoelectric magnetic (TEM) flows on liquid-solid interface shape

After TEM flows have been evaluated for different typical length scales, whether TEM flows behave in the same manner as predicted by the evaluations or not is experimentally examined in this section. In another aspect, these experiments can test and verify the ability of TEM flows to modify the structure during directional solidification as well.

4.2.1 Experimental apparatus

Al-0.85wt%Cu and Al-2.5wt%Cu used in the present study were both prepared with high-purity Al (99.99%) and Cu (99.99%). The master alloys were melted in a cold crucible electromagnetic induction furnace as shown in figure 4.3 (a) and melted for several times to achieve perfect uniformity. As shown in figure 4.3 (c), the prefabricated specimens with 3mm in diameter and about 150mm in length were prepared by the vacuum suction casting system

shown in figure 4.3 (b). The vacuum of suction casting system were pumped together with the induction furnace to about 10^{-5} Pa, and the fill the the induction furnace only with argon gas to about 10^{5} Pa, which provides about a 10^{10} Pa pressure difference. This is sufficient high to hold an Al-Cu alloy melts column with about 150mm length. The prefabricated specimens were enveloped in a high-purity alumina tube with 3mm inner diameter and 200mm length for experiment.

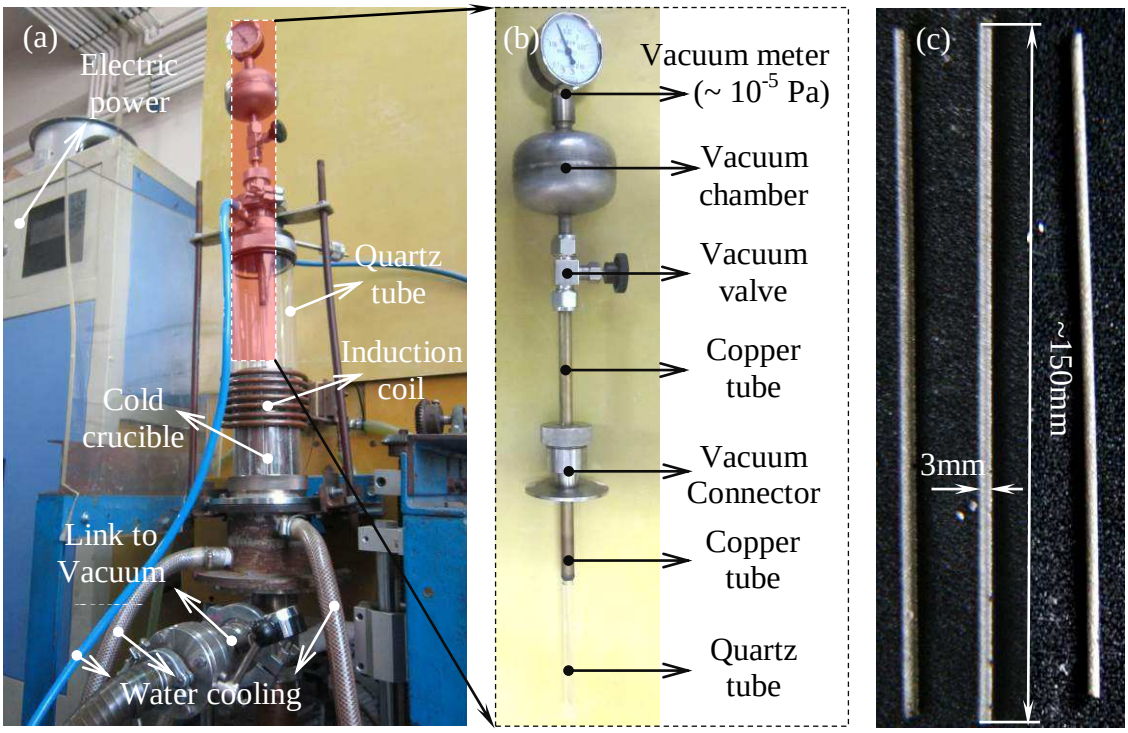

Figure 4.3 (a) Cold crucible electromagnetic induction furnace used to melt master alloys; (b) Vacuum suction casting system used to prepare prefabricated specimens; (c) The prefabricated specimens and their dimensions.

The entire experimental apparatus consists of two main parts which are external magnet and the Bridgman type directional solidification furnace. The external magnet is an electromagnet whose two copper coils are water cooled. In order to increase and concentrate the magnetic fields, iron yokes are used as shown in figure 4.4 (a). This electromagnet can provide static or alternating transverse magnetic fields depends on the type of input electric currents. According to the coordinate and (0, 0, 0) point defined in figure 4.4 (a), the distribution of static transverse magnetic field (TMF) in *x*-*y* plane at *z*=5cm and in *x*-*z* plane at *y*=6.5cm were measured and respectively shown in figure 4.4 (b) and (c). It can find that the nearly homogeneous magnetic field area in the middle part of the air gap is about $6\times6cm^2$, which is sufficient big to ensure the concerning part of specimens being under a uniform magnetic fields. The air gap of this electromagnet is 10cm in width.

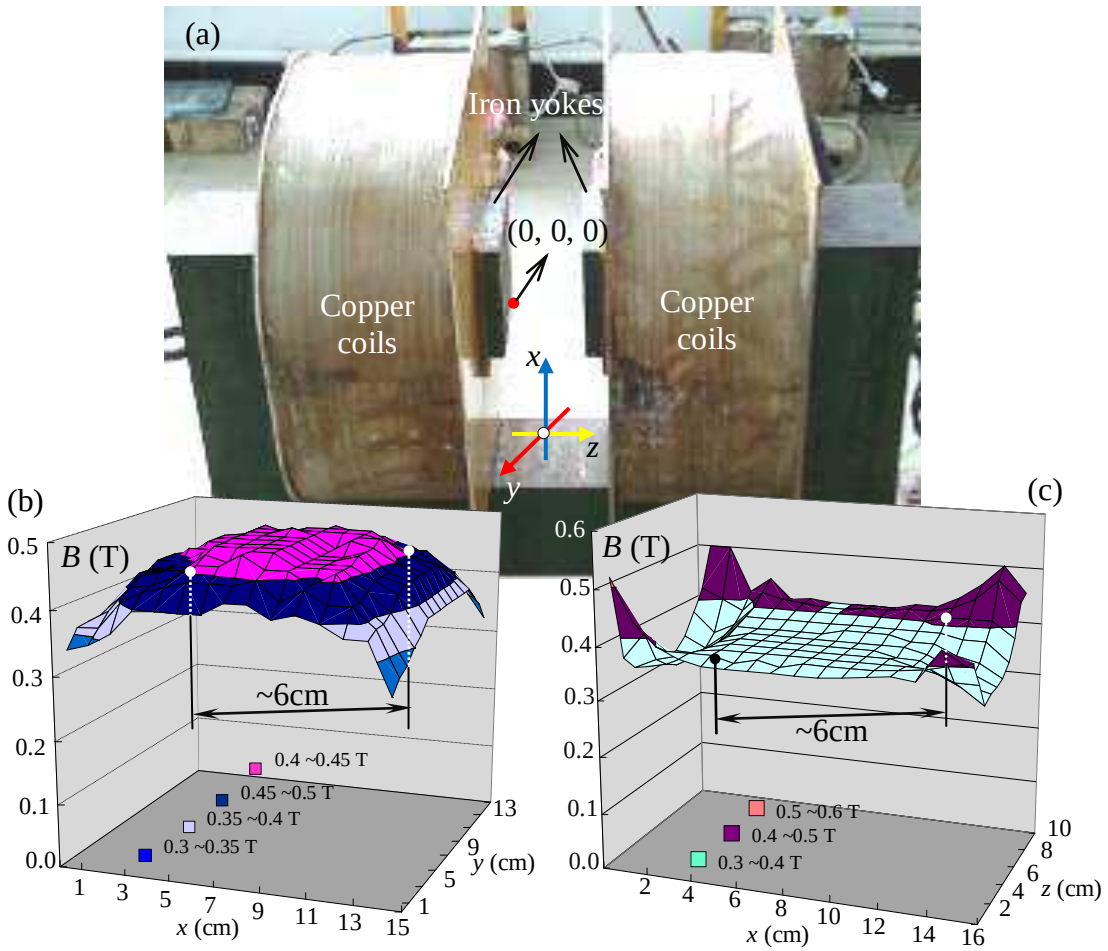

Figure 4.4 (a) Photo of electromagnet and the static magnetic fields distributing in *x*-*y* plane (b) at *z*=5cm and *x*-*z* plane (c) at *y*=6.5cm.

Figure 4.5 shows the general assembly drawing of experimental apparatus. Bridgman type furnace made by nonmagnetic materials with negligible effect on the field uniformity can reach 1200K with the precision of ±1K. A water-cooled can containing Ga-In-Sn liquid metal is used to cool down the sample that called liquid metal cooling (LMC). The thermal gradient in the specimen can be adjusted via controlling the temperature of the hot zone in furnace that is insulated from the LMC cylinder by a refractory disc. The high-purity alumina tube with prefabricated specimen inside is sealed to a stainless steel rod, and this rod is controlled by a high-accuracy servo motor. This realizes the vertical movement of the tube and the specimen with constant velocity while the furnace is being fixed at the same time. The pulling-down speed ranges from 0.5μm/s to 5000μm/s with the precision of 0.01μm/s. In order to obtain the shape of liquid-solid interface, quenching experiments were carried out via quickly withdrawing the specimen into the LMC can to cool the specimen down to the room temperature immediately. Processing conditions were adjusted to form a planar, cellular and dendritic interface. Longitudinal and transverse microstructures of samples were examined in the etched conditions with an optical microscope, and the solute distributions were analyzed by electron probe mass analysis (EPMA).

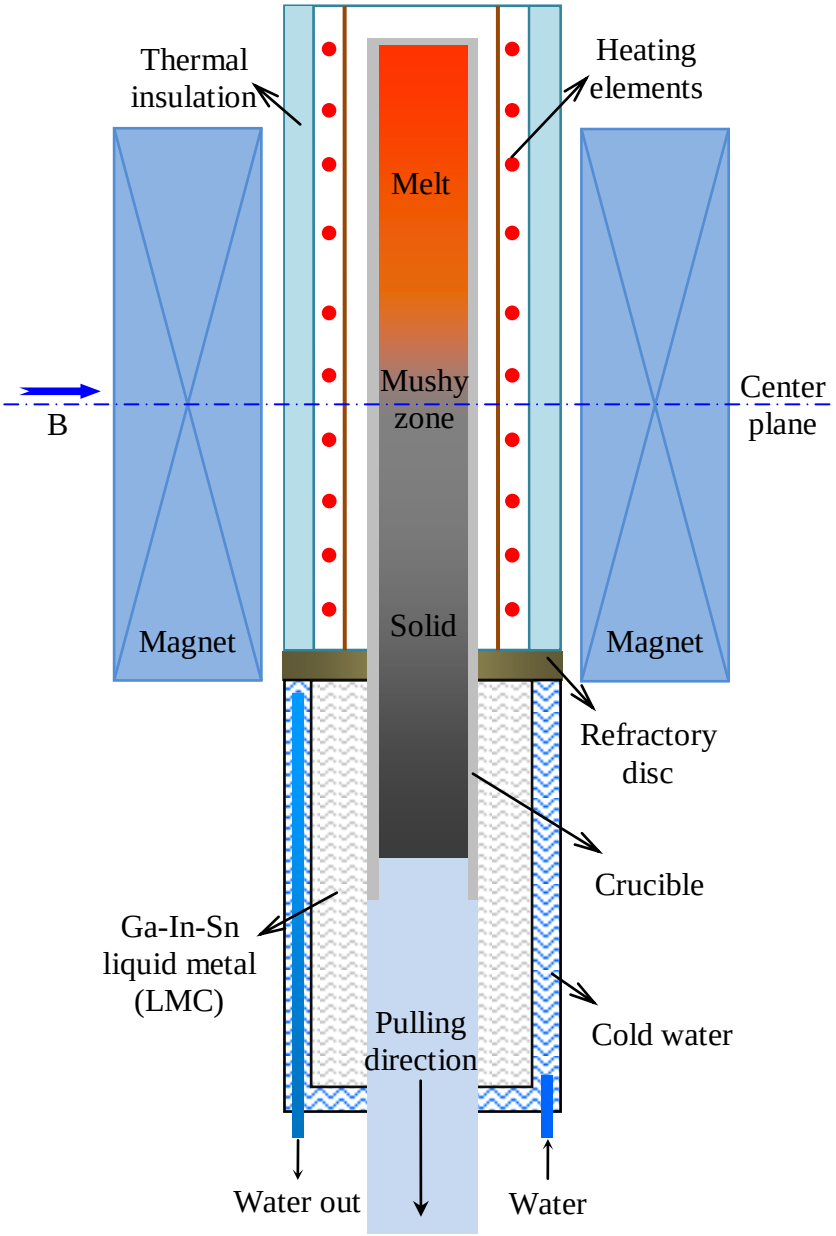

Figure 4.5 General assembly drawing of experimental apparatus used under external static traverse magnetic fields.

4.2.2 Results and discussions

As shown in figure 4.6 (a), typical planar liquid-solid interface has been achieved via pulling down the specimens of Al-0.85wt%Cu alloys at constant velocity, *R*, of 0.6μm/s and applying a constant thermal gradient, *G*, of 6000K/m. Kept all these conditions unchanged, directional solidifications were performed under different TMF flux intensities. The longitudinal structures of specimens obtained from these experiments are shown in figure 4.6 (b) to (d). It can find that the planar interface is almost flat when TMF is zero. Imposed a 0.05T TMF, planar interface can be achieved as well but its shape is not even anymore. The right part of the planar interface that adjoins to the wall of crucible became degenerated as shown in figure 4.6 (b). Increased the flux intensities of imposed TEM, figure 4.6 (c) and (d)

respectively shows the structure of liquid-solid interface obtained under 0.1T and 0.3T TMF. It suggests that the degeneration at the right part of the planar interface gradually disappears and becomes an entire flat interface when the TMF flux intensity is 0.3T.

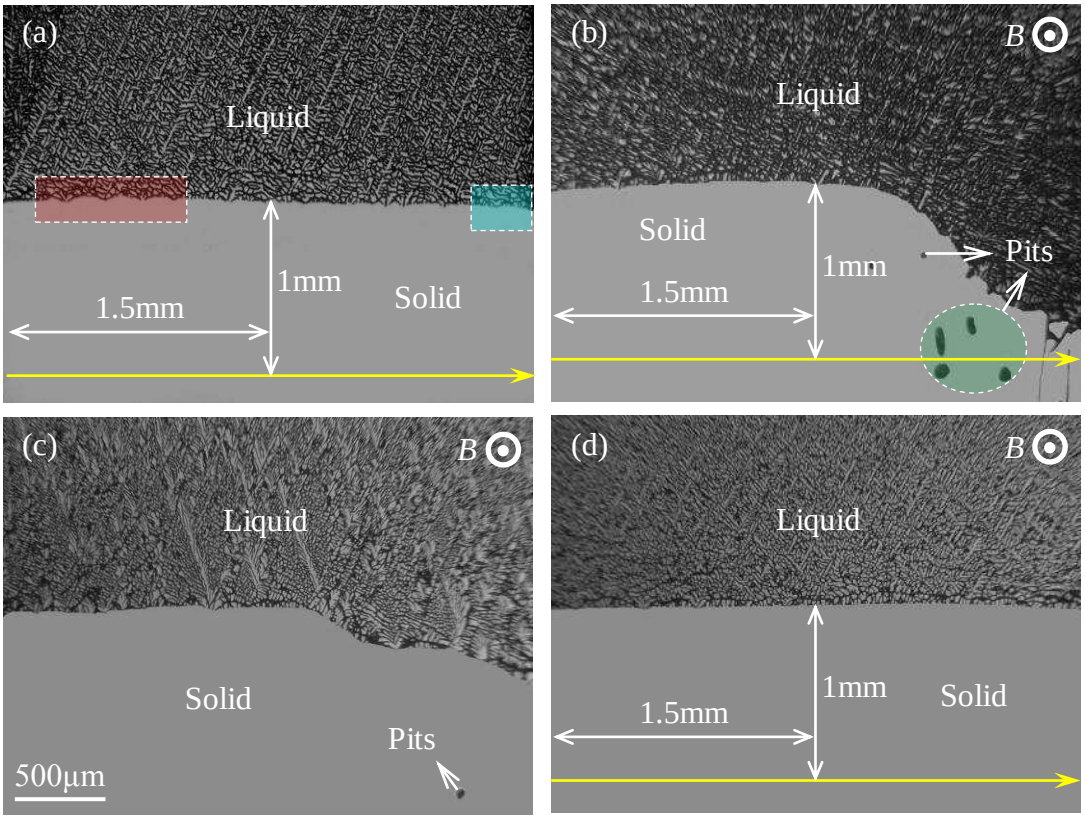

Figure 4.6 Longitudinal (parallel to the growth direction and perpendicular to the magnetic field) structure of planar interface of Al-0.85wt%Cu alloy solidified under different TMF (R=0.6μm/s; G=60K/cm): (a) 0T; (b) 0.05T; (c) 0.1T; (d) 0.3T.

It has been well known that liquid-solid interface shape results from the joint effects of local solute concentration, temperature field and thermal conductivities of the solid and the crucible [281]. For the present cases, it is reasonable to attribute the degenerations to solute enrichment in the melt in front the right part of the interface because both alloys and processing conditions remained unchanged. In fact, the appearance of pits in solid following the degenerated interface as shown in figure 4.6 (b) and (c) can demonstrate the enrichment of Cu solutes in this region because the instability occurs at the interface with higher solute concentration melt ahead when the other conditions are the same. Even though, distributions of Cu element along the horizontal line as indicated by the yellow arrows in figure 4.6 (a), (b) and (c) were analyzed by EMPA in order to prove the solute enrichment. The results are displayed in figure 4.7. These curves clearly show that apparent Cu element segregation forms at the right side of the sample solidified under a 0.05T TMF, whilst, distribution of Cu element is almost uniform when the planar interface is flat whatever it is solidified without or wiht a 0.03T TMF. This confirms that the melt in front of degenerated interface are enriched

because the solid with high Cu composition must be solidified from the melt containing more Cu solutes. Next, mechanism leads to this solute enrichment should be made clear.

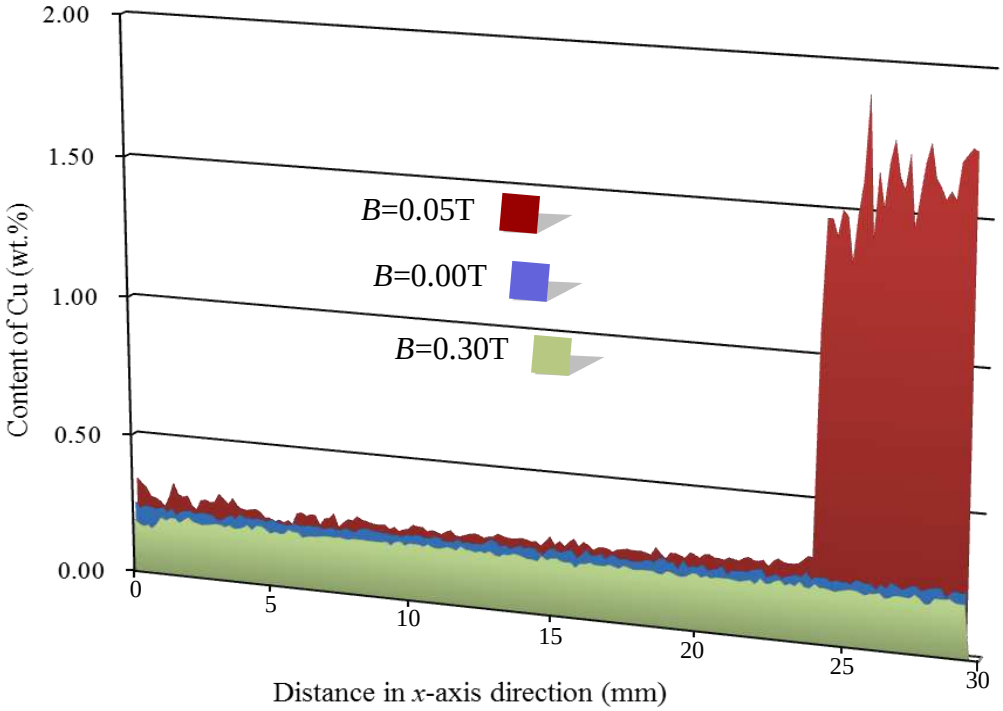

Figure 4.7 EPMA analysis of the distribution of Cu element along the horizontal lines at 1mm below the planar interface of directionally solidifying Al-0.85wt%Cu specimens. (R=0.6μm/s G=6000K/m)

According to the wide accepted fact that sufficient intense flows in melt close to the interface are capable to transport the rejected solutes [282] and discussions in chapter 3.3, it can argue that, the sole possibility to transport the rejected Cu solutes is TEM flows for the present case. Although TEC cannot appear if the planar interface is horizontal and perfectly flat with a vertical thermal gradient (no temperature difference existing along the interface), TEC can occur in the present cases because the planar interfaces are not perfectly flat as shown in figure 4.8. This figure is the magnified views of regions that outlined by the rectangle in figure 4.6 (a). Based on the classical interface stability theory [283-285], planar interface growth means that the perturbations of interface will not develop during solidification proceeding. So that perturbations or saying waves do exist at the interface. For this reason, the planar interface cannot be perfectly flat such as the waves at liquid-solid interface shown in figure 4.8 (a). Moreover, affect by the different surface tensions and wetting properties between the crucible and liquid or solid, their contacting angles cannot be 90 degrees. Consequently, slight curved interface must be obtained at the periphery as shown in figure 4.8 (b). Just these small waves and slight curved interface at the periphery of samples permit the appearance of TEC in the present cases, and how these currents act is respectively illustrated in figure 4.9 (a) and (b) with respect to the waves and curved interface.

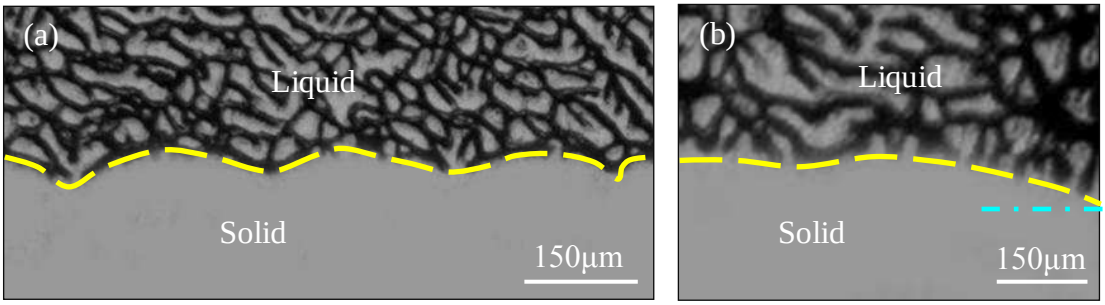

Figure 4.8 (a) View magnified from the region outlined by the red rectangle at the left side of figure 4.6 (a); (b) View magnified from the region outlined by the blue rectangle at the right side of figure 4.6 (a)

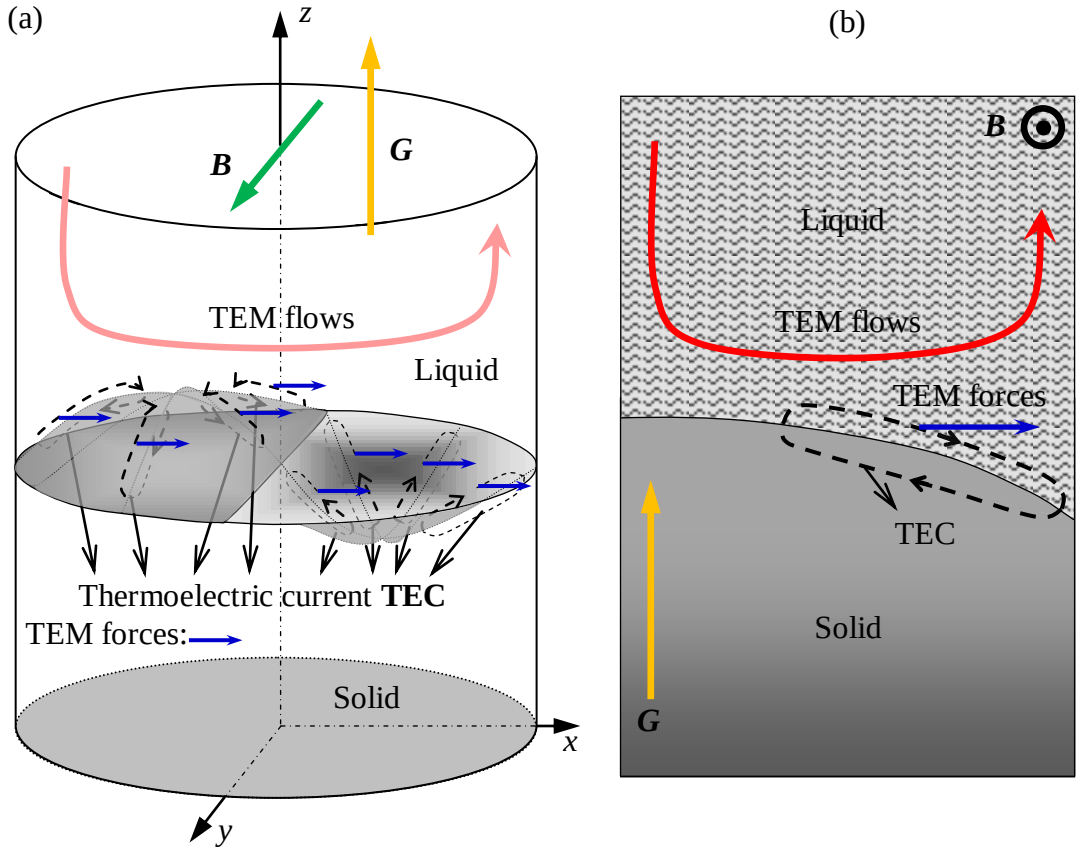

Figure 4.9 Schematic illustration of how TEC are caused by perturbations (a) and slightly curved (b) planar interface at the periphery of samples and the one-way flowing TEM flows produced by these TEC interacting with the TMF.

Based on equations 4.1 and material parameters in table 4.1, TEC in these experiments should act in the manner as indicated by the black dotted circles with arrows in figure 4.9. TEM forces are produced by interaction between these TEC and the imposed TMF and point to the same direction as marked by the blue arrows. Consequently, TEM flows in melt are driven and flow from the left to the right. Brought by such left-to-right flowing TEM flows the rejected Cu solutes must concentrate to the right side of samples, and the solutes enrichment can slow down the local growth velocity of the interface and then lead to the degeneration. In another aspect, the recovery of the degenerated part of planar interface under higher magnetic field can be explained by the damping effect of magnetic field as evaluated in

section 4.1. It seems the maximum velocities of TEM flows in these experiments appear under a 0.05T TEM that is slightly different from the evaluated B_{max} with typical length scale of 3mm that is 0.097T. This difference can be partly from the inaccuracy of parameters used in evaluations, such as the real thermal gradient both in liquid and solid cannot be a constant value of 6000K/m during the whole solidification process. In another aspect, 0.05T TMF may not be the real B_{max} for the planar interface growth because there are no directional solidification being conducted under TMF between 0.05T and 0.1T.

Investigations of the ability of TEM flows to modify the interface shape were taken on the cellular interface growth as well. Increased the pulling-down speed to 5μm/s, kept the same thermal gradient that is 6000K/m and used the same alloy that is Al-0.85wt%Cu, typical cellular interfaces were achieved in the absence of external magnetic field as shown in figure 4.10 (a). Additionally, longitudinal structure of liquid-solid interface of samples directionally solidified under 0.1T, 0.3T and 0.5T TMF are respectively displayed in figure 4.10 (b) to (d). It can be observed that except the slightly curved at the periphery of the sample the cellular interface shape is nearly flat in the case of no magnetic field. Similar to the phenomena observed in the planar interface growth, applying a relative weak TMF makes the interface become sideling to the right side, and the degree of the obliquity reaches the maximum when TMF is 0.1T. TMF higher than 0.1T make the cellular interfaces tend to gradually back to flat. Moreover, the corresponding transverse structures at the position that 100μm below liquid-solid interface are examined and shown in figure 4.10 (e) to (h) respectively. It can be noticed that macrosegregation occurs and corresponds to the concave part of the cellular interface indicated in the longitudinal structure. This suggests that Cu solutes must be transported to these regions during solidification proceeding. Considering the area of macrosegregation can reasonably represent the magnitudes of segregations, it can also find that the macrosegregation reaches the maximum under 0.1T TMF as circled by the yellow dotted lines.

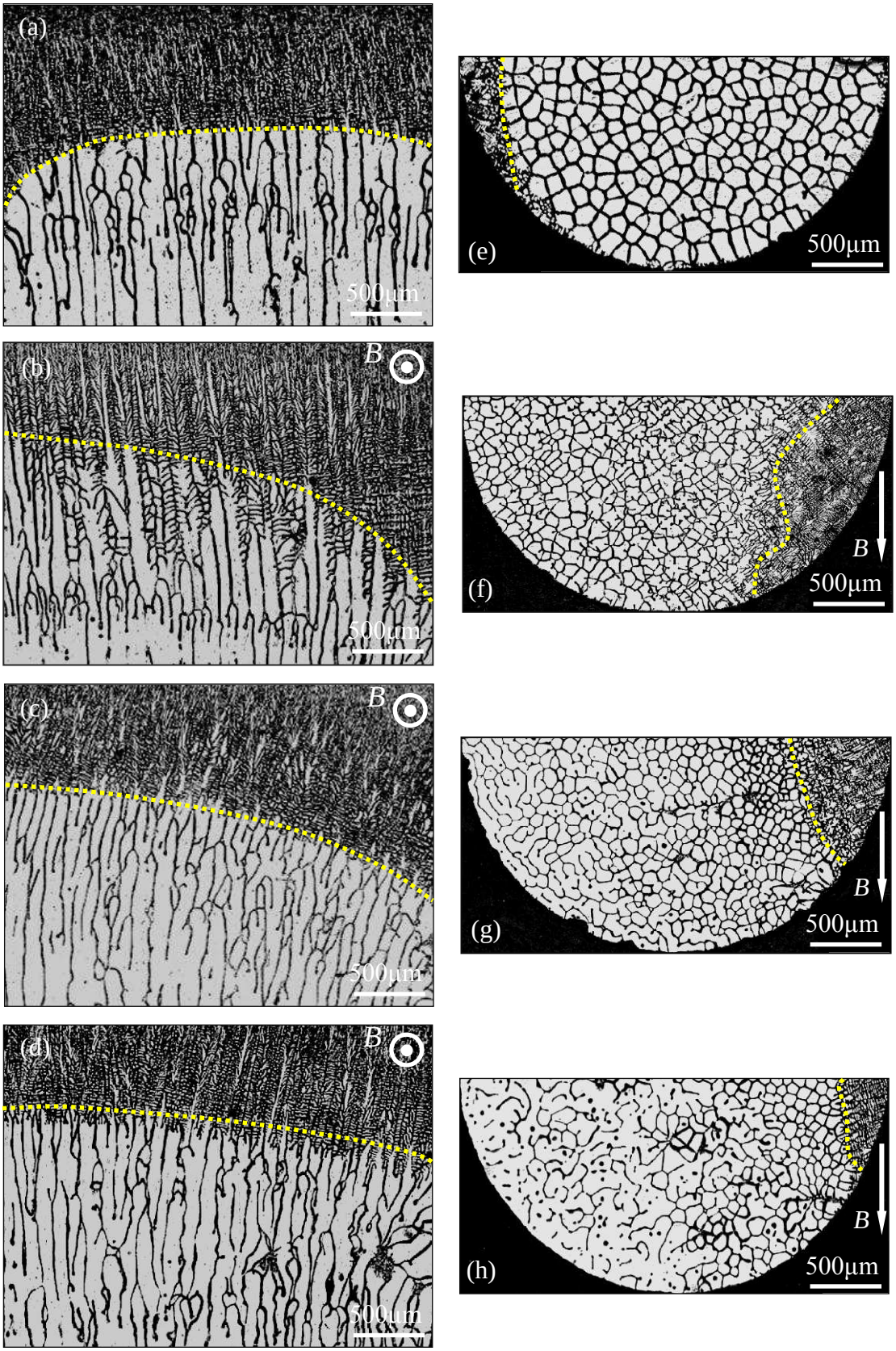

Figure 4.10 Longitudinal (a-d; parallel to the growth direction and perpendicular to the magnetic field) structure of cellular interface of Al-0.85wt%Cu alloy solidified under various TMF intensities and their corresponding transverse (e-h; perpendicular to the growth direction and parallel to the magnetic field) structure at the position that 100μm below the liquid-solid interface (R=5μm/s; G=6000K/m): (a) & (e) 0T; (b) & (f) 0.1T; (c) & (g) 0.3T; (d) & (h) 0.5T.

Furthermore, because it has been well know that flows or convections (natural or forced) within the mushy zone can decrease the sizes of cells [286-288]. The conclusion that left-to-right flowing TEM flows exist in the cellular interface growth and are capable to transport the rejected Cu solutes from the left to the right can be confirmed via comparing the size of cells. Therefore, the sizes of cells solidified under different TMF intensities were measured. Figure 4.11 shows the curve of the average sizes of those cells plotted versus the corresponding magnetic field flux intensities, which suggests that the sizes of cells decrease to the minimum when the imposed TMF is 0.1T and increase when TMF further rise. This demonstrates that there must be flows in the mushy zone once the TMF is presnt, and these flows should have the same flowing direction that from the left side of the sample to the right, moreover, such flows shoule speed up until TMF is 0.1T and slow down under higher TMF. Compare to the character of TEM flows predicted in accordance to the cellular interface growth conditons, it can conclude that the variation the sizes of cells should be attributed to the occrance of TEM flows in the cellular interface growth under TMF.

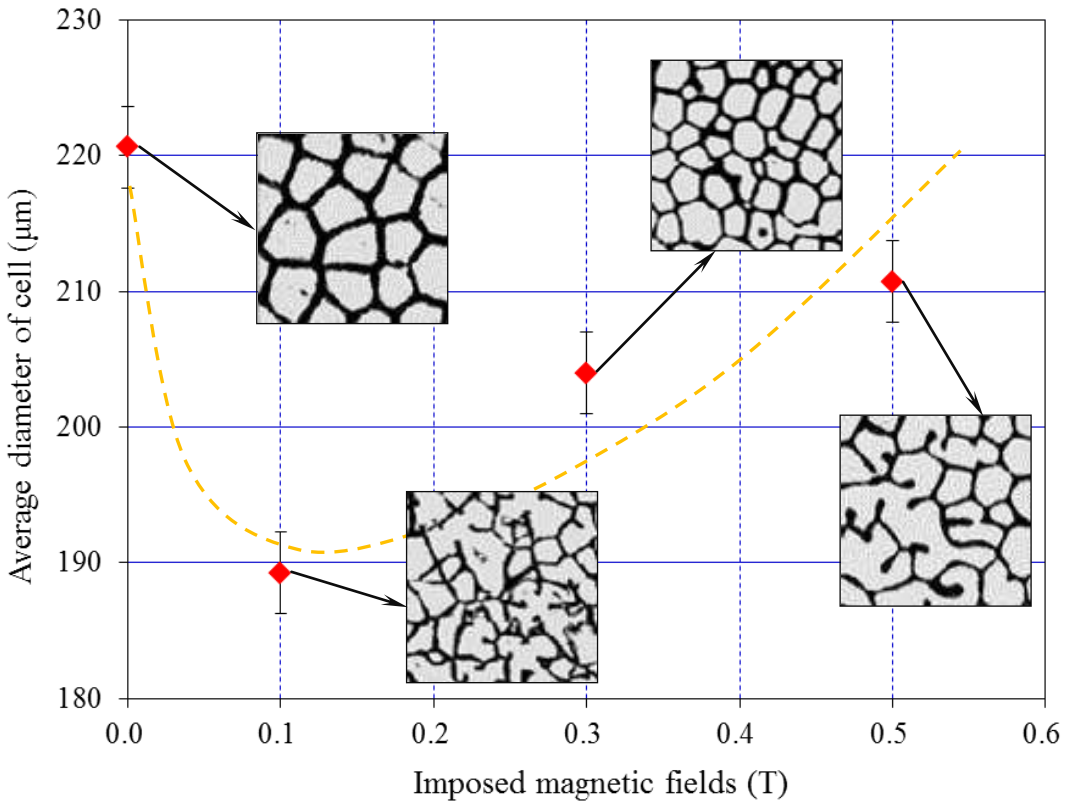

Figure 4.11 The average sizes of cells solidified under different TMF intensities.

How TEM flows appear and behave in the cellular interface growth process are illustrated by figure 4.12, which is similar to the schematic shown in figure 2.4 (c) and (d) in chapter 2.1.3. Use equation 4.1 and material parameters in table 4.1, direction of TEC along the cell can be determined and indicated by the light-blue dotted circles with arrows in figure 4.12. Intereactiong of these TEC and the imposed TMF produces TEM forces both in liquid

and solid, as marked by the green arrows in figure 4.12, and these TEM forces all point to the right that positive *x*-axis direction. TEM forces in liquid are able to drive TEM flows within the intercellular spaces as revealed by the red arrows in figure 4.12. Such TEM flows may cause the global one-way flowing motions of melt close to the front of the mushy zone, which are simply represented by the pink lines with arrows in figure 4.12. With those left-to-right flowing TEM flows, rejected Cu solutes should be transported from the left side of specimens to the right. This results in the appearance of macrosegregation and the degeneration of interface at these places as reflected by figure 4.10. Moreover, it should be noticed that the maximum velocities of TEM flows were achieved under a 0.1T TMF in this cellular growth case, which is higher than 0.05T the one obtained in planar interface growth case. This is because the typical length of cellular interface is smaller than that of planar interface. Indeed, 0.1mm is usually chosen as the typical length of cellular interface in the evaluations of TEM flows, whilst, 1mm is used for planar interface case. The evolution of velocities of flows in melt with increasing TMF indicated by these cellular interface growths perfectly agrees with that obtained from evaluations of TEM flows in section 4.1, which can confirm that the flows in these experiments are TEM flows from another aspect.

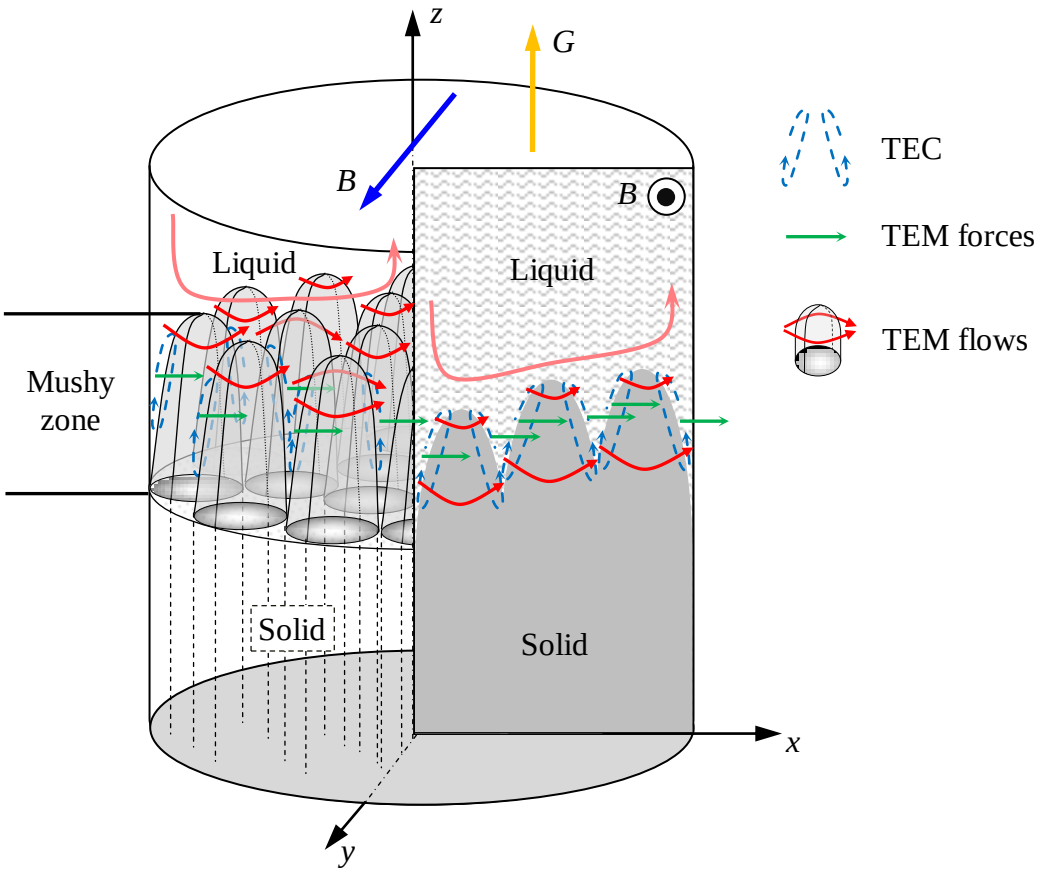

Figure 4.12 Schematic illustration of how TEC appear in cellular interface growth.

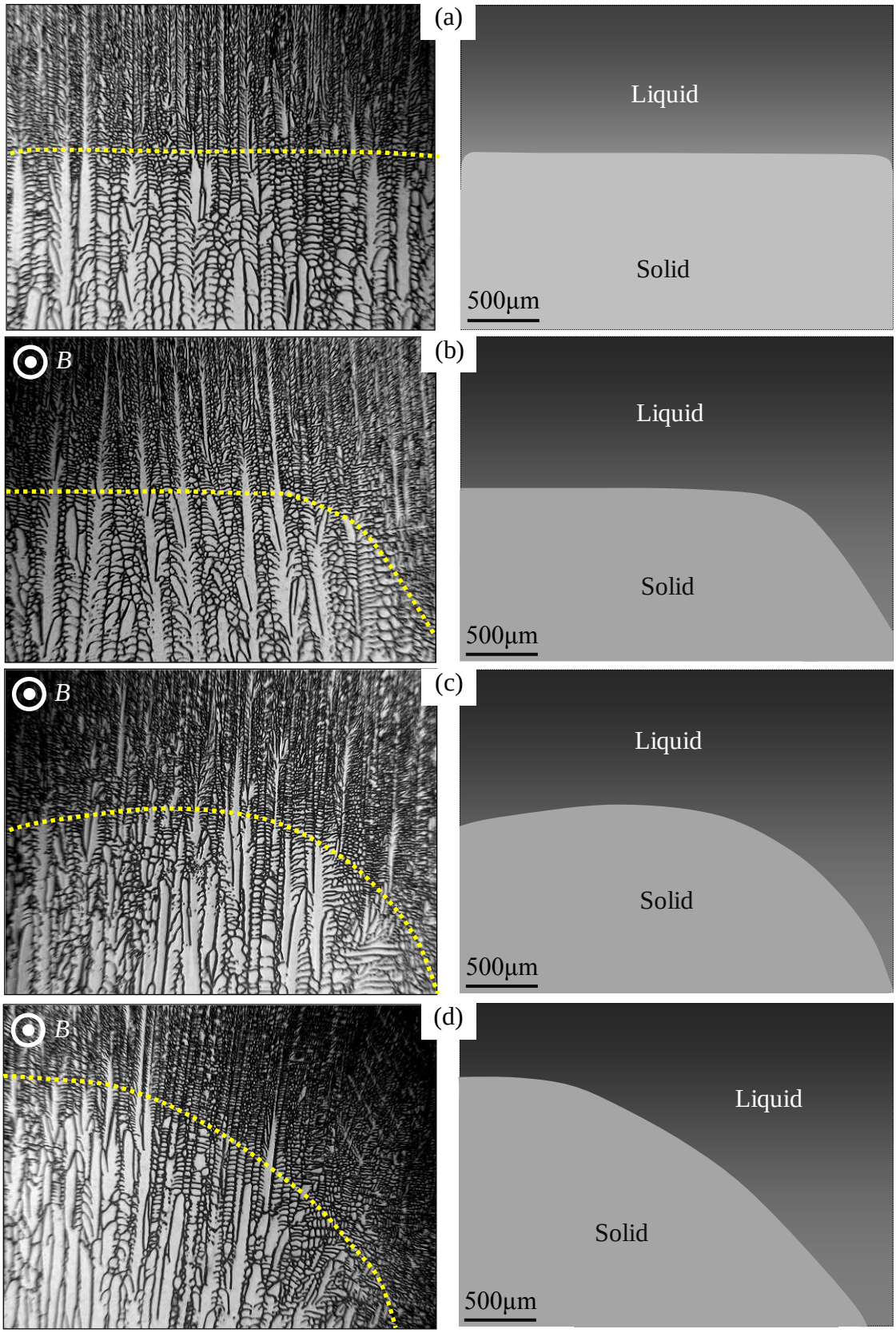

Figure 4.13 Longitudinal (parallel to the growth direction and perpendicular to the magnetic field) structure of dendritic interface of Al-2.5wt%Cu alloy solidified under various TMF flux intensities and their corresponding interface shape profile (R=50μm/s; G=6000K/m): (a) 0T; (b) 0.05T; (c) 0.3T; (d) 0.5T.

Using the higher compositional alloys of Al-2.5wt%Cu, increasing the pulling-down speed to 50μm/s and applying the thermal gradient of 6000K/m, typical dendritic interface were achieved as shown in figure 4.13 (a). The investigations of influence of TEM flows on dendritic interface growth were taken via imposing differernt flux intensities of TMF with other process conditions unchanged. The interface morphology and the corresponding profile of their shape obtained under 0.05T, 0.3T and 0.5T are shown in figure 4.13 (b) to (d) respectively. Similar to what obtained during cellular interface growth, it can observe that the shape of dendritic interface is nearly flat when TMF is absent. Presence of TMF leads to the degeneration at the right part of dendritic interface. However, dislike the planar and cellular interface cases, the degree of the obliquity of dendritic interface constnatnly increased till the TMF is 0.5T that the maximum magnetic field our electromagnet can provide. This is understandable because higher magnetic field is needed for TEM flows reach the maximum velocities when the typical length is smaller. Based on the evaluated of TEM flows with the typical length of 0.01mm that similar to the width of interdendritic space, TEM flows should reach the maximum velocities under about 3T TMF in dendritic interface growth. Therefore, decrese of the degrees of dendritic interfaces' obliquity cannot be observed in these experiments.

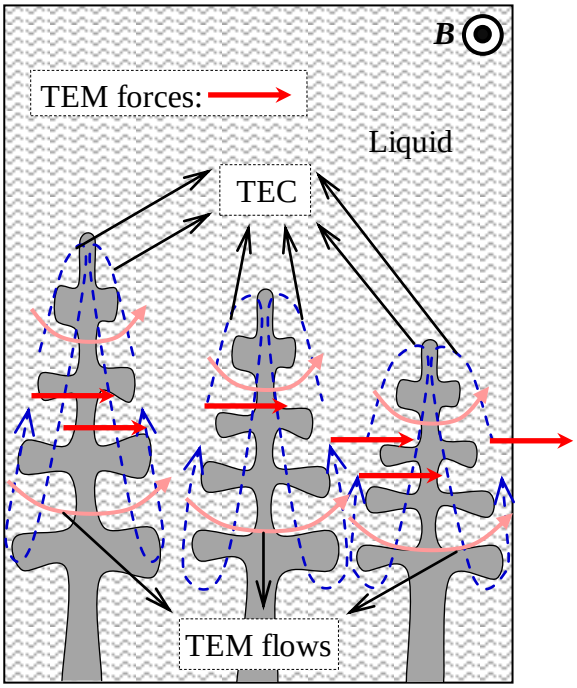

Figure 4.14 Schematic illustration of how TEC appear in dendritic interface growth.

Similar to the schematic illustration in figure 4.12, the left-to-right flowing TEM flows can be produced by TEC interacting with TMF as simply illustrated in figure 4.14. With such TEM flows, the rejected Cu solutes come from the left side of specimens to the right and concentrate there. Consequently, the solutes enrichment causes the degeneration of the

corresponding parts of dendritic interfaces. Although thermoelectric potential exist along the secondary arms as well it resulting TEC should be generally along the primary arms of dendrites. This is because that the electric currents always flow through the smallest electrical resistivity path, and the resistivity is proportional to the reciprocal of the dimensions of subject. Moreover, considering the typical lengths of the primary and secondary arms of dendrites are respectively about 10 and 1 micrometer, the velocities of TEM flows between secondary arms should be 10 times slower than those between primary arms. This permits us to concern TEM flows produced by the TEC along the primary arms of dendrites and TMF only. However, it is also needed to emphasize that explanation and discussion above are valid only if the TMF flux intensity is lower than the one corresponding to the maximum velocities of TEM flows when the typical length is 0.01mm.

Experiments above have proved the existence and the ability of TEM flows to affect the liquid-solid interface shape during directionally solidifying the alloys under TMF. Moreover, the evolution of the velocities of TEM flows with the imposed magnetic fields indicated from these experiments perfectly agrees with that obtained by evaluations. The deviations of the critical magnetic fields corresponding to the maximum velocities of TEM flows between experiments and evaluations should be attributed to the inaccuracy parameters used in evaluations, such as the typical length scales used for planar, cellular or dendritic interface may be not precise. Although the experimental results have been qualitatively explained by schematic illustrations 3D simulations with the same conditions used in above experiments are performed to get quantitive information about TEM flows in directional solidification of alloys in the following section.

4.3 Numerical simulation of thermoelectric magnetic (TEM) flows in directional solidification of Al-Cu alloys under static magnetic field

Before consider the more general case, 3D simulations of TEM flows are firstly performed with the configuration that the planar interface is slightly curved at the periphery of the sample to further confirm and investigate how TEM flows appear and behave in the planar interface growth case. After that, a convex liquid-solid interface as the one employed to illustrate TEME in figure 2.3 (d) is selected to perform the 3D simulations of TEM flows for the general cases. This is because that except the planar interface the convex liquid-solid interface can be regarde as one cell or the tip of one dendrite when it has the same dimensions with the cells or dendrites. Moreover, how the velocities of TEM flows vary with the increasing magnetic fields is examined as well. In order to extend the knowledge on how TEM flows behave under different magnetic fields, 3D simulations of TEM flows for the

general cases are performed with both TMF and axial magnetic field (AMF). Thanks to the simulation method that introduced and verified in chapter 2.3, TEM forces in solid can be achieved from the computed results of TEM flows as well. Therefore, TEM forces in solid are aslo discussed in this section.

4.3.1 Simulation of TEM flows in directional solidification under a transverse static magnetic field

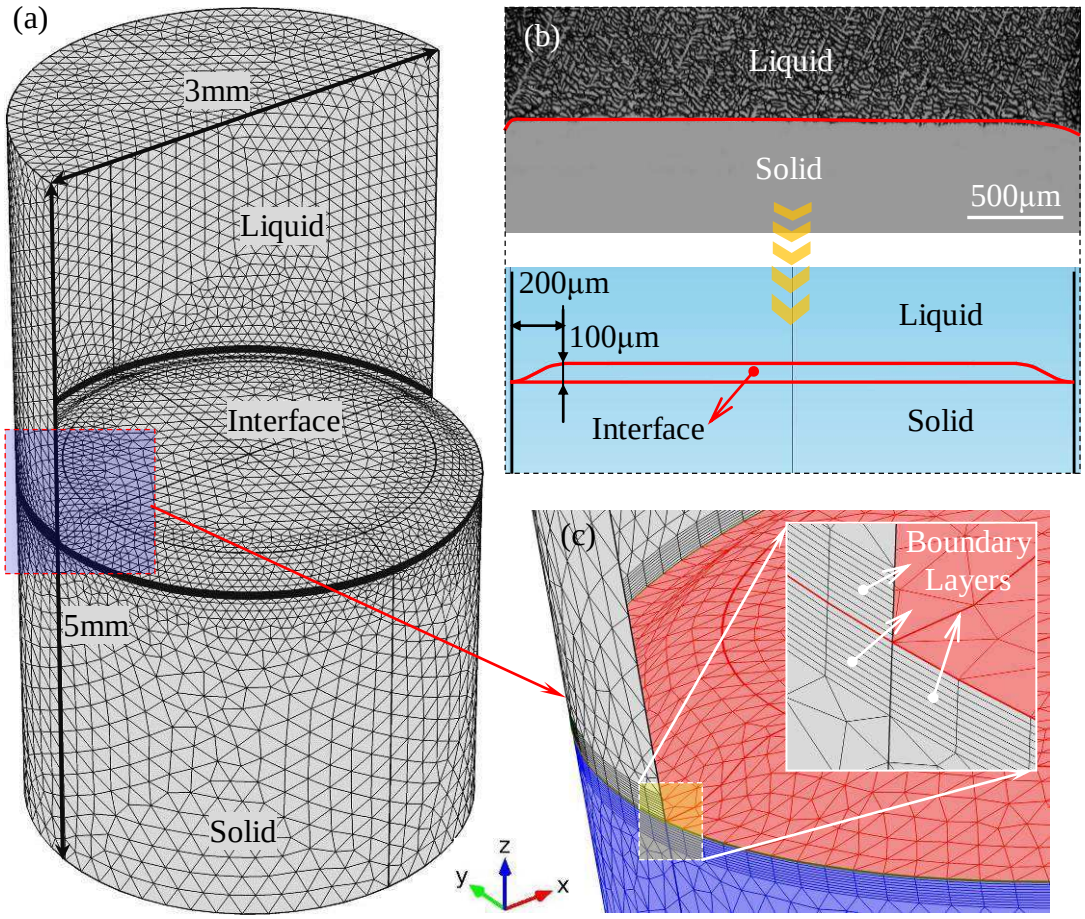

Figure 4.15 (a) Meshes and dimensions of the computed domain; (b) Illustration of the similarity between structure obtained in planar interface growth and the geometry used in 3D simulations of TEM flows; (c) Boundary layer refinement.

In order to confirm the possibility of the occurrence of TEC and TEME in the planar interface growth cases, the similar geometry was built as shown in figure 4.15 (b). Although two types of structures as shown in figure 4.8 may lead to TEC and then TEME only the small curved shape at the periphery of interface is concerned here. It is because that the waved interface can be approximately represented by the convex liquid-solid interface as well. Considering the simulation method has been introduced and verified in chapter 2.3, only the meshes and geometry used in the 3D simulations of TEM flows are respectively illustrated in figure 4.15 (a) and (c). Triangular meshes were created in solid under the physical phenomena control and in liquid under the fluid flow control. Besides, the liquid-solid interface was

refined by adding 10 boundary layers with 5μm in thickness to both solid and liquid sides as shown in figure 4.15 (c).

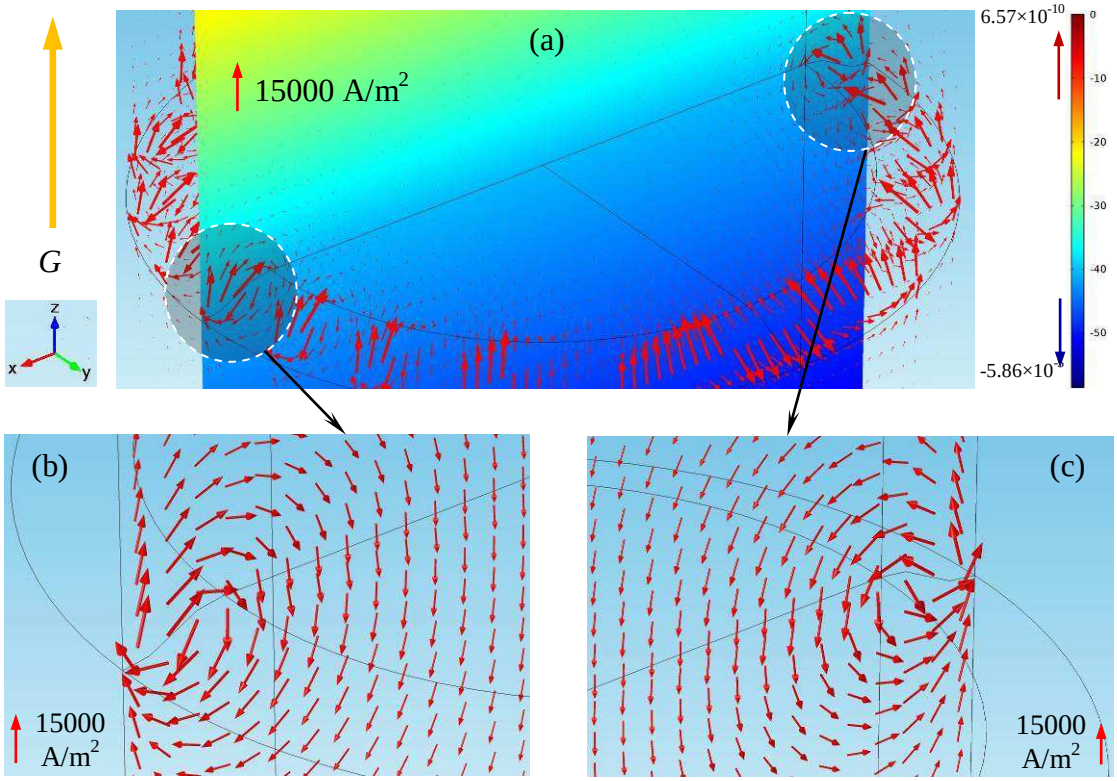

Figure 4.16 (a) 3D view of computed thermoelectric potential (colored slice) and TEC (red arrows), and the unit of legend is V; (b) & (c) Magnified view of TEC distribution in the regions marked by the circles in figure (a). (*G*=6000K/m)

Used the parameters list in table 4.1 and combined the COMSOL predefining electric current and heat transfer modules, how TEC behave was simulated. Figure 4.16 shows the 3D view of the computed thermoelectric prtential and the corresponding TEC. It can observe that thermoelectric potential gradually increases from the bottom to the top with the applied thermal gradient, and TEC mostly concentrate at the vicinity of liquid-solid interface, particularly, at the peripheral curved places. The magnified view of regions marked by the circles in figure 4.16 (a) show that TEC close themselves along the curved interface. Further, imposing a 0.01T TMF and adding the fluid flow module, the TEM forces and flows are simulated and shown in figure 4.17 and 4.18 respectively. Because the N-S equation was solved in both liquid and solid TEM forces in liquid and solid can be achieved together and respectively shown in figure 4.17 (a) and (b). In liquid, TEM forces in the region very close to the crucible wall point to negative *x*-axis direction, and reversely, in the inner region they point to positive *x*-axis direction. In solid, TEM forces point to positive *x*-axis direction at the top part of interface and to the opposite direction at the bottom part of interface. TEM flows driven by such TEM forces in liquid are shown in figure 4.18, which suggests that their maximum velocities appear at the curved interface region. Moreover, it can be found that

TEM flows having maximum velocities mostly flow to negative *x*-axis direction at both positive and negative *y*-axis sides of the interface when we observe the flows field from the top of the crucible as shown in figure 4.18 (b) . The backflows return in the region higher in bulk liquid as indicated by figure 4.18 (c). Given the Al-0.85wt%Cu alloys are directionally solidified with such TEM flows in melt, it can image that Cu solutes rejected from the flat interface should be brought by the backflows to the positive *x*-axis side and sink down to the concave interface region because they are heavier than the surrounding melt. After that, these solutes together with the Cu solutes rejected from the curved interface are all transported to the negative *x*-axis side by the most intense TEM flows at the vicinity of curved interface. Consequently, melt at the region marked by the yellow circle in figure 4.18 (b) and (c) is greatly enriched by Cu solutes. In fact, if see the *x*-*z* plane from positive *y*-axis it can have the same view as shown in figure 4.6, and it can know that the sideling interface obtained when the directional solidification of Al-0.85wt%Cu alloys were conducted under weak TMF should be attributed to the TEM flows shown in figure 4.18. This further demonstrates the explanation that the small curved liquid-solid interface at the periphery can be the reason for the appearance of TEM and thus TEM flows in the nearly flat planar interface growth.

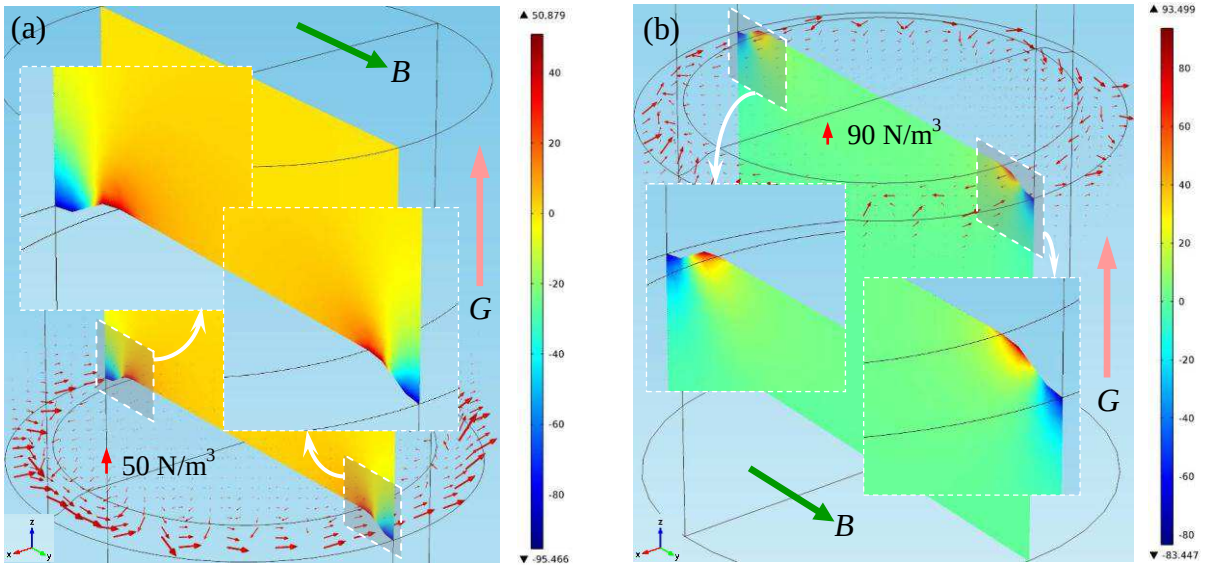

Figure 4.17 3D views of computed TEM forces in liquid (a) and solid (b), in which the colored slices denote the magnitudes of the *x* component of TEM forces and red arrows present the norm TEM forces, and the unit of legend is N/m^3. (*B*=0.01T, *G*=6000K/m)

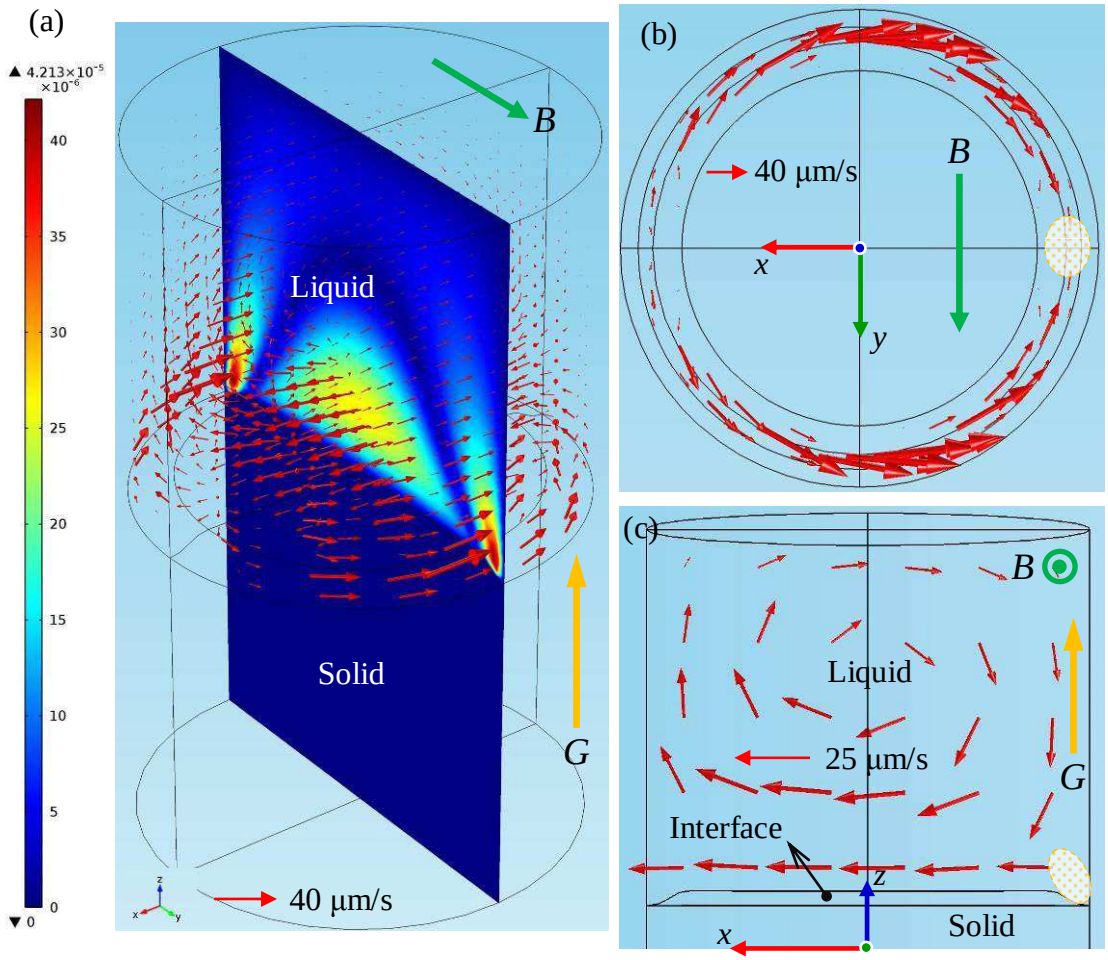

Figure 4.18 (a) General view of computed TEM flows (red arrows presente flow field, the colored slice is the magnitude of the *x* component velocities of TEM flows), and the unit of legend is m/s; (b) TEM flows near the interface seen from positive *z*-axis; (c) TEM flows in bulk liquid seen from positive *y*-axis. (*B*=0.01T, *G*=6000K/m)

Because the configuration with convex liquid-solid interface as shown in figure 4.19 can reasonable stand for cellular or dendritic morphologies when it has the comaprable dimensions. The examination of how the velocities of TEM flows vary with constantly increasing magnetic field can be made by 3D simulations of TEM flows with such configureation. In another aspect, dependence of the critical magnetic field responding to the maximum velocities of TEM flows on the typical length scale can also be investigated when set the diameter of such geometry as 1mm, 0.1mm or 0.01mm. Besides, as indicated in figure 4.20, *H*/*D* is remained constant in order to make sure the shap of interface to be the same when change its diameter. Triangular meshes were created under fluid flow condition control in liquid and physical phenomena control in solid. Meshes near the interface was refined by adding 10 boundary layers to both liquid and solid sides as shown in figure 4.19 (d). The thicknesse of these boundary learyers is respectively 10μm for 1mm diameter geometry, 1μm for 0.1mm and 0.1μm for 0.01mm.

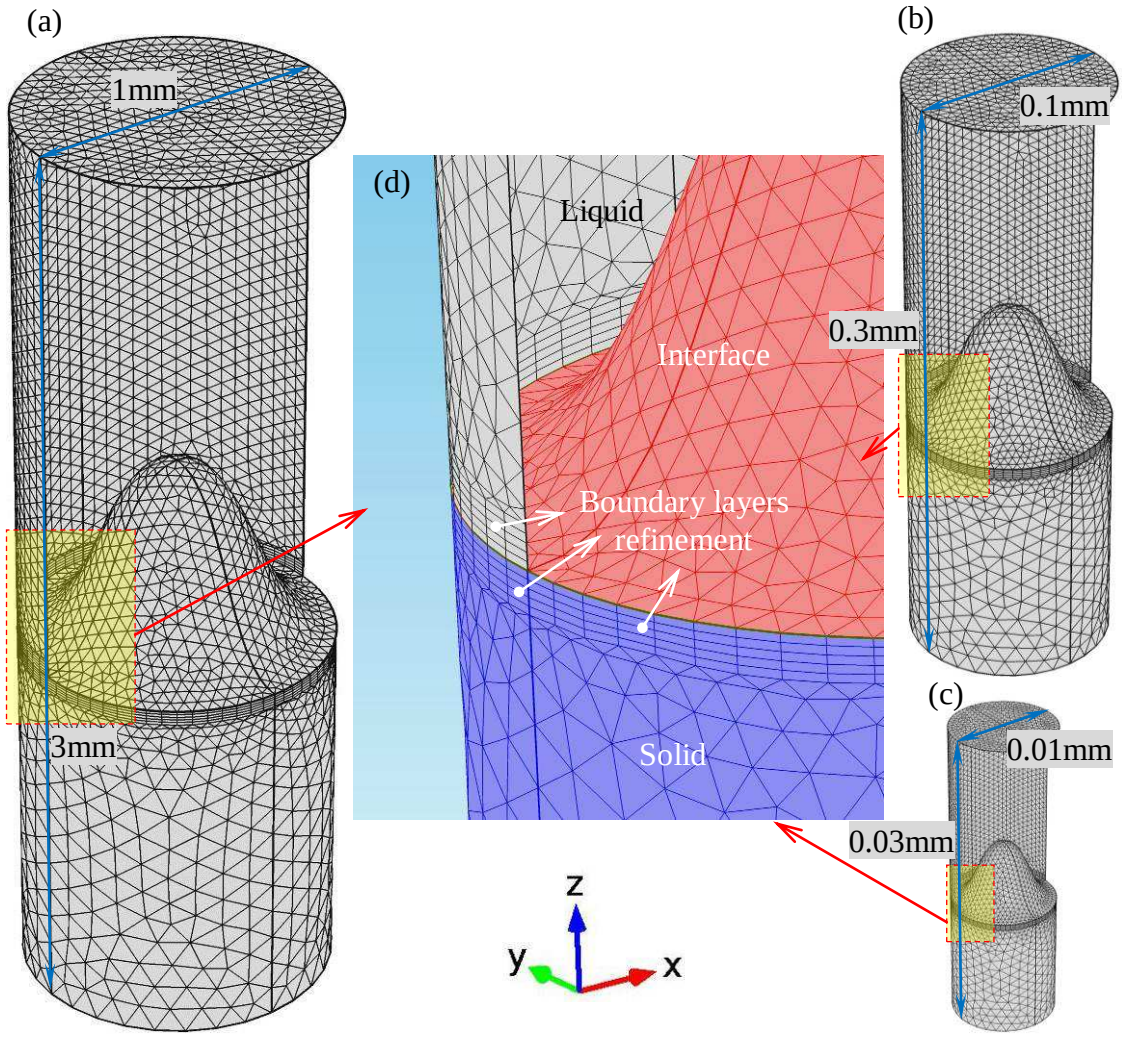

Figure 4.19 Meshes and dimensions of three different sizes geometries (a) to (c) used in 3D simulations of TEM flows and the boundary layer refinement (d).

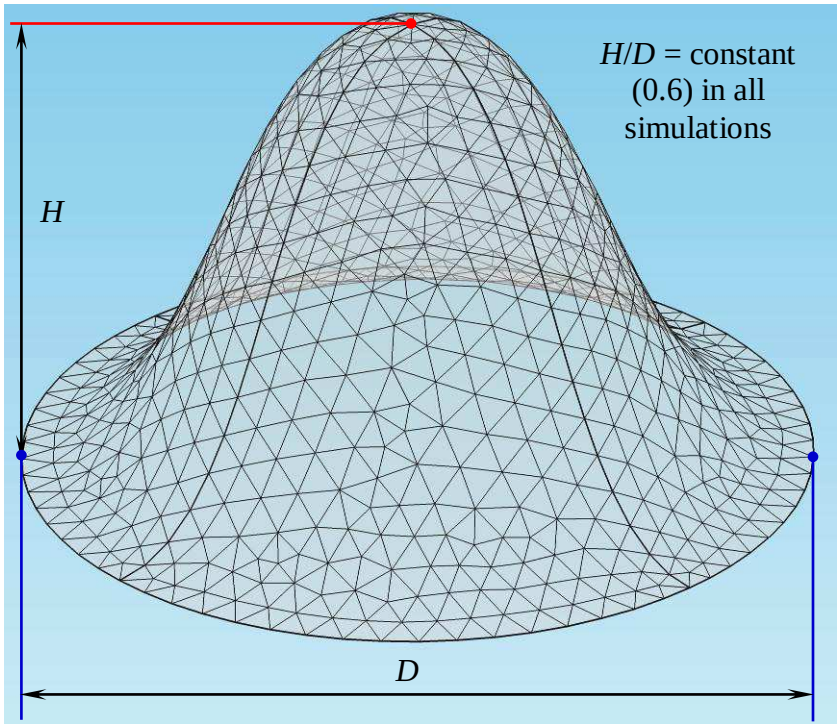

Figure 4.20 Illustration of dimensions of the convex liquid-solid interface shape that should be kept unchanged via setting H/D as a constant.

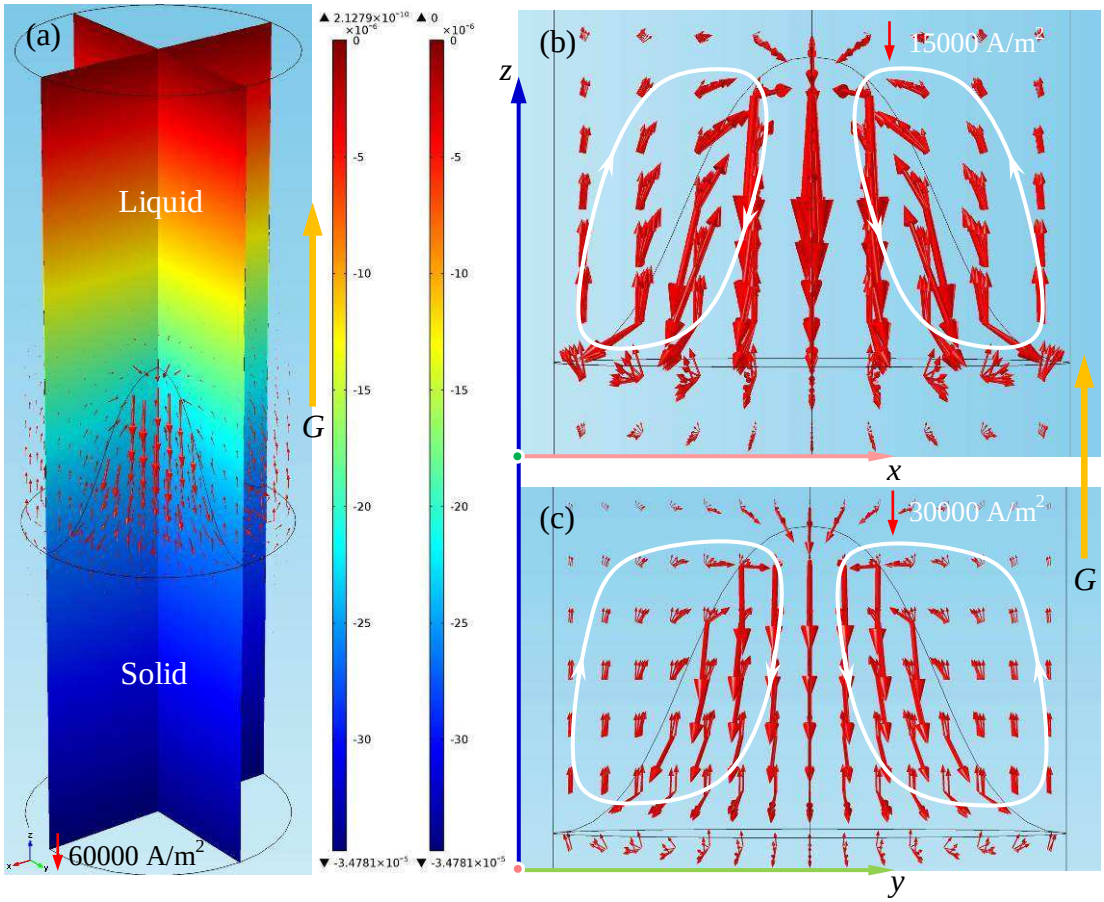

Figure 4.21 (a) General 3D view of computed thermoelectric potential (colored slices) and TEC (red arrows), and the unit of the legend is V; (b) TEC seen from positive *y*-axis; (c) TEC seen from positive *x*-axis. (*G*=6000K/m)

Combined the COMSOL predefining electric current and heat transfer modules and employed the relevant parameters list in table 4.1, TEC generated by applying a constant thermal gradient of 6000K/m was simulated with the geometry shown in figure 4.19 (a) that 1mm in diameter. Figure 4.21 shows the computed thermoelectric potential and the corresponding TEC. It can see from the general 3D view shown in figure 4.21 (a) that the thermolelectric potential is coincident with the applying thermal gradient and the corresponding TEC mostly concentrate near the liquid-solid interface. Magnified the region near interface, figure 4.21 (b) and (c) shows the view of TEC seen from positive *y*- and *x*- axis respectively. These two figures suggest that TEC form the circuits along the liquid-solid interface and have the most intense densities in the region near interface. Further, it can find that TEC around the entire convex interface flow in the same direction as indicated by the white circles with arrows. It must be noticed that TEC at the middle part of solid are parallel to each other, which should be attribute to the assumption that ATP of solid is constant. This agrees with the predictions made by analytical calculation in chapter 2.3.2.

Imposed a 0.1T TMF in positive *y*-axis direction, both TEM forces and TEM flows can be simulated by adding the fluid flow module to the previous electric current and heat transfer

modules. Figure 4.22 shows the computed TEM forces in liquid and in solid respectively. Similar to the results shown in figure 4.17 (b), TEM forces have two opposite directions in solid. At the top and in the middle part of the solid side of interface TEM forces point to positive *x*-axis, and inversely, at the low and peripheral part of interface TEM forces in solid point to negative *x*-axis as marked by the magnified picture inserted in figure 4.22 (b). TEM forces in liquid have two reversed directions as well. The ones in the concave region of interface orientate to negative *x*-axis, and the others in front of the convex region of interface are in positive *x*-axis direction. The behavior of TEM flows driven by such TEM forces in liquid is shown in figure 4.23. Because TEC are very close to the liquid-solid interface TEM flows also gather in the interface nearby region as shown in figure 4.23 (a). Moreover, it can find that the most intense TEM flows appear surround the convex interface and locate at its concave region and these TEM flows unidirectionally flow from positive *x*-axis to the negative as revealed by by red arrows in figure 4.23 (b) and (c). The backflows flow through the region in melt ahead of the top of interface. Carried by such kind of TEM flows, the rejected solutes must be gathered at the places as pointed out by the yellow circles in figure 4.23 (b) and (c) and make this parts of interface degenerate.

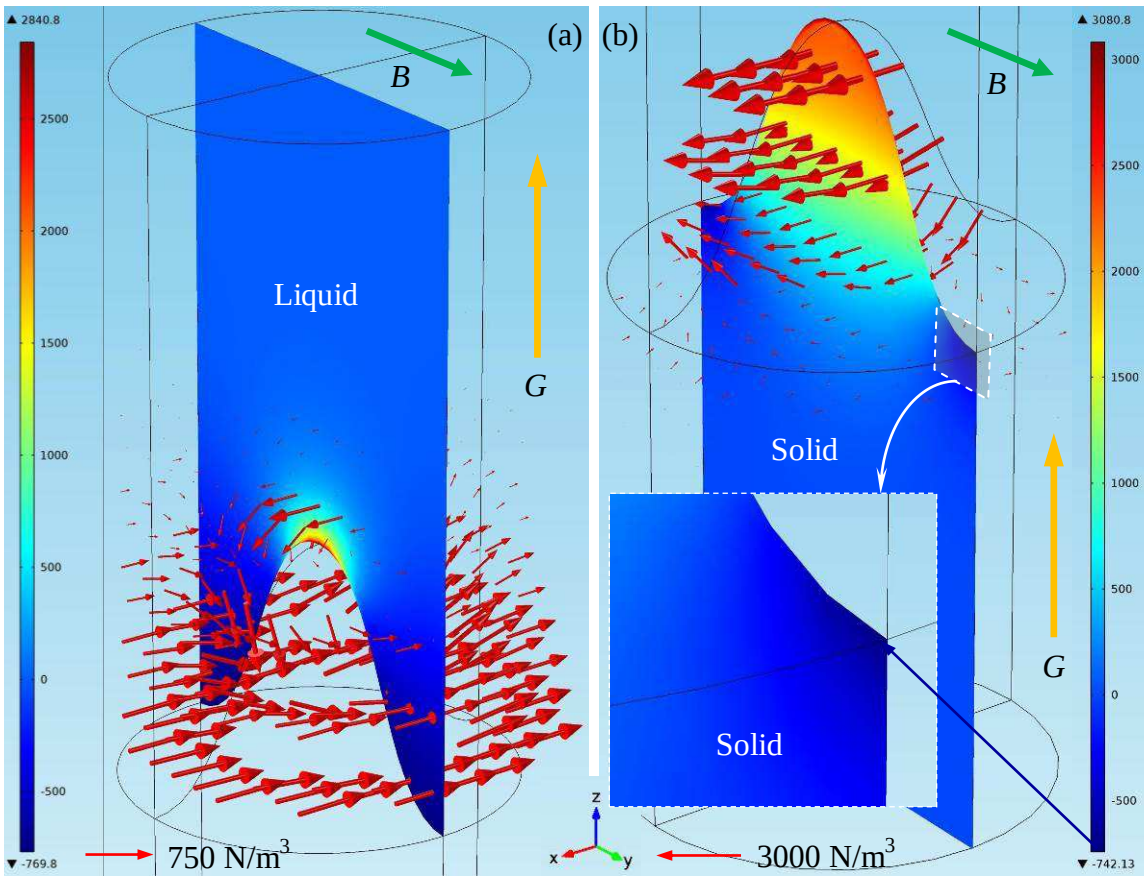

Figure 4.22 Computed TEM forces (colored slice is the magnitude of the *x* component of TEM forces and red arrows denote the norm TEM forces), and the unit of legend is N/m^3. (a) TEM forces in liquid; (b) TEM forces in solid. (*B*=0.1T, *G*=6000K/m)

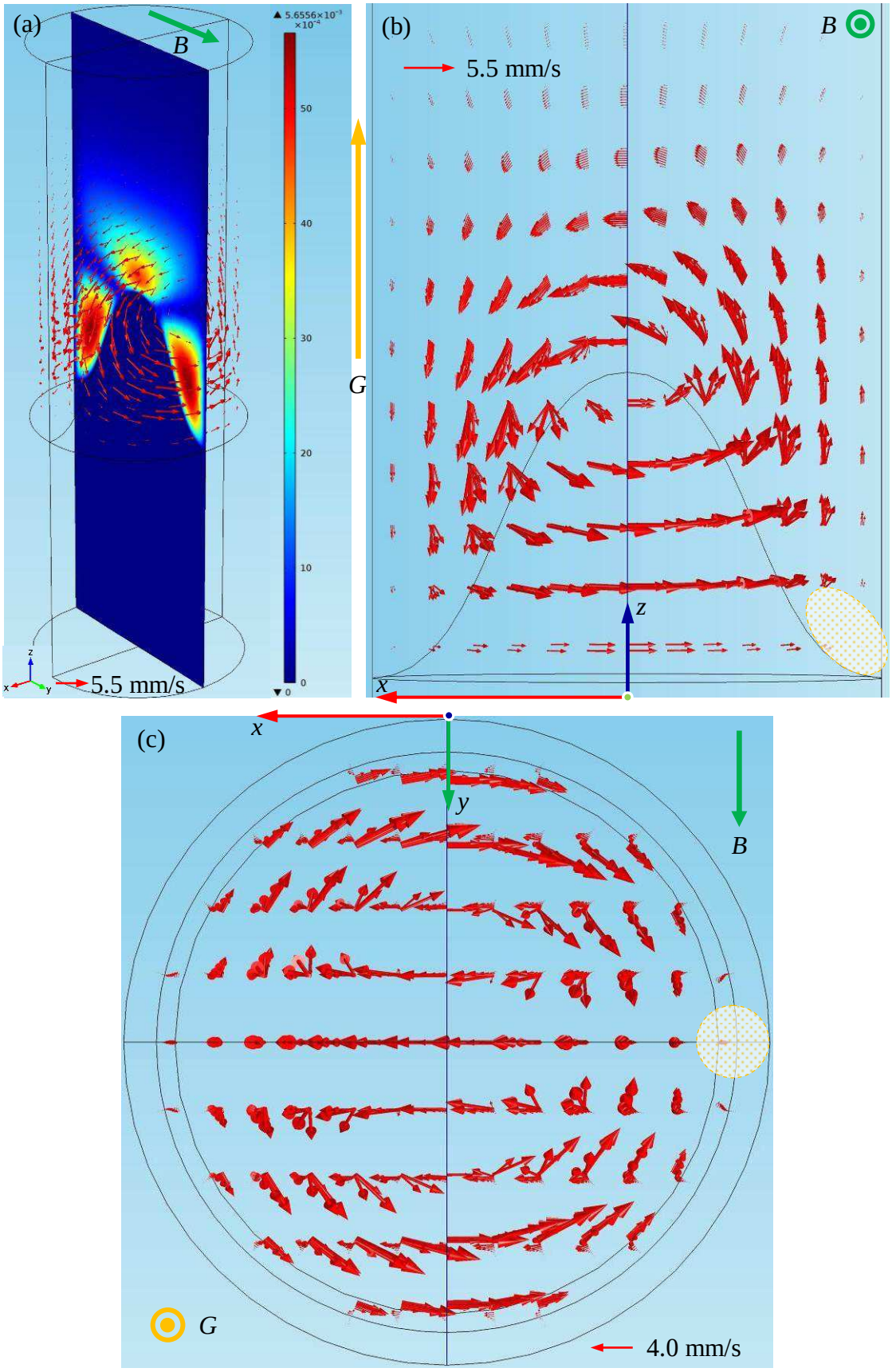

Figure 4.23 Computed TEM flows presented by the red arrows and its *x* component magnitudes denoted by the colored slice: (a) General 3D view; (b) TEM flows seen from positive *y*-axis; (c) TEM flows seen from positive *z*-axis. (*B*=0.1T, *G*=6000K/m), and the unit of legend in (a) is m/s.

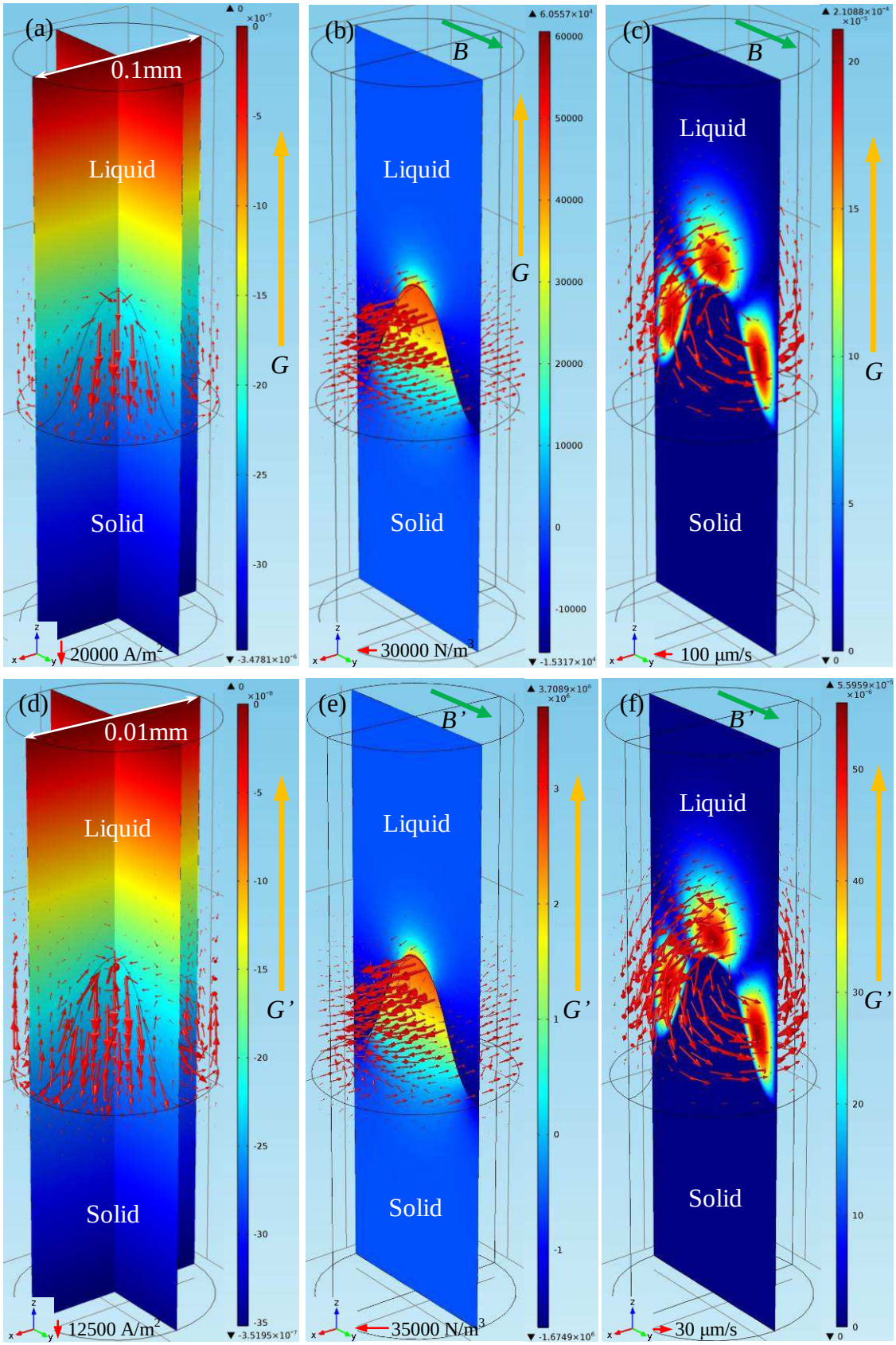

Figure 4.24 (a) to (c) Simulation of TEME with the geometry 0.1mm in diameter; (d) to (f) Simulation of TEME with the geometry 0.01mm in diameter. (a) & (d) Colored slices are thermoelectric potential (V) and red arrows are TEC; (b) & (e) Colored slices are magnitude of the *x* component of TEM forces (N/m^3) and red arrows denote the distributuion of TEM force; (c) & (f) Colored slices present the magnitude of the x component velocities of TEM flows (m/s) and red arrows are TEM flows fields. (*G*=6000K/m, *B*=1T and *B*'=10T)

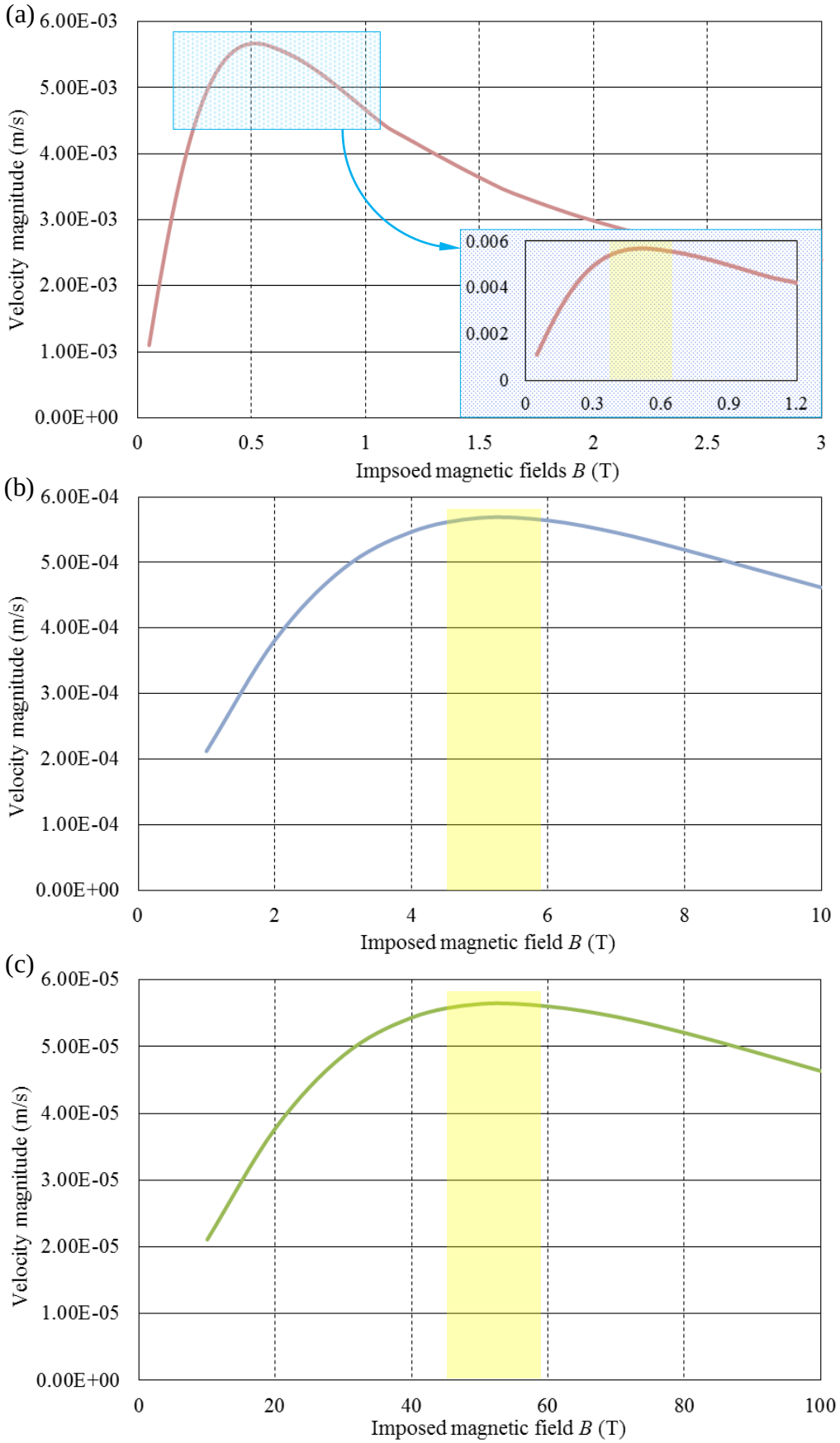

Figure 4.25 Evolution of the velocities of computed TEM flows with increasing TMF intensities for different typical length scales: (a) TEM flows simulated with 1mm diameter geometry; (b) TEM flows simulated with 0.1mm diameter geometry; (c) TEM flows simulated with 0.01mm diameter geometry.

TEC, TEM forces and TEM flows were simulated with the geometries have smaller diameters (typical lengths) of 0.1mm and 0.01mm as well. Figure 4.24 shows the computed results. It can see that the patterns of all TEC, TEM forces and TEM flows are the same as those obtained in simulation with geometry has 1mm diameter (typical length). However, the absolute values of computed TEC, TEM forces and flows are different when the diameters of geometries are different. TEM flows were simulated under various imposed TMF flux intensities and with the same thermal gradient of 6000K/m for geometries with three different diameters as shown in figure 4.19 (a) to (c). Plotted the maximum velocity of computed TEM flows versus the TMF flux intensities, how the velocities of TEM flows vary with constantly increasing TMF can be seen from the curves shown in figure 4.25. It shows that whatever the typical length scale is the change tendency of the velocities of TEM flows with magnetic fields is the same that TEM flows firstly speed up and reach the maximum velocities under the correspondingly critical TMF and then slow down when the TMF further rise. This agrees with the conclusion made by the evaluations of TEM flows in section 4.1. In fact, this consistent can be validated by the similarity between curves shown in figure 4.25 and the yellow line shown in figure 4.2 (c) as well. In another aspect, it can find that the critical TMF intensity responding to the maximum velcoties of TEM flows is about 0.5T for 1mm diameter geometry, 5T for 0.1mm and 50T for 0.01mm. It should be emphasized that the accurate critical TMF intensity for each typical length scale can be any value within the range as marked by the yellow rectangular boxed in figure 4.25 because the magnetic field difference between two simulating steps may not be sufficient small to give the accurate one. Further, it is also needed to point out that the deviations between the critical TMF intensity achieved by these simulations, experiments in chapter 4.2 and and the evaluations in chapter 4.1 are reasonable because the evaluations takes some simplifies and the parameters in real experiments must be difference from the ones used in evaluations and simulations.

4.3.2 Simulation of TEM flows in directional solidification under an axial static magnetic field

With the purpose to extend the knowledge on how TEM flows behave under an axial static magnetic field the corresponding 3D simulations were performed. Except refining the meshes at the top wall of the liquid domain by adding boundary laryers as shown in figure 4.26, the same simulation method, geometries, dimensions, meshes and parameters used in chapter 4.2.2 are all employed in the following simulations as well. Similarly, coupled COMSOL predefining electric current and heat transfer modules, TEC were simulated with a constant thermal gradient of 6000K/m for three different typical length scales. The computed

results are shown in figure 4.27. It can be observed that the patterns of thermoelectric potentials obtained from the three cases are the same except their absolute values, and so do the flowing pattens of the corresponding TEC. These TEC mostly distribute near the interface and form the cirruits via flowing downward in solid and upward in liquid. Actually, the general pattern of TEC is determinated once the simulating system and the applied thermal gradient are decided. However, the densities of TEC depend on the geometery and its size such as the shape of liquid-solid interface. For the present cases, differences of the magnitudes of the simulated thermoelectric potential and TEC between three different typical lenghes should be mostly attributed to the differernt heights of the shape unchanged liquid-olid interface shape. This is because both of thermoelectric potential and TEC are the function of temperature differentce that is linearly proportional to the height of interface once the applied thermal gradient is desided.

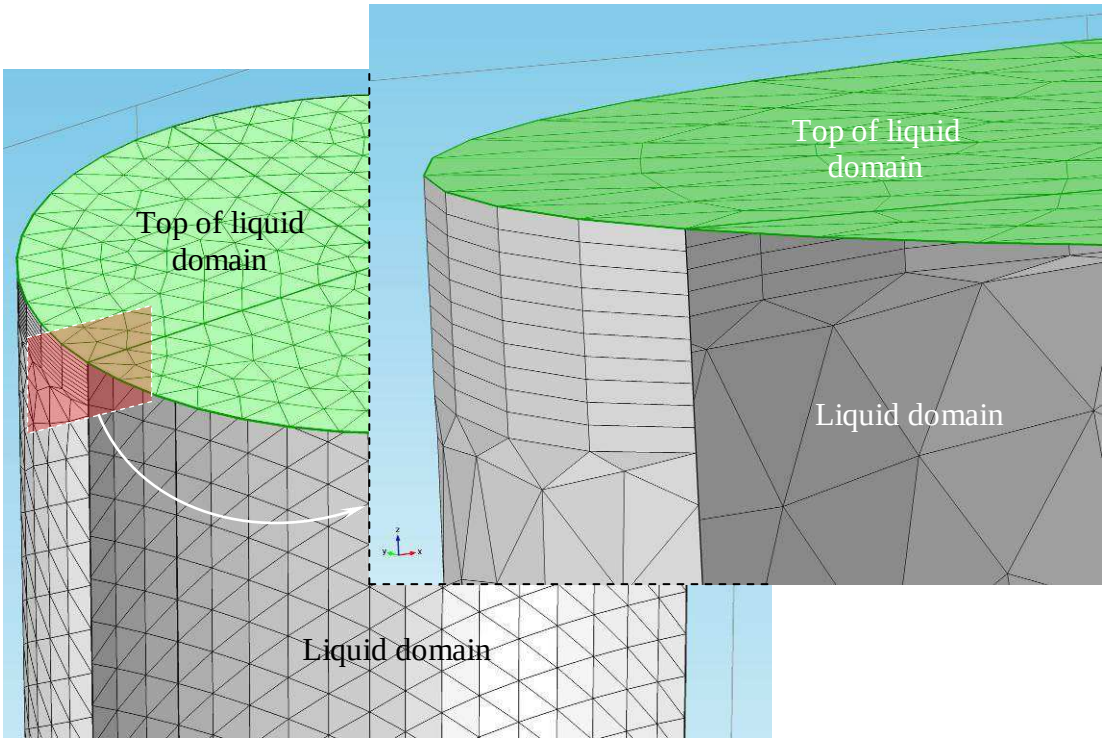

Figure 4.26 Boundary layer refinements of meshes at the top of liquid domain used in 3D simulations of TEM flows under an axial magnetic field.

TEM forces produced by interaction between the imposed AMF and the TEC shown in figure 4.27 were simulated, so do their resulting TEM flows in liquid. Figure 4.28 (a) to (c) gives the computed TEM forces both in liquid and solid for three different diameter geometries respectively. It shows that the patterns of TEM forces in these three cases are the same that vortically surround the *z*-axis and distribute near the interface. This must be easy understood because the direction of TEC and imposed upward axial static magnetic field are remained unchanged for these three cases. Furthermore, carefully examine the *x* component of TEM forces indicated by the colored slices, it can find that TEM forces in liquid are all

clockwise and in solid lead to a pair of opposite direction torques as uncovered by the inserted picture in figure 4.28 (a_1), (b_1) and (c_1). This makes interface at the solid side tend to revolve anti-clockwise at the top and clockwise at the bottom, which may give rise to midifying the solidified structure during the solidification process. Indeed, some indications of the possibility of TEM forces in solid to affect the structure formation have been uncovered by some pioneer experimental attempts [246-248], but such topic would not be further discussed here because it has exceedd the concering range of this thesis.

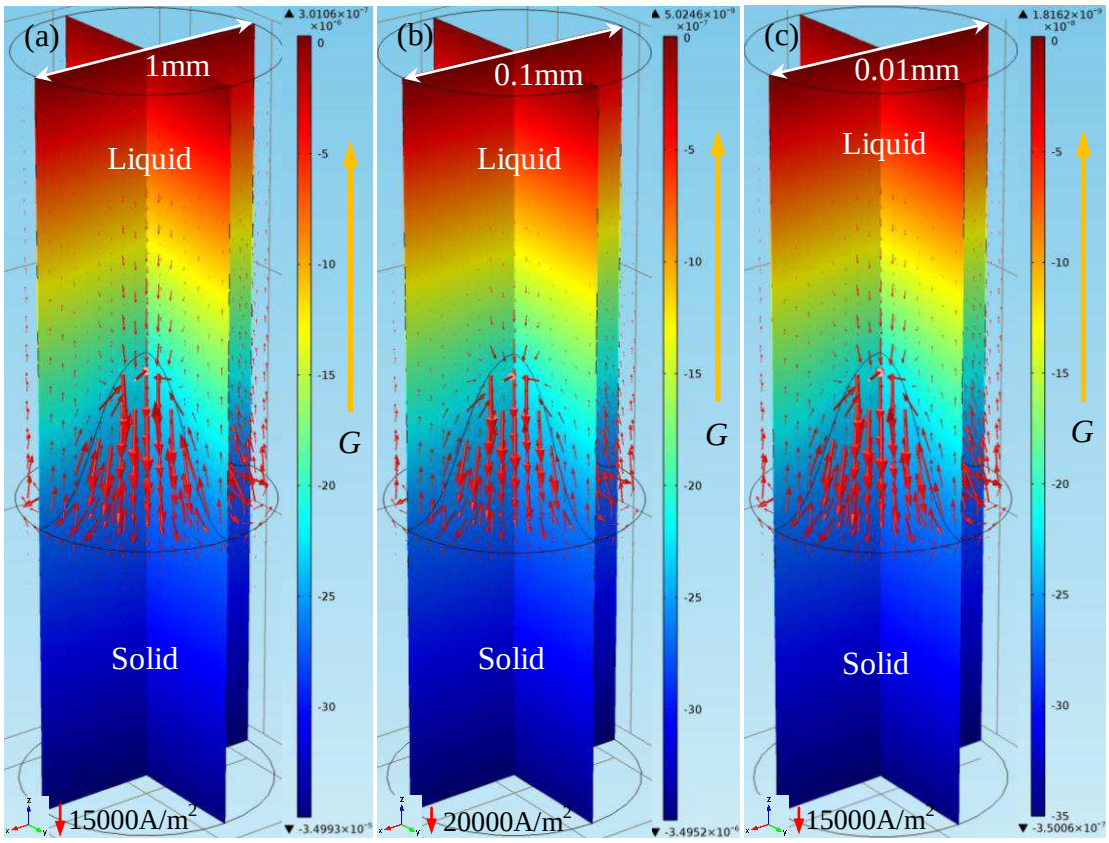

Figure 4.27 Computed TEC generated by a thermal gradient of 6000K/m, *G*, for different diameter geometries (colored slices are thermoelectric potential and red arrows are TEC): (a) TEC in 1mm diameter geometry; (b) TEC in 0.1mm diameter geometry; (c) TEC in 0.01mm diameter geometry. The unit of legend is V.

Figure 4.29 displays TEM flows driven by the TEM forces in liquid shown in figure 4.28 (a), (b) and (c) respectively. Under the axisymmetrically vortical distribution TEM forces, the rotational TEM flows formed as shown in figure 4.29 (a_1), (b_1) and (c_1). Although the isotropous flows in melts during solidification may not cause any redistributuion of solutes, the rotational TEM flows can result in vertical secondary convections like the situation described by Geoffrey Ingram Taylor [289], which is able to affect the solutes distribution in melt. In another aspect, the centrifugal pulling effect of rotational flows can affect the transportation of solutes due to the density difference between the solutes enriched melt and the original ones. Therefore, the rotational flows concentrate the solutes at the periphery of

the sample in accordance to the centrifugal pulling effect if the rejected solutes are heavier than the original metl. And then, the solutes enrichment can affect the formation of structure during solidification process.

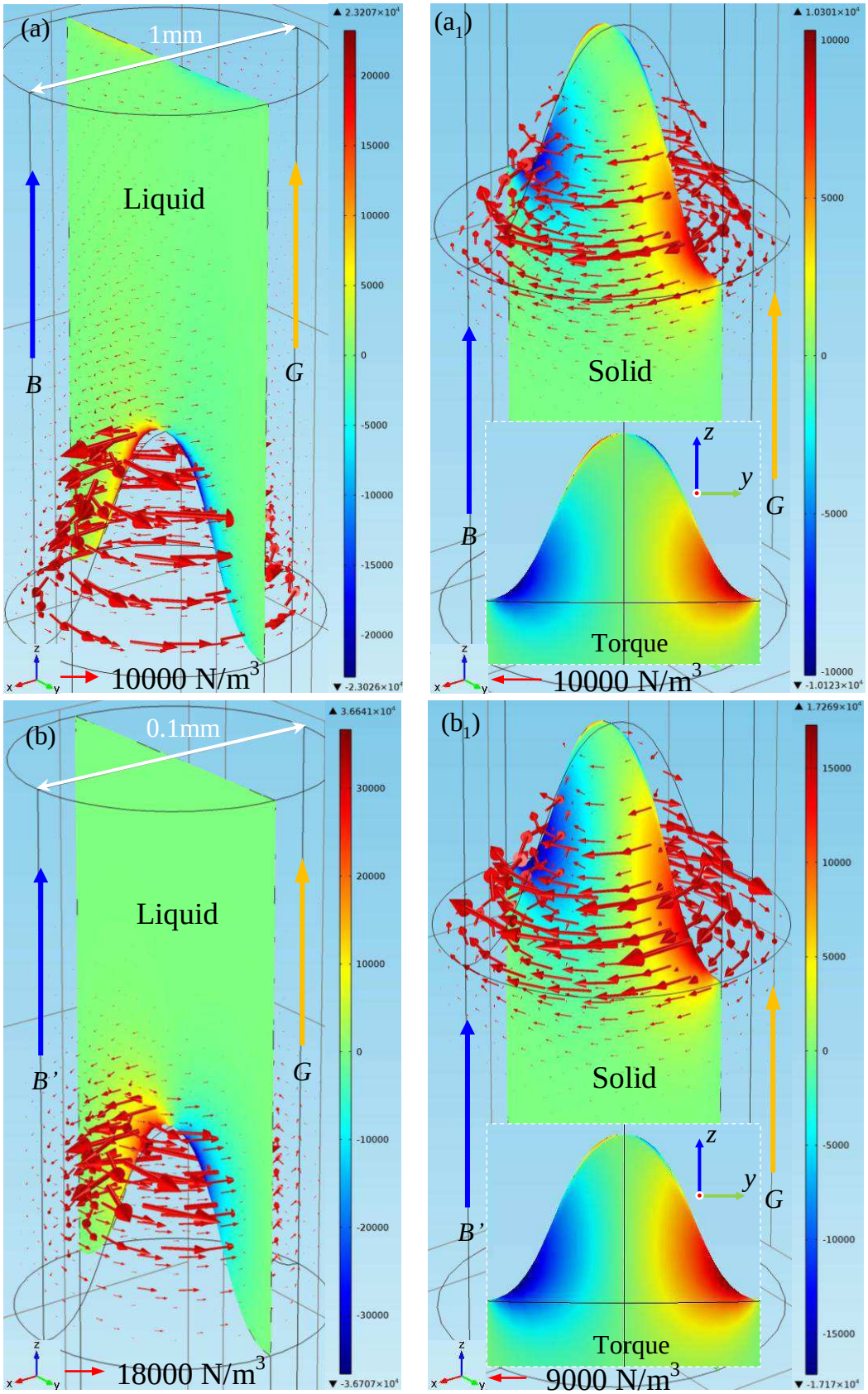

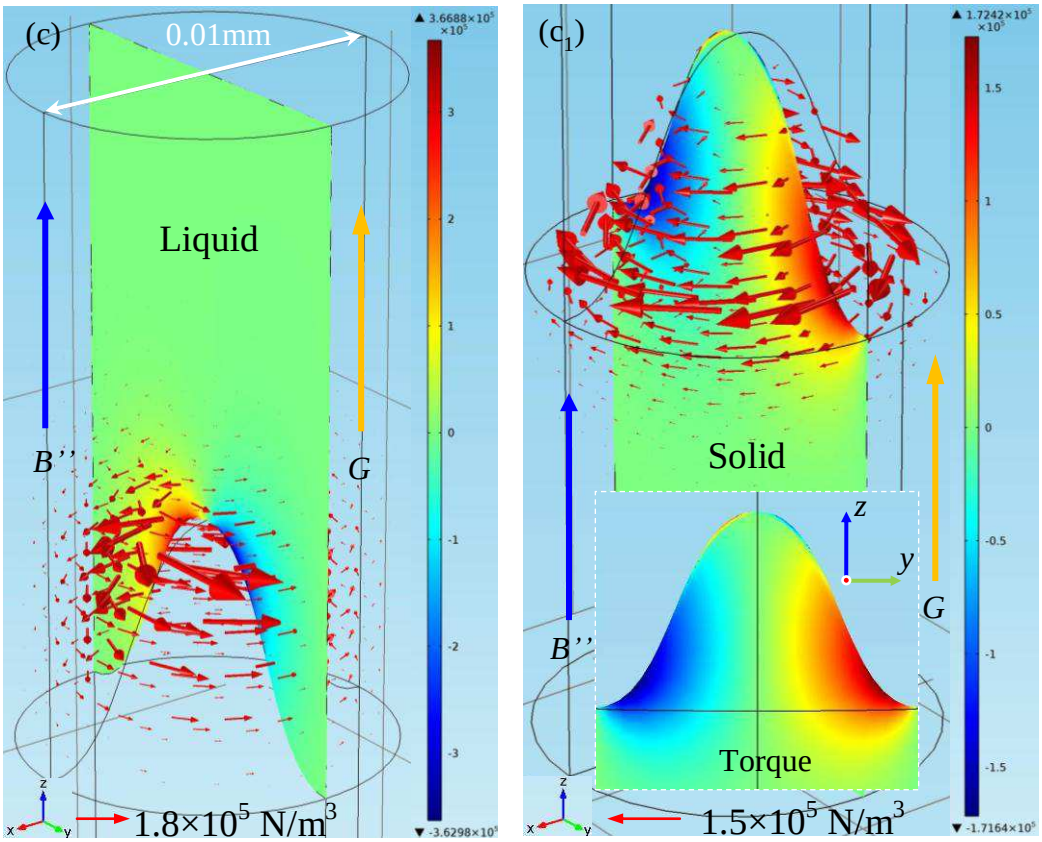

Figure 4.28 Computed TEM forces with different diameter geometries (colored slices represent the magnitude of the *x* component of TEM forces and red arrows give the direction of norm TEM forces): (a) & (a_1) TEM forces in 1mm diameter geometry; (b) & (b_1) TEM forces in 0.1mm diameter geometry; (c) & (c_1) TEM forces in 0.01mm diameter geometry. The unit of legend is N/m^3. (G=6000k/m, B=0.1T, B'=1T and B''=10T)

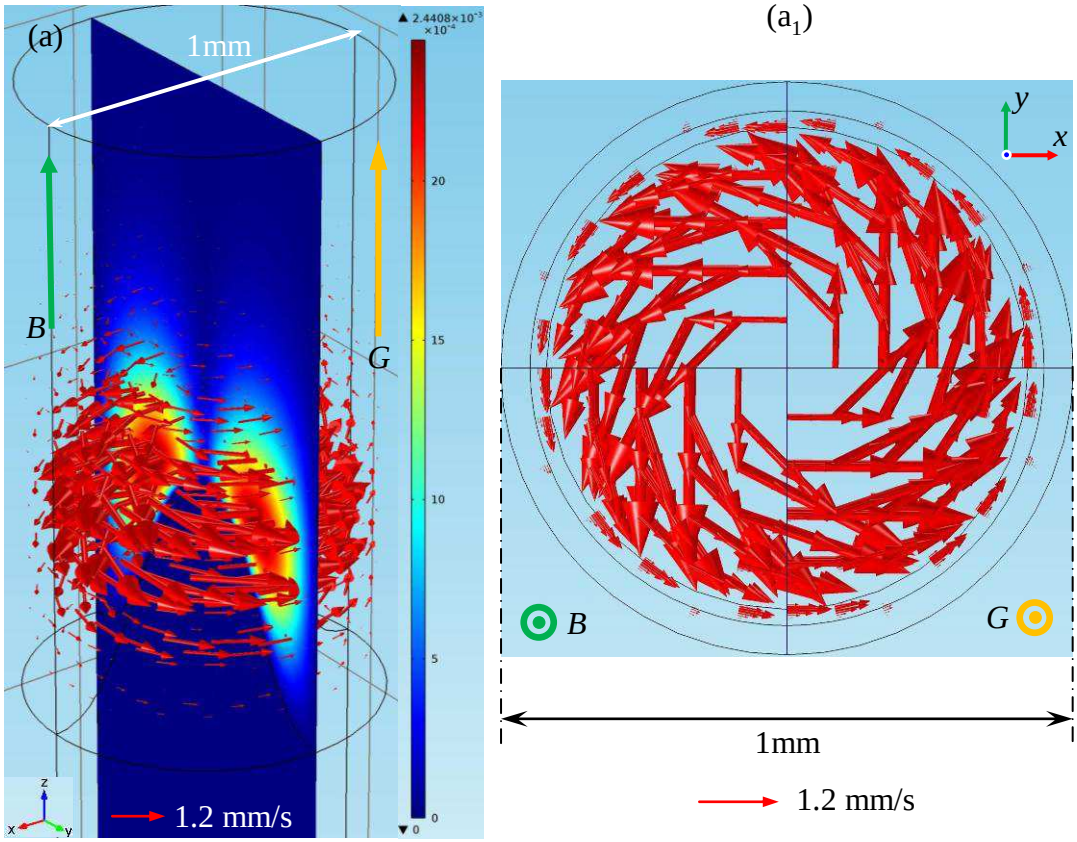

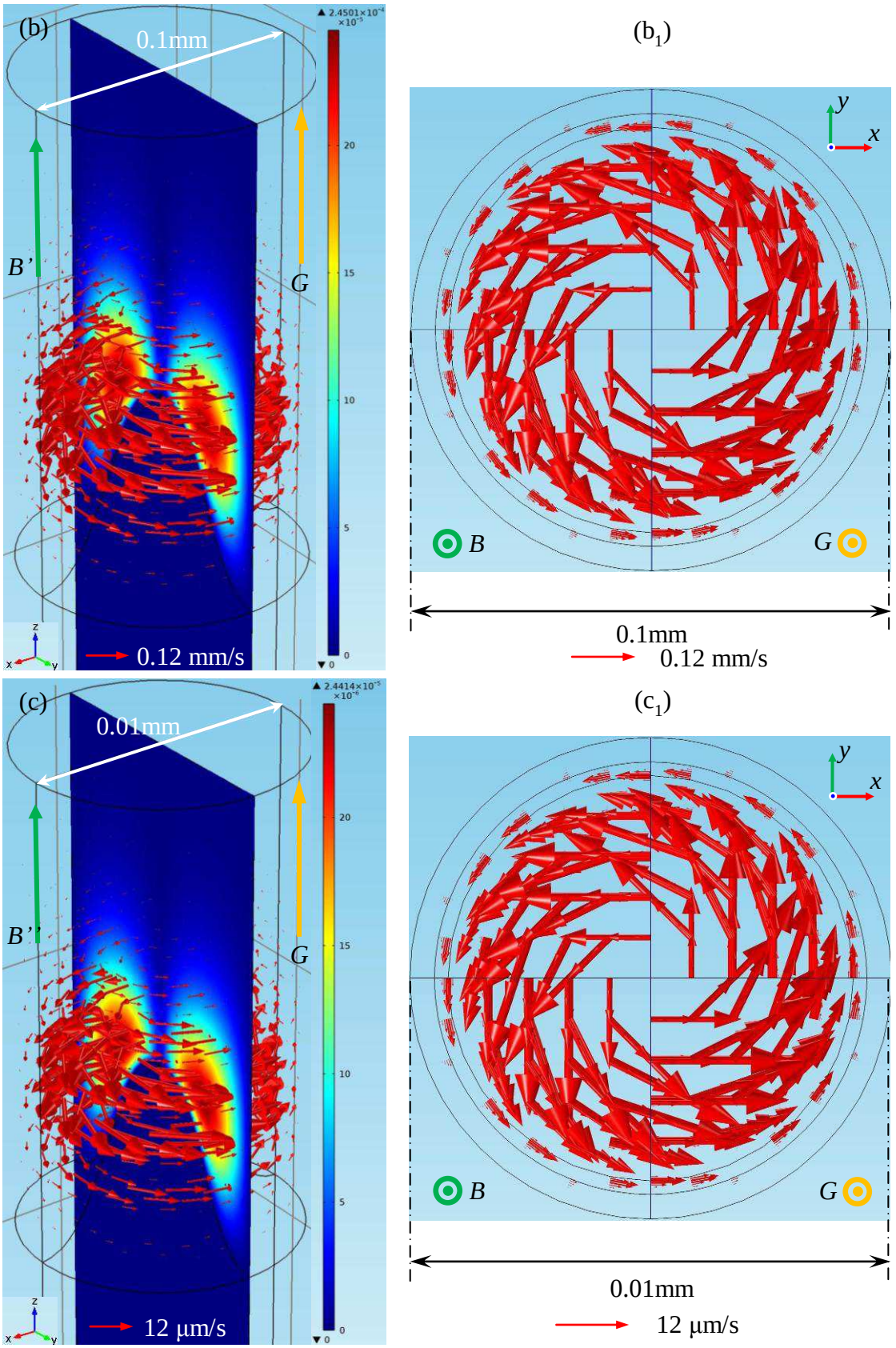

Figure 4.29 Computed TEM flows with different diameter geometries (colored slices represent the magnitude of the x component velocities of TEM flows and red arrows give TEM flows fields). General 3D views of TEM flows in (a) 1mm, (b) 0.1mm and (c) 0.01mm diameter geometries, and their corresponding *x*-*y* plane views (a_1) to (c_1) seen from positive *z*-axis. The unit of legend is m/s. (*G*=6000k/m, *B*=0.1T, *B*'=1T and *B*''=10T)

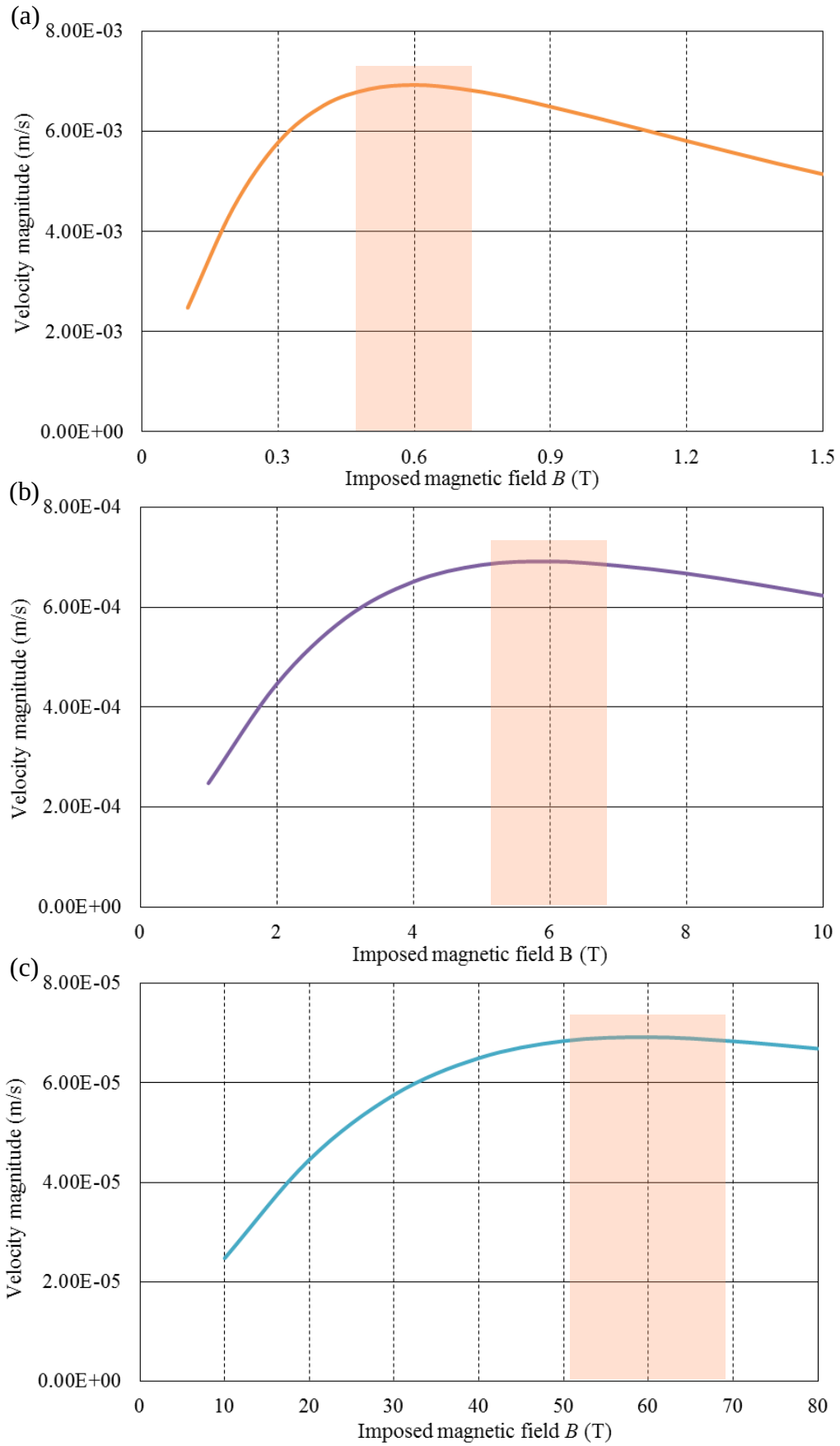

Figure 4.30 Evolution of the velocities of computed TEM flows with increasing AMF flux intensities for different typical length scales: (a) 1mm diameter geometry; (b) 0.1mm diameter geometry; (c) 0.01mm diameter geometry.

By simulating TEM flows under various AMF flux intensities, how the velocities of TEM flows vary with the AMF were investigated for different typical lengths as well. Figure 4.30 displays the curves of the velocities of computed TEM flows plotted with AMF. It can find that the same change tendency of the velocities of TEM flows with the constantly increasing AMF is achieved from all the three different typical lengths. The only difference is that the critical AMF flux intensities responding to the maximum of TEM flows is about 0.6T for the typical length of 1mm, 6T for 0.1mm and 60T for 0.01mm. It must have been noticed that the critical AMF flux intensities are different from the TMF ones. This deviation should be attributed to inaccuracy selection of typical length scales because the areas perpendicular to the magnetic field lines are different when the magnetic field is imposed axially and transversely for the size fixed sample. In fact, how accurately select the typical length to perform the MHD related calculations is an important and unclear topic [290], so that the present thesis will not and cannot make any further discussions about that. Nevertheless, how the velocities of TEM flows vary with AMF has been found and shows reasonable agreement with the evaluations of TEM flows in chapter 4.1. Considering TEM flows obtained under the TMF, it can conclude that whatever the direction of the imposed magnetic fields are TEM flows in melt during directional solidification process always speed up firstly and reach their maximum velocites under a critical magnetic field and then slow down with the magnetic field further increasing. Finally, it can know that the geometry, dimensions, typical length, thermal gradient in both solid and liquid, direction of the imposed magnetic field and the real growth velocity of liquid-solid interface must be considered overall if we expect to precisely estimate the velocities of TEM flows for a given alloy.

4.4 Summary

Considering the size of the sampe (particularly the 200μm thinckness) used by the in-situ observation experiments in chapter 3 is not common in the pratical production, this chapter confirmed and investigated TEME and its influences in the directional solidification with relative bigger samples those are millimeter scales in three dimensiones. Before experiments, the evaluations of the velocities of TEM flows and how they vary with the imposed magnetic fields were taken. Because TEM forces are linearly proportional to the magnetic field flux intensity TEM flows always speed up firstly. The magnetic damping effect will occur once the melt begin to flow, and the corresponding damping forces increase with the increase of the velocities of TEM flows in melt. Finally, the damping forces should dominate under a sufficient high magnetic field because it is proportional to the square of magnetic field. So that, there is a critical magnetic field resulted from the competition between TEM forces and

damping forces. Under this critical magnetic field, TEM flows reach their maximum velcoties and then slow down when the imposed magnetic field over the critical value. Moreover, according to the evaluation in chapter 4.1 it can know that the critical magnetic field is closely related to the typical length sacle that varies with different morphologies in directional solidification. For instance, the typical length of a planar interface can be roughly regarded as 1mm, and that of the cellular interface should be 0.1mm. Therefore, the critical magnetic field should be different for different solidified structures. Indeed, the smaller the typical length is the higher the critical magnetic field is. After the evaluations, some corresponding experiments were performed. In order to investigate how the velocities of TEM flows vary with imposed magnetic field for different typical lengths, three typical morphologies that planar, cellular and dendritic interface growth were realized and solidified under different TMF flux intensities. Experimental results showed reasonable consistent with the evaluations, particularly, the change tendency of the velocities of TEM flows with constantly increasing TMF obtained from experiments perfectly agreed with that achieved from evaluations. Based on the results achieved in experiments, how TEME appear was explained by schematic illustrations firstly and then confirmed by the 3D simulations. Further, the 3D simulations of TEME were performed with a general geometry for three different typical lengths. Computed results showed that either the imposed magnetic field is transverse or axial the change tendency of the velocities of TEM flows with constantly increasing magnetic fields kept fixed and was consistent with the results obtained in evolutions and experiments. Additionally, these simulations uncovered another important phenomenon that TEM forces in solid are anisotropic. Actually, TEM forces in solid under TMF point to positive *x*-axis at the top and middle of the solid side of interface and to negative *x*-axis at the very periphery. TEM forces in solid under AMF form a torque that makes the top of the solid side of interface tend to revolve anti-clockwise and the bottom part rotate clockwise at the same time. Dislike TEM forces in liquid, TEM forces in solid constantly increase with the imposed magnetic fields increasing. Therefore, TEM forces in solid can be sufficient strong when the imposed magnetic field is high, and the strong TEM forces in solid must play a crucial role on microstructure modification. This may be another promising direction for the research of TEME.

Chapter 5: Influence of magnetic field on formation of structure during directionally solidifying near-eutectic alloys

The ability of TEME to modify the structure of single phase alloys during directionally solidification has been examined in chapter 4. Except the single phase alloys, eutectic alloys are another kind of widely used metallic materials because the eutectic structure or saying coupled growth structure is the excellent candidate for in-situ composite materials [291]. So that how the external magnetic field, particularly the TEME, influences the formation of structure during directionally solidifying the near-eutectic alloys is examined in this chapter. Results show that distances between the tip of primary α-Al dendrites and the eutectic structure front that so-called mushy zone length changes when the hypoeutectic Al-26wt%Cu alloys are directionally solidified under different magnetic fields. More important, a nearly entire coupled growth structure is achieved under a 4T AMF. TEM flows and the change of nucleation temperature of the primary and the eutectic phases caused by the magnetic field are employed to explain these results. Indeed, a specialized differential thermal analysis (DTA) apparatus that can be used in high magnetic field is introduced and applied to verify the effect of magnetic field on changing the nucleation temperature of the primary and the eutectic phases. In another aspect, hypereutectic Al-40wt%Cu alloys are directionally solidified under various magnetic fields as well. The experimental results show that other than the alteration of the mushy zone length the growth of the intermetallic compound Al_2Cu phase is enhanced by the magnetic field. Transmission electron microscope analysis suggests that the growth enhancement of the faceted Al_2Cu phase should be attributed to the defects multiplication in this phase. TEM forces acting on solid during directional solidification can lead to the defects multiplication.

5.1 Alloys and experimental apparatus

Al-Cu alloys were chosen as the research object in this chapter as well because Al-Al_2Cu is a typical eutectic alloy that widely used in electronic and engineering industries. Besides, thermophysical parameters of Al-Cu system are relatively complete. Hypoeutectic Al-26wt%Cu and hypereutectic Al-40wt%Cu alloys were chosen because they have almost the same melting temperature and compositional difference between the eutectic reaction composition that Al-33.2wt%Cu, and more, they precipitate different primary phases and reject different types of solutes during solidification proceeding. Upon Al-26wt%Cu alloys, α-Al phase is the primary phase and heaver Cu solutes are rejected, whereas, Al-40wt%Cu

alloys primarily precipitate the Al_2Cu phase and reject lighter Al solutes. Figure 5.1 gives a partial phase diagram of Al-Cu system containing the two using alloys.

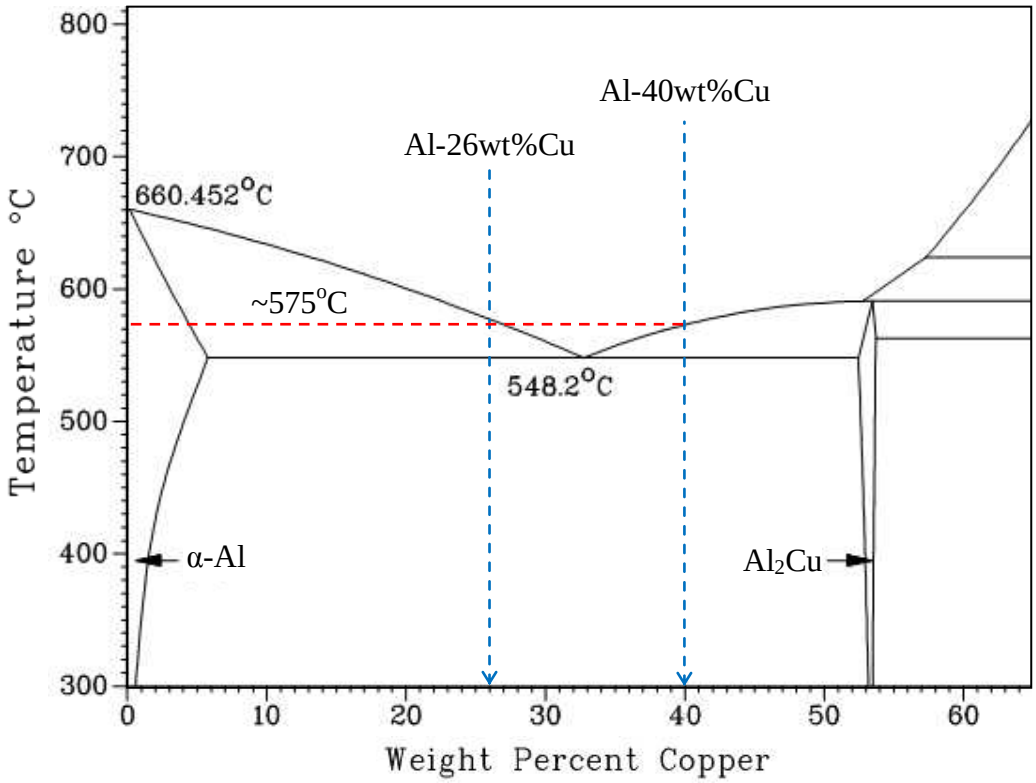

Figure 5.1 Partial phase diagram of Al-Cu system that showing the composition of hypo- and hyper- eutectic alloys used in this chapter.

Al-26wt%Cu and Al-40wt%Cu alloys used in the present studies were both prepared with high-purity Al (99.99%) and Cu (99.99%) by the vacuum suction casting method as introduced in chapter 4.2.1. Therefore, dimensions of the prefabricated specimens are the same as indicated in figure 4.3 (c). Directional solidifications were performed with the same Bridgman type furnace detailedly described in chapter 4.2.1, but the magnet is different. In this chapter, a superconducting magnet as shown in figure 5.2 (b) that can provide the axial upward magnetic field up to 14T was used. This superconducting magnet was made by Oxford Instrument Company with a columnar working place 98mm in diameter and 1174mm in height. The magnetic field flux intensities along the axially central line of working column were measured when it was set as 10T, and the profile is shown in figure 5.2 (a). The corresponding $B_z \cdot (dB_z/dz)$ was calculated and shown in figure 5.2 (a) as well.

A specialized differential thermal analysis (DTA) apparatus that can be used in high magnetic field has been design and built by Changjun Li and Zhongming Ren et al. in Shanghai University [292]. Here, we employed this apparatus to verify the influence of high magnetic field on the nucleation temperature of the primary α-Al, Al_2Cu and the eutectic phases. Figure 5.3 (a) shows the general drawing of the DTA apparatus used in high magnetic field, and photo of real matter is given in figure 5.3 (b).

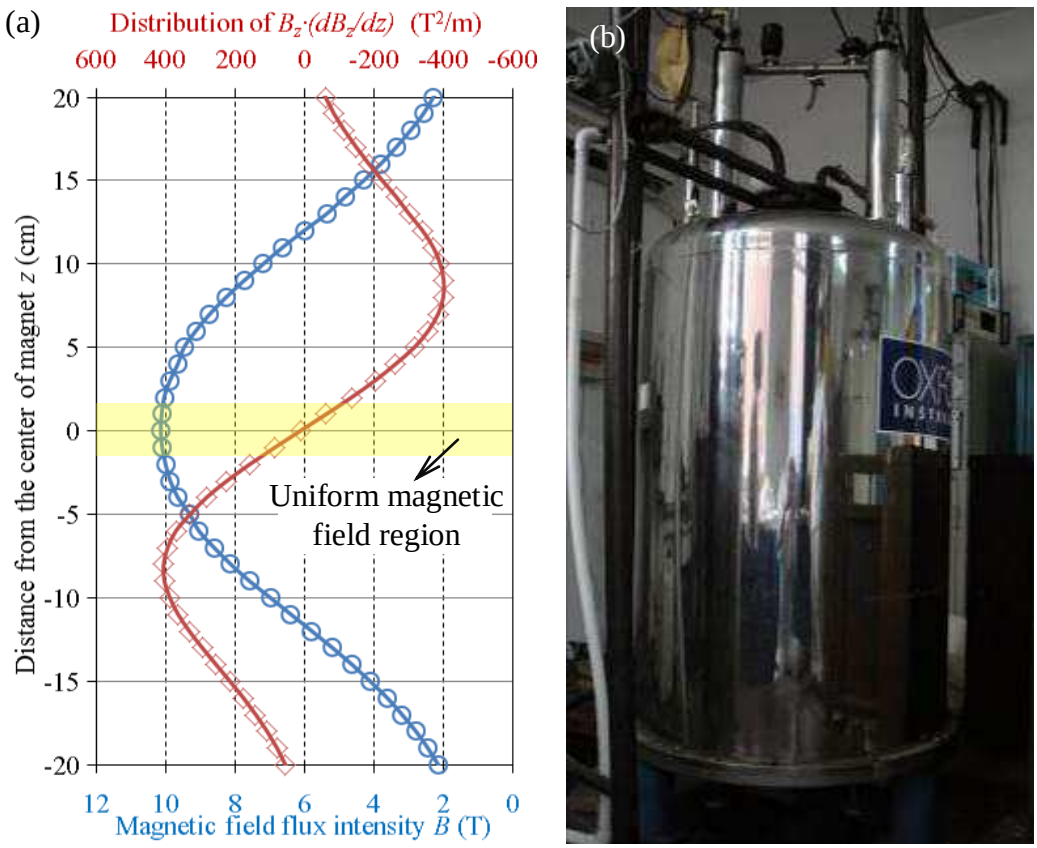

Figure 5.2 (a) Profile of magnetic field measured at 10T along the axial direction and the corresponding vertical distribution of $B_z \cdot (dB_z/dz)$; (b) Photo of the superconducting magnet.

DTA is a thermo-analytic technique, during such process the studying sample and the inert reference together undergo an identical thermal cycles, and meanwhile, record any temperature difference between the sample and reference. Because the inert reference will not have any temperature fluctuation during the thermal cycles, heat absorption or release for instance, any temperature fluctuation of the studying sample compared to the reference can be detected [293]. And then, the differential temperature is plotted against temperature to obtain the DTA curve. Because the physical and chemical reactions of materials during heating or cooling are mostly accompanied thermal effect, particularly the metallic alloys, DTA curve can indicate the events that have happened during the thermal cycles [294], such as the beginning of nuclearation or saying solidification and phase transformation during cooling the metallic melts. Figure 5.4 (a) simply illustrates the basic principle of DTA, figure 5.4 (b) shows the example of data obtained during the experiments, and two typical DTA curves achieved during heating and cooling the metallic sample are given in figure 5.4 (c) and figure 5.4 (d) respectively.

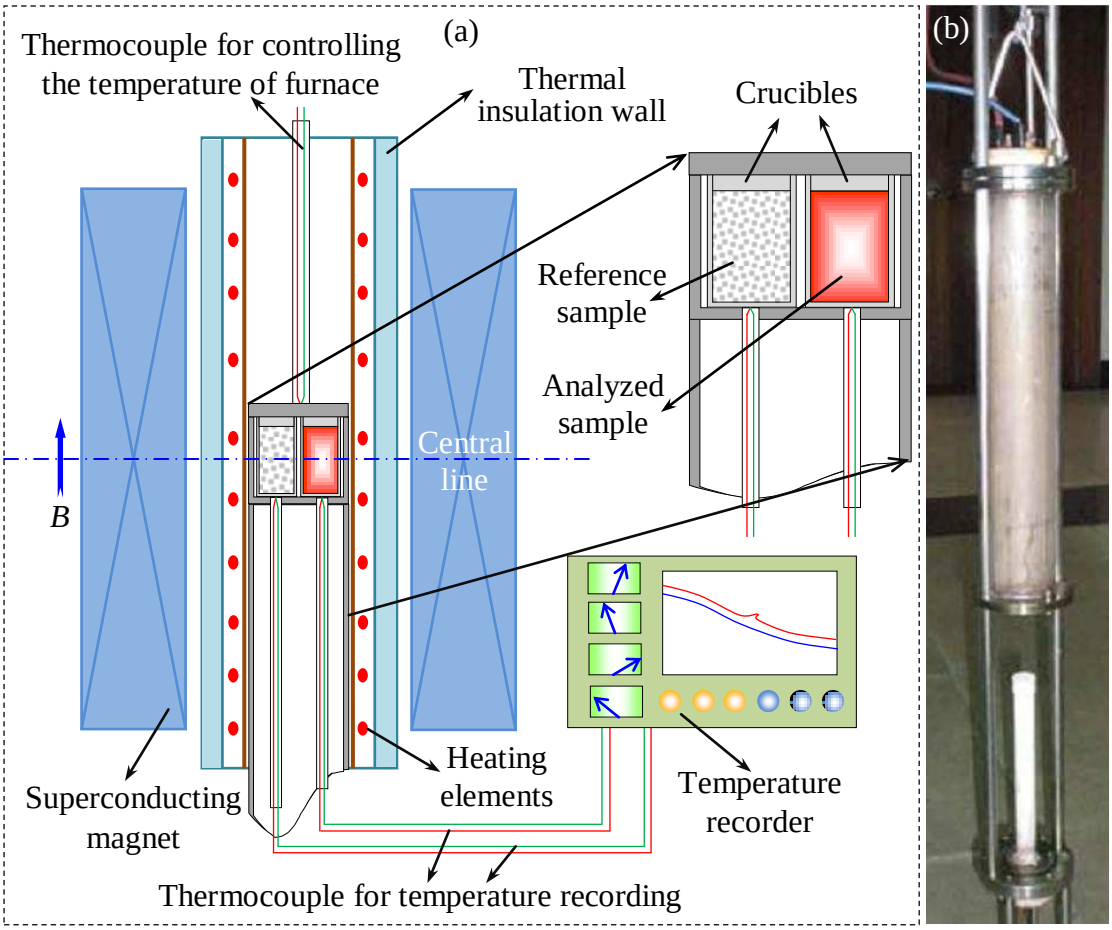

Figure 5.3 (a) General drawing of differential thermal analysis apparatus used in high magnetic field; (b) Photo of real DTA apparatus.

Several parameters manifesting the events happening during melting or cooling can be achieved from the DTA curves [295-297] are explained with the help of examples shown in figure 5.4 (c) and (d).

(1) T_p appears both in heating and cooling process that is the temperature at which the maximum temperature difference occurs. This parameter varies with the applied heating or cooling rate during the thermal cycles when the other conditions remain unchanged.

(2) T_m appears in the DTA curve obtained during the heating process only, as illustrated in figure 5.4 (c), which responds to the intersection point between the extended basic line and the tangent line of the maximum slope of the low temperature side of endothermic peak. This temperature is generally regarded as the melting temperature of the studying sample.

(3) T_n appears in the DTA curve obtained during the cooling process only, as illustrated in figure 5.4 (d), which responds to the intersection point between the extended basic line and the tangent line of the maximum slope of the high temperature side of exothermic peak. This temperature stands for the beginning of nucleation temperature of the studying sample.

(4) The slop of the high temperature side of exothermic peak, $\boldsymbol{tan}\alpha$, as indicated in figure 5.4 (d), can be regarded as the nucleation rate in some cases.

(5) Half-width of the exothermic peak, Δw, reveals the scatter of obtained grain sizes. The smaller the Δw is the lower scatter of the grain sizes is.

Except these parameters, for cooling a metallic sample, more information can be obtained through calculating the parameters directly achieved from the DTA curve. For example, T_n-T_p can uncover the rate of nuclearation or saying solidification. High value of (T_n-T_p) presents lower solidification rate, which means the crystals will grow slowly after their nuclearation.

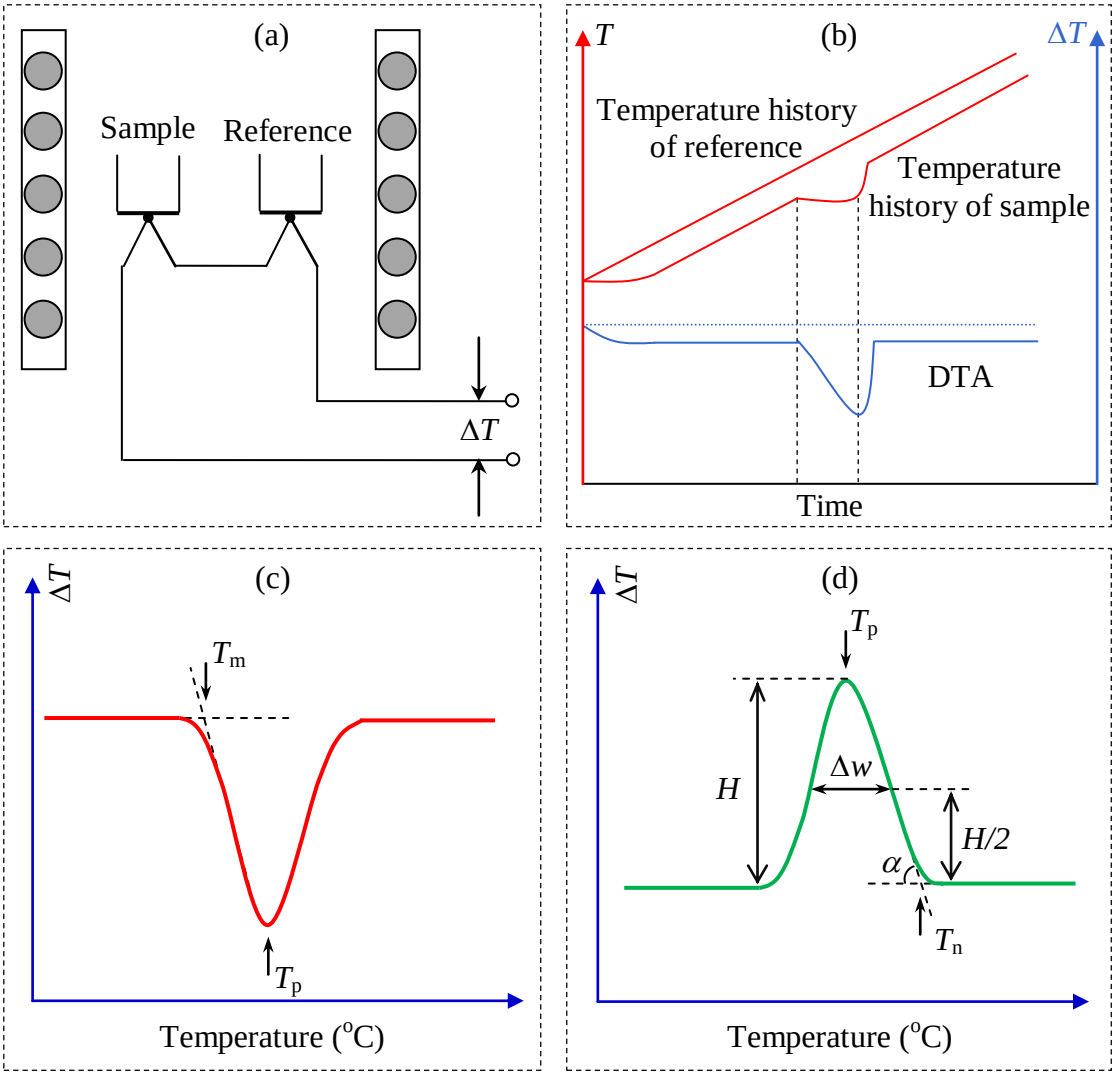

Figure 5.4 (a) Schematic illustration of DTA; (b) Example of DTA curve; (c) Example of DTA curve obtained during heating a metallic sample (endothermic peak); (d) Example of DTA curve obtained during cooling a metallic sample (exothermic peak).

5.2 Influence of axial magnetic field during directionally solidifying hypoeutectic Al-26wt%Cu alloy

As a typical hypoeutectic alloy, Al-26wt%Cu alloys are directionally solidified with an unchanged pulling-down velocity of 2μm/s and under various AMF flux intensities. Results

show that under low AMF the distance between the tips of primary α-Al dendrites and the eutectic front that the mushy zone length changes when AMF varies and a nearly entire coupled growth structure formed under a 4T AMF.

5.2.1 Influence of low magnetic field on the mushy zone length during directionally solidifying Al-26wt%Cu alloy

Generally, directional solidification of hypoeutectic alloys provides a dendrite-plus-eutectic solid structure, in which, α-Al dendrites lead ahead the eutectic phase and act as the primary phase. Figure 5.5 (a) shows the longitudinal structure that achieved by directional solidifying the Al-26wt%Cu alloy with a constant pulling-down speed of 2μm/s. This is the typical solid structure of hypoeutectic Al-Cu alloys obtained by directional solidification. With the aids of Al-Cu alloy phase diagram as shown in figure 5.5 (b), the distance between the tips of leading α-Al dendrites and the eutectic front that so-called mushy zone length can be estimated approximately. Supposed the temperature of the tips of primary dendrites is regarded as the liquidus temperature of Al-26wt%Cu alloy as marked by the red dot in figure 5.5 (b) that about 577.7 ^{o}C, and the temperature of eutectic front during growth is thought to be the eutectic temperature that is 548.2 ^{o}C, the mushy zone length can be roughly calculated when the applied thermal gradient is decided. Because the temperature difference between the the tips of dendrites and eutectic front is 29.5K in accordance to the phase diagram, the length of mushy zone can be obtained by dividing 29.5K by the applied thermal gradient of 6200K/m, which is about 4.76mm. The mushy zone length obtained from experiment is about 4.38mm as indicated in fiure 5.5 (a), which is shorter than the estimating one. It is understandable because Cu solutes will be rejected from the primary α-Al phase during the directional solidification and then enrich the melt ahead of the primary dendrites. This makes the primary dendrites surrounded by higher composition melt, and which make the growth temperature of the dendritic interfaces lower than the liquidus temperature of Al-26wt%Cu alloy. For this reason, the real temperature difference between the tips of the primary dendrites and eutectic front should be smaller, and as well as the mushy zone length if the thermal gradient is unchanged. Indeed, the growth temperature of both the tips of the primary dendrites and the eutectic front are affected by the pulling-down speed, *R*, as well. However, such influence is negligible because *R* is the high order term in the equation for calculating the real growth interface temperature of dendrites [298] and *R* was small here. In another aspect, using eutectic temperature presenting the eutectic growth interface temperature is reasonable because this is widely accepted simplification [299]. Therefore, it can be thought that the length of mushy zone during directional solidification is determined by the

composition of melt ahead of the tips of the primary dendrites if the pulling-down speed and the thermal gradient are fixed. With this in mind, influence of the magnetic field on the mushy zone length is discussed following. Figure 5.6 is the longitudinal solid structure containing both dendritic and eutectic interfaces of hypoeutectic Al-26wt%Cu alloys directionally solidified under different AMF flux intensities, *B*, with constant thermal gradient of 6200K/m, *G*, and pulling-down speed of 2μm/s, *R*.

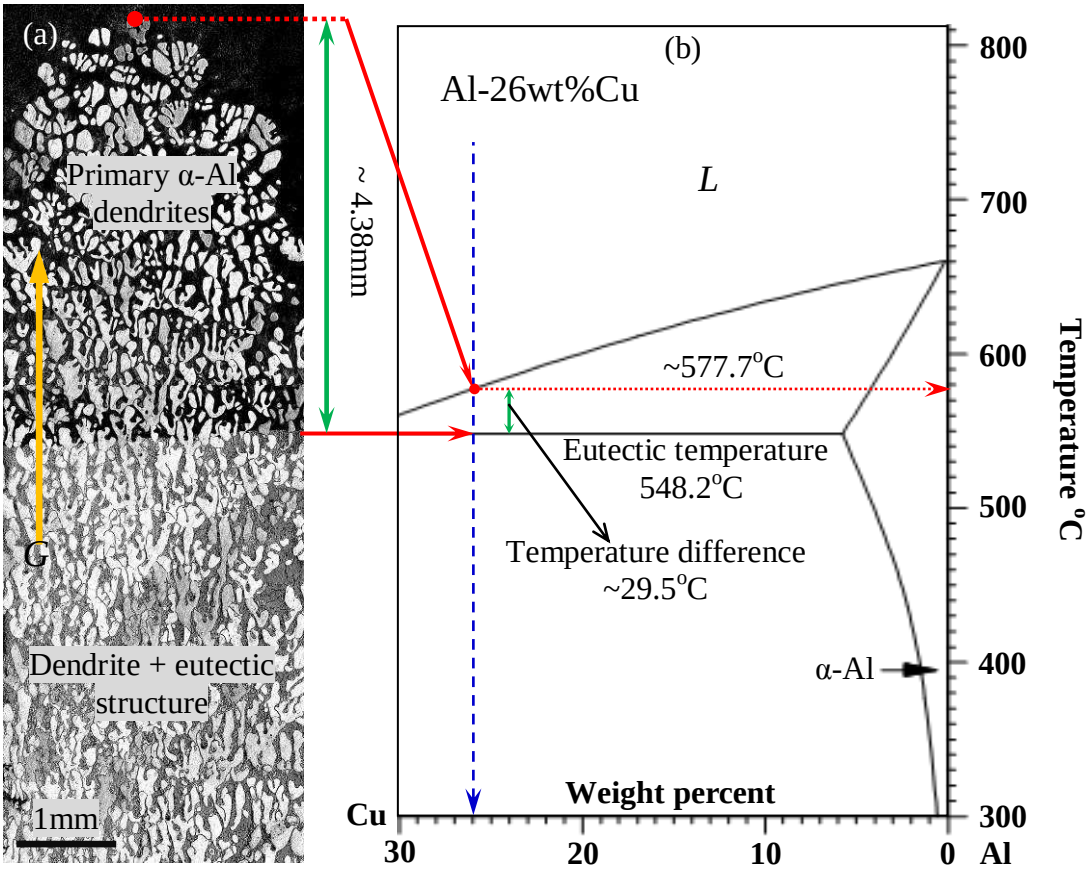

Figure 5.5 (a) Longitudinal (parallel to the growth direction) structure of dendritic and eutectic interfaces achieved by directionally solidifying the Al-26wt%Cu alloy with a pulling-down speed *R* of 2μm/s in the absence of magnetic field; (b) illustration of method to simply estimate the mushy zone length. (*G*=6200K/m)

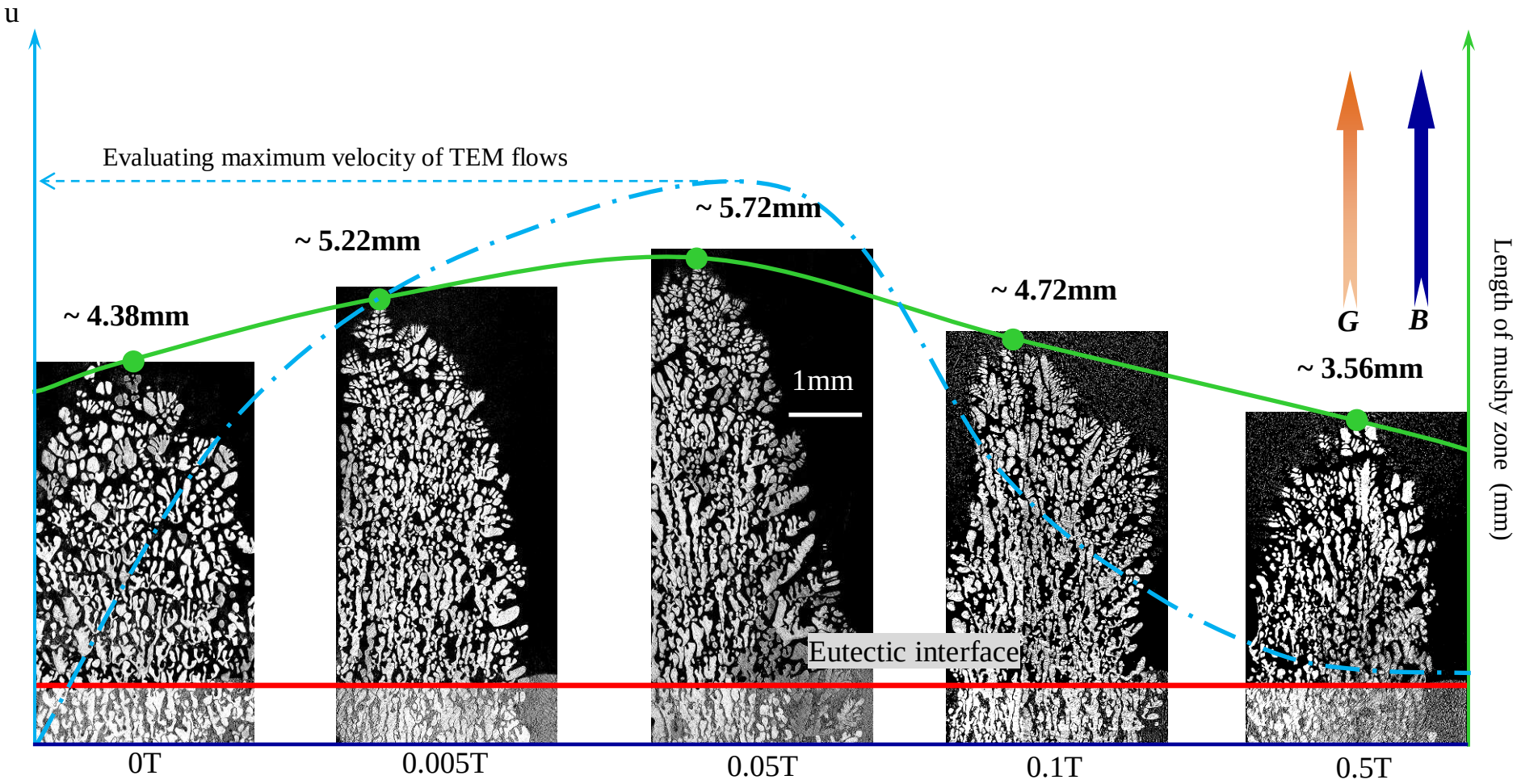

Figure 5.6 Longitudinal (parallel to both growth and magnetic field direction) structure containing both dendritic and eutectic interfaces achieved by directionally solidifying Al-26wt%Cu alloys under different AMF flux intensities that 0T, 0.005T, 0.05T, 0.1T and 0.5T. Red line marks the eutectic front, green dots indicate tips of dendritic interfaces and blue line approximately illustrates how the evaluating velocities of TEM flows vary with AMF flux intensities, and the measured mushy zone lengths are given at the top of each figure. (R=2μm/s, G=6200K/m)

It can be observed from figure 5.6 that the typical dendrite-plus-eutectic structure is remained under the AMF lower than 0.5T. However, the mushy zone length changes when the imposed AMF is different. Further, it can find that mushy zone elongates its length from about 4.38mm when the magnetic field is absent to about 5.72 when AMF is 0.05T, and further increasing AMF makes the mushy zone become shorter, finally, it is about 3.56mm when AMF is 0.5T. Based on the factors in determining the length of mushy zone as discussed above, it can attribute the elongating of mushy zone to the dilution of melt in front of the α-Al dendrites. In another word, reducing of the solute enrichment of melt ahead the α-Al dendrites elongates the mushy zone length. Considering discussions about TEME in the previous chapters, TEM flows around the primary α-Al dendrites are capable to change the composition of melt surrounding and ahead. Therefore, it is thought that TEM flows should response to the change of mushy zone length under different AMF flux intensities.

Table 5.1 Physical parameters of α-Al, Al_2Cu phase and the liquid used in simulation

Names, symbols and units of the parameters	Magnitude
Electrical conductivity of Al_2Cu phase, σ_{S2}, $\Omega^{-1}\cdot m^{-1}$	6.20×10^{6} [275]
Electrical conductivity of α-Al phase, σ_{S1}, $\Omega^{-1}\cdot m^{-1}$	7.90×10^{6} [275]
Electrical conductivity of liquid, σ_{l}, $\Omega^{-1}\cdot m^{-1}$	3.05×10^{6} [275]
Absolute thermoelectric power of Al_2Cu phase, S_{S2}, $V\cdot K^{-1}$	-0.60×10^{-6} [238]
Absolute thermoelectric power of α-Al phase, S_{S1}, $V\cdot K^{-1}$	-1.50×10^{-6} [238]
Absolute thermoelectric power of liquid, S_{l}, $V\cdot K^{-1}$	-2.25×10^{-6} [238]

However, whether TEME can occur or not in the typical dendrite-plus-eutectic structure needs to be verified. For this reason, used the simulation method has been validated in chapter 2.3.2 and taken the geometry shown in figure 5.7 (a) TEC in a simplified case that considering only one primary α-Al dendrite followed by eutectic phase were simulated via combining the COMSOL predefining electric current and heat transfer modules. In addition, meshes used in this simulation and dimensions of the geometery are also indicated in figure 5.7 (a). The meshes are extremely fine and triangular, which were created under the criterion of physical phenomena control. The physical parameters of α-Al, Al_2Cu phase and the liquid used in this 2D simulation of TEC are list in table 5.1. Figure 5.7 (b) shows the computed thermoelectric potential and the corresponding TEC obtained under a constant thermal

gradient of 6200K/m that the same one used in the experiments. Although there are some small TEC circuits along or between the secondary arms of the dendrites as shown by the inserted picture in figure 5.7 (b), it can see that the main and the more intense TEC form the global circuit along the first arms of the dendrites as indicated by the white lines with arrows in figure 5.7 (b). Moreover, this agrees with the discussions about the flowing path of TEC around the dendrites in chapter 4.2.2.

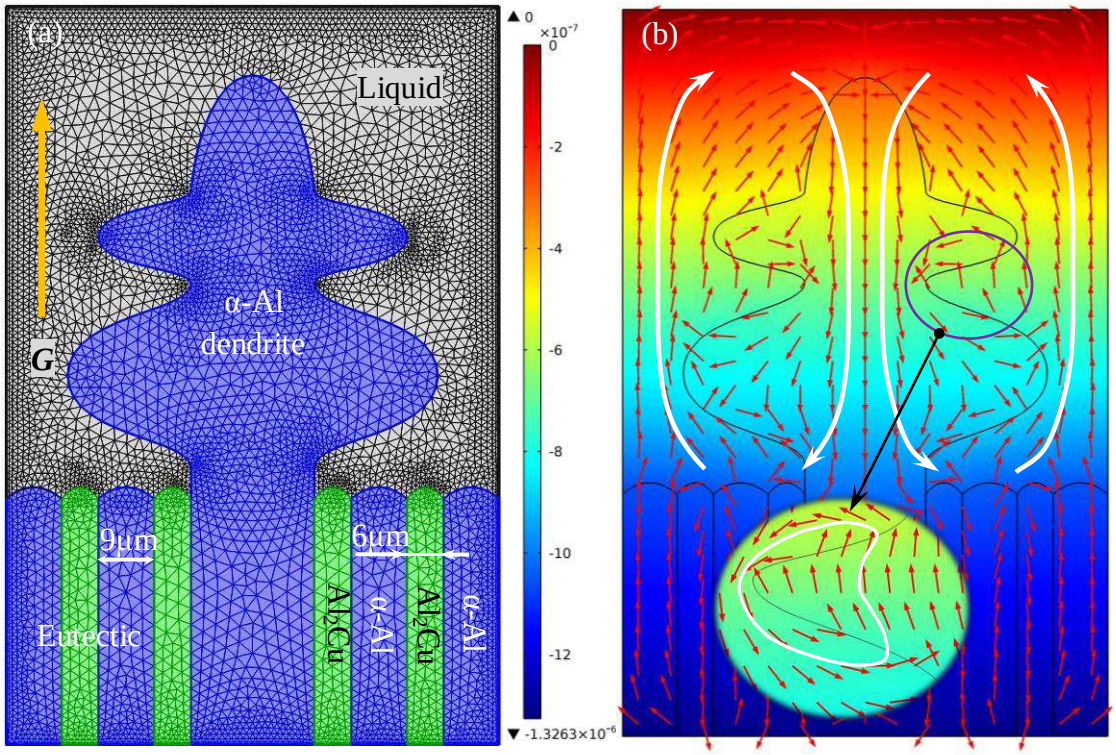

Figure 5.7 (a) Geometry, dimensions and meshes used in 2D simulation of TEC in the dendrite-plus-eutectic structure; (b) Computed thermoelectric potential (colored slice) and the corresponding TEC (red arrows) produced by the constant thermal gradient of 6200K/m. The unit of legend is V, and the red arrows are normalized.

Further, imposing AMF and considering the main circuits of TEC as indicated by the white lines with arrows in figure 5.7 (b), how TEME happen and behave in the dendrite-plus-eutectic structure is schematically illustrated in figure 5.8. It must have been known that TEM forces should be produced once the magnetic field is present if TEC exist. As indicated by the light-blue marks, TEM forces in liquid are perpendicular to and go out of the paper at the left side of the tip of α-Al dendrite, conversely, the ones at the right side point to the opposite direction. Driven by such TEM forces, swirl TEM flows should appear around the dendrites, particularly near their tips. These swirl TEM flows may respond to the reducing of the Cu solute enrichment of melt. It can image that if there are not any other disturbing factors the

rejected Cu solutes manifested by the yellow solid lines with arrows should sink down due to the gravity. However, TEM flows near to the dendrite should emerge and affect the sinking down of rejected Cu solutes once AMF is present. Although the isotropous swirl flows are commonly regarded as having no influence on the distribution of soluts in melt their conetrigual effect can facilitate the radially transport of the rejected Cu solutes as shown he dotted yellow lines with arrows in figure 5.8 due to the density difference between solute enriched and not enriched melt. Consequently, melt ahead the primary dendrites become dilute compared to those in the case no magnetic field is present. The dilute melt enable the dendrites to grow into higher temperature region and thus the mushy zone length elongates. This can explain the above experimental results that mushy zone increases its length as AMF incrases from 0T to 0.05T. Next, why the mushy zone becomes shorter under AMF higher than 0.05T should be answered as well.

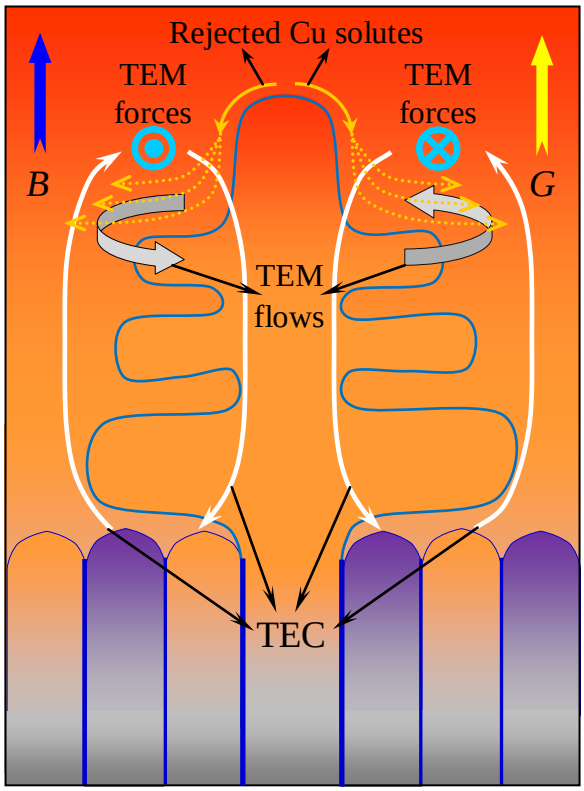

Figure 5.8 Schematic illustration of the occurrence of TEME in the dendrite-plus-eutectic structure based on the TEC simulated with the similar structure.

Actually, shortening of mushy zone length as shown in figure 5.6 can be understood easily as long as the TEM flows is accepted to be able to affect the transportation of rejected Cu solutes. Based on the previous evaluations of TEM flows in chapter 4.1, there should be a critical magnetic field flux intensity under which TEM flows reach their maximum velocities.

More intuitively, how the velocities of TEM flows vary with increasing magnetic field can be approximately revealed by the light-blue dot-dash line drawn in figure 5.6. It can know that TEM flows in the directional solidification of hypoeutectic Al-26wt%Cu reach their maximum velocities under 0.05T AMF, and thus the longest mushy zone should be achieved under the same AMF flux intensity. When AMF is higher than 0.05T it is natural to obtain shorter mushy zone because TEM flows slow down under such high AMF. Furthermore, another phenomenon is worthy to emphasize that the mushy zone obtained under 0.5T AMF is shorter than the one achieved without magnetic field. This should be attributed to the damping effect of the static magnetic field on the other flows in melt [300]. It has been well known that sinking of the rejected heaver Cu solutes can lead to vertically solutal convections during directional solidification of hypoeutectic Al-Cu alloys in the absent of magnetic field [301]. Therefore, if the solutal convections are damped by the sufficient high magnetic field as well, it should be certain to get farther shorter mushy zone length compared to the one obtained without magnetic field.

5.2.2 Formation of coupled growth structure in hypoeutectic Al-26wt%Cu alloy solidified under high magnetic field

Remaining the directional solidification conditions unchanged and continuously increasing the flux intensities of imposed AMF, evolution of the solidified structure of hypoeutectic Al-26wt%Cu alloy was investigated under higher magnetic field. The longitudinal solid structure containing both dendritic and eutectic interfaces and the corresponding transverse solid structure are shown in figure 5.9. It can be seen that the mushy zone achieved under 1T AMF is shorter than the one obtained under 0.5T AMF, and the 2T AMF does not make any obvious change of the mushy zone length. Further increasing AMF to 4T, a dramatic structure changing appeared that nearly entire coupled growth structure is achieved as shown in figure 5.9 (c) and (f). The farther shortening of mushy zone length under 1T should be attributed to the stronger damping of TEM flows and solutal convections by the higher magnetic field. Almost the same mushy zone length obtained under 2T AMF suggests that flows in melt cannot be slowed down farther even under much higher magnetic field, 2T for instance. In another word, flows in melt with the present conditions may have

been almost suppressed under a 1T AMF. Considering the mushy zone length should not become much shorter under 4T AMF, the the appearance of nearly entire coupled growth structure under such AMF suggesuts another mechanism. Here, it is thought to be attributed to the thermodynamic effect of magnetic field that high magnetic field can change the nucleation temperature of non-ferromagnetic alloy during solidification [302]. Before confirm this thermodynamic effect of the magnetic field, it is necessary to brief introduce the concept of coupled growth structure.

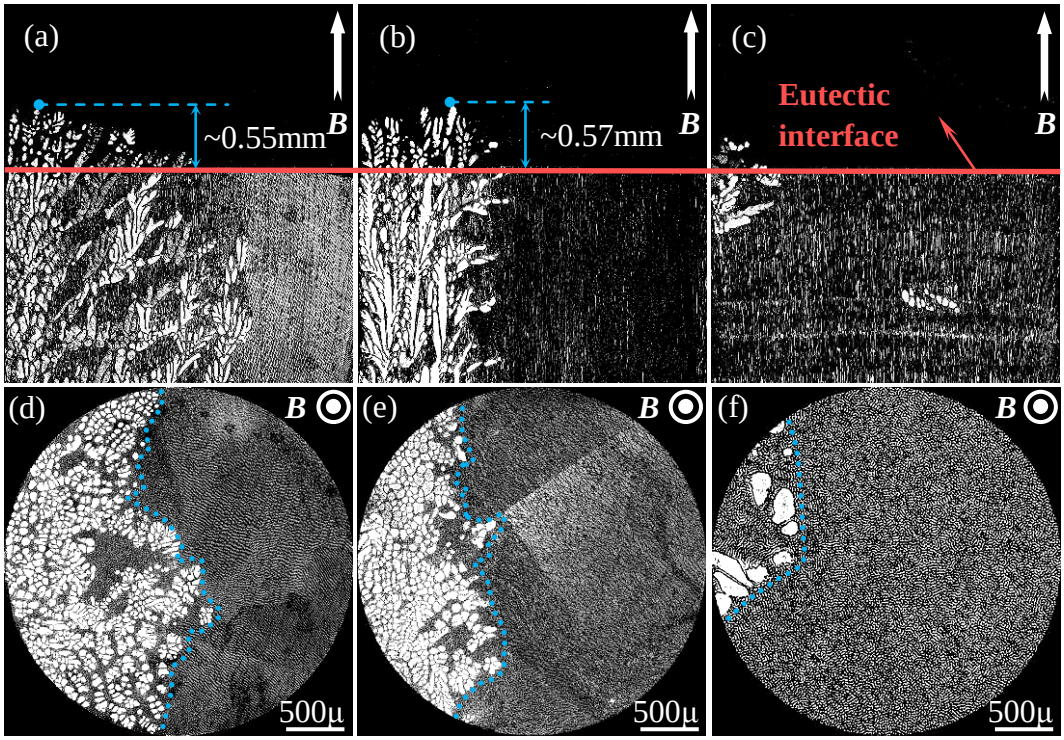

Figure 5.9 Longitudinal (parallel to both the growth and the magnetic field direction) structure containing both dendritic and eutectic interfaces of Al-26wt%Cu alloy solidified under various AMF flux intensities and the corresponding transverse (perpendicular to both the growth and the magnetic field direction) structure: (a) & (d) 1T; (b) & (e) 2T; (c) & (f) 4T. (R=2μm/s G=6200K/m)

Coupled growth structure refers a phenomenon that a similar eutectic structure forms over a range of compositions but not only from the eutectic point. This concept is originated from an experimental finding achieved by Sauveur and Boynton in 1903 that the pearlite could form over a range of compositions [303]. This discovery was confirmed by Tammann and Botschwar in the 1920s', they obtained a similar eutectic structure when solidified the transparent organics with compositions different from but near to the eutectic point [304]. After this, a series of the coupled growth structure of organics were reported by a German

pharmacologist, Kofler. In another aspect, the coupled growth structure obtained by solidification of the metallic materials was firstly found in 1954 [305]. At that time, it was thought that such kind of structure can be achieved only by a sufficient high solidifying rate. This limitation was extended by Jackson and Hunt in 1966, they pointed out that directional solidification can provide the coupled growth structure for the alloys with composition near to the eutectic point (near eutectic alloys) at not only the sufficient high but also the low growth rate [306]. At almost the same time, Mollard and Flemings achieved the entire coupled growth structure of near eutectic Sn-Pb alloy by directional solidification and found that the composition range that permits the formation of coupled growth structure is proportional to the ratio of temperature gradient in front of liquid-solid interface and growth rate [307]. Since then, a novel method to obtain coupled growth structure from a relative wide composition range had been established. In order to precisely predict whether the proceeding conditions can provide coupled growth structure or not for a given alloy system, numerous investigations had been made [308-310]. Consequently, a general accepted principle is founded that the coupled growth structure can prevail if the growth temperature of the primary dendrite is lower than that of the eutectic front [311]. Together with the relationship between the growth temperatures of the primary and the eutectic phases and the given conditions [312] the boundary between dendrite-plus-eutectic and coupled growth structures can be approximately calculated as [313]:

$$V = \frac{GD_l}{m_\alpha (C_E - C_0)} \tag{5.1}$$

where, V is the critical velocity responding the transition (m/s), G, D_l and m_α denotes thermal gradient (K/m), diffusion coefficient (m^2/s) and the liquidus slope of α-Al phase respectively, C_E and C_0 responds to the composition of the eutectic point and the studying hypoeutectic alloys. The coupled growth structure can be achieved only when the growth velocity is slower than the one calculated by equation 5.1. Use the parameters given in table 5.2, the curves responding to the transition between dendrite-plus-eutectic and coupled growth structures without and with magnetic field (considering the damping effect of magnetic field only) are shown in figure 5.10. It can find that, for hypoeutectic Al-26wt%Cu alloy, the coupled growth structure should be achieved when the growth velocity is about 0.48μm/s with the thermal

gradient of 6200K/m if magnetic field is absent. Although such predictions are approximate, it can reasonable enhance us to conclude that the coupled growth structure can not form under the present experimental conditions that thermal gradient of 6200K/m and pulling-down speeds of 2μm/s. Besides, one thing should be stated that though the real growth velocity is different from the pulling-down speed they can be regarded as the same uring the stable period if the pulling-down speed is small [314]. Therefore, the appearance of nearly entire coupled growth structure as shown in figure 5.9 (c) and (f) must be attributed to the presence of AMF, particularly, the higher one.

Table 5.2 Physical parameters of hypoeutectic Al-26wt%Cu alloy

Names, symbols and units of parameters	Magnitude
Diffusion coefficient, D_l, m^2/s	
Pure diffusion cases	2.4×10^{-9} [313]
Case considering solutal convections	3.2×10^{-9} [313]
Liquidus slope of α-Al phase, $m_{l\alpha}$, $K\cdot(wt\ pct.)^{-1}$	5.7 [313]
Thermal gradient, G, $K\cdot m^{-1}$	6.2×10^{3}
Eutectic composition of Al-Cu alloys, C_E, wt pct.	33.2 [275]

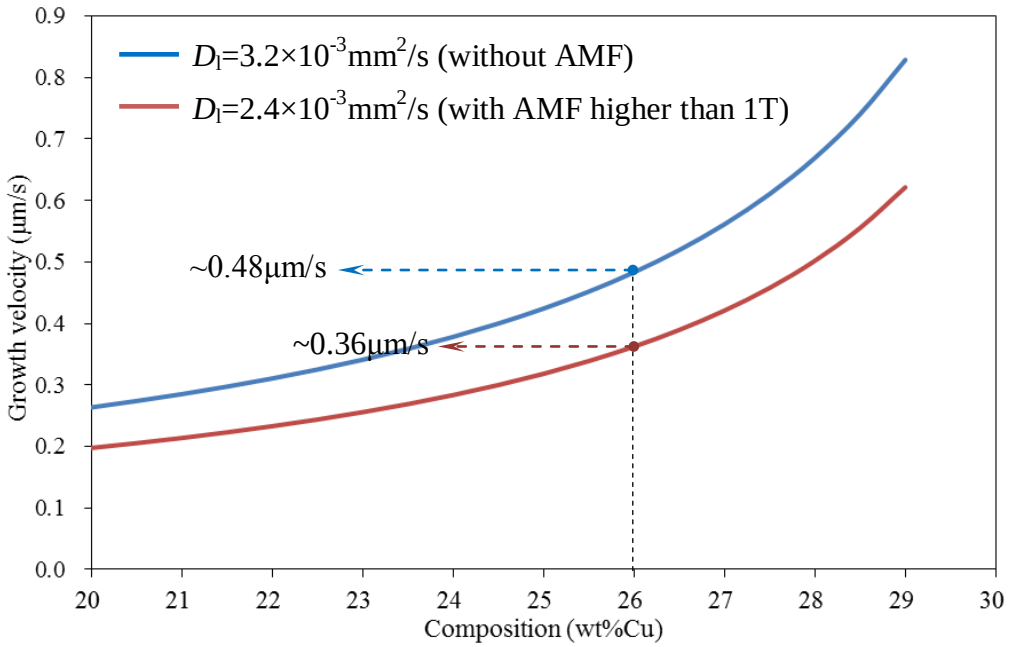

Figure 5.10 Calculated critical growth velocities corresponding to the ransition between the α-Al dendrites plus Al-Al_2Cu eutectic structure and the coupled growth structure without and with AMF higher than 1T (considering the damping effect of high magnetic field only).

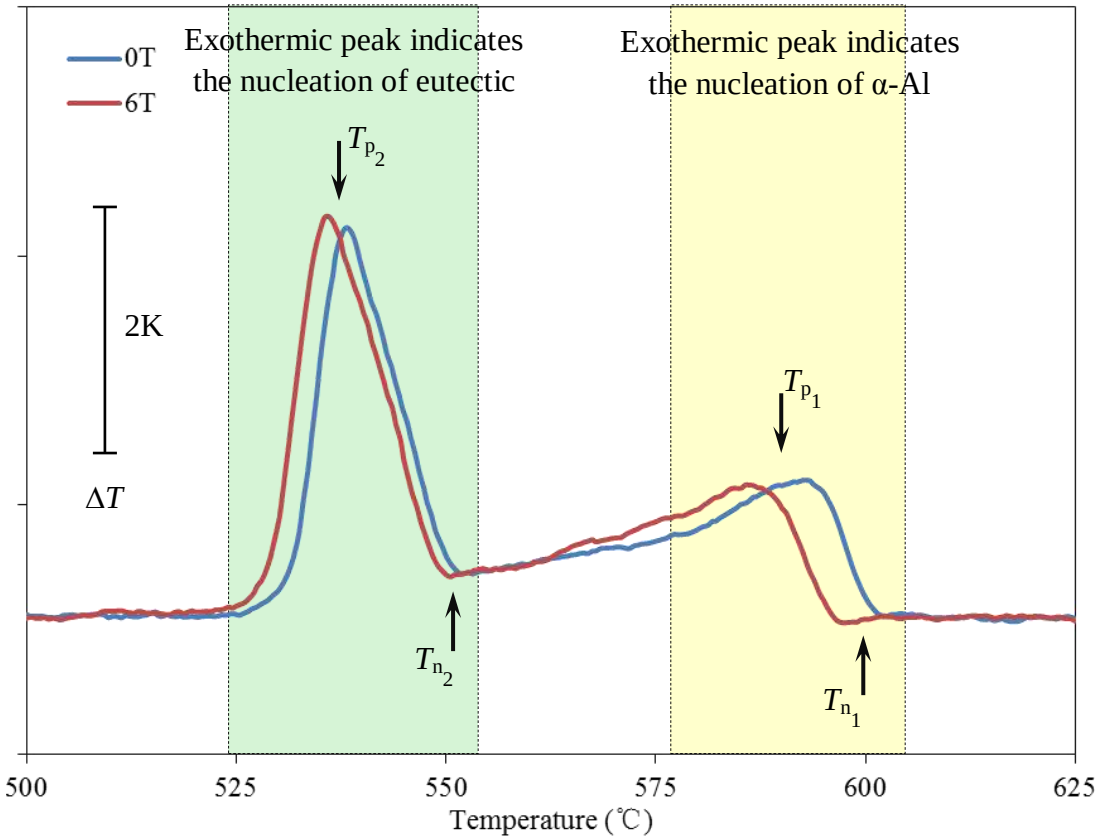

Figure 5.11 DTA curves obtained during solidifying hypoeutectic Al-10at%Cu alloy without and with a 6T AMF, and the cooling rate is kept constant at 5K/min.

It had been discussed and proved that the mushy zone length is sensitive to the flows in melt around and ahead of the dendrites. Therefore, it is reasonable to argue that TEM flows and solutal convections were not slowed down farther when AMF increased from 1T to 2T. This is reasonable because it has been proved that flows in melt cannot be entirely stopped no matter how high the magnetic field is imposed [315]. This can explain why nearly no apparent change of mushy zone length is found between the strucutre shown in figure 5.9 (a) and (b) respectively. In another aspect, this explanation also reminds us that it cannot expect to shorten the mushy zone length by further increasing AMF intensities. So that, the appearance of nealy entire coupled growth structure shown in figures 5.9 (c) and (f) cannot be attricbuted to the stronger damping effect of high magnetic field. In fact, even though the pure diffusional phenomenon is assumed to be achieved under AMF higher than 1T, for example 4T, the dendrite-plus-eutectic structure should still prevail because the coupled growth structure can be achieved only when the growth velocity is lower than about 0.36μm/s as revealed by figure 5.10. Therefore, there must be another mechanism leading to the appearance of nearly entire coupled growth structure under 4T AMF. It is thought to be the effect of high magnetic field

on the modification of the nucleation temperature and growth velocity of each phase during solidifying the hypoeutectic Al-Cu alloys.

Table 5.3 Parameters obtained from DTA curves shown in figure 5.11

B (T)	0T	6T	Remarks
T_{n_1} (℃)	601.58	596.52 **(-5.06)**	Nucleation temperature of α-Al **decreases**.
T_{p_1} (℃)	592.81	586.36	———
T_{n_2} (℃)	553.14	551.37 **(-1.77)**	Nucleation temperature of eutectic **decreases**.
T_{p_2} (℃)	538.13	537.25	———
T_{n_1} - T_{n_2} (K)	48.44	45.15 **(-3.29)**	Nucleation temperature difference between α-Al and eutectic **decreases**.
$T_{n_1} - T_{p_1}$ (K)	8.77	10.16 **(+1.39)**	Growth velocity of α-Al **decreases**.
$T_{n_2} - T_{p_2}$ (K)	15.01	14.12 **(-0.89)**	Growth velocity of eutectic **increase**.

In order to prove this suppose, DTA tests were taken during solidifying the hypoeutectic Al-10at%Cu alloy with a constant cooling rate of 5K/min in the absence and presence of 6T AMF. Al-10at%Cu (about Al-21wt%Cu) was selected to perform DTA test because it has bigger temperature difference between its liquidus and eutectic reaction temperatures and thus the exothermic peaks separate to each other distinguishedly. It can be observed that the exothermic peaks for both α-Al and eutectic phases switched to lower temperature region under a 6T AMF. According to the illustration of DTA curves in figure 5.4, this suggests that the imposed AMF retarded the nucleation of these two phases. Further, examined the exact values of parameters listed in table 5.3 that obtained from the DTA curves, it can be found that the retarding degrees of the nucleation temperatures of two phases are different. Indeed, the nucleation temperature of primary α-Al phase is decreased by 5.06K, and that of eutectic phase is retarded by 1.77K only. This shortens the nucleation temperature difference between α-Al and eutectic phases from 48.44K to 45.15K, which enhances the superiority of eutectic phase in the growth competition with the primary phase. In another aspect, based on the interpretation of parameters obtained from DTA curve at the end of chapter 5.1, the growth velocities of phases can be revealed by the difference between nucleation and peak

temperatures, T_n-T_p. Therefore, it can find from table 5.3 that the growth velocity of α-Al is slightly superessed by the 6T AMF, conversely, the growth velocity of Al-Al_2Cu eutectic phase is increased by the 6T AMF. This can further enhance the eutectic phase to dominate in the final solidified structure. These DTA results enable us to conclude that the nearly entire coupled growth structure in the hypoeutectic Al-26wt%Cu alloy directionally solidified under 4T AMF must be attributed to the influence of high magnetic field on the nucleation temperature and the growth velocity of both α-Al and eutectic phases. In another aspect, it can find that, upon the hypoeutectic Al-Cu alloy, only the alloys with composition higher than 31.45wt%Cu can form coupled growth structure under the present experimental conditions that G=6200K/m and R=2μm/s if there no magnetic field is imposed. Therefore, it can say that high static magnetic field extends the composition range for the hypoeutectic Al-Cu alloys forming coupled growth structure.

5.3 Influence of axial magnetic field during directionally solidifying hypereutectic Al-40wt%Cu alloy

Influence of imposing AMF during directionally solidifying the hypereutectic Al-40wt%Cu alloys was investigated as well. Results show that length of the mushy zone, which referring to distance between the tips of primary Al_2Cu dendrites and the following eutectic front here, changes when the AMF varys. Dislike the situation achieved in directional solidification of the hypoeutectic alloys, the lighter Al solutes are rejected during directionally solidifying the hypereutectic Al-Cu alloys. Therefore, TEM flows have the reversed effect on the variation of mushy zone length. Indeed, the mushy zone length decreases firstly as the AMF increase from 0T to 0.5T and reaches the minimum maginitude under 0.5T AMF, and then slightly increase with further increasing AMF. Further, longitudinal and transverse structures of solidified structures obtained under various AMF flux intensities are examined. It finds that the growth of primary Al_2Cu phase is enhanced by the magnetic field, and this enhancement is dramatic when AMF is higher than 1T. This may be because that the metl within mushy zone become dilute when the flows are mostly suppressed by sufficient high magnetic field and the defect multiplication in faceted Al_2Cu phase caused by TEM forces acting on them.

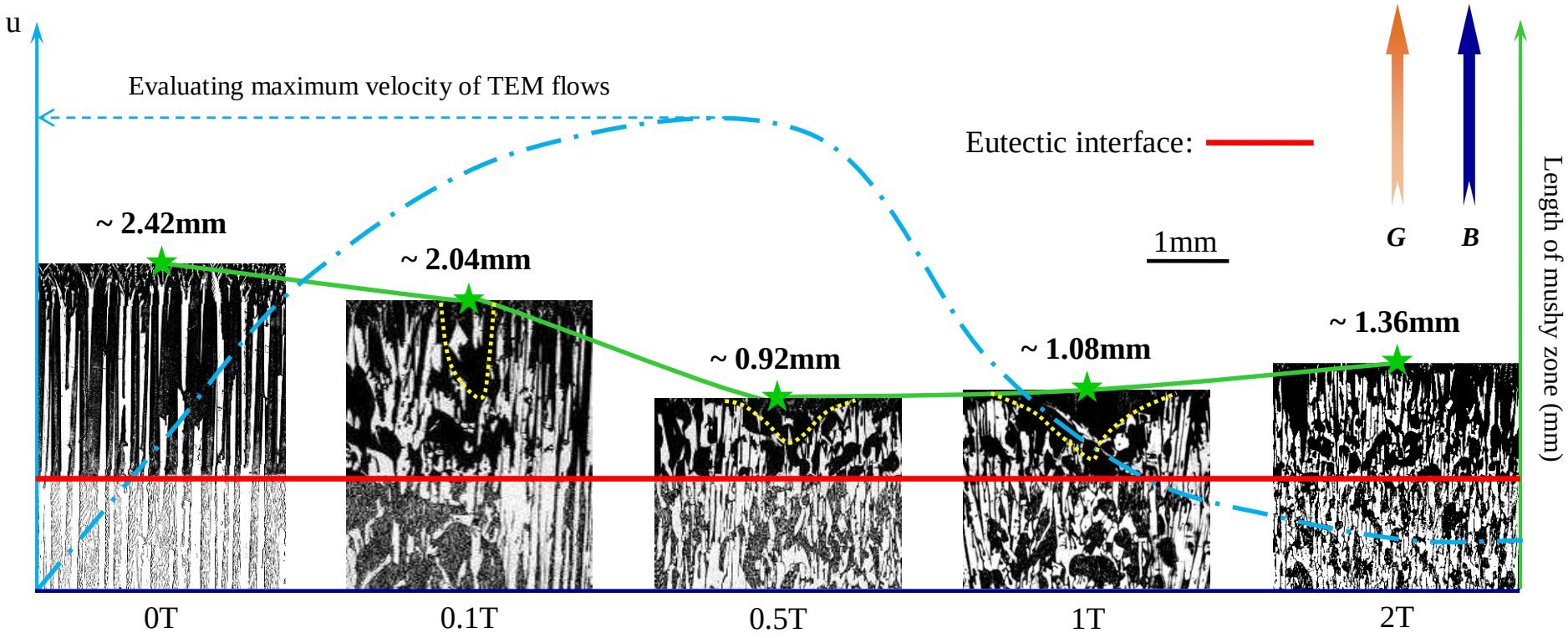

Figure 5.12 Longitudinal (parallel to both growth and magnetic field direction) solidified structure containing both dendritic and eutectic interfaces achieved via directionally solidifying the Al-40wt%Cu alloy under different AMF flux intensities that 0T, 0.1T, 0.5T, 1T and 2T. Red line marks the eutectic front, green stars point the tips of dendritic interfaces, blue line approximately illustrates how the velocities of TEM flows vary with AMF flux intensities, and the mushy zone lengths are given at the top of each figure. (R=2μm/s, G=6200K/m)

5.3.1 Influence of low magnetic field on the mushy zone length during directionally solidifying Al-40wt%Cu alloy

Place the eutectic front at the same height level, figure 5.12 compares the length of mushy zone obtained during directionally solidifying the hypereutectic Al-40wt%Cu alloys under different AMF flux intensities. It is clear that a typical dendrite-plus-eutectic structure is achieved when the magnetic field is absent and its mushy zone length is about 2.42mm. This length is also shorter than the one estimated via employing the method shown in figure 5.5, because the rejected Al solutes make the composition of melt ahead the primary Al_2Cu dendrite and in the mushy zone smaller than 40wt%Cu. Moreover, it can see that the mushy zone becomes shorter and shorter when the AMF is increased from 0T to 0.5T. Further increasing AMF flux intensities enlongates the mushy zone a little bit such as the ones obtained under 1T and 2T AMF. Simular to the mushy zone length variation observed in directional solidification of Al-26wt%Cu alloys, it is thought that the mushy zone length variation obtained here should be casued by TEM flows around the primary Al_2Cu dendrites.

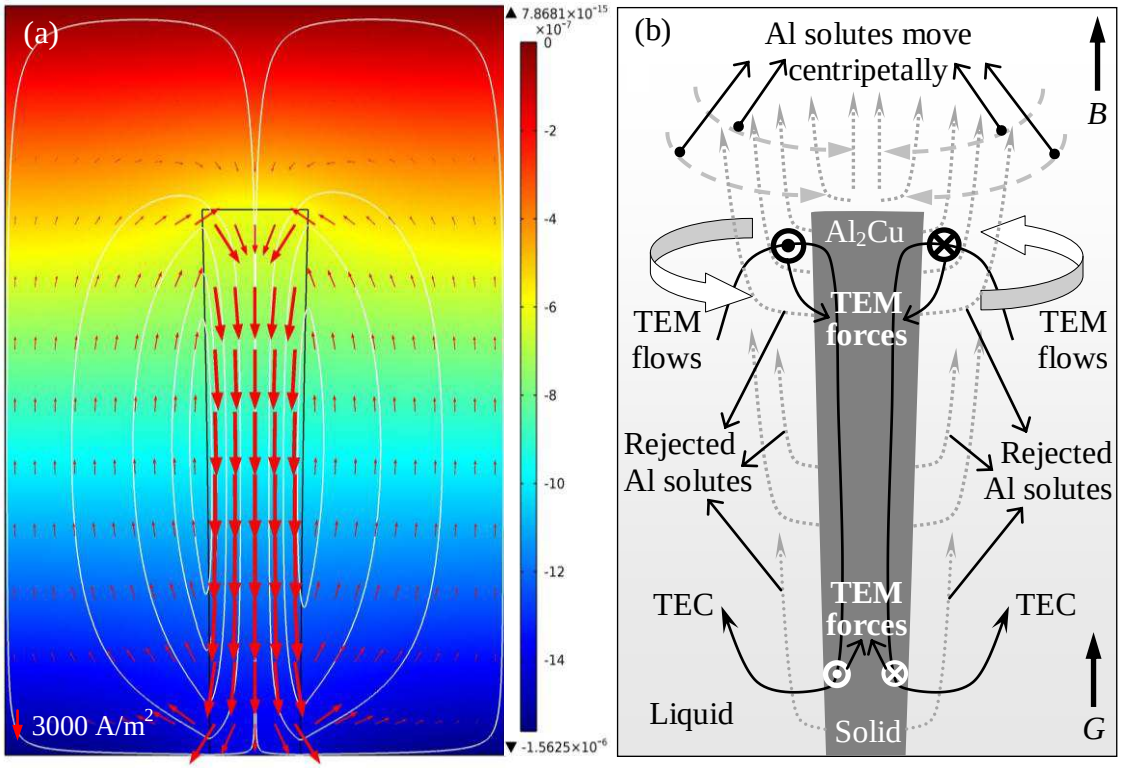

Figure 5.13 (a) Computed thermoelectric potential (colored slice) and the corresponding TEC (red arrows and white streamlines), and the unit of legend is V; (b) Schematic illustration of TEME in case of Al_2Cu dendrites being the primary phase during directionally solidifying hypereutectic Al-Cu alloys.

In order to confirm whether TEME can occur or not in the structure that primary Al_2Cu dendrite leading to the Al-Al_2Cu eutectic phase with a certain distance, TEC was simulated with the similar sturcutre. Taken the relevant physical parameters listed in table 5.1 and applied the same conditions used in experiments, the 2D simulation of TEC were performed.

Figure 5.13(a) shows the computed thermoelectric potential and the TEC around the leading Al_2Cu dendrites. It can be seen that TEC do exist in this case and flow through both the solid Al_2Cu dendrite and the melt surrounding as shown by the white streamlines. Provided that such TEC are unchanged and impose an AMF, how TEME behave is schematically illustrated in figure 5.13(b). As it has been stated in the previous chapter, TEM forces should be produced once the magnetic field is imposed because TEC exist already. So that, in the present case, TEM forces exist in both the faceted Al_2Cu phase and the surrounding melt as indicated respectively by the white and black marks in figure 5.13 (b). Consequently, as indicated by the white arrows in figure 5.13 (b), swirl TEM flows around the primary Al_2Cu dendrite are driven by such kind of TEM forces in liquid. Considering the rejecte Al solutes are ligher than the original melts and based on the principle that lighter inclusions can be gathered by rotating the melt [316], the swirl TEM flows can disturb the floating of the Al solute enriched melt and gather them near to the primary dendirtes as revealed by the dotted light-grey arrows surrounding the Al_2Cu phase in figure 5.13 (b). This increases the concentration of Al element of local melt and thus suppresses the growth of primary Al_2Cu dendrite. Consequently, the mushy zone becomes shorter. The gathering effect of swirl TEM flows in the present cases can be confirmed by the longitudinal structure obtained under 0.1T, 0.5T and 1T as well. As marked by the yellow dotted concave curves in figure 5.12, the degeneration of the middle region of mushy zone suggests that the rejected Al solutes are gathered at these regions. Beside, one thing must be pointed out that the floating of Al solutes should be taken into account when consider the gathering effect of the swirl TEM flows because the gathering effect can be apparent only if the velocities of TEM flows are higher than those of the floating of Al solutes. For this reason, it can be found that the shortening of mushy zone length is tiny (about 0.38mm) when TEM flows are relative weak under 0.1T, and apparent shortening (about 1.5mm) is found when TEM flows reached their maximum velocities under 0.5T AMF. Increased AMF to higher than 0.5T, as indicated by the light-blue dot-dash line in figure 5.12, TEM flows were damped. Correspondingly, the length of mushy zone increases slightly compared to the one achieved under 0.5T. The consistence between the change of mushy zone length and the variation of the velocities of TEM flows with the constantly increasing AMF flux intensities can prove that TEM flows do exist in directional solidification of both hypo- and hyper- eutectic alloys and are able to modify the mushy zone length.

Figure 5.14 shows the mushy zone structure of Al-40wt%Cu alloys solidified under higher AMF flux intensities that are respectively 2T, 4T and 6T. It shows that the mushy zone elongates with AMF flux intensities rising, and it (about 2.39mm) become as the same long as

the one obtained without magnetic field (about 2.42mm) under a 6T AMF. This is because the floating of Al solutes does not affect a lot by the high AMF but the swirl TEM flows are almostly suprresed.

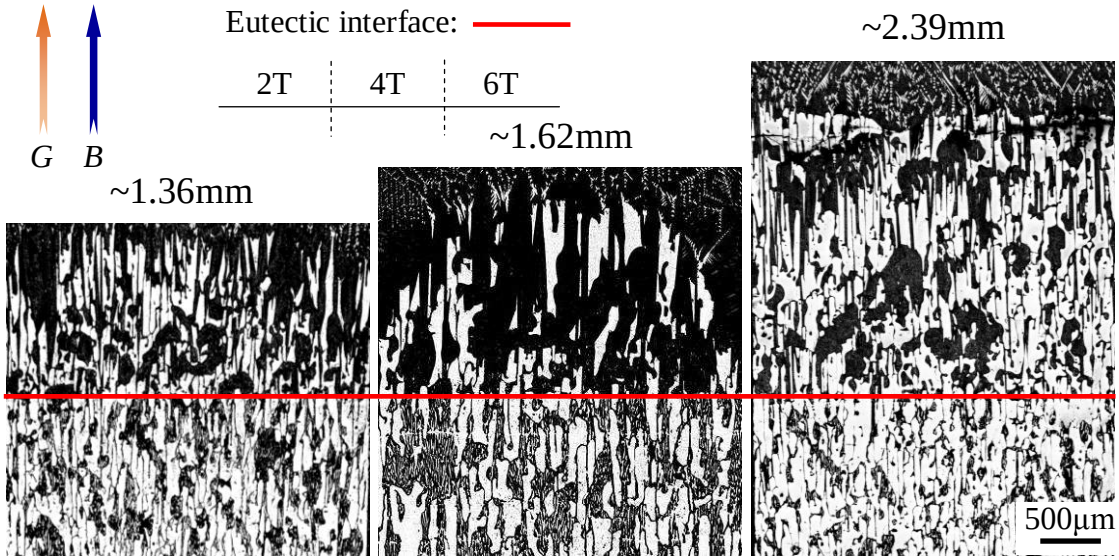

Figure 5.14 Longitudinal (parallel to both growth and magnetic field direction) mushy zone structure of Al-40wt%Cu alloys directionally solidified under different AMF flux intensities that 2T, 4T and 6T. Red line marks the eutectic front, the mushy zone length are given at the top of each figure. (R=2μm/s, G=6200K/m)

5.3.2 Enhancement of the growth of Al_2Cu phase in hypereutectic Al-40wt%Cu alloy solidified under high magnetic field

In addition to observe the quenching interface, the solid structure of samples solidified under different AMF flux intensities were examined as well. Figure5.15 (a) shows a typical directionally solidified structure of hypereutectic Al-40wt%Cu alloy obtained without magnetic field. It can see that the Al_2Cu phase is continuously growing along the heat flux direction and surrounded by the eutectic phase. The deformed structure of Al_2Cu phase is observed in the structure achieved under a 0.5T AMF, at the same time, freckles appear as pointed out by the white arrows in figure 5.15 (b). According to the mechanism of the formation of freckles during solidification [317-319], these freckles can manifest the existence of new flows in melt around and ahead the primary Al_2Cu phase. Therefore, this is another evidence for the occurrence of TEM flows when directional solidification is conduceted under magnetic field. Moreover, both the number and the magnitude of freckles decrease when TEM flows are suppressed under high magnetic field such as 6T and 12T AMF. In another aspect, it can find from the transverse structures that, the area fraction of the faceted Al_2Cu phase increase when AMF rises from 0T to 12T. Further, the area measurement were made on both longitudinal and transverse solid structures of samples obtained under different AMF flux intensities to get quantitative information about the area fraction of the

Al_2Cu phase. The results are displayed in figure 5.16, which shows that the area of Al_2Cu phase extended with AMF increasing. Moreover, as indicated by the red and blue dot-dash lines in the inserted curves, the area extension is slight when the AMF is lower than 1T and becomes apparent when AMF is higher than 1T. Because area fraction of the phase can approximately represent its growth during solidification [320, 321], it is reasonable to conclude that the growth of faceted Al_2Cu phase is enhanced by the AMF.

Considering TEM forces should appear and act on both solid and liquid if the directional solidification is conducted under a magnetic field, the enhancement of the growth of the faceted Al_2Cu phase is thought to be caused by the TEM forces in solid. Dislike the velocities of TEM flows in melt the magnituedes of TEM forces in solid increase constantly with the raising magnetic fields if the solid does not move. Correspondingly, TEM forces in solid Al_2Cu phase will constantly increase with the imposed AMF rising. Because it had been widely accepted and proved that the defects can be produced by stresses acting on the crystals during their growth and the defects in crystals are benefit on the thire growth [322-324], the constantly increasing TEM forces in Al_2Cu phase can cause the defect multiplication and thus enchance the growth of primary Al_2Cu phase. In fact, the defect multiplication caused by imposing high magnetic field during solidification of Al-40wt%Cu alloy had been proved by my colleagues [325]. As shown in figure 5.17, it can find abundant dislocations in both α-Al and Al_2Cu phases when the Al-40wt%Cu alloy was directionally solidified under 10T AMF. At last, one thing should be stated briefly that the magnitude of the growth enhancement effect of TEM forces in solid slightly decreases when AMF is higher than 6T as revealed by the red and blue dotted lines in figure 5.16. This is because the sufficient strong TEM forces in solid will lead to the break of the brittle Al_2Cu phase but not always increase the defects in them. The break of primary Al_2Cu dendrites can be also indicated by the solid structures as shown in figure 5.15 (c) and (d). For this reason, the magnitude of the growth enhancement effect of TEM forces in solid must slightly decrease when they are strong enough to break the Al_2Cu dendrites.

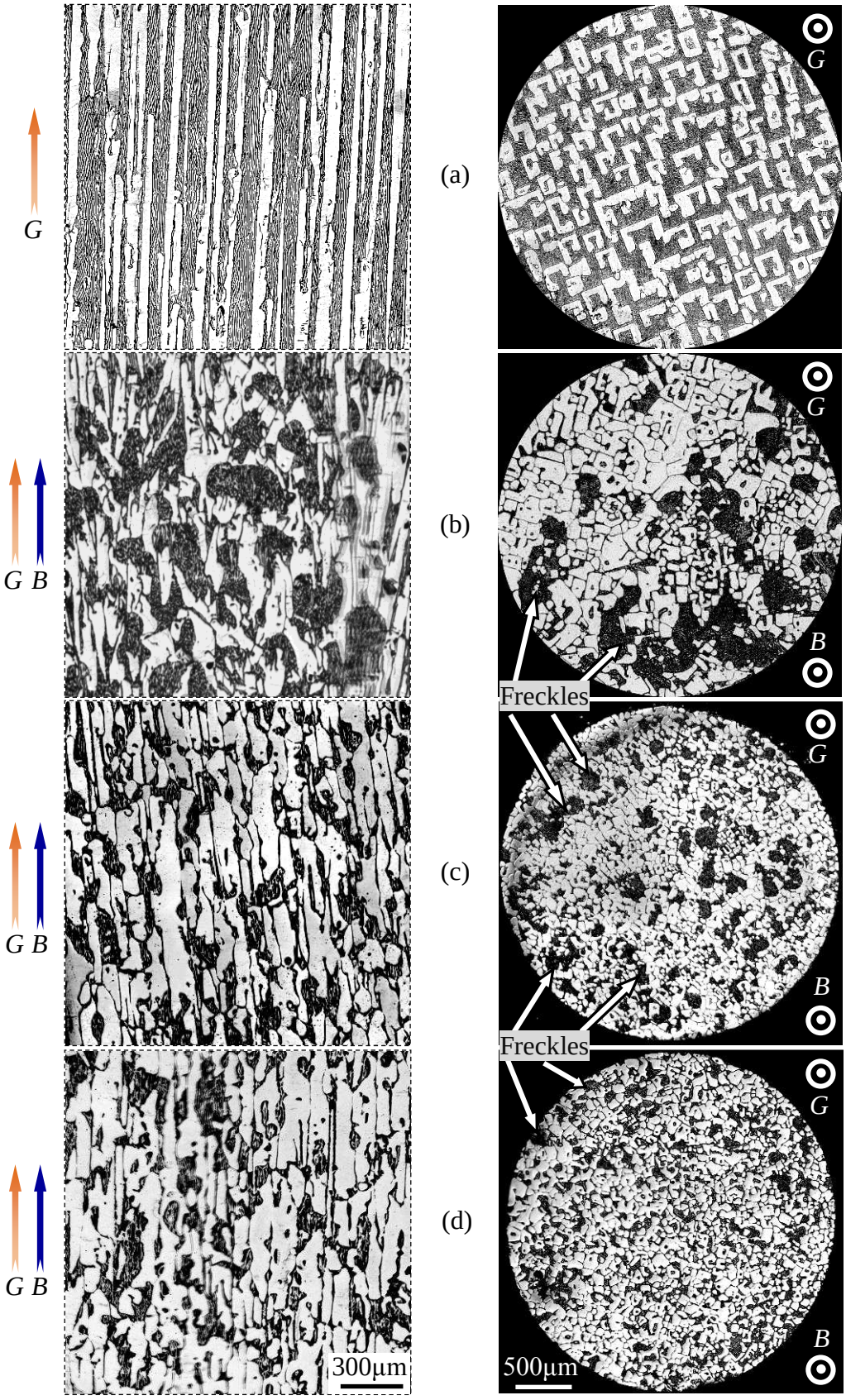

Figure 5.15 Longitudinal (parallel to both growth and magnetic field direction) and transverse (perpendicular to both growth and magnetic field direction) solid structures of Al-40wt%Cu alloys solidified under different AMF flux intensities that (a) 0T, (b) 0.5T, (c) 6T and (d) 12T. (R=2μm/s, G=6200K/m)

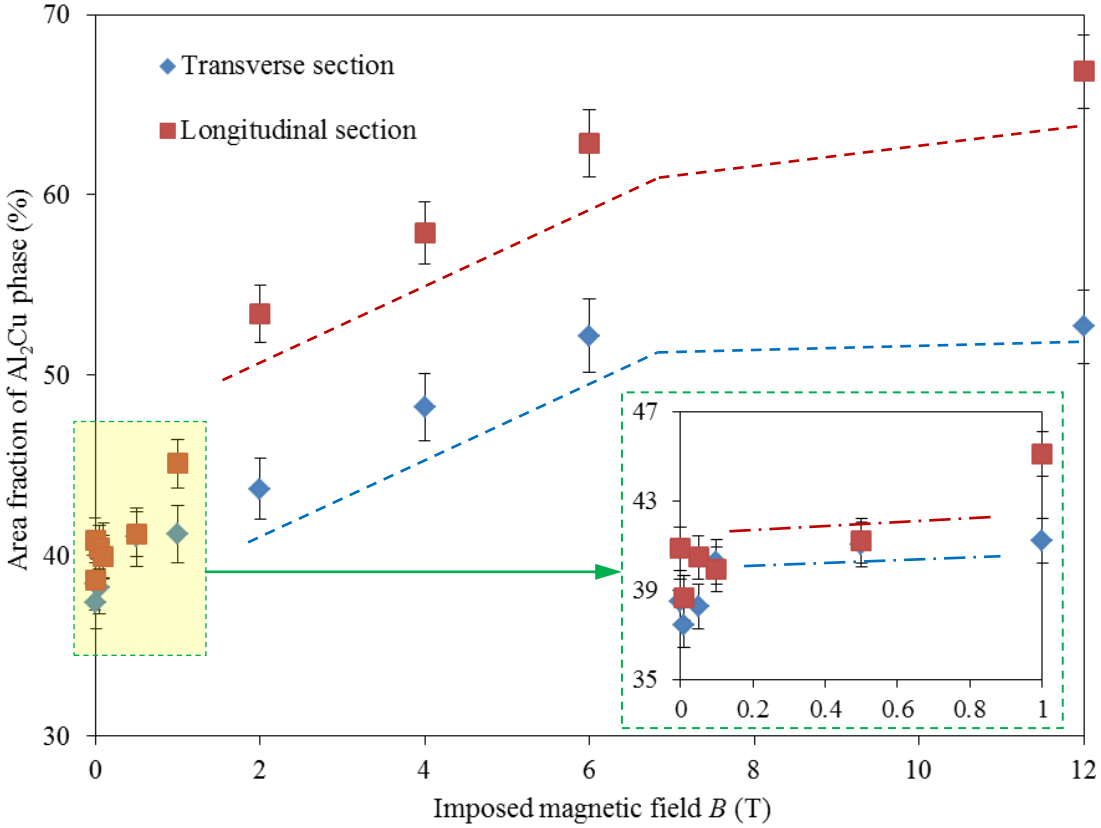

Figure 5.16 Curves of area fractions of primary Al_2Cu phase in solid structures plotted versus the imposed AMF flux intensities, and the magnified view of curves in the region marked by the yellow box.

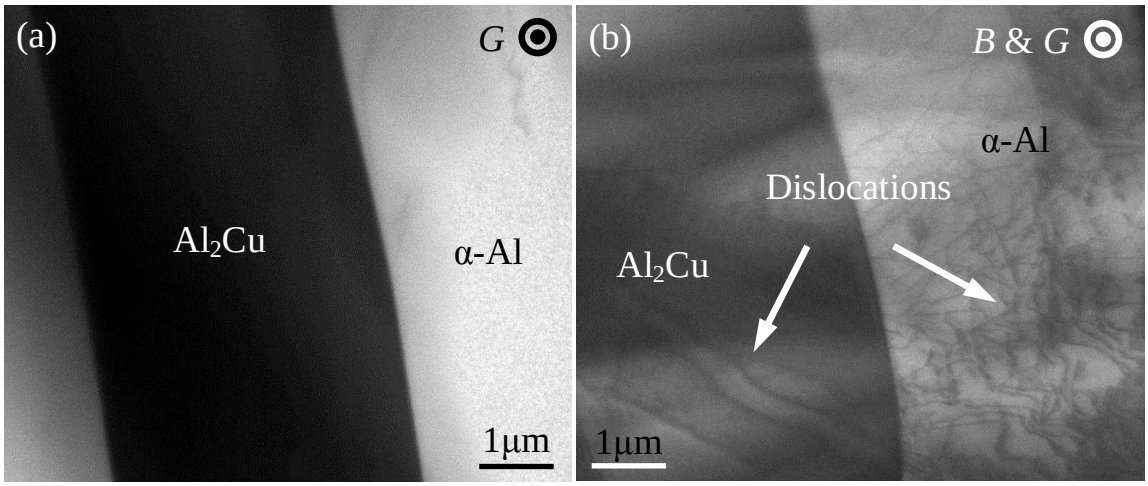

Figure 5.17 Bright field transmission electron microscope image of Al-40wt%Cu alloys directionally solidified without (a) and with a 10T magnetic field (b). (G=37.8K/cm, R=1μm/s)

5.4 Summary

With prospect to investigate the influence of magnetic field on formation of structure during directionally solidifying the near eutectic alloys, as well as examine whether the TEME can affect or not, hypoeutectic Al-26wt%Cu and hypereutectic Al-40wt%Cu alloys were directionally solidified under different AMF flux intensities. Without magnetic field, a

typical dendrite-plus-eutectic structures were achieved in both hypo- and hyper- eutectic alloys under the conditions that thermal gradient of 6200K/m and pulling-down speed of 2μm/s. Imposed magnetic field lower than 1T, the mushy zone length changed with imposed AMF varying, and the length changes had the same tendency as the change of the velocities of TEM flows with the increasing magnetic fields. 2D simulations of TEC with the parameters used by the experiments and the configuration similar to the structure obtained in experiments were performed. The computed results showed that TEC can appear in the dendrite-plus-eutectic structures and mostly flow along the first arms of the primary dendrites. This gives rise to the occurrence of TEM forces as well as TEM flows when the magnetic field is present. According to the illustration, the TEM flows are swirl and around the primary dendrites. The swirl TEM flows may be capable to influence the composition of melt ahead and around the primary dendrites due to the density difference between the solute enriched melt and the original ones. Therefore, the mushy zone length was changed. Continously increase the flux intensities of AMF, a nearly entire coupled growth structure was achieved in Al-26wt%Cu alloy when the directional solidification was conducted under 4T AMF. DTA tests showed that this dramatic structure modification should be attributed to the change of the nucleation temperature of the α-Al and the eutectic phases and their growth velocities by the high magnetic field. This result suggests that the high magnetic field is capable to extend the composition range for the hypoeutectic Al-Cu alloys forming coupled growth structure. In another aspect, enhancement of the primary faceted Al_2Cu phase was found in the solid structure of Al-40wt%Cu alloys solidified under AMF, and such growth enhancement became dramatic when AMF is higher than 1T. Because it has been well known that stresses in crystals can cause the defect multiplication, and the defects are benefit on the growth of the faceted phases, the enhancement of the growth of faceted Al_2Cu phase was thought to be attributed to the TEM forces acting on them. TEM forces in Al_2Cu phase are not all employed to increase the amount of defects because they will break the Al_2Cu dendrites when they are surfficient strong under a high magnetic field, higher than 6T for instance. Break of the primary dendirtes can be proved by the increasing number of Al_2Cu phases with decreased dimensions in the solid structure of Al-40wt%Cu solidified under 12T AMF. For this reason, the magnitude of the growth enhancement effect of TEM forces in solid should slightly decrease when the imposed magnetic field is high. Dislike the hypoeutectic system, high magnetic cannot extend but reduce the composition range for the hypereutectic Al-Cu alloys forming coupled growth structure.

Chapter 6: Conclusions and prospects

Thermoelectric magnetic effect (TEME) is the result of interaction between internal thermoelectric currents (TEC) and external magnetic field, which contains two aspects named TEM forces and TEM flows. Before this thesis, many fragmented post-mortem experiments had provided some indications of the existence of these two phenomena when they studied the influence of imposing magnetic field on solidification. However, systematical investigation has not been made. With the desire to uncover TEME in the magnetic field assisting directional solidification of metallic alloys, this thesis firstly introduced the context of the related theories and illustrated TEC and TEME schematically and numerically, and secondly proved the existence of TEME in solidification by direct observation, and finally, experimentally examined whether TEME can or not affect in directional solidification of the single and the near eutectic Al-Cu alloys with relative big samples.

- *TEME in magnetic field assisting directional solidification is a newly and promising branch in electromagnetic process of materials (EPM) field, particularly, in the research topic of solidification under static magnetic field.*

The first proposal on studying thermoelectric magnetohydrodynamics (TEMHD) flows (the same ones we call TEM flows in this thesis) in metallurgy was put forward by Prof. Shercliff. Theory of TEMHD flows was given in his paper published in 1979. However, the unintentional indications of the existence of TEM flows in solidification can be found when Prof. Youdelis and Dorward studied the influence of magnetic field on directional solidification of Al-Cu alloys in 1965. This can be categorized to the EPM field, particularly, the research topic of solidification under static magnetic field.

- *TEC, TEM forces and TEM flows are formulated, schematically illustrated and numerically simulated.*

Aim at displaying the TEM forces and flows in solidification process, chapter 2 introduced the thermoelectric (TE) effect and its corresponding phenomena in directional solidification process. It was found that TE effect is inevitable during directionally solidifying the metallic alloys because liquid and solid have different thermophysical properties such as ATP. According to the the approximate estimations the influence of Peltier and Thomson effects and the investigation from Dr. Makoto Tanaka [263], only Seebeck effect was considered in this thesis. Numerical simulations showed that TEC does exist and close their circuits along the liquid-solid interface. With such internal TEC, TEME appeared once the external magnetic field was present. Correspondingly, TEM forces and TEM flows in

magnetic field assisting directional solidification were illustrated schematically and numerically simulated.

- *TEM forces and TEM flows are proved by direct observation of the magnetic field assisting directional solidification process via synchrotron X-ray imaging method.*

With the purpose to directly observe TEME during directionally solidifying the metallic alloys, in-situ synchrotron X-ray imaging method was used to record the process of directional solidification of Al-4wt%Cu and Al-10wt%Cu alloys under a 0.08T static transverse magnetic field. Because it is hard to directly measure stresses, we consider TEM forces to be in-situ observed if their direct resulting phenomenon is seen. Therefore, the consistency between the observed movements of crystals and those predicted by analytical calculations proved the existence of TEM forces in solid. Similar, it is yet difficult to in-situ watch flows in melt, so that, once the direct resultant of TEM flows is observed we think that the in-situ observation of TEM flows is achieved. Considering the shape of liquid-solid interface is sensitive to the solute concerntration of melt ahead, and which should be influenced by flows in melt, abnormal change of liquid-solid interface shape under the external magnetic field was considered as the indication of the existence of TEM flows in melt. Moreover, 3D simulations of TEM flows showed that TEM flows in the in-situ experiments had the same direction as that of the solute transportation which can cause the observed abnormal shape change of the interface.

However, there are still some lacks in the present synchrotron X-ray in-situ observation experiments, such as the direction and the magnitude of imposed magnetic field cannot be adjusted within a single solidification process. Supposed that these can be optimized, it would be possible to get more information about TEME in magnetic field assisting directional solidification. For example, whether or not the TEM forces in solid are able to break dendrites can be determined, and if yes, the exact critical magnetic field flux intensities responding to the fracture can be found. Moreover, the magnitude of forces responding to the fragmentation of dendrites can be known as well.

- *Influence of TEME in big smaple is studied by directional solidification of single phase Al-Cu alloys under various magnetic fields.*

Motivated by the wish to examine the influence of TEME in more realistic situations, directional solidification of Al-Cu alloys with big samples were conducted under various transverse magnetic field (TMF) flux intensities. Before experiments, the velocities of TEM flows were evaluated. It was found that TEM flows speed up firstly with increasing magnetic fields and reach their maximum velocities under a critical magnetic field, and then slow down when the imposed magnetic field further increased. Such critical magnetic field flux intensity

was estimated. It was found that the critical magnetic field was closely related to a parameter λ that the so-called typical length scale, indeed, the smaller the λ is the higher the critical magnetic field flux intensity is. Because the typical length scale varies with different morphologies of interfaces in directional solidification, the critical magnetic field flux intensity would be different for different solidified structures as well. Experimental results showed reasonable consistency with these evaluations, particularly, the change tendency of the velocities of TEM flows with increasing TMF. Schematic illustrations and corresponding 3D simulations were made to explain how TEME appear in these experiments. Rather than this specialized case, 3D simulations were performed with a general geometry for three different typical lengths that 1mm, 0.1mm and 0.01mm. These simulations revealed that either the imposed magnetic field is transverse or axial the change tendency of the velocities of TEM flows with increasing magnetic fields is the same and has a highly consistent with the ones obtained from evaluations and experiments respectively. In addition, these simulations uncovered another important phenomenon that TEM forces in solid are anisotropic. When impose TMF, TEM forces in solid point to positive *x*-axis at the top and the middle of the solid side of interface and to negative *x*-axis at the periphery. In the case of imposing AMF, TEM forces in solid form a torque that makes the top of interface tend to revolve anti-clockwise and the bottom part rotate clockwise.

Dissimilar to TEM forces in liquid, TEM forces in solid will constantly increase with the increasing magnetic fields. This is worth to be paid mare attentions in the future works because once the sufficient high magnetic field is imposed the strong TEM forces must exist in the solid. For example, about 10^6 N/m^3 force in solid can be achieved if directionally solidifying the Al-Cu alloy under a 10T magnetic field. Such strong forces in solid must play a crucial role on microstructure modification. Besides, precisely determining the appropriate typical length scale of different morphologies should be also taken serious because it is an important parameter in the calculations and simulations of TEME problems in solidification. Further, whether or not the same typical length can be used when the direction of imposed magnetic field changes is another problem needs to be solved.

- *Influence of magnetic field as well as TEME on directional solidification of near-eutectic Al-Cu alloys is investigated respectively.*

With purposes to investigate the influence of magnetic field during directionally solidifying the near-eutectic alloys, as well as to examine whether the TEME can affect or not, hypoeutectic Al-26wt%Cu and hypereutectic Al-40wt%Cu alloys were directionally solidified under various AMF flux intensities. It was found that a typical dendrite-plus-eutectic structures were achieved in both hypo- and hyper- eutectic alloys solidified with a constant

thermal gradient of 6200K/m and pulling-down speed of 2μm/s in the absence of magnetic field. However, the mushy zone length that referring distance between the tips of primary dendrites and the eutectic front changed when the imposed AMF varied within 1T. It was thought that swirl TEM flows around the primary dendrites occurred and influenced the transportation of rejected solutes and thus modified the mushy zone length. Coupled growth structure was found in Al-26wt%Cu alloys solidified under a 4T AMF. DTA tests showed that the nucleation temperature and growth velocityof the α-Al and eutectic phases were changed by the high magnetic field, and which was benefit on the prevailing of coupled growth structure. This result suggests that the high magnetic field is capable to extend the composition range for hypoeutectic Al-Cu alloys forming coupled growth structure. Enhanced growth of the primary faceted Al_2Cu phase was found in the Al-40wt%Cu solidified under AMF, and which became dramatic when AMF is higher than 1T. Because the stresses in crystals can cause defect multiplication, and defects in solid are able to facilitate the growth of faceted crystals, it can reasonable attribute the growth enhancement of Al_2Cu phase to TEM forces acting on it. However, the magnitude of the growth enhancement effect of TEM forces in solid slightly decreased when TEM forces were strong under higher magnetic field because part of them would be employed to break the Al_2Cu phase dendrites. Dislike the hypoeutectic alloys, high magnetic reduces but not exteneds the composition range for hypereutectic Al-Cu alloys forming coupled growth structure.

Because the above investigationes are preliminary and other related studies are rare, more works are necessary to extend and deep our knowledge on the influence of magnetic field as well as TEME on the formation of structure during directionally solidifying the near eutectic alloys.

Appendix:

Publications

1. ***Jiang Wang***, Yves Fautrelle, Zhongming Ren, Xi Li, Henri Nguyen-Thi, Nathalie Mangelinck-Noel, Georges Salloum Abou Jaoude, Yunbo Zhong, Imants Kaldre, Andris Bojarevics, Leonid Buligins, Thermoelectric magnetic force acting on the solid during directional solidification under a static magnetic field, *Applied Physics Letters* (SCI, IF 3.84), 2012, Vol.101, p.251904.
2. ***Jiang Wang***, Zhongming Ren, Yves Fautrelle, Xi Li, Henri Nguyen-Thi, Nathalie Mangelinck-Noel, Georges Salloum Abou Jaoude, Yunbo Zhong, Imants Kaldre, Andris Bojarevics, Modification of liquid/solid interface shape in directionally solidifying Al–Cu alloys by a transverse magnetic field, *Journal of Materials Science* (SCI, IF 2.06), 2013, Vol.48 (1), p.213-219.
3. ***Jiang Wang***, Yunbo Zhong, Yves Fautrelle, Tianxiang Zheng, Fu Li, Zhongming Ren, François Debray, Influence of static high magnetic field on the liquid-liquid separation of hyper-monotectic alloy, *Applied Physics A* (SCI, IF 1.64), 2013, Vol. 112, p.1027-1031.
4. ***Jiang Wang***, Yves Fautrelle, Zhongming Ren, Xi Li, Henri Nguyen-Thi, Nathalie Mangelinck-Noel, Georges Salloum Abou Jaoude, Yunbo Zhong, Imants Kaldre, Andris Bojarevics, Leonid Buligins, In-situ analyzing the influence of thermoelectromagnetic convection on the nucleation ahead of the advancing interface during directional solidification, The 7th international EPM conference, Beijing, China.
5. ***Jiang Wang*** Yunbo Zhong Tianxiang Zheng Fu Li Zhongming Ren, Influence of strong static magnetic field on dynamics of solidifying hyper-monotectic Zn-Bi alloy, The 4th international conference on magneto-science, Shanghai&Xi'an, China.
6. ***Jiang Wang*** Yunbo Zhong Chao Wang Zhiqiang Wang Zhongming Ren Kuangdi Xu, Physical simulation of homogenous Zn-Bi monotectic alloy prepared by electric-magnet compound field, *Acta Physica Sinica* (SCI, IF 1.26), 2011, Vol. 60, p.1-9.
7. ***Jiang Wang*** Yunbo Zhong Zhongming Ren, Influence of High Static Magnetic Field on Dynamics of Solidification Hyper-monotectic Zn-Bi alloys, The 3rd international conference on Advances in Solidification Processes, Aachen, Germany.
8. ***Jiang Wang*** Yunbo Zhong Weili Ren Zuo-sheng Lei Zhongming Ren Kuangdi Xu,

Effect of high static magnetic field and AC current on solidification of Zn-30wt%Bi monotectic alloy, *Acta Physica Sinica* (SCI, IF 1.26), 2009, Vol.58, p.893-900.

9. ***Jiang Wang*** Yunbo Zhong Zhingqiang Wang Weili Ren Zuosheng Lei Zhongming Ren, Solidification of Zn-30wt％Bi Monotectic Alloy By Superimposing High Static Magnetic Field and AC Current Simultaneously, The 6th international EPM conference, Dresden, Germany. (**Best Poster Reward**)
10. Yunbo Zhong, ***Jiang Wang***, Zhongming Ren, Chinese Patent: A method to fabricate the homogenous monotectic alloy and the equipment, No. 200710047493.4.
11. Yunbo Zhong, ***Jiang Wang***, Fu Li, Chinese Patent: A method to prepare the uniform structure and composition monotectic materials, No. 201110429216.6.
12. Yunbo Zhong, ***Jiang Wang***, Tianxiang Zheng, Fu Li, Yves Fautrelle, Zhongming Ren, In-situ analysis of bulk solidifying the hyper-monotectic alloy under a compound electric-magnetic field by physical simulation, The 7th international EPM conference, Beijing, China.
13. Yunbo Zhong, ***Jiang Wang***, Tianxiang Zheng, François Debray, Yves Fautrelle, Solidification of hyper-monotectic Zinc-Bismuth alloy in a strong magnetic field, The 7th international EPM conference, Beijing, China.
14. Yunbo Zhong, ***Jiang Wang***, Fu Li Tianxiang Zheng Zhongming Ren, Physical simulation on the dynamics of the solidifying hyper-monotectic alloy under coupled electric and magnetic field, The 4th international conference on magneto-science, Shanghai&Xi'an China.
15. Tianxiang Zheng, Zongqiang Sun, ***Jiang Wang***, Qiufang Wu, Meilong Feng, Yunbo Zhong, Zhongming Ren, The effect of electromagnetic compound field on the solidified microstructure of Zn-10wt%Bi hyper-monotectic alloy, *Acta Physica Sinica* (SCI, IF 1.26), 2012, Vol.61, p.238501.
16. Chao Wang, Yunbo Zhong, ***Jiang Wang***, Effect of magnetic field on electroplating Ni/nano-Al2O3 composite coating, *Journal of Electro-analytical Chemistry* (SCI, IF 2.67), 2009, Vol.630, p.42-48.

References

[1] FARADAY Michael. The bakerian lecture: experimental researches in electricity. *Phil. Trans. R. Soc. Lond.*, 1832, 122, p. 163-194.

[2] WILLIAMS E. J. The induction of electromotive forces in a moving liquid by a magnetic field and its application to an investigation of the flow of liquids. *Proc. Phys. Soc.*, 1930, 42, p. 466-478.

[3] ALFVEN Hannes. Existence of electromagnetic-hydrodynamic waves. *Nature*, 1942, 150, p.405-406.

[4] DAVY Humphry. Farther researches on the magnetic phenomena produced by electricity; with some new experiments on the properties of electrified bodies in their relations to conducting powers and temperature. *Phil. Trans. R. Soc. Lond.*, 1821, 111, p. 425-439.

[5] RITCHIE William. Experimental researches in voltaic electricity and electro-magnetism. *Phil. Trans. R. Soc. Lond.*, 1832, 122, p. 279-298.

[6] SHERCLIFF Arthur J. *A textbook of magnetohydrodynamics*. London: Pergamon, 1965, 2 p.

[7] WOLLASTON C. Induced electromotive force in sea. *J. Soc. Tel. Engrs.*, 1881, 10, p.50-67.

[8] MOLOKOV S., MOREAU R., MOFFATT K. H. *Magnetohydrodynamics: Historical evolution and trends*. Dordrecht: Springer, 2007, p. 3-26.

[9] FAWWAZ Ulaby. *Fundamentals of applied electromagnetic (5^{th} ed.)*. Pearson: Prentice Hall, 2007, 255 p.

[10] Waterloo Bridge - http://en.wikipedia.org/wiki/Waterloo_Bridge

[11] SHERCLIFF Arthur J. *A textbook of magnetohydrodynamics*. London: Pergamon, 1965, 5 p.

[12] BERRY F. Arthur. *Improvements in or relating to Apparatus for the Electrical Production of Heat for Cooking and other purposes*. UK Patent, 1906, GB190612333.

[13] NORTHRUP F. Edwin. Some newly observed manifestations of forces in the interior of an electric conductor. *Phys. Rev.*, 1907, 24, p.474-497.

[14] BACHELET Emile. Electromagnetic apparatus. U.S. Patent, 1907, 849653.

[15] GARNIER Marcel. Electromagnetic processing of liquid materials in Europe. *ISIJ Inter.*, 1990, 30, p.1-7.

[16] LARMOR sir Joseph. *Engineering*, 1919, 108, p.461-473.

[17] PETERSEN Richard. *Electronic still camera*, U.S Patent, 1919, 1443091.

[18] HARTMANN J. Hg-Dynamics 1. Theory of the laminar flow of an electrically conductive liquid in a homogeneous magnetic field. *Det. Kgl. Danske. Vid Sels. Mat-Fys Medd*, 1937, 15, p.1-27.

[19] ELSASSER Walter. On the origin of the earth's magnetic field. *Phys. Rev.*, 1939, 55, p.489-498.

[20] ALLEM E. John. Transient pinched plasmas and strong hydromagnetic waves. *Magnetohydrodynamics: Historical evolution and trends*/ MOLOKOV S., MOREAU R., MOFFATT K. H. ed. Dordrecht: Springer, 2007, p.118-127.

[21] COWLEY Martin. Early years of MHD at Cambridge University engineering department. *Magnetohydrodynamics: Historical evolution and trends*/ MOLOKOV S., MOREAU R., MOFFATT K. H. ed. Dordrecht: Springer, 2007, p.131-154.

[22] COWLING T. G. Magnetohydrodynamics. *Rep. Prog. Phys.*, 1962, 25, p.244-286.

[23] HUNT J. C. R., MOREAU R. Liquid-metal magnetohydrodynamics with strong magnetic fields: a report on Euromech 70. *J. Fluid Mech.*, 1976, 78, p.261-288.

[24] KOLESNICHENKO Fedorovich Anatoliy. Electromagnetic process in liquid material in the USSR and East European countries. *ISIJ Inter.*, 1990, 30, p.8-26.

[25] ASAI Shigeo. Recent development and prospect of electromagnetic processing of materials. *Sci. Tech. Adv. Mater.*, 2000, 1, p.191-200.

[26] FAUTRELLE Yves, ERNST Roland, MOREAU Rene. Magnetohydrodynamics applied to materials processing. *Int. J. Mat. Res.*, 2009,100, p.1389-1398.

[27] ASAI Shigeo. Overview of electromagnetic processing of materials. *Magnetohydrodynamics: Historical evolution and trends*/ MOLOKOV S., MOREAU R., MOFFATT K. H. ed. Dordrecht: Springer, 2007, p.315-327.

[28] YOSHIFUMI Tanimoto, Effect of magnetic orientation magnetic force and Lorentz force. *Magneto-Science - magnetic field effects on materials: fundamentals and applications*/ YAMAGUCHI M., TANIMOTO Y. ed. Berlin: Kodansha and Springer, 2006, p.17-24.

[29] AOGAKI R., FUEKI K., MUKAIBO T. Application of magneto hydrodynamic effect to the analysis of electrochemical reactions 1. *Denki kagaku*, 1975, 43, p.504-509.

[30] AOGAKI R., FUEKI K., MUKAIBO T. Application of magneto hydrodynamic effect to the analysis of electrochemical reactions 2: diffusion process in MHD forced flow of electrolyte solution. *Denki kagaku*, 1975, 43, p.509-514.

[31] NAKAGAWA Y., Research in steady high magnetic fields at Sendai. *Phyica B*, 1994, 201, p.49-56.

[32] CONRAD Hans, Influence of an electric or magnetic field on the liquid-solid transformation in materials and on the microstructure of the solid. *Mater. Sci. Eng. A*, 2000, 287, p.205-212.

[33] YASUDA Hideyuki, TOH Takehiko, IWAI Kazuhiko, *et al.* Recent progress of EPM in steelmaking, casting and solidification processing. *ISIJ Int.*, 2007, 47, p.619-626.

[34] GILLON Pascale. Uses of intense d.c. magnetic fields in materials processing. *Mater. Sci. Eng. A*, 2000, 287, p.146-152.

[35] ASAI Shigeo. Application of high magnetic fields in inorganic materials processing. *Modelling Simul. Mater. Sci. Eng.*, 2004, 12, p.R1-R12.

[36] 7th International conference on electromagnetic processing of materials - http://epm2012.dconference.cn/dct/page/1.

[37] DAVIES E. J. *Conduction and Induction heating*. London: Peter Peregrinus, 1990, 13p.

[38] MUHLBAUER Alfred, *History of Induction heating and melting*. Hardcover: Vulkan-Verlag GmbH, 2008, 52p.

[39] DETLING Miles, NOESKE W. Ottmar. Aluminizing engine valves with induction heating. Wear, 1959, 2, p.411.

[40] IAN Harvey, Induction heating - http://www.thermopedia.com/content/874/.

[41] RANKIN Kennedy. *Electrical Installations of electric light, power, traction and industrial electrical machinery*. London: Blackwood, 1903.

[42] MOROS A., HUNT R. C. J. Recirculating flows in the cross-section of a channel induction furnace. *Int. J. Heat Mass Transfer*, 1988, 31,p.1497-1515.

[43] GHOJEL I. J., IBRAHIM N. R. Computer simulation of the thermal regime of double-loop channel induction furnaces. *J. Mater. Proc. Tech.*, 2004, 153-154, p.386-391.

[44] BRUNELLI K., DABALA M., DUGHIERO F., *et al*. Diffusion treatment of Ni-B coatings by induction heating to harden the surface of Ti-6Al-4V alloy. *Mater. Chem. Phys.*, 2009, 115, p.467-472.

[45] AHMED T. J., STAVROV D., BERSEE N. E. H., BEUKERS A. Induction welding of thermoplastic composites – an overview. *Composites: part A*, 2006, 37, p.1638-1651.

[46] EGGER A. Untersuchungen der schmelzenstromung und des warmetransports im inductions-rinnenofen. *Fortschritt-Berichte VDI*, 1993, 19, p.63-75.

[47] FASHOLZ J., ORTH G. Induktive erwarmung. Essen: RWE-Energie, 1991.

[48] LUPI S., DUGHIERO F., FORZAN M. Modelling single- and double-frequency induction hardening of gear-wheels. *Proceedings of the 5th international symposium on electromagnetic processing of materials*, 2006, p.473-478.

[49] MISAK Y., KUIYOSAWA Y., KAWASAKI K., *et al.* Gear contour hardening by micropulse induction heating systems. *Auto. Eng. Soc.*, 1997, p.121-130.

[50] JONES L. P., AUBER P., AVILOV V., *et al.* Towards advanced welding methods for the ITER vacuum vessel sectors. *Fusion Eng. Des.*, 2003, 69, p.200-215.

[51] AVILOV V.V., BERGER P., AMBROSY G. Electromagnetic melts support system for overhead position laser and electron beam welding of thick metal plates. *Proceedings of the 5th international symposium on electromagnetic processing of materials*, 2006, p.237-241.

[52] AVILOV V. V., LOWER T., AMBROSY G., *et al*. *Method for treatment of metal subjected by high power beam, especially by welding*. German Patent, 2002, DE 10225781.

[53] FAUTRELLE Yves. Electromagnetic processing of liquid metal: review of the research activity in France. *Proceedings of the 5th international symposium on electromagnetic processing of materials*, 2006, p.9-14.

[54] NACKE Bernard. New application of EPM in metal, oxide and semiconductor processing. *Proceedings of the 5th international symposium on electromagnetic processing of materials*, 2006, p.496-501.

[55] Simens & Halske. *Verfahren zum schmelzen schwerschmelzbarer metalle, insbesondere von tantal, wolfram, thorium oder legierungen dieser metalle in einem wassergekuhlten behalter*. German Patent, 1931, 518.499.

[56] BOJAREVICS V., PERICLEOUS K., HARDING R. A., *et al.* Cold crucible melting of reactive metals using combined DC and AC magnetic fields. *Proceedings of the 5th international symposium on electromagnetic processing of materials*, 2006, p.778-783.

[57] UMBRASHKO A., BAAKE E., NACKE B., *et al*. Experimental investigations and numerical modelling of the melting process in the cold crucible. *Proceedings of the international symposium on heating by electromagnetic sources*, 2004, p.31-37.

[58] WRONA E., NACKE B., SCHWENK W. Solving complex induction hardening tasks by numerical methods. *Proceedings of the international symposium on heating by electromagnetic sources*, 2004, p.593-598.

[59] YANG Jieren, CHEN Ruirun, DING Hongsheng, *et al.* Thermal characteristics of induction heating in cold crucible used for directional solidification. App. Ther. Eng., 2013, 59, p.69-76.

[60] ALHERITIERE Edouard, DRIOLE Jean, GAGNOUD Annie, *et al*. *Apparatus for melting and continuous casting of metals, the process involved and use of the apparatus*. US Patent, 1989, US 4838933 A.

[61] CHE Ruirun, DING Hongsheng, GUO Jingjie, *et al*. Process on cold crucible electromagnetic casting for titanium alloy. *China Foundry*, 2007, 4, p.190-193.

[62] SUGILAL G. Experimental analysis of the performance of cold crucible induction glass melter. *App. Therm. Eng.*, 2008, 28, p.1952-1961.

[63] PERICLEOUS K., BOJAREVICS V., BJAMBAZOV G., *et al*. Experimental and numerical study of the cold crucible melting process. *App. Math. Model.*, 2006, 30, p.1266-1280.

[64] BACHELET Emile. *Levitating transmitting apparatus*. US Patent, 1912, US 1020942.

[65] ROTE M. Donald, CAI Yigang. Review of dynamic stability of repulsive-force maglev suspension systems. *IEEE Trans.Magnetics*, 2002, 38, p.1383-1390.

[66] OKRESS C. E., WROUGHTON M. D., COMENETZ G., *et al*. Electromagnetic levitation of solid and molten metals. *J. Appl. Phys.*, 1952, 23, p.545-552.

[67] GILLON Pascale. Contactless processing of metallic materials by stabilized electromagnetic levitation. *Mater. Trans.*, 2000, 41, p.1000-1004.

[68] BOJAREVICS V., PERICLEOUS K., CROSS M. Modeling the dynamics of magnetic semi-levitation melting. *Metall. Materials Trans. B*, 2000, 31, p.179-189.

[69] JAYAWANT B. V. Electromagnetic suspension and levitation. *Rep. Prog. Phys.*, 1981, 44, p.411-474.

[70] AMINI Shaahin, kalaantari Haamun, MOJGANI Sasan, et al. Graphite crystals grown within electromagnetically levitated metallic droplets. *Acta Mater.*, 2012, 60, p.7123-7131.

[71] STRINGHAM H. G. *Electrical drink mixer*. US Patent, 1917, US 1242493.

[72] MAFFATT H. K. Electromagnetic stirring. *Phys. Fluids A*, 1991, 3, p.1336-1343.

[73] ZI Bingtao, BA Qixian, CUI Jiangzhong, *et al*. Study on axial changes of as-cast structures of Al-alloy sample treated by the novel SPMF technique. *Scripta Mater.*, 2000, 43, p. 377-380.

[74] JOHNSTON W. C., TILLER W. A. Fluid flow control during solidification – magnetic stirring in the plane of solute. *Tans. Metall. Soc. AIME*, 1961, 221, p.331-336.

[75] DOLD P., BENZ W. K. Rotating magnetic fields: fluid flow and crystal growth applications. *Progress in Crystal Growth Characterization of Materials*, 1999, 38, p.7-38.

[76] LI Xi, REN Zhongming, FAUTRELLE Yves. Effects of the simultaneous imposition of electromagnetic and magnetic forces on the solidification structure of pure Al and Al-4.5wt%Cu alloy. *J. Mater. Proc. Tech.*, 2008, 195, p.125-134.

[77] LI Mingjun, TAMURA Takuya, MIWA Kenji. Controlling microstructures of AZ31 magnesium alloys by an electromagnetic vibration technique during solidification: From experimental observation to theoretical understanding. *Acta Mater.*, 2007, 55, p.4635-4643.

[78] WANG Jiang, ZHONG Yunbo, REN Weili, *et al*. Effect of high static magnetic field and AC current on solidification of Zn-30wt%Bi monotectic alloy. *Acta Phys. Sin.*, 2009, 58, p.893-900.

[79] YU Jiangbo, REN Zhongming, REN Weili, *et al*. Solidification structure of eutectic Al-Si alloy under a high magnetic field-aid-electromagnetic vibration. *Acta Metall. Sin.*, 2009, 22, p.191-196.

[80] HERNANDEZ ROBLES C. F., SOKOLOWSKI H. J. Comparison among chemical and electromagnetic stirring and vibration melt treatments for Al–Si hypereutectic alloys. *J. Alloys Comp.*, 2006, 426, p.205-212.

[81] ABRAMOV O. V., SOMMER F., ORLOV D. Properties of Al-Pb base alloys applying electromagnetic forces and ultrasonic vibration during casting. *Mater. Letts.*, 1995, 23, p.17-20.

[82] WANG Bin, YANG Yuansheng, MA Xiaoping, et al. Simulation of electromagnetic flow fields in Mg melt under pulsed magnetic field. *Tran. Nonferrous Met. Soc. China*, 2010, 20, 283-288.

[83] CHOWDHURY Joydeep, GANGULY Suvankar, CHAKRABORTY Suma. Numerical simulation of transport phenomena in electromagnetically stirred semi-solid materials processing. *J. Phys. D, 2005, 38*, p.2869-2880.

[84] WILLERS B., ECKERT S., NIKRITYUK A. P., *et al*. Efficient melt stirring using pulse sequences of a rotating magnetic field. *Metall. Mater. Trans. B*, 2008, 39, p.304-316.

[85] UMBRASHKO A., BAAKE E., NACKE B., *et al*. Experimental investigations and numerical modelling of the melting process in the cold crucible. *Inter. J. Comp. Math. Elect. Elect. Eng.*, 2005, 24, p.314-323.

[86] ZAIDAT Kader, MANGELINCK-NOEL Nathalie, MOREAU Rene. Control of melt convection by travelling magnetic field during the directional solidification of Al-Ni alloys. *C. R. Mecanique*, 2007, 335, p.330-335.

[87] GARNIER Marcel, MOREAU Rene. *Electromagnetic nozzle*. French Patent, 1977, No. 77.21.121.

[88] KADAR L. I., BIRINGER P. P., LAVERS J. D. Modification of the nozzle flow using electromagnetic induction. *IEEE Trans. Magnetic*, 1994, 30, p.4686-4688.

[89] YU Haiqi, WANG baofeng, LI Huiqin, *et al*. Influence of electromagnetic brake on flow field of liquid steel in the slab continuous casting mold. *J. Mater. Proc. Tech.*, 2008, 202, p.179-187.

[90] BLOFGREN B. Hans, AKERSTEDT O. Hans. Electromagnetic braking of the flow of a liquid metal with a free surface. *Fluid Dy. Res.*, 1998, 23, p.1-25.

[91] CHU Xiangcheng, XING Zengping, GONG Wen, *et al*. Vibration analysis of stepping piezoelectric micro-motor using wiggle mode. *Mater. Sci. Eng. B*, 2003, 99, p.306-308.

[92] VIDAL N., AGUIRRE-ZAMALLOA G., BARANDIARAN M. J., *et al*. FEM analysis of an eddy current water flow meter. *J. Magnetism Magnetic Mater.*, 2006, 304, p.e838-e840.

[93] BOTTAUSCIO Oriano, CHIAMPI Mario, MANZIN Alessandra. Modeling analysis of the electromagnetic braking action on rotating solid cylinders. *App. Math. Modeling*, 2008, 32, p.12-27.

[94] CHUNG D. Y., LEE Y. C., JANG Y. J., *et al*. Theoretical and FEM analysis of suspension and propulsion system with HTS hybrid electromagnets in an EMS Maglev model. *Phys. C*, 2011, 471, p.1487-1491.

[95] ZUECO Joaquin, BEG Anwar O. Network numerical analysis of hydromagnetic squeeze film flow dynamics between two parallel rotating disks with induced magnetic field effects. Tribology Int., 2010, 43, p.532-543.

[96] WANG Engang, LI Kang, LI Fei, *et al*. Numerical simulation of magnetic field and fluid flow in continuous casting mold with a new pattern electromagnetic brake. *Proceedings of 6th international conference on electromagnetic processing of materials*, 2009, Dresden, German.

[97] CONRATH Michael, KOCOUREK Vaclav, KARCHER Christian. Behavior of a liquid metal disk in the magnetic field of a circular current loop. *Proceedings of 5th International symposium on electromagnetic processing of materials*, 2006, p.210-213.

[98] FAUTRELLE Yves, SNEYD Alfred, ETAY Jacqueline. Effect of AC magnetic fields on free surface. *Magnetohydrodynamics: Historical evolution and trends*/ MOLOKOV S., MOREAU R., MOFFATT K. H. ed. Dordrecht: Springer, 2007, p.345-355.

[99] MOHRING U. J., KARCHER C. SCHULZE D. Dynamic behaviour of a liquid metal interface under the influence of a high frequency magnetic field. *Phys. Rev. E*, 2005, 71, 047301.

[100] HENROT Antoine. Behaviour of the free boundary in electromagnetic shaping when the surface tension vanishes. *Nonlinear Analysis*, 1993, 20, p.965-978.

[101] SANTOS A. C., SPIM A. J. GARCIA A. Modeling of solidification in twin-roll strip casting. *J. Mater. Proc. Tech.*, 2000, 102, p.33-39.

[102] WANG Bo, ZHANG Jieyu, FAN Junfei, *et al*. Water Modeling of Twin-Roll Strip Casting. *J. Iron Steel Resh. Int.*, 2006, 13, p.14-17.

[103] XIA Xiaojiang, WANG Hongming, DAI Qixun, *et al*. Numerical simulation of high frequency magnetic field for electromagnetic soft-contact continuous casting. *Chinese J. Nonferrous Metals*, 2008, 3, p.367-372.

[104] LI Tingju, NAGAYA Shiji, SASSA Kensuke, *et al*. Study of meniscus behavior and surface properties during casting in a high-frequency magnetic field. *Metall. Mater. Trans. B*, 1995, 26, p.353-359.

[105] LI Shuangming, LI Jinshan, HAO Qitang, *et al*. Research on the dual-frequency electromagnetic shaping of liquid metal. *J. Mater. Proc. Tech.*, 2003, 137, p.204-207.

[106] ALBANO G. P., BORGHI A.C., CRISTOFOLINI A., *et al*. Industrial applications of magnetohydrodynamics at the University of Bologna. *Energy Conversion and Management*, 2002, 43, p.353-363.

[107] HIROTA Noriyuki, HARA Soma. In situ microscopic observation of magnetic field effects on the silver dendrites growth. *Proceedings of 5th International symposium on electromagnetic processing of materials*, 2006, p.805-809.

[108] NISHIKAWA Kei, FUKUNAKA Yasuhiro, CHASSAING Elisabeth, *et al*. On electrodeposition of metals in microgravity conditions. *Electrochim. Acta*, 2013, 100, p.342-349.

[109] XIAO Feng, HANGARTER Carlos, YOO Bonguoung, *et al*. Recent progress in electrodeposition of thermoelectric thin films and nanostructures. *Electrochim. Acta*, 2008, 53, p.8103-8117.

[110] SIMKA Wojciech, PUSZCZYK Dagmara, NAWRAT Ginter. Electrodeposition of metals from non-aqueous solutions. *Electrochim. Acta*, 2009, 54, p.5307-5319.

[111] AOGAKI Ryoichi. Recent progress in magneto-electrochemistry. *Proceedings of 5th International symposium on electromagnetic processing of materials*, 2006, p.799-804.

[112] WANG Chao, ZHONG Yunbo, REN Weili, *et al*. Effects of parallel magnetic field on electrocodeposition behavior of Ni/nanoparticle composite electroplating. *App. Sur. Sci.*, 2008, 254, p.5649-5654.

[113] MOGI Iwao, KAMIKO Masao. Magnetic-field-induced diffusion-limited-aggregation in electrodeposition. *J. Phys. Soc. Japan*, 1995, 64, p.4500-4503.

[114] ALEMANY Antoine, CHOPART Jean Paul. An outline of magnetoelectrochemistry. *Magnetohydrodynamics: Historical evolution and trends*/ MOLOKOV S., MOREAU R., MOFFATT K. H. ed. Dordrecht: Springer, 2007, p.391-407.

[115] FAHIDY T. Z. Magnetoelectrolysis. *J. Appl. Electrochem.*, 1983, 13, p.553-563.

[116] AOGAKI Ryoichi, TAKAGI Satosi, MORIMOTO Ryoichi, et al. Chiral electrodeposition by rotation in a vertical magnetic field. *Proceedings of 6th International symposium on electromagnetic processing of materials*, 2009, Dresden, Germany.

[117] ZHONG Yunbo, WANG Chao, REN Weili, *et al*. Micro flow and its effect on the structure of electrodeposited coating in high magnetic field. *Proceedings of 6th International symposium on electromagnetic processing of materials*, 2009, Dresden, Germany.

[118] ZHONG Yunbo, LONG Qiong, ZHOU Penwei, *et al*. Transfers behavior of composite deposition process in static magnetic field. *Proceedings of 7th International symposium on electromagnetic processing of materials*, 2012, Beijing, China.

[119] MOGI I., KAMIKO M. Striking effects of magnetic field on the growth morphology of electrochemical deposits. *J. Cryst. Growth*, 1996, 166, p.267-280.

[120] KONIG Jorg, MUHLENHOFF Sascha, ECKERT Kerstin, *et al*. Velocity measurements inside the concentration boundary layer during copper-magneto-electrolysis using a novel laser Doppler profile sensor. *Electrochim. Acta*, 2011, 56, p.6150-6156.

[121] THESS A., VOTYAKOV V. E., KOLESNIKOV Y. Lorentz force velocimetry. *Phys. Rev. Letts.*, 2006, 96, p.164501-164505.

[122] ELKINS J. Christopher, ALLEY T. Marcus. Magnetic resonance velocimetry: applications of magnetic resonance imaging in the measurement of fluid motion. *Exp. Fluids*, 2007, 43, p.823-858.

[123] TSE C. H., MAN C. H., YUE M. T. Effect of electric and magnetic fields on plasma control during CO2 laser welding. *Opt. Lasers Eng.*, 1999, 32, p.55-63.

[124] TSE C. H., MAN C. H., YUE M. T. Effect of magnetic field on plasma control during CO2 laser welding. *Opt. Laser Tech.*, 1999, 31, p.363-368.

[125] KOIKE Kazuo, ONO Norifumi. Light intensity analysis of plasma jet constriction with applied magnetic field. *Vacuum*, 2008, 83, p.25-28.

[126] ISHIZAKI K., STIR M., GOZZO F., *et al*. Magnetic microwave heating of magnetite–carbon black mixtures. *Mater. Chem. Phys.*, 2012, 134, p.1007-1012.

[127] UMEKI Senshin, KATO Takuya, SHIMABUKURO Haruki, *et al*. Prevention of scale deposits in a water pipe by fluctuating electromagnetic treatment. *Proceedings of 5th International symposium on electromagnetic processing of materials*, 2006, p.694-699.

[128] TANIGUCHI Shoji, SHIMASAKI Shin-ichi, YOSHIKAWA Noboru, *et al*. Recent efforts of EPM application to environmental technology at Tohoku University. *Proceedings of 5th International symposium on electromagnetic processing of materials*, 2006, p.677-680.

[129] CHALMERS Bruce. The preparation of single crystals and bi-crystals by the controlled solidification of molten metals. *Can. J. Phys.*, 1953, 31, p.132-146.

[130] TILLER W. A., RUTTER W. J. The effect of growth conditions upon the solidification of a binary alloy. *Can. J. Phys.*, 1956, 34, p.96-121.

[131] LANGER James. Issues and opportunities in materials research. *Phys. Today*, 1992, 45, p.24-31.

[132] THOMPSON B. W. Thermal convection in a magnetic field. *Philosophical Magazine Series 7*, 1951, 42, p.1417-1432.

[133] LEHNERT B., LITTLE C. N. Experiments on the effect of inhomogeneity and obliquity of a magnetic field in inhibiting convection. *Tellus*, 1957,9, p.97-103.

[134] SPITZER Karl-heinz, DUBKE Mathias, SCHWERDTFEGER Klaus. Rotational electromagnetic stirring in continuous casting of round strands. *Metall. Trans. B*, 1986, 17, p.119-131.

[135] CHEDZEY A. H., HURLE J. T. D. Avoidance of growth-striae in semiconductor and metal crystals growth by zone-melting techniques. *Nature*, 1966, 210, p.933-934.

[136] UTECH P. Harver, FLEMINGS C. Merton. Elimination of solute banding in indium antimonite crystals by growth in a magnetic field. *J. App. Phys.*, 1966, 37, p.2021-2024.

[137] YOUDELIS W. V., COLTON D. R., CAHOON J. On the theory of diffusion in a magnetic field. *Can. J. Phys.*, 1964, 42, p.2217-2237.

[138] HE Lizi, LI Xiehua, ZHU Pei, *et al*. Effects of high magnetic field on the evolutions of constituent phases in 7085 aluminum alloy during homogenization. *Mater. Characterization*, 2012, 71, p.19-23.

[139] LIU M. K., LU P. D., ZHOU T. H., *et al*. Influence of a high magnetic field on the microstructure and properties of a Cu-Fe-Ag in situ composite. *Mater. Sci. Eng. A*, 2013, 584, p.114-120.

[140] LIU Tie, LIU Yin, WANG Qiang, *et al*. Microstructure magnetic and magnetostricitive properties of $Tb_{0.3}Dy_{0.7}Fe_{1.95}$ prepared by solidification in a high magnetic field. *J. Phys. D*, 2013, 46, p.12005.

[141] HOLLOMON J., TURNBULL D. Nucleation. *Progress in Metal Phys.*, 1953, 4, p.333-388.

[142] MASIHIRO I. B., YAMAGUCHI M. Magnetic energy and magneto-thermodynamic effect. *Magneto-Science - magnetic field effects on materials: fundamentals and applications*/ YAMAGUCHI M., TANIMOTO Y. ed. Berlin: Kodansha and Springer, 2006, p.9-15.

[143] YU Y. S., YAN S. S., KANG S. S., *et al*. Magnetic field-induced martensite-austenite transformation in Fe-substituted NiMnGa ribbons. *Script. Mater.*, 2011, 65, p.9-12.

[144] KAKESHITA T., SHIMIZU K., ONO M., *et al*. Magnetic field induced martensitic transformations in a few ferrous alloys. *J. Magnetism and Magnetic Mater.*, 1990, 90&91, p.34-36.

[145] MURGAS M., BIACOVSKA A. The effect of a magnetic field on the kinetics of phase transformations. *Chem. Papers.*, 1991, 45, p.731-734.

[146] OHTSUKA Hideyuki. Effects of strong magnetic fields on bainitic transformation. *Current Opinion in Solid State & Mater. Sci.*, 2004, 8, p.279-284.

[147] CHOI J. K., OHTSUKA H., XU Y. *et al*. Effects of a strong magnetic field on the phase stability of plain carbon steels. *Script. Mater.*, 2000, 43, p.221-226.

[148] KAKESHITA T., SABURI T., SHIMIZU K. Effects of hydrostatic pressure and magnetic field on martensitic transformation. *Mater. Sci. Eng. A*, 1999, 273-275, p.21-39.

[149] JOO D. H., KIM U. S., SHIN S. N., *et al*. An effect of high magnetic field on phase transformation in Fe-C systems. *Mater. Letts.*, 2000, 43, p.225-229.

[150] LI Xi, REN Zhongming, FAUTRELLE Yves. Investigation of the effect of high magnetic field on the MnBi/Mn1.08Bi phase transformation in Mn-Bi alloys by measuring the magnetic force in gradient magnetic field. Mater. Letts., 2006, 60, p.3379-3384.

[151] REN Zhongming, LI Xi, SUN Yanhui, *et al*. Influence of high magnetic field on peritectic transformation during solidification of Bi-Mn alloy. *Comp. Coup. Phases Diagrams Thermochemistry*, 2006, 30, p.277-285.

[152] LI Xi, FAUTRELLE Yves, REN Zhongming. High-magnetic-field-induced solidification of diamagnetic Bi. *Script. Mater.*, 2008, 59, p.407-410.

[153] LI Chuangjun, YANG Hui, REN Zhongming, *et al*. Application of differential thermal analysis to investigation of magnetic field effect on solidification of Al-Cu hypereutectic alloy. *J. Alloy Comp.*, 2010, 505, p.108-112.

[154] LI Chuanjun, CHENG Long, REN Zhongming. Application of ring method to measure surface tensions of liquids in high magnetic field. *Rev. Sci. Instrum.*, 2012, 83, p.0439061-5.

[155] HAXHIMALI Tomorr, KARMA Alain, GONZALES Frederic, *et al*. Orientation selection in dendritic evolution. *Nature Mater.*, 2006, 5, p.660-664.

[156] ASAI Shigeo. Magnetic crystalline alignment. *ISIJ Int.*, 2007, 47, p.519-522.

[157] SUGIYAMA Tsubasa, TAHASHI Masahiro, SASSA Kensuke, *et al*. The control of crystal orientation in non-magnetic metals by imposing a high magnetic field. *ISIJ Int.*, 2003, 43, p.855-861.

[158] TOURNIER F. Robert, BEAUGNON Eric. Texturing by cooling a metallic melt in a magnetic field. *Sci. Technol. Adv. Mater.*, 2009, 10, p.0145011-10.

[159] ASAI Shigeo, SASSA Ken-suke, TAHASHI Massahiro. Crystal orientation of non-magnetic materials by imposition of a high magnetic field. *Sci. Technol. Adv. Mater.*, 2003, 4, p.455-460.

[160] GLASER R. E., KENNEDY A. T., DOVERSPIKE K., *et al*. Optically detected magnetic resonance of GaN films grown by organometallic chemical-vapour deposition. *Phys. Rev. B*, 1995, 51, p. 13326–13336.

[161] MOLODOV A. D., BOZZOLO N. Observations on the effect of a magnetic field on the annealing texture and microstructure evolution in zirconium. *Acta Mater.*, 2010, 58, p.3568-3581.

[162] NUMOTO Nobutaka, SHIMIZU Ken-ichi, MATSUMOTO Kazuya, et al. Observation of the orientation of membrane protein crystals growth in high magnetic fields. *J. Cryst. Growth*, 2013, 367, p.53-56.

[163] CUI G. X., CUI Y. C., CHENG N. X., *et al*. Effects of alignment on the magnetic and mechanical properties of sintered Nd–Fe–B magnets. *J. Alloys Comp.*, 2013, 563, p.161-164.

[164] SUN Zhi, GUO Muxing, VLEUGELS Jef, *et al*. Strong magnetic field-induced segregation and alignment of nonmagnetic particles. *J. App. Phys.*, 2011, 109, p.07E301.

[165] CHIAKI Uyeda. Alignment of diamagnetic and paramagnetic particels. *Magneto-Science - magnetic field effects on materials: fundamentals and applications*/ YAMAGUCHI M., TANIMOTO Y. ed. Berlin: Kodansha and Springer, 2006, p.240-248.

[166] ZHANG Yudong, GEY Nathalie, HE Changshu, *et al*. High temperature tempering behaviours in a structural steel under high magnetic field. *Acta Mater.*, 2004, 52, p.3467-3474.

[167] MATSUNAGA Chika, UCHIKOSHI Tetsuo, SUZUKI S. Tohru, *et al*. Fabrication of the c-axis oriented zeolite L compacts using strong magnetic field. *Mater. Letts.*, 2013, 93, p.408-410.

[168] THOMPSION G. A., WAGNER W. J. Preparation and properties of InAs1-*x*P*x* Alloys. *J. Phys. Chem. Sol.*, 1971, 32, p.2613-2619.

[169] HU Zhaohua, ZHANG Yongzhong, SHE Jia. The role of Nd on the microstructural evolution and compressive behavior of Ti–Si alloys. *Mater. Sci. Eng. A*, 2013, 560, p.583-588.

[170] BRANDT H. E. Levitation in physics. *Science*, 1989, 243, p.349-355.

[171] NORIYUKI Hirota. Magneto-Archimedes effect and related effect. *Magneto-Science - magnetic field effects on materials: fundamentals and applications*/ YAMAGUCHI M., TANIMOTO Y. ed. Berlin: Kodansha and Springer, 2006, p.55-70.

[172] JONES B. T. A necessary condition for magnetic levitation. *J. App. Phys.*, 1979, 50, p.5057-5058.

[173] BEAUGNON E., TOURNIER R. Levitation of organic materials. *Nature*, 1991, 349, p.470.

[174] HIROTA Noriyuki, IKEZOE Yasuhiro, UETAKE Hiromichi, *et al*. Magneto-Archimedes levitation and its application. *RIKEN Rev.*, 2002, 44, p.159-161.

[175] IKEZOE Y., KAIHATSU T., SAKAE S., *et al*. Separation of feeble magnetic particles with magneto-Archimedes levitation. *Energy Conversion and Management*, 2002, 43, p.417-425.

[176] VALLES M. James, LIN Kevin, DENEGRE M. James, *et al*. Stable magnetic field gradient levitation of Xenopus laevis: toward low-gravity simulation. *Biophysical J.*, 1997, 73,p.1130-1133.

[177] WANG Qiang, LIU Tie, GAO Ao, *et al*. A novel method for in situ formation of bulk layered composites with compositional gradients by magnetic field gradient. *Script. Mater.*, 2007, 56, p.1087-1090.

[178] LI Xi, REN Zhongming, FAUTRELLE Yves. Phase distribution and phase structure control through a high gradient magnetic field during the solidification process. *Mater. Des.*, 2008, 29, p.1796-1801.

[179] RATKE L., STEINBACH S., MULLER G., *et al*. MICAST – The effect of magnetically controlled fluid flow on microstructure evolution in cast technical Al-alloys. *Microgravity Sci. Technol.*, 2005, 151, p.99-103.

[180] STEINBACH S., RATKE L. The effect of rotating magnetic fields on the microstructure directionally solidified Al-Si-Mg alloys. *Mater. Sci. Eng. A*, 2005, 413-414, p.200-204.

[181] FAVIER J. J., ROUZAUD A. Experimental study of morphological and convective instabilities: the MEPHISTO space program. *Adv. Space Res.*, 1986, 6, p.111-122.

[182] CHANDRASEKHAR S. On the inhibition of convection by a magnetic field. *Philosophical Magazine*, 1952, 43, P.501-532.

[183] SERIES W. R., HURLE J. T. D. The use of magnetic fields in semiconductor crystal growth. *J. Cryst. Growth*, 1991, 113, p.305-328.

[184] KIMURA Hiroshi, HARVEY F. M., O'CONNOR J. D., *et al*. Magnetic field effects on float-zone Si crystal growth. *J. Cryst. Growth*, 1983, 62, p.523-531.

[185] KAISER T., BEN W. K. Floating-zone growth of silicon in magnetic fields 3: numerical simulation. *J. Cryst. Growth*, 1998, 183, p.564-572.

[186] WITT F. A., HERMAN J. C., GATOS C. H. Czochralski-type crystal growth in transverse magnetic field. *J. Mater. Sci.*, 1970, 5, p.822-824.

[187] OREPER M. G., SZEKELY J. The effect of an externally imposed magnetic field on buoyancy driven flow in a rectangular cavity. *J. Cryst. Growth*, 1983, 64, p.505-515.

[188] GANAPATHYSUBRAMANIAN Baskar, ZABARAS Nicholas. On the control of solidification using magnetic fields and magnetic field gradients. *Int. J. Heat Mass Transfer*, 2005, 48, p.4174-4189.

[189] SAMPATH Rajiv, ZABARAS Nicholas. Numerical study of convection in the directional solidification of a binary alloy driven by the combined action of buoyancy, surface tension, and electromagnetic forces. *J. Computational Phys.*, 2001, 168, p.384-411.

[190] WAKAYAMA I. Nobuko, ATAKA Mitsuo, ABE Haruo. Effect of a magnetic field gradient on the crystallization of hen lysozyme. *J. Cryst. Growth*, 1997, 178, p.653-656.

[191] BOETTINGER J.W., BIANCANIELLO S. F., CORIELL R. S. Solutal convection induced macrosegregation and the dendrite to composite transition in off-eutectic alloys. *Metall. Trans. A*, 1981, 12, p.321-327.

[192] TEWARI N. S., SHAH Rajesh, SONG Hui. Effect of magnetic field on the microstructure and macrosegregation in directionally solidified Pb-Sn alloys. *Metall. Mater. Trans. A*, 1994, 25, p.1535-1544.

[193] KISHIDA Yutaka, TAKEDA Kouichi, MIYOSHINO Ikuto, *et al*. Anisotropic effect of magnetohydrodynamics on metal solidification. *ISIJ Int.*, 1990, 30, p.34-40.

[194] SPITTLE A. J. Columnar to equiaxed grain transition in as solidified alloys. Inter. Mater. Rev., 2006, 51, p.247-269.

[195] KAO Andrew. *Thermoelectric magnetohydrodynamics in dendritic solidification*. Ph. D Thesis of University of Greenwich, 2010, p.1-7.

[196] SHERCLIFF A. J. Thermoelectric magnetohydrodynamics. *J. Fluid Mech.*, 1979, 91, p.231-251.

[197] Thermoelectric effect: http://en.wikipedia.org/wiki/Thermoelectric_effect.

[198] Brief history of thermoelectric: http:// thermoelectrics.caltech.edu/thermoelectrics.

[199] JAWORSKI M. A.,GRAY T. K., ANTONELLI M., *et al*. Thermoelectric MHD stirring of Liquid Metals. Phys. Rev. Lett., 2010, 104, p.094503.

[200] LUEBKE E., VANDENBERG B. L. *Heat exchanger pump*. US Patent, 1956, US 2.748.710.

[201] MURGATROYD W. *Improvements in or relating to heat transfer systems*. UK Patent, 1951, UK appl. 20911/51.

[202] SCHOCH K. F. An experimental liquid metal thermoelectric electromagnetic pump - heat exchange. *Report of General Electric Company*, 1956, No. R56GL94.

[203] REX Von D. Thermoelektrische Pumpen fur flussige Metalle. *VDI Z.*, 1961, 103, p.17-23.

[204] OSTERLE J. F., ANGRIST S. W. The thermoelectric hydromagnatic pump. *Trans. ASME C*, 1964, 86, p.166-179.

[205] ROCKLIN R. S. *Thermoelectric pump*. US Patent, 1964, US 3116693.

[206] PERLOW A. M., DIECKAMP M. H. *Thermoelectric pump*. US Patent, 1966, US 3288070.

[207] CACHARD de M. CAUNES P. Thermosyphon à sodium pour irradiation en pile d' é1ements combustibles. *Centre d'Etudes Nucleaires Grenoble Rep*. 1969, 69, p.472-485.

[208] MAKAROV V. S., CHERKASSKII A. Kh. Pressure consumption characteristic and efficiency of a thermoelectriomagnetic pump. *Magnitnaya Gidrodinamika*, 1969, 5, p.127-141.

[209] SHERCLIFF A. J. The pipe end problem in thermoelectric MHD. *J. App. Math. Phys.*, 1980, 30, p.94-112.

[210] SHERCLIFF A. J. Thermoelectric MHD with walls parallel to the magnetic field. Int. *J. Heat Mass Transfer.*, 1980, 23, p.1219-1228.

[211] MIKELSON E. A., KARKLIN Kh. Ya. Control of crystallization processes by means of magnetic fields. *J. Cryst. Growth.*, 1981, 52, p.524-529.

[212] GORBUNOV A. L. Effect of thermoelectromagnetic convection on the production of bulk single crystals consisting of semiconductor melts in a constant magnetic field. *Magnitnaya Gidrodinamiks*, 1987, 4, p.65-69.

[213] GORBUNOV A. L., LYUMKIS D. E. Unique features encountered in the influence exerted by thermoelectromagnetic convection on melt hydrodynamics in the process of monocrystal growth by the czochralski method in a magnetic field. *Magnitnaya Gidrodinamiks*, 1990, 7, p.75-82.

[214] ALBOUSSIERE Thierry, MOREAU Rene, CAMEL Denis. Influence of a magnetic field on the solidification of metallic alloys. *C. R. Acad. Sci. Paris*, 1991, 313, p.749-755.

[215] MOREAU R., LASKER O., TANAKA M., *et al*. Thermoelectric MHD effects on solidification of metallic alloys in the dendritic regime. *Mater. Sci. Eng.*, 1993, 173, p.93-100.

[216] LIELAUSIS Ojgerts, KJAVINS Janis, MIKELSONS Arturs, *et al*. Potentials, currents and thermoelectric effects at continuous casting. *Proceedings of 1st international symposium on electromagnetic processing of materials*, Nagoya, Japan, 1994, p.555-560.

[217] KADDECHE S., HADID B. H., HENRY D. Macrosegregation and convection in the horizontal Bridgman configuration 1: dilute alloys. *J. Cryst. Growth.*, 1994, 135, p.341-353.

[218] MOREAU Rene, LASKER Oliver, TANAKA Makoto. Thermoelectric and MHD effects on solidification alloys. *Proceedings of 1st international symposium on electromagnetic processing of materials*, Nagoya, Japan, 1994, p.549-554.

[219] LEHMANN P., MOREAU R., CAMEL D., Bolcato R., Modification of interdendritic convection by a magnetic field. *Mater. Sci. Forum*, 1996, 217-222, p.235-240.

[220] LEHMANN P., MOREAU R., CAMEL D., Bolcato R., Modification of interdendritic convection in directional solidification by a uniform magnetic field. *Acta Mater.*, 1998, 46, p.4067-4079.

[221] LEHMANN P., MOREAU R., CAMEL D., Bolcato R., A simple analysis of the effect of convection on the structure of the mushy zone in the case of horizontal Bridgman solidification comparison with experimental results. *J. Cryst. Growth*, 1998, 183, p.690-704.

[222] CROLL A., SZOFRAN R. F., DOLD P., *et al*. Floating zone growth of silicon in magnetic fields 2: strong static axial fields. *J. Cryst. Growth*, 1998, 183, p.554-563.

[223] KHINE Y. Y., WALKER S. J. Thermoelectric MHD effects during Bridgman semiconductor crystal growth with a uniform axial magnetic field. *J. Cryst. Growth*, 1998, 183, p.150-158.

[224] KHINE Y. Y., WALKER S. J., SZOFRAN R. F. Thermoelectric MHD effects during Bridgman semiconductor crystal growth with a uniform axial magnetic field. *J. Cryst. Growth*, 2000, 212, p.584-596.

[225] YESILYURT Serhat, VUJISIC Ljubomir, MOTAKEF Shariar, *et al*. A numerical investigation of the effect of thermoelectriomagnetic convection on the Bridgman growth of $Ge_{1-x}Si_x$. *J. Cryst. Growth*, 1999, 207, p.278-291.

[226] YESILYURT Serhat, VUJISIC Ljubomir, MOTAKEF Shariar, *et al*. The influence of thermoelectromagnetic convection on the Bridgman growth of semiconductors. *J. Cryst. Growth*, 2000, 211, p.360-364.

[227] WALKER S. J., CROLL A., SZOFRAN R. F. Thermoelectromagnetic convection in floating zone silicon growth with a nonaxisymmetric temperature and a strong magnetic field. *J. Cryst. Growth*, 2001, 223, p.73-82.

[228] DOLD P., SZOFRAN R. F., BENZ W. K. Thermoelectromagnetic convection in vertical Bridgman grown germanium-silicon. *J. Cryst. Growth*, 2006, 291, p.1-7.

[229] LIU Qing. *Thermoelectric MHD effects on directional solidification structure of Al-Cu alloy*. Master Thesis of Liaoning Technical University, 2002.

[230] GAO Zhiyu. *Effect of TEMHD on the micorstructure of directionally solidified Al alloy*. Master Thesis of Liaoning Technical University, 2006.

[231] LI Xi, FAUTRELLE Yves, REN Zhongming. Influence of an axial high magnetic field on the liquid-solid transformation in Al-Cu hypoeutectic alloys and on the microstructure of the solid. *Acta Mater.*, 2007, 55, p.1377-1386.

[232] LI Xi, FAUTRELLE Yves, REN Zhongming. Influence of thermoelectric effects on the solid-liquid interface shape and cellular morphology in the mushy zone during the

directional solidification of Al-Cu alloys under a magnetic field. *Acta Mater.*, 2007, 55, p.3803-3813.

[233] LI Xi, REN Zhongming, FAUTRELLE Yves, *et al*. Degeneration of columnar dendrites during directional solidification under a high magnetic field. *Script. Mater.*, 2009, 60, p.443-446.

[234] CRAMER A., ZHANG X., GERBETH G. Macroscopic thermomagnetic convection: a more generic case and optimization. *Magnetohydrodynamics*, 2009, 45, p.505-510.

[235] LI Xi, GAGNOUD Annie, REN Zhongming, *et al*. Investigation of thermoelectric magnetic convection and its effect on solidification structure during directional solidification under a low axial magnetic field. *Acta. Mater.*, 2009, 57, p.2180-2197.

[236] YASUDA Hideyuki, NOGITA Kazuhiro, GOURLAY Christopher, *et al*. In-situ observation of Sn alloy solidification at Spring8. *J. Japan Welding Soc.*, 2009, 78, p.6-9.

[237] REN Weili, ZHANG Tao, REN Zhongming, *et al*. A dramatic increase in dendrite number for directionally solidified superalloy DZ417G with a strong static magnetic field. *Mater. Letts.*, 2009, 63, p.382-385.

[238] SHEN Yu, REN Zhongming, LI Xi, *et al*. Effect of a low axial magnetic field on the primary Al_2Cu phase growth in a directionally solidified Al-Cu hypereutectic alloy. *J. Cryst. Growth.*, 2011, 336, p.67-71.

[239] LI Xi, FAUTRELLE Yves, REN Zhongming, *et al*. Effect of a high magnetic field on the morphological instability and irregularity of the interface of a binary alloy during directional solidification. *Acta Mater.*, 2009, 57, p.1689-1701.

[240] LI Xi, ZHANG Yudong, FAUTRELLE Yves, *et al*. Experimental evidence for liquid/solid interface instability caused by the stress in the solid during directional solidification under a strong magnetic field. *Script. Mater.*, 2009, 60, p.489-492.

[241] SUN Z., GUO M., VLEUGELS J., *et al*. Strong static magnetic field processing of metallic materials: a review. *Current Opinion in Solid State and Mater. Sci.*, 2012, 16, p.254-267.

[242] OLIVA B. A., BIRD D. M., BOLE T. S., *et al*. Development of the superconducting outserts for the series connected hycrid program at the national high magnetic field laboratory. *IEEE Trans. Appl. Superconductivity*, 2008, 18, p.529-535.

[243] LI Xi, FAUTRELLE Yves, ZAIDAT Kader, *et al*. Columnar-to-equiaxed transition in al-based alloys during directional solidification under a high magnetic field. *J. Cryst. Growth*, 2010, 312, p.267-272.

[244] LI Xi, GAGNOUD Annie, FAUTRELLE Yves, *et al*. Investigation of thermoelectric magnetic force in solid and its effects on morphological instability in directional solidification. *J. Cryst. Growth*, 2011, 324, p.217-224.

[245] LI Xi, FAUTRELLE Yves, REN Zhongming. Morphological instability of cell and dendrite during directional solidification under a high magnetic field. *Acta Mater.*, 2008, 56, p.3146-3161.

[246] LI Xi, GAGNOUD Annie, FAUTRELLE Yves, *et al*. Dendrite fragmentation and columnar-to-equiaxed transition during directional solidification at lower growth speed under a strong magnetic field. *Acta Mater.*, 2012, 60, p.3321-3332.

[247] LI Xi, FAUTRELLE Yves, REN Zhongming. Morphological instability of interface, cell and dendrite during directional solidification under strong magnetic field. *J. Cryst. Growth*, 2011, 318, p.23-27.

[248] WANG Jiang, FAUTRELLE Yves, REN Zhongming, *et al*. Thermoelectric magnetic force acting on the solid during directional solidification under a static magnetic field. *App. Phys. Letts*. 2012, 101, p.2519041-4.

[249] BATTY George. Controlled directional solidification. *J. Amer. Soc. Naval Eng.*, 1934, 46, p.299-315.

[250] SOMMERFELD A. The statistical theory of thermoelectric, Galvano- and thermo-magnetic phenomena in metals. *Rev. Mod. Phys.*, 1931, 3, p.1-42.

[251] BRIDGMAN W. P. The connections between the four transverse Galvanomagnetic and thermomagnetic phenomena. *Proc. Amer. Acad.*, 1918, 53, p.269-386.

[252] MORSE M. P. The quantum mechanics of electrons in crystals. *Phys. Rev.*, 1930, 35, p.1310-1324.

[253] Thomas Johann Seebeck: http://www.dea.icai.upco.es/romano/sp4/tpares_all.pdf.

[254] OERSTED Christian Hans, *The soul in nature with supplementary contributions*/ LEONORA, horner B. J. ed. London: Henry G. Bohn, 1852.

[255] Jean Charles Athanase Peltier: http://en.wikipedia.org/ Jean-Charles-Athanase-Peltier.

[256] WOODALL J. A. The direct measurement of the Peltier coefficient. *Proc. Phys. Soc.*, 1935, 47, p.615-625.

[257] History of thermoelectric: http://www.customthermoelectric.com/History.html.

[258] TRAINER Matthew, Lord Kelvin - recipient of the John Fritz Medal in 1905, *Phys. Perspective*, 2008, 10, p.212-223.

[259] KALDRE Imants. *Influence of thermoelectric on the liquid metal in an external magnetic field*. Co-joint Ph. D Thesis of University of Latvia & University of Grenoble, 2010, p.23-33.

[260] JOULE Prescott James. On the mechanical equivalent of heat. *Philosophical Trans. Royal Soc. London*, 1850, 140, p.61-82.

[261] DURAND Isabelle, KASSNER Klaus, MISBAH Chaouqi, *et al*. Strong coupling between diffusive and elastic instabilities in directional solidification. *Phys. Rev. Letts.*, 1996, 76, p. 3013-3016.

[262] KALDRE I., FAUTRELLE Y., ETAY J., *et al*. Investigation of liquid phase motion generated by the thermoelectric currents and magnetic field interaction. *Magnetohydrodynamics.*, 2010, 46, p.317-326.

[263] TANAKA Matoko. *Study on the influence of thermoelectric effect on the liquid-solid interface stability*. Ph. D Thesis, Grenoble Institute of Technology, 1994.

[264] BUTLER L. S., SINHA G. Forward modelling of applied geophysics methods using COMSOL and comparison with analytical and laboratory analogy models. *Comput. Geosci.*, 2012, 42, p.168-176.

[265] COMSOL Multiphysics: http://www.comsol.com/.

[266] TARSHIS A. L., WALKER L. J., GIGLIOTTI X. F. Solidification. *Ann. Rev. Mater. Sci.*, 1972, 2, p.181-216.

[267] KALDRE I., FAUTRELLE Y., ETAY J., *et al*. Thermoelectric current and magnetic field interaction influence on the structure of directionally solidified Sn-10wt%Pb alloy. *J. Alloy Com.*, 2013, 571, p.50-55.

[268] MATHIESEN H. R., ARNBERG L., RAMSOSKAR K., *et al*. Time-resolved X-ray imaging of Al alloy solidification process. *Mater. Metall. Trans. B.*, 2002, 33, p.613-623.

[269] SCHENK T., NGUYE-THI H., GASTALDI J., *et al*. Application of synchrotron X-ray imaging to the study of directional solidification of Al-based alloys. *J. Cryst. Growth.*, 2005, 275, p.201-208.

[270] MATHIESEN H. R., ARNBERG L., MO F., *et al*. Time-resolved X-ray imaging of dendritic growth in binary alloys. Phys. Rev. Letts., 1999, 83, p. 5062-5065.

[271] BUFFET A., NGUYEN THI H., BOGNO A., *et al*. Measurement of solute profiles by means of synchrotron X-ray radiography during directional solidification of Al-4wt%Cu alloys. *Mater. Sci. Forum*, 2010, 649, p.331-336.

[272] BURDEN H. M., HEBDITCH J. D., HUNT D. J. Macroscopic stability of a planar, cellular or dendritic interface during directional freezing. *J. Cryst. Growth*, 1973, 20, p.121-124.

[273] TRIVEDI R., LIU S., MAZUMDER P., *et al.* Microstructure development in the directionally solidified Al-4.0wt%Cu alloy system. *Sci. Tech. Adv. Mater.*, 2001, 2, p.309-320.

[274] TRIVEDI R., MIYAHARA H., MAZUMDER P., *et al.* Directional solidification microstructures in diffusive and convective regimes. *J. Cryst. Growth*, 2001, 222, p.365-379.

[275] PLEVACHUK Y., SKLYARCHUK V., YAKYMOVYCH A., *et al.* Density, viscosity and electrical conductivity of hypoeutectic Al-Cu liquid alloys. *Metall. Mater. Trans. A*, 2008, 39, p.3040-3045.

[276] CHANG H. C., WILLCOX R. W. Control of interface shape in the vertical Bridgman-Stockbarger technique. *J. Cryst. Growth*, 1974, 21, p.135-140.

[277] ZAWILSKI T. K., CUSTODIO C. C. M., DEMATTEI C. R., *et al.* Control of growth interface shape using vibroconvective stirring applied to vertical Bridgman growth. *J. Cryst. Growth*, 2005, 282, p.236-250.

[278] EL-MAHALLAWY A. N. Effect of some thermal parameters on the directional solidification process. *J. Cryst. Growth*, 1978, 44, p.251-258.

[279] SZEKELY J., CHHABRA S. P. The effect of natural convection on the shape and movement of the melt-solid interface in the controlled solidification of lead. *Metall. Trans.*, 1970, 1, p.1195-1203.

[280] World record: The strongest magnetic fields created: http://phys.org/news/2011-06-world-strongest-magnetic-fields.html.

[281] KARAL Robert. Study on influence of growth conditions on position and shape of crystal/melt interface of alkali lead halide crystals at Bridgman growth. *J. Cryst. Growth*, 2012, 360, p.162-166.

[282] SHAEFER J. R., CORIELL R. S. Convection-induced distortion of a solid-liquid interface. *Metall. Trans. A*, 1984, 15, p.2109-2115.

[283] BURTON A. J., PRIM C. R., SLICHTER P. W. The distribution of solute in crystals growth from the melt: part 1 theoretical. *J. Chem. Phys.*, 1953, 21, p.1987-1991.

[284] BURTON A. J., PRIM C. R., SLICHTER P. W. The distribution of solute in crystals growth from the melt: part 2 experimental. *J. Chem. Phys.*, 1953, 21, p.1991-1996.

[285] TILLER A. W., JACKSON A. K., RUTTER W. J., *et al.* The redistribution of solute atoms during the solidification of metals. *Acta Metall.*, 1953, 1, p.428-437.

[286] BOLLING F. G., TILLER A. W. Growth from the melt. part 2: Cellular interface morphology. *J. Appl. Phys.*, 1960, 31, p.2040-2045.

[287] MA X. D., SAHM R. P. Primary spaceing in directional solidification. *Metall. Mater. Trans. A*, 1998, 29, p.1113-1119.

[288] CHEN Q. Y., XU J. J. Global theory of steady deep-cellular growth in directional solidification. *Phys. E.*, 2011, 83, p.04160101-15.

[289] LI Xi, GAGNOUD Annie, FAUTRELLE Yves, *et al*. Influence of thermoelectric effects on the morphology of Al-Si eutectic during directional solidification under an axial strong magnetic field. *J. Cryst. Growth*, 2013, 367, p.94-103.

[290] FAUTRELLE Y., CHILDRESS S. Convective dynamos with intermediate and strong fields. *Geophys. Astrophys. Fluid Dyanmics*, 1982, 22, p.235-279.

[291] BEI H., GEORGE P. E., KENIK A. E., *et al*. Directional solidification and microstructures of near-eutectic Cr-Cr_3Si alloys. *Acta Mater.*, 2003, 51, p.6241-6252.

[292] LI Chuangjun, REN Zhongming, REN Weili, *et al*. Design and application of differential thermal analysis apparatus in high magnetic field. *Rev. Sci. Instrum.*, 2009, 80, p.073907-5.

[293] LI Chuangjun. *Investigation of nucleation and growth of metals in high magnetic fields by differential thermal analysis*. Ph. D Thesis of Shanghai University, 2010, p.33-45.

[294] KISSINGER H. E. Reaction kinetics in differential thermal analysis. *Anal. Chem.*, 1957, 29, p.1702-1706.

[295] GUPTA K. A., GUPTA B. V., PETERS H. R., *et al*. The effect of addition of high-density polyethylene on the crystallization and mechanical properties of polypropylene and glass-fiber-reinforced polypropylene. *J. Appl. Poly. Sci.*, 1982, 27, p.4669-4686.

[296] GUPTA K. A., PURWAR N. S. Crystallization of PP in PP/SEBS blends and its correlation with tensile properties. *J. Appl. Poly. Sci.*, 1984, 29, p.1595-1609.

[297] CHEN Cheng, FEI Bin, PENG Shuwen, *et al*. Nonisothermal crystallization and melting behavior of poly(3-hydroxybutyrate) and maleated poly(3-hydroxybutyrate). *Euro. Poly. J.*, 2002, 38, p.1663-1670.

[298] HUANG C. S., GLICKSMAN E. M. Fundamentals of dendritic solidification 1: steady-state tip growth. *Acta Meatll.*, 1981, 29, p.701-715.

[299] ELLIOTT R. *Eutectic solidification processing-crystalline and glassy alloys*. London: Butterworths,1983, p.92-156.

[300] VIVES C., PERRY C. Effects of magnetically damped convection during the controlled solidification of metals and alloys. *Int. J. Heat Mass Transfer.*, 1987, 30, p.479-496.

[301] LAPPA M. Review: Thermal convection and related instabilities in models of crystal growth from the melt on earth and in microgravity: past history and current status. *Cryst. Res. Technol.*, 2005, 40, p.531-549.

[302] LIU Tie, WANG Qiang, GAO Ao, *et al*. Effects of a high magnetic field on the phase equilibria of Mn-Sb system during solidification process. *J. Alloy. Comp.*, 2001, 509, p.5822-5824.

[303] HOGAN M. L. The 'coupled region' concept in eutectic solidification. *J. Aust. Inst. Metal.*, 1964, 9, p.228-239.

[304] ATASOY A. O., YILMAZ F., ELLIOTT R. Growth structures in Al-Si alloys 1: the coupled zone. *J. Cryst. Growth*, 1984, 66, p.137-146.

[305] VERHORVEN D. J., HOMER H. R. The growth of off-eutectic composites from stirred melts. *Metall. Trans.*, 1970, 1, p.3437-3441.

[306] CLARK N. J., EDWARDS T. J., ELLIOTT R., Eutectic solidification. *Metall. Trans. A*, 1975, 6, p.232-233.

[307] JORDAN M. R., HUNT D. J. Morphological observations of the eutectic-dendrite breakdown in the Al-$CuAl_2$ system. *J. Cryst. Growth*, 1971, 11, p.141-146.

[308] HOGAN M. L. The solidification of binary eutectic alloys. *J. Aust. Inst. Metal.*, 1961, 6, p.279-288.

[309] VERHOEVEN D. J., GIBSON D. E. Hysteresis in the composite-to-dendrite transition in off-eutectic Sn-Pb alloys. *Metall. Trans.*, 1972, 3, p.1893-1898.

[310] VERHOEVEN D. J., KINGERY K. K., HOFER R. The effect of solute convection upon macrosegregation in off-eutectic composite growth. *Metall. Trans. B*, 1975, 6, p.647-652.

[311] BURDEN H. M., HUNT D. J. The extent of the eutectic range. *J. Cryst. Growth*, 1974, 22, p.328-330.

[312] BURDEN H. M., HUNT D. J. Cellular and dendritic growth. *J. Cryst. Growth*, 1974, 22, p.109-116.

[313] LI Shuangming, MA Bole, LI Xiaoli, *et al*. Competitive growth of different phases in eutectic alloys under directional solidification. *Sci. in China Ser. E*, 2005, 48, p.270-281.

[314] RAMANI A., BECKERMANN C. Dendrite tip growth velocities of setting NH_4Cl equiaxed crystals. *Script. Mater.*, 1997, 36, p.633-638.

[315] GOWLING G. T. Magnetohydrodynamics. *Rep. Prog. Phys.*, 1962, 25, p.244-286.

[316] CABLE M. Deformation of fluid inclusions in glass melts, part 1: infinitely deformable inclusions. *Phys. Chem. Glasses*, 2002, 43, p.271-275.

[317] COPLEY M. S., GIAMEI F. A., JOHNSON M. S., *et al*. The origin of freckles in unidirectionally solidified castings. *Metall. Trans.*, 1970, 1, p.2193-2204.

[318] YUANG Lang, LEE D. Peter, A new mechanism for freckle initiation based on microstructural level simulation. *Acta Mater.*, 2012, 60, p.4917-4926.

[319] GIAMEO F. A., KEAR H. R. On the nature of freckles in nickel base superalloys. *Metall. Trans.*, 1970, 1, p.2185-2192.

[320] SHIRTCLIFFE L. G. T., HUPPERT E. H., WORSTER G. M. Measurement of the solid fraction in the crystallization of a binary melt. *J. Cryst. Growth*, 1991, 113, p.566-574.

[321] MAKKONEN L. Solid fraction in dendritic solidification of liquid. *Appl. Phys. Lett.*, 2010, 96, p.0919101-3.

[322] MCNALLY J. P. 3D imaging of crystal defects. *Nature*, 2013, 496, p.37-38.

[323] GRANGE G., JOURDAN C., GASTALDI J., *et al*. Strain visualization of the onset of morphological instability and defect formation in cellular solidification of a dilute Al-Cu alloy. *Acta Mater.*, 1997, 45, p.2329-2338.

[324] REINHART G., BUFFET A., NGUYEN-THI H., *et al*. In-situ and Real-time analysis of the formation of strains and microstructure defects during solidification of Al-3.5wt Pct Ni alloys. *Metall. Mater. Trans. A*, 2008, 39, p.865-874.

[325] ZHU Weiwei, REN Zhongming, REN Weili, *et al*. Effects of high magnetic field on the unidirectionally solidified Al-Al_2Cu eutectic crystal orientations and the induced microstructures. *Mater. Sci. Eng. A*, 2006, 441, p.181-186.

[326] LI Xi, REN Zhongming, FAUTRELLE Yves. Effect of a high axial magnetic field on the microstructure in a directionally solidified Al-Al2Cu eutectic alloy. *Acta Mater.*, 2006, 54, p.5349-5360.